Ultra-wideband coherent optical transmission systems : from modeling and optimization to experimental demonstrations beyond 100 Tbit/s

Salma Escobar Landero

INSTITUT POLYTECHNIQUE DE PARIS

NNT : 2024IPPAS012

Thèse de doctorat

Ultra-wideband coherent optical transmission systems: from modeling and optimization to experimental demonstrations beyond 100 Tbit/s

Thèse de doctorat de l'Institut Polytechnique de Paris
préparée à Télécom SudParis

École doctorale n°626 École doctorale de l'Institut Polytechnique de Paris (EDIPP)
Spécialité de doctorat: Électronique et optoélectronique

Thèse présentée et soutenue à Boulogne-Billancourt, le 28 Mai 2024, par

Salma ESCOBAR LANDERO

Composition du Jury :

Christophe Peucheret Professeur, Université de Rennes (FOTON Institute)	Président
Gabriella Bosco Professeur, Politecnico di Torino	Rapporteur
Elie Awwad Maître de Conférences, Télécom Paris	Examinateur
Sylvie Lebrun Maître de Conférences, L'Institut d'Optique Graduate School	Examinateur
Badr-Eddine Benkelfat Professeur, Télécom SudParis	Directeur de thèse
Abel Lorences-Riesgo Docteur, Huawei Paris Research Center	Co-directeur de thèse

Acknowledgments

First, I would like to extend my deepest gratitude to the members of the jury for their time and effort in reading and evaluating my report.

The path of my PhD journey was guided by the support of two remarkable industrial advisors, Dr. Ivan Fernandez de Jauregui Ruiz and Dr. Abel Lorences Riesgo. I thank Ivan for his patience and guidance, crucial throughout the foundational steps of my PhD. His mentorship has shaped my professional trajectory, and for that, I am very grateful. I am also deeply grateful to Abel for stepping into the role of supervisor unexpectedly. His support during this transition has been invaluable. Moreover, I thank him for the valuable feedback that helped me navigate through complex challenges with a clearer perspective. His advice and encouragement have been instrumental in my progress and have significantly enhanced my research experience and outcomes.

My sincere thanks to Prof. Badr-Eddine Benkelfat, my university supervisor. His assistance through all the administrative processes, coupled with his keen interest in my progress and evolution both within the university and the company, have been invaluable. I also extend my gratitude to the SmartNet program, which was essential for the start of my life in research. A special thanks goes to Dr. Stylianos Sygletos for his trust and encouragement.

I would like to extend a special thanks to all the people at Huawei Optical Communications Laboratory, particularly the WDM team, for their assistance and collaboration in the research related to this thesis. I want to thank Prof. Yann Frignac for his incredibly motivating leadership driving us to strive for excellence. Many thanks to Dylan Le Gac and Xiaohui Zhao, for the knowledge exchanged in the lab and the memorable experiences, especially during the field trial in Bayonne. I also thank Sami Mumtaz, Xin Yang, Tarek Eldahrawy and Flavio Nogueira, for the fun times and the ping pong games.

I appreciate the positive atmosphere provided by everyone in our laboratory. I am particularly grateful to Dr. Gabriel Charlet, for all the opportunities I have received since my Master's internship and his ongoing guidance throughout this journey.

The friendship of Monserrat Roman, Daryna Kravchenko, Shuqi Yu and Juan Marcelo Parra since the Master's program has been a source of encouragement and strength. Their support has been invaluable in my decision to pursue a PhD and through this process. And those I have met along the way, Samuel Batissou, Charles Pillet, Gianpietro Consolaro, Matei Moldoveanu, Roberto Medina, Harenome Razanajato,

Celena Nsungani and Jiaxin Xu, thank you for your friendship and the incredible moments we have shared together.

To my family in Mexico, who have consistently provided me comfort and encouragement. Particularly to my parents and sister, their love has been the driving force behind my efforts. Lastly, to Julien, his unconditional love and support have been a constant source of strength in this journey. Sharing this adventure with him makes every step worthwhile.

To everyone who has been a part of this adventure, I am deeply grateful for your contributions to my academic and personal growth.

Contents

Table of Acronyms

Notation	Description
ADC	analog-to-digital converter.
AIR	achievable information rate.
ASE	amplified-spontaneous emission.
AWGN	additive white Gaussian noise.
B2B	back-to-back.
BDFA	bismuth-doped fiber amplifier.
BER	bit error rate.
BICM	bit-interleaved coded modulation.
COI	channel of interest.
DAC	digital-to-analog converter.
DBP	digital backpropagation.
DCF	dispersion compensating fibers.
DM	dispersion-managed.
DPD	digital pre-distortion.
DRA	distributed Raman amplifier.
DSP	digital signal processing.
EDFA	erbium-doped fiber amplifier.
EGN	enhanced Gaussian noise.
FEC	forward error correction.
FWM	four-wave mixing.
GA	genetic algorithm.
GD	gradient descent.
GFF	gain flattening filter.
GMI	generalized mutual information.
GN	Gaussian noise.
GVD	group velocity dispersion.
IGN	incoherent Gaussian noise.
INT	interfering channel.
ISRS	inter-channel stimulated Raman scattering.
ITU	international telecommunication union.
LO	local oscillator.
MCF	multicore fiber.
MCI	multi-channel interference.
MI	mutual information.
ML	machine learning.
MZM	Mach-Zehnder modulator.
nGMI	normalized generalized mutual information.
NF	noise figure.

Notation	Description
NLI	nonlinear interference.
NLSE	nonlinear Schrödinger equation.
NSR	noise-to-signal ratio.
OADM	optical add-drop multiplexer.
ODE	ordinary differential equation.
OMS	optical multiplexing section.
OSA	optical spectrum analyzer.
OSNR	optical signal-to-noise ratio.
PAS	probabilistic amplitude shaping.
PBC	polarization beam combiner.
PBS	polarization beam splitter.
PCS	probabilistic constellation-shaped.
PDL	polarization dependent loss.
PMD	polarization mode dispersion.
PSCF	pure-silica-core fiber.
PSO	particle swarm optimization.
PSD	power spectral density.
QAM	quadrature amplitude modulation.
QoT	quality of transmission.
QPSK	quadrature phase shift keying.
RSNR	required signal-to-noise ratio.
SCI	self-channel interference.
SDM	space division multiplexing.
SE	spectral efficiency.
SNR	signal-to-noise ratio.
SSMF	standard single mode fiber.
SOA	semiconductor optical amplifier.
SPM	self-phase modulation.
SRS	stimulated Raman scattering.
SSFM	split-step Fourier method.
TDFA	thulium-doped fibre amplifier.
TIA	transimpedance amplifier.
TLS	tunable laser source.
UT	uncompensated transmission.
VOA	variable optical attenuator.
WDL	wavelength-dependent loss.
WDM	wavelength division multiplexing.
WS	waveshaper.
WSS	wavelength selective switches.
UWB	ultra-wideband.
XCI	cross-channel interference.
XPM	cross-phase modulation.

List of Figures

List of Tables

Chapter 1

Introduction

Over the past few decades, the world has witnessed a major digital revolution that transformed the use of communication networks. As the backbone of our information society, optical fiber communications have continuously evolved to support the unprecedented traffic growth brought by the digital era. The foundational development of optical systems started in the 1970s, driven by the advent of compact and efficient semiconductor lasers [1] and the introduction of low-loss optical fibers [2]. Further technological progress was achieved in 1987 with the development of optical amplification, boosting the signal power and extending transmission distance [3, 4]. During the 1990s, the focus shifted towards the implementation of wavelength-division multiplexing (WDM) to enhance system capacity, by transmitting multiple optical channels over a single fiber through various lasers operating at different wavelengths. The commercial availability of coherent receivers and the integration of digital signal processing (DSP) in 2008 enabled the use of advanced modulation formats that utilize both amplitude and phase of the optical carrier for encoding information [5].

In recent years, the demand for data traffic has significantly increased due to the rise of new digital applications such as high-definition video streaming and cloud-based services. These trends are expected to continue, especially with the development and widespread adoption of virtual/augmented reality technologies. In response, optical fiber communications will need to adopt new strategies to cope with the expected growth in network traffic.

Ultra-wideband (UWB) systems are a promising solution to tackle the capacity challenges in the upcoming years. This technology increases the per-fiber throughput by extending the transmission bandwidth beyond the traditional C-band. Therefore, a greater number of WDM channels are transmitted without the need to add or replace fibers, making it a cost-effective technique able to exploit the currently deployed fibers.

Figure 1.1 shows the throughput evolution of UWB systems over the last three decades by citing some published works. Soon after the erbium-doped fiber amplifier (EDFA) invention [3, 4], in the early 1990s, EDFAs emerged as a technology that paved the way for WDM systems in the C-band (1530 nm to 1565 nm). Consequently, to increase the optical bandwidth transmission, the development of EDFA with flattened and

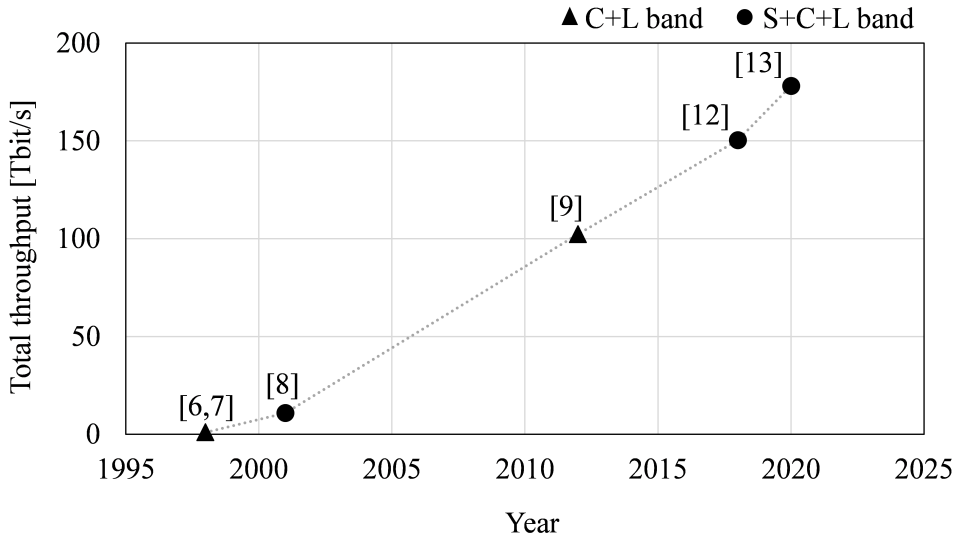

Fig. 1.1: Historical evolution of the throughput achieved by UWB transmissions over C+L band (triangles) and S+C+L band (circles).

broader bandwidths of amplification was crucial. In 1998, advances in optical broadband amplification toward the long wavelength band or L-band (1565 nm to 1625 nm) enabled the first 1 Tbit/s transmissions in C+L systems over more than 400 km of fiber [6, 7]. In subsequent years, the neighboring S-band (1460 nm to 1530 nm) appeared to be a viable option to further expand the transmission bandwidth due to the low-loss characteristic of silica fibers and the availability of gain-shifted thulium-doped fiber amplifiers (TDFA). In 2001, the combination of TDFA and distributed Raman amplification (DRA) registered 10.9 Tbit/s over the S+C+L band along 117 km [8].

Furthermore, thanks to the use of coherent detection and DSP, a notable growth in throughput was observed a decade later, such as a C+L demonstration achieving 102.3 Tbit/s over 240 km of pure-silica-core fibers (PSCF) [9]. These capacity benefits have driven the evolution of C+L systems into a mature solution, which is currently used in deployed optical communications [10, 11]. To further exploit UWB systems, during the last years, many research efforts have been dedicated to enhancing the multi-terabit-capacity of S+C+L transmissions [12, 13].

Figure 1.2 offers a comprehensive review of the state-of-the-art in UWB transmissions from 2021 to 2024, as context for this work. Particular emphasis is placed on the trade-off between data rate and distance, analyzing the number of bands and spans of each demonstration. Recent advancements in UWB technology have led to impressive demonstrations, achieving data transmission rates exceeding 200 Tbit/s in standard single mode fibers (SSMF) [14, 15]. Alternatively, some of them incorporate space division multiplexing (SDM) through the use of multicore fibers (MCF) [16]. A key factor in these demonstrations was the utilization of a low symbol rate, typically less than 25 Gbaud. This approach, in contrast to higher baud rates, enhances signal performance by reducing the transceiver's sensitivity to noise. Recent experiments using UWB silicon

photonic-based transceivers with larger baud rates, around 49 Gbaud, registered 214.7 Tbit/s of estimated total throughput [17].

Although the previously mentioned transmissions have reached very high data rates, their application has been primarily limited to single spans of approximately 50 km of fiber. However, by applying forward and backward DRA, demonstrations with a relative large baud rate, about 67 Gbaud, have achieved a real-time capacity of 112.8 Tbit/s across 101 km of large-core low-loss fiber [18]. To explore the potential of long-distance UWB systems, recirculating loops have been used to transmit data over considerable distances. These include S+C+L transmissions along 3,001 km of low-loss, four-MCF and 10,072 km of SSMF, achieving throughput of 85.7 Tbit/s [19] per core and 46 Tbit/s [20], respectively.

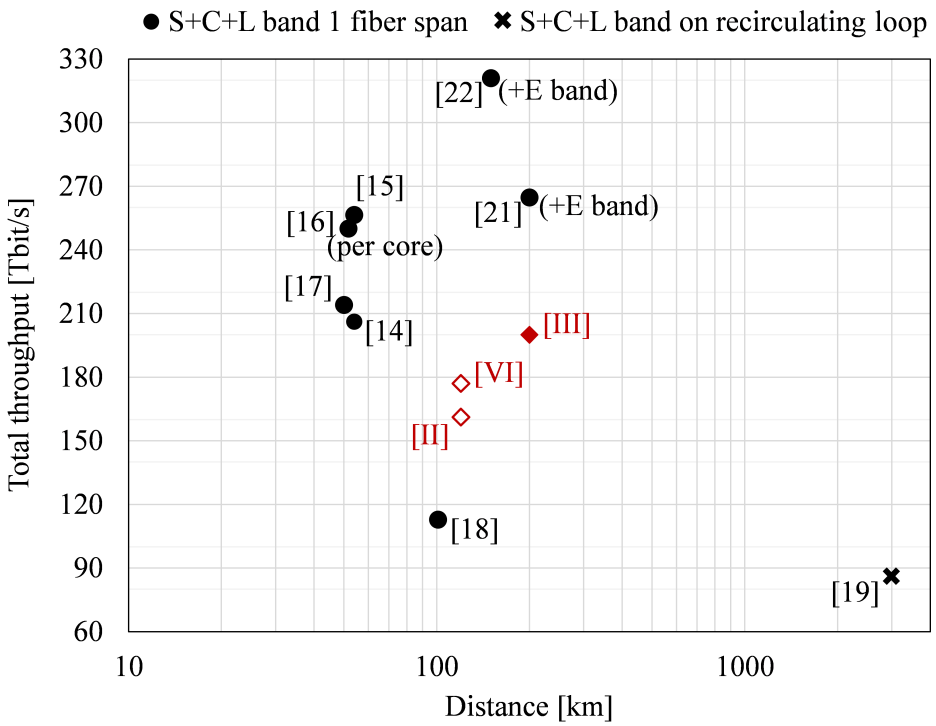

Fig. 1.2: Throughput versus distance for experimental UWB demonstrations registered from 2021 to 2024. The positioning of this work is shown in red markers. Filled markers indicate that the throughput is measured for all the channels and unfilled markers indicate that the throughput is estimated based on the average measurements of each band.

Beyond S+C+L band transmission, recently it has been demonstrated that with the use of bismuth-doped fiber amplifiers (BDFAs) the total system bandwidth can be expanded to over 206.6 nm (27 THz) by the integration of the E-band (1360 nm to 1460 nm). This bandwidth expansion supported by the incorporation of rare-earth doped amplifiers and DRA, increased the capacity of UWB systems to 264.7 Tbit/s over 200 km [21] and levels beyond 300 Tbit/s up to 150 km of SSMF [22].

Notably, these demonstrations prove that UWB systems are a promising technology to increase the throughput in optical transmissions. How-

ever, this technology faces several challenges, such as the wavelength dependence of fiber parameters such as fiber loss, chromatic dispersion, and effective area. Another relevant issue is the nonlinear inter-channel stimulated Raman scattering (ISRS) effect. This phenomenon transfers power from higher to lower frequencies during propagation, severely affecting performance and compromising system stability.

To address these issues, multiple research efforts led to the development of various mathematical models designed to accurately represent physical impairments in UWB systems. The derivation of approximate closed-form models allowed the prediction of transmission performance in real-time [23]. Furthermore, as will be discussed in this thesis, such models can play an important role in understanding and maximizing the performance of UWB systems, as well as providing strategies to overcome the main challenges of UWB systems.

1.1 This work

This PhD thesis focuses on investigating the enablers, challenges, and opportunities associated with UWB systems. It reviews and builds upon the theoretical models that describe the wavelength-dependent impairments and nonlinear distortions imposed by the ISRS effect. By integrating these models with practical approaches, one of the main goals of this thesis is to propose a solution for optimizing power pre-emphasis and inline amplifier settings, thereby improving UWB transmission performance and system design. To evaluate the proposed optimization strategy, a numerical validation is conducted using machine learning-based algorithms. This comparison not only validates the strategy to closely maximize capacity but also highlights its potential as a simpler alternative to more complex optimization methods.

The second major contribution of this thesis includes the experimental validation within an S+C+L WDM system, further confirming the practical applicability of the proposed strategy in an actual UWB transmission. These experimental results are presented with red markers in Fig. 1.2, in order to compare our UWB transmission efforts with those of the current state-of-the-art.

Considering the limitations seen in previous S+C+L transmissions, our experiments incorporate:

- The use of a relatively large symbol rate, around 60 Gbaud or 70 Gbaud, which is in line with current industry trends.
- Longer transmissions without any active power equalization between each span, over two spans of 60 km of SSMF or two spans of 100 km of PSCF.

Despite addressing these realistic conditions and with the aid of model-based optimization techniques, we achieved significant throughput of 161.1 Tbit/s [II], 177 Tbit/s [VI] and 200.5 Tbit/s [III] across a total bandwidth of 150 nm (18.7 THz).

Lastly, this thesis integrates experimental measurements from the UWB transmissions to refine the accuracy of model-based predictions. By creating a virtual replica of the physical layer, this work stands as one of the first experimental studies conducted to validate the accuracy of signal-to-noise ratio (SNR) estimations through closed-form models for transmissions beyond the C+L band. Furthermore, using these models, this research offers valuable insights into the impairments affecting transmission quality, investigates scenarios for UWB system failure and outlines a strategy for recovery.

To summarize, the goal of this thesis is to integrate experimental measurements with theoretical models, leveraging model-based predictions and optimization techniques to improve UWB system performance.

1.2 Thesis outline

The remaining chapters of this thesis are organized as follows:

Chapter 2 lays the foundational theoretical background required for the later chapters. It covers the basic concepts of coherent optical communications and the key propagation effects in optical fibers.

Chapter 3 is structured into two parts, first, we review the Gaussian noise (GN) model, focusing on its application in optimizing optical transmissions. Additionally, we explore the ISRS GN closed-form model, which is an extension of the GN model more accurate for UWB systems. The second part is dedicated to this work. We present the ASE-NL heuristic, a simple and fast optimization strategy for multi-band systems and using this tool, we study how capacity scales with bandwidth. This chapter aims to highlight the importance of model-based power optimization techniques in the design of UWB systems and introduce practical equalization techniques, supported by simulation results that validate these approaches.

Chapter 4 presents an in-depth analysis of three experimental S+C+L transmissions shown in Fig. 1.2 [II,III,VI]. The ASE-NL heuristic is experimentally validated as a power optimization technique for S+C+L systems. In particular, we highlight the relevance of the digital twin as a significant tool to provide accurate model-based predictions of performance. Additionally, we present an important challenge in UWB systems: the system failure of one band (amplifiers loss). We assess the impact on system performance after the loss of either the S-band or the L-band, and we include recovery strategies for dealing with such failures.

Chapter 5 summarizes this thesis, highlighting the most significant contributions of this work. We also present a perspective for future research, built upon the work established in this thesis.

1.3 List of publications

As first author

I **S. Escobar-Landero**, I. F. de Jauregui Ruiz, A. Ferrari, D. Le Gac, Y. Frignac, and G. Charlet. "Link Power Optimization for S+C+L Multi-band WDM Coherent Transmission Systems". *Optical Fiber Communications Conference and Exhibition (OFC)*, paper W4I.5 (2022)

II **S. Escobar-Landero**, X. Zhao, A. Lorences-Riesgo, D. Le Gac, Y. Frignac, and G. Charlet. "Modeling and Optimization of Experimental S+C+L WDM Coherent Transmission System". *Optical Fiber Communications Conference and Exhibition (OFC)*, paper Th3F.4 (2023)

III **S. Escobar-Landero**, X. Zhao, D. Le Gac, A. Lorences-Riesgo, T. Viret-Denaix, Q. Guo, L. Gan, S. Li, S. Cao, X. Xiao, N. El Dahdah, A. Gallet, S. Yu, H. Hafermann, L. Godard, R. Brenot, Y. Frignac and G. Charlet. "Demonstration and Characterization of High- Throughput 200.5 Tbit/s S+C+L Transmission over 2x100 PSCF Spans". *Journal of Lightwave Technology (JLT)*, vol. 41, pp. 36683673 (2023)

IV **S. Escobar-Landero**, A. Lorences-Riesgo, X. Zhao, Y. Frignac, and G. Charlet. "Ultra-Wideband High-Capacity Transmission Systems: Challenges and Opportunities". *European Conference on Optical Communication (ECOC)* (Invited), paper M.A.5.1 (2023)

V **S. Escobar-Landero**, A. Lorences-Riesgo, X. Zhao, Y. Frignac, and G. Charlet. "S+C+L High-Capacity Transmission Systems: Challenges and Opportunities".*Journal of Lightwave Technology (JLT)*, vol. 42, pp. 4260-4270 (2024)

As co-author

VI X. Zhao, **S. Escobar-Landero**, A. Lorences-Riesgo, D. Le Gac, L. Godard and et al. "Impact of WDM-Band Drop on S+C+L Multi-Band Optical Transmission Systems". *Asia Communications Photonics Conference (ACP)*, paper ACPPOEM-0731146 (2023)

VII Y. Frignac, D. Le Gac, A. Lorences-Riesgo, L. Godard, **S. Escobar - Landero**, X. Zhao, E. Pincemin, B. Le Guyader, N. Brochier, Q. Guo, L. Gan, S. Li, S. Cao, X. Xiao, N. El Dahdah, A. Gallet, I. Demirtzioglou, S. Yu, H. Hafermann, R. Brenot, H. Kechao and G. Charlet. "Record 158.4 Tb/s Transmission over 2x60 km Field SMF Using S+C+L 18THz-Bandwidth Lumped Amplification". *European Conference on Optical Communication (ECOC)*, paper M.A.5.2 (2023)

VIII X. Zhao, D. Le Gac, **S. Escobar-Landero**, A. Lorences-Riesgo, I. Demirtzioglou, H. Hafermann, L. Godard, N. El Dahdah, G.

Gao, M. Tornatore, R. Brenot, Y. Frignac and G. Charlet. "Real-Time 59.2 Tb/s Unrepeated Transmission Over 201.6 km Using Ultra-Wideband SOA as High-Power Booster". *Journal of Lightwave Technology (JLT)*, vol. 41, pp. 3925-3931 (2023)

IX X. Zhao, **S. Escobar-Landero**, D. Le Gac, A. Lorences-Riesgo, T. Viret-Denaix, Q. Guo, L. Gan, S. Li, S. Cao, X. Xiao, N. El Dahdah, A. Gallet, S. Yu, H. Hafermann, L. Godard, R. Brenot, Y. Frignac and G. Charlet. "200.5 Tb/s Transmission with S+C+L Amplification Covering 150 nm Bandwidth over 2x100 km PSCF Spans". *European Conference on Optical Communication (ECOC)*, paper Th3C.4 (2022)

X X. Zhao, D. Le Gac, **S. Escobar-Landero**, I. Demirtzioglou, A. Lorences-Riesgo, L. Godard, N. El Dahdah, G. Gao, R. Brenot, Y. Frignac and G. Charlet. "Real-Time 59.2 Tb/s Unrepeated Transmission Over 201.6 km Using Ultra-Wideband SOA as High-Power Booster". *European Conference on Optical Communication (ECOC)*, paper We4D.5 (2022)

XI X. Yang, A. Ferrari, N. Morette, D. Le Gac, **S. Escobar-Landero**, G. Charlet and Y. Pointurier. "Experimental Impact of Power Re-Optimization in a Mesh Network". *European Conference on Optical Communication (ECOC)*, paper Mo3B.3 (2022)

XII I. Demirtzioglou, D. F. Bendimerad, I. F. de Jauregui Ruiz, D. Le Gac, A. Lorences-Riesgo, N. El Dahdah, A. Gallet, H. Elfaiki, S. Yu, G. Gao, **S. Escobar-Landero**, R. Brenot, Y. Frignac and G. Charlet. "107.6 Tb/s GMI Throughput over 220 km SSMF using Discrete C- and L-Band Amplification across >12 THz". *Optical Fiber Communications Conference and Exhibition (OFC)*, paper W6A.28 (2021)

Patents

P1 92011835PCT01 - Method for amplifier configuration in an ultra-wideband optical network

Chapter 2

Coherent optical communications systems

This chapter aims to lay the foundational physical principles of optical communication necessary to follow the research conducted in this thesis. It offers a review of the basic concepts of an optical transmission system, fiber properties and system performance. Special consideration is given to UWB scenarios, highlighting the amplification techniques that facilitate these transmissions.

Similar to any telecommunication system, an optical communication system transmits information between two locations, whether separated by a few kilometers or even by transoceanic distances. Fundamentally, this system comprises an *optical transmitter* and an *optical receiver*, which are interconnected by a *communication channel*.

The optical transmitter is the origin point where the data is generated and converted into light for transmission. This work is centered on fiber-optic communication systems; therefore, we exclusively employ optical fibers as communication channels, also referred to as *optical link*. As presented in Fig. 2.1, the optical link is composed of several spans of optical fiber. The number of spans depends on the transmission's application. These spans are interconnected by optical amplifiers, placed to compensate for signal loss incurred as the light travels through the

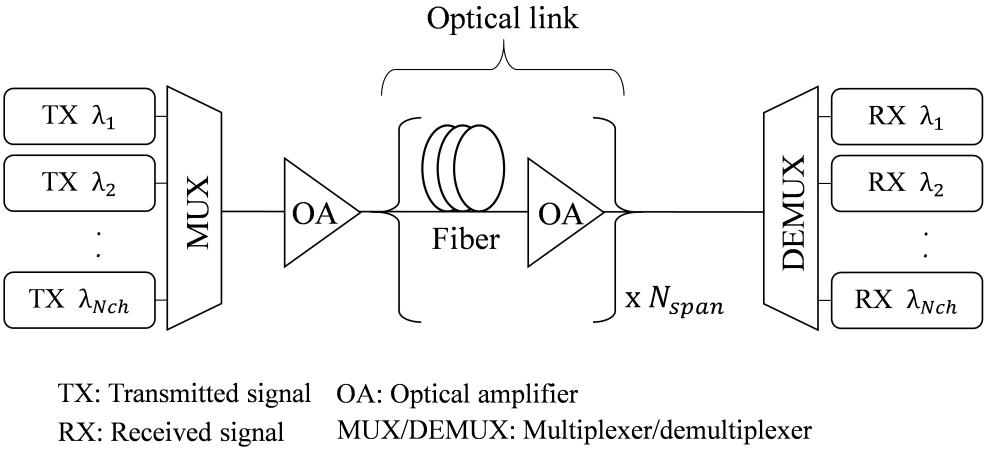

Fig. 2.1: Block diagram of a generic optical communication system.

fiber. However, both the amplifiers and the fiber introduce challenges to signal integrity; amplifiers can add noise, while the fiber can cause signal distortion due to nonlinearities. These factors collectively influence the maximum data throughput achievable over a given distance. Finally, the receiver acquires the signal and treats it to recover the original data.

This section intends to provide a foundational understanding of a generic optical communication system. In the following sections, we will delve into detailed examinations of the components previously mentioned, exploring their roles, functions, and interactions within the system.

2.1 Optical transmitter

The goal of the optical transmitter is to transform signals from the electrical to the optical domain. This is achieved through the modulation of electrical data in an optical carrier, effectively embedding the digital information within the optical signal. This work is focused on coherent dual-polarization transmissions as it is the dominant technology in research and commercial development in optical long-haul systems.

Modern coherent systems enable efficient transmissions, not just by depending on the optical intensity but using all the available physical properties of light, such as amplitude, phase and polarization. Additionally, coherent systems enable access to the optical electric field through digital signal processing (DSP) techniques. For a detailed understanding of this process, we refer to the block diagram shown in Fig. 2.2. Within the scope of this thesis, DSP includes a series of algorithms that perform signal equalization and ensure synchronization between the receiver and the transmitter, in addition to the necessary numerical transforms to restore the signals from physical impairments. As we will discuss in Section 2.3, chromatic dispersion and nonlinearities stand out as one of the most relevant impairments in optical communications. To counter these challenges, *pre-dispersion compensation* and electronic *pre-compensation of nonlinearity* can be implemented at the transmitter [24].

Another significant benefit of DSP is source encoding, which enhances the signal's resilience to noise. Forward error correction (FEC), is a

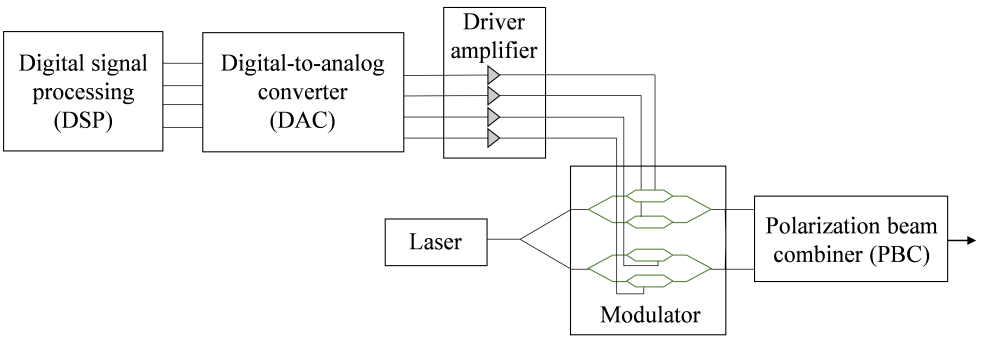

Fig. 2.2: Block diagram of a coherent optical transmitter using dual-polarization division multiplexing (DP-IQM).

control method that introduces redundancy bits, *parity checks*, to the digital source to reduce errors during transmission. The coded bits are subsequently *mapped to symbols* from a specific constellation alphabet, known as a modulation format. Section 2.1.1 includes a more detailed presentation of these schemes.

Once the DSP has been applied, the transmitter modulates the electrical data into the optical carrier before transmitting it over the channel. The discrete waveforms generated by the DSP are split into their real and imaginary part, known as the I and Q components. These components are then converted into electrical analog waveforms through the use of four digital-to-analog converters (DACs) and amplified by the driver.

At the same time, the optical source, typically a semiconductor laser, is split into two to feed two nested Mach-Zehnder modulators (MZMs), which are also driven by the amplified electrical waveforms. After modulation, a polarization beam combiner (PBC) recombines the two polarizations.

In the context of this work, it is important to note that optical transmitters are non-ideal devices that introduce noise and distortions to the signal, which degrades its quality. Section 2.6 will discuss the modeling of these impairments and how they are included in the estimation of transmission performance.

2.1.1 Modulation formats

As we previously discussed, the development of coherent detection enabled modulation formats where information is encoded using both the amplitude and phase of the optical carrier. Figure 2.3, introduces the constellation formats of some of the most well-known modulation formats.

Assuming A as the constellation alphabet of size M and with constellation points such that $A = \{a_1, a_2, ...a_M\}$, the number of coded bits per symbol can be determined as m=$\log_2$(M). The constellation symbols are formed by two real-valued components, Re(a_k) and Im(a_k). Where *Re* and *Im* denote the real and imaginary parts of the complex electric field and are known as the in-phase *(I)* and quadrature *(Q)* components.

Figure 2.3 a) shows the quadrature phase-shift keying (QPSK) format in which the optical phase takes four possible values. This approach allows the transmission of two bits in each time slot, providing a factor of two between the bit rate and symbol rate ($M = 4, m = 2$). To boost capacity, more advanced multi-level modulation techniques are employed, such as 16-level quadrature amplitude modulation (16QAM) presented in Fig. 2.3 b) ($M = 16, m = 4$), which leverages both the intensity and phase of optical signals. Figure 2.3 c) ($M = 64, m = 6$) illustrates how the modulation can be extended to higher-level formats such that each symbol carries 6 bits.

In recent years, probabilistic constellation-shaped (PCS) modulations have attracted particular interest [25]. This technique can be applied to

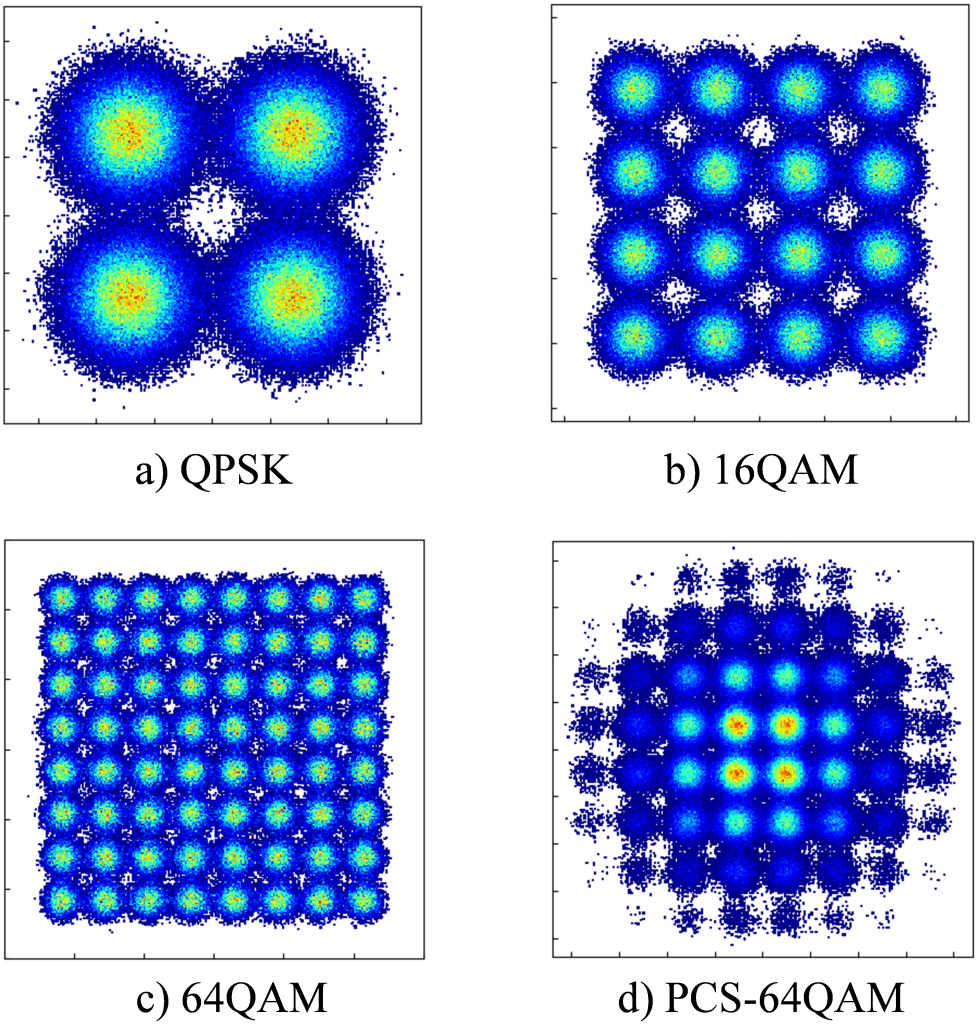

Fig. 2.3: Constellation format for a) QPSK, b) 16QAM, c) 64QAM and d) PCS-64QAM.

any square QAM constellation, where nonuniform probabilities are assigned to the constellation points to approximate the Gaussian distribution. Figure 2.3 d) presents an example of PCS-64QAM with an entropy (H) of 5 bit/symbol. In this technology, a *distribution matcher* will process the uniformly distributed bits from the digital source to set the desired distribution of amplitudes. The bits that represent the shaped amplitudes are subsequently encoded using a *FEC encoder*. The parity bits, which possess a uniform distribution, are allocated to the sign bits of the constellation. It has been demonstrated that PCS-QAM outperforms standard QAM modulation formats without increasing a lot the system and implementation complexity [26]. Another advantage is the flexible bit rate achieved through adaptive entropy. Due to its multiple advantages, PCS has been widely adopted by the industry, which led us to choose to implement this technology in this work.

Moreover, the relevance of choosing certain modulation formats in our research relies on their influence on nonlinear interference generation. In Chapter 3, we will introduce the models developed to capture this dependency.

2.2 Channel multiplexing

The introduction of wavelength division multiplexing (WDM) around 1992 [27] marked a key breakthrough in optical communications, significantly enhancing the throughput capabilities of optical systems. This technique multiplexes several independently modulated channels, each operating at different wavelengths, such that multiple data streams are transmitted simultaneously over the same optical fiber. The success of this technology led to the development of lightwave systems capable of operating at bit rates of 1 Tbit/s by 1996, which represented a capacity increase by a factor of 400 over a period of 6 years [27].

The goal of WDM systems is to increase the number of channels transmitted over a single fiber by incorporating an increasing number of lasers, each operating at different wavelengths. To prevent overlap of channel spectra, the carrier frequencies of two neighboring channels are spaced more than the channel bandwidth. To facilitate the allocation of multiple channels within the optical spectrum, frequency grids have been established by the International Telecommunication Union (ITU). The standard ITU-T G.692 has assigned a set of spectral grids for commercial WDM applications.

Most of the commercial WDM systems are designed to work within the wavelength range from 1530 nm to 1570 nm, referred to as the *conventional* band or C-band, which corresponds to the minimum loss in a silica fiber. Nevertheless, as presented in Section 1, ultra-wideband (UWB) systems emerged to expand system capacity by exploiting the neighboring low-loss spectral window of the L, the S band and beyond. Following the definition of ITU-T G.sup 39, Table 2.1 summarizes the spectral bands.

Band	Descriptor	Wavelength range [nm]	Bandwidth in frequency [THz]
O	Original	1260 to 1360	17.5
E	Extended	1360 to 1460	15.1
S	Short wavelength	1460 to 1530	9.4
C	Conventional	1530 to 1565	4.4
L	Long wavelength	1565 to 1625	7.1
U	Ultra-long wavelength	1625 to 1675	5.5

Table 2.1: Spectral band definition according to ITU-T G.sup 39.

Although the research efforts of transmission systems beyond the C band date back to the late 1990s, the immediate deployment of these technologies has been hindered due to their comparative inefficiency in enhancing capacity, especially when contrasted with the dramatic improvements in spectral efficiency (SE) achieved through digital coherent transceivers, denser WDM systems with narrower channel spacing, and higher-order modulation formats that transmit more bits per symbol. However, after decades of advancements in digital coherent transceiver technology, it has been observed that the improvements in SE started

to decelerate as it approaches the Shannon capacity limit [28]. Consequently, the interest in expanding the wavelength band re-appeared, leading to renewed efforts and investigations into UWB systems as a viable approach to overcome the capacity plateau faced by current technologies.

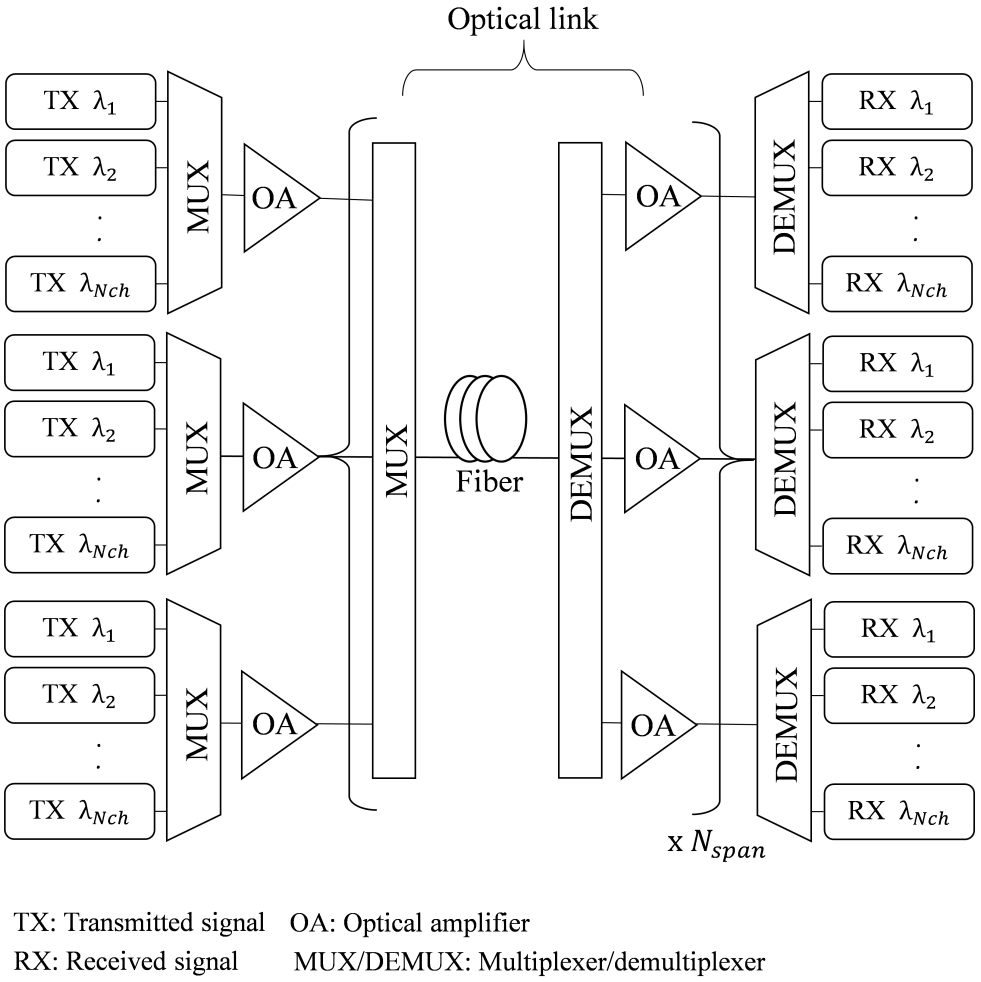

Fig. 2.4: Block diagram of a generic WDM UWB optical communication system.

In the context of UWB systems, the core of our study, we now revise the block diagram of a standard WDM system, depicted in Fig. 2.1, to incorporate the bandwidth extension across multiple windows of spectra. Figure 2.4 introduces the scheme of a generic optical WDM UWB system, designed under the assumption of transmission across three bands. This thesis is focused on transmissions within the C+L and S+C+L bands. However, it is important to acknowledge that a significant amount of research has been dedicated to exploring and integrating alternative bands [22, 29–31].

2.3 Optical link

As previously discussed, in WDM UWB systems, multiple optical channels, denoted as N_{ch}, are combined by an optical multiplexer within each transmission band, with N_b as the total number of bands in the system. Then, using a band multiplexer, a WDM signal is integrated and subsequently propagated through the optical link as shown in Fig. 2.4. In the optical link, optical fibers enable the transmission of light over long distances by confining the optical wave into a microscopic cylindrical glass core. Figure 2.5 illustrates the multiple sections of optical fibers: the core, the cladding, and a protective coating that envelopes them. Specifically, an optical fiber that is designed to support a single spatial mode typically features a core diameter of less than 10 µm, also presented in Fig. 2.5.

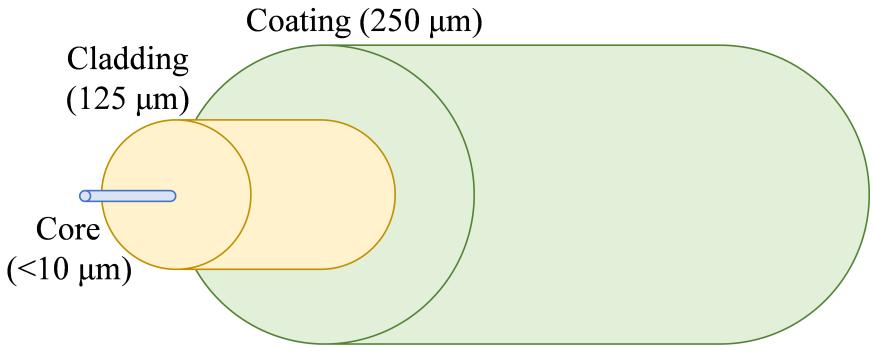

Fig. 2.5: The internal structure of an SSMF, indicating the typical size of each part.

The most commonly used fiber in telecommunications is known as standard-single-mode fiber (SSMF), standardized for widespread use in ITU-T G.652. The core of these fibers is constructed from silica glass, doped with germania to slightly increase its refractive index (by approximately 0.5%) relative to the cladding, which is also made of silica glass [27]. Alternatively, there are fibers designed with a slightly fluorine-doped center core, surrounded by a pure-silica ring-core and fluorine-doped depressed claddings, known as pure-silica-core fiber (PSCF). These fibers have been demonstrated to be suited for broadband transmission in the C and L-bands, offering an attractive option to expand the transmission capacity through fiber [32]. This is explained by two main attributes of the PSCF, the lower wavelength-dependent loss and lower fiber nonlinearities induced by larger effective area (A_{eff}). The low loss is particularly beneficial as it enables to extend the transmission distances. Furthermore, compared with the SSMF A_{eff} of 80 µm^2, PSCF with typical A_{eff} values of 112 µm^2 (Z+ULL), 130 µm^2 (Z+130) and 150 µm^2 (Z+150) are commercially available [33]. The nonlinear reduction caused by larger A_{eff} is especially valuable in UWB systems, as it decreases the impact of the ISRS effect, thus enhancing system performance. Given the attributes and performance advantages of SSMF and PSCF, our work will explore the use of these two types of fiber in different UWB applications.

Regardless of the fiber type, whether SSMF or PSCF, an optical signal will inevitably face losses and distortion resulting from phenomena like

chromatic dispersion and Kerr nonlinearity. Next, we introduce these fundamental challenges associated with light wave propagation in optical fibers, with a special focus on UWB transmission.

In the frame of fiber optical communications, the wave scalar optical field denoted as $A(z,t)$ is assumed to be slowly varying, in both time t and distance z. In its simplest form, the evolution of this wave along the optical fiber can be written as [34]

$$\frac{\partial A}{\partial z} = \underbrace{-\frac{\alpha}{2}A}_{\text{Loss}} \underbrace{-j\frac{\beta_2}{2}\frac{\partial A^2}{\partial t^2}}_{\text{Dispersion}} + \underbrace{j\gamma|A|^2A}_{\text{Kerr nonlinearities}} \tag{2.3.1}$$

referred to as the nonlinear Schrödinger equation (NLSE). The first right-hand side element in eq. (2.3.1) describes the undergoing power loss suffered by the wave at a rate set through α. The detailed characterization of this value will be elaborated in Section 2.3.1.

The second term accounts for the dispersion in the time domain t. This means that different spectral components of the electromagnetic field within an optical fiber travel with different velocities during propagation accounted by β_2. This variation causes waves to arrive at the receiver at different times compared to the transmitter, leading to signal distortion known as intersymbol interference. The issue is typically solved through optical or mainly electronic dispersion compensation as previously mentioned in Section 2.1.

The third term in eq. (2.3.1) represents the nonlinear Kerr effect, where γ is the fiber nonlinear coefficient defined as

$$\gamma = \frac{2\pi}{\lambda}\frac{n_2}{A_{\text{eff}}} \tag{2.3.2}$$

having n_2 as the nonlinear index, λ as the signal wavelength and A_{eff} as the fiber's effective area. Additionally, the nonlinearity is influenced by the signal power ($|A|^2$). Consequently, the nonlinear effects become significant primarily at high power levels. An overview of the elements involved in this phenomenon will be presented in Section 2.3.3 and some nonlinear models will be extensively discussed in Chapter 3.

2.3.1 Fiber attenuation

A crucial parameter in optical fibers is the measure of power loss that occurs when optical signals are transmitted. In the absence of ISRS, the transmitted optical power described by $P(z,f) = |A(z,f)|^2$, can be estimated as [34]

$$P(z,f) = P(0,f)\exp(-\alpha(f)z) \tag{2.3.3}$$

where $P(0,f)$ is the power launched at the input of the fiber with length z and the attenuation coefficient α accounts for the wavelength-dependent loss (WDL) of the fiber.

In the 1960s, optical fibers were characterized by very high losses such that only about 10% of the light entered would emerge from a fiber with

a few meters of length [27]. However, a significant breakthrough came in 1979 when a Japanese research group succeeded in reducing the optical fiber loss to nearly 0.2 dB/km in the infrared wavelength region around 1550 nm [2]. This development came close to the fundamental loss limit set by Rayleigh scattering, representing a notable advancement in optical fiber technology. Loss values in today's SSMF remain comparable to those first recorded in 1979. Figure 2.6 shows the attenuation measured for SSMF and PSCF emphasizing the behavior along the different spectrum bands. These profiles characterize the WDL used in the simulations of Chapter 3, which rely upon the experimental measurements of Chapter 4.

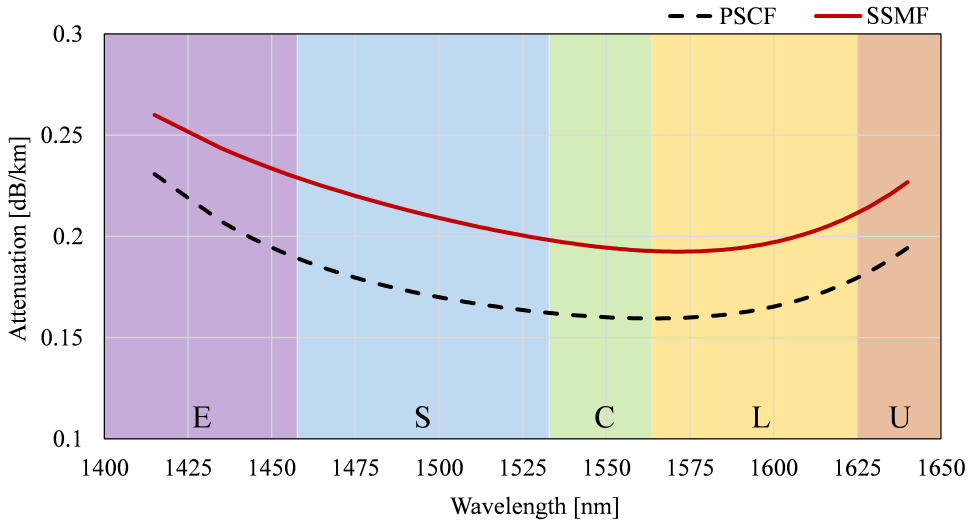

Fig. 2.6: Experimental characterization of the attenuation profile of SSMF and PSCF from 1415 nm to 1640 nm.

The main impurity contributing to fiber loss are the hydroxide ions (OH^-). In earlier fibers, a significant absorption peak occurred around 1380 nm. Nevertheless, advancements in fiber manufacturing processes have significantly reduced these water peaks in modern fibers, making the entire low-loss region accessible for use in state-of-the-art optical transmissions [27]. This development has opened up the potential for utilizing all available transmission bands, as shown in Fig. 2.6, resulting in a bandwidth increase of 9.4 times compared to using the C-band alone, thereby offering substantial potential to enhance fiber capacity. However, Fig. 2.6 also highlights the wavelength-dependency issue, where different WDM channels across these bands experience varying levels of attenuation during propagation, leading to discrepancies in performance.

2.3.2 Fiber dispersion

Chromatic dispersion refers to the dependence of the group velocity with frequency. This dependency implies that different components of a light signal, each with its unique frequency, propagate at different speeds through the fiber. This effect is known as group velocity dispersion

(GVD) and it is related to the refractive index of the fiber. Fiber dispersion significantly impacts the transmission of optical pulses, since the variation in speed leads to the broadening of the transmitted pulses in the time domain, resulting in intersymbol interference.

From a mathematical view, the effects of fiber dispersion are addressed by expanding the mode-propagation constant β using a Taylor series around the central frequency of the pulse spectrum. The parameter β_2 represents the GVD and is responsible for pulse broadening. The dispersion coefficient D is related to β_2 by the relation [34]

$$D = -\frac{2\pi c}{\lambda^2}\beta_2 \tag{2.3.4}$$

having λ as the channel of interest (COI) wavelength and c as the speed of light in vacuum. Similarly, the third order dispersion β_3 is used to compute the linear change of the dispersion coefficient D over the optical bandwidth. This is called the dispersion slope parameter S defined by

$$S = \frac{4\pi c}{\lambda^3}(\beta_2 + \frac{\pi c}{\lambda}\beta_3) \tag{2.3.5}$$

For SSMF, D is approximately 17 ps/nm/km at 1550 nm. Similar to fiber attenuation, this parameter changes with the wavelength. Nevertheless, it has been observed that the linear approximation through S is quite precise within the wavelength range of 1380 nm to 1620 nm [35], including the S, C and L bands which are the main focus of this research. In Fig. 2.7, the dispersion parameter D is presented for both of the fiber types used in this work.

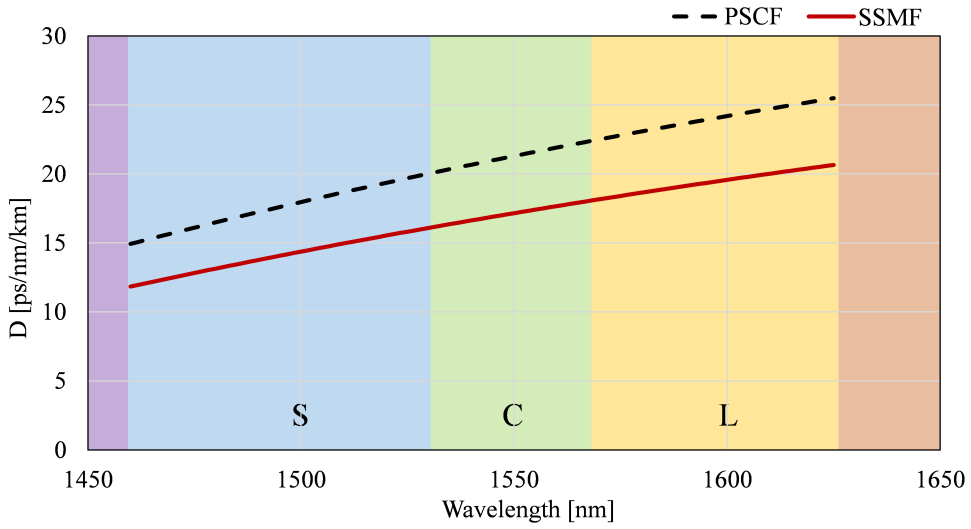

Fig. 2.7: Experimental characterization of the dispersion profile of SSMF and PSCF from 1460 nm to 1625 nm.

Dispersion is influenced by fiber-design parameters. Therefore, before the advent of coherent systems, dispersion compensating fibers (DCF) were commonly used in optical transmissions to counteract dispersion and mitigate intersymbol interference [36]. This led to dispersion - managed (DM) systems, whereby integrating spans of DCF with negative

dispersion coefficients along the transmission link, the total dispersion encountered by the receiver was effectively reduced. However, after the emergence of coherent systems, chromatic dispersion is now compensated with DSP by applying a digital filter.

Furthermore, the elimination of dispersion compensation from the link resulted in *uncompensated* transmissions (UT) that have drastically changed the key features of signal propagation and nonlinearity generation in the fiber. As will be elaborated in Chapter 3, the models used in this work profit from the benefits of uncompensated transmissions to predict the system performance based on simple analytical nonlinear propagation models.

2.3.3 Fiber nonlinearities

The two previous sections of this work were dedicated to discussing the linear effects produced in an optical fiber. This section aims to introduce the final term of eq. (2.3.1), representing the nonlinear distortions.

Most of the nonlinear interactions result from the Kerr effect. This effect is caused by changes in the fiber's refractive index that are directly proportional to the power of the optical field. Based on their impact on the optical signal, the Kerr nonlinear effects can be classified into self-phase modulation (SPM), cross-phase modulation (XPM) and four-wave mixing (FWM). SPM happens when the intensity of light causes the signal's phase to change over time. Additionally, when multiple WDM channels travel together through the fiber, they can influence each other due to the fiber's nonlinearity, leading to XPM. In XPM, the phase of one optical signal changes because of the intensity of other copropagating signals. This effect is increased when signals are packed closely together in the spectrum.

In addition to inducing phase shifts, Kerr nonlinearities can lead to FWM, a process where any three frequency components combine to produce a fourth frequency component. Considering that the signal spectrum can be decomposed into a Q finite number of spectral components, their propagation through the fiber results in three spectral tones at frequencies f_k, f_m and f_n interacting to produce a *fourth* spectral line at frequency $f_{\text{FWM}} = f_k + f_m - f_n$ as illustrated in Fig. 2.8. It is important to note that k, m, n are independent over $\{1, 2...Q\}$, so there are Q^3 possible triples (k, m, n) [37]. This phenomenon affects dense WDM transmissions as the unintended signals coincide to the signal frequencies.

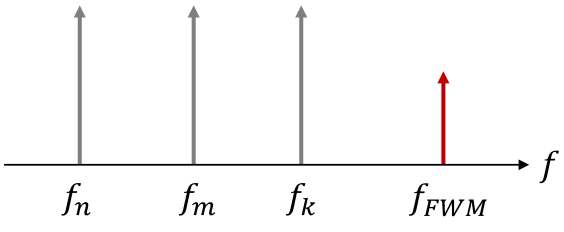

Fig. 2.8: Generation of a FWM frequency component f_{FWM} due to Kerr nonlinearity in three spectral tones at frequencies f_k, f_m and f_n.

The performance degradation in optical fiber communications due to Kerr nonlinearity can be evaluated by numerically solving the NLSE described in eq. (2.3.1) by e.g. the split-step Fourier method (SSFM) [37]. The SSFM is widely used and considered a highly accurate method. However, it exhibits significant computational complexity due to the frequent use of large fast Fourier transforms. To overcome this, and assuming that nonlinearity is relatively small compared to the useful signal, perturbative nonlinear models have been proposed to approximate analytical solutions to the NLSE.

This thesis relies on one of the most well-known perturbative nonlinear models, the Gaussian noise (GN) model, where the nonlinear interactions are modeled as a FWM process between four frequency components of the optical spectrum [38]. It is crucial to note that the GN model has been derived on multiple occasions over the years. The earliest was introduced in 1993 [39]. However, one of its core assumptions, known as the "signal-Gaussianity" assumption (Section 3.1), was not applicable to the DM systems used at that time, thereby limiting its adoption. Later, the appearance of UT systems led to the reconsideration of the GN model, so that in 2011, an integral GN reference formula was derived for dual-polarization WDM systems [40]. The detailed description of this model and novel re-derivations for more accurate estimations in UWB systems will be reviewed in the first half of Chapter 3.

2.3.3.1 Inter-channel stimulated Raman scattering (ISRS)

Another relevant nonlinear process is the inter-channel stimulated Raman scattering (ISRS) effect. Spontaneous Raman scattering occurs when a photon strikes a silica molecule, causing the molecule to absorb energy into vibrational excitation. This energy is then scattered as another photon at a frequency lower than the original. The incident light serves as a pump, generating frequency-shifted radiation known as *Stokes waves*. The stimulated Raman scattering effect (SRS) is the result of a signal light stimulated by a pump allocated with a proper frequency shift. Here, the pump and the signal light are coherently coupled by the Raman process [41]. Within the framework of WDM, as a consequence of the channel interaction, the Raman scattering results in inter-channel stimulated Raman scattering (ISRS), leading to a power transfer between WDM channels.

The Raman effect produces photons across the Raman gain spectrum's bandwidth, amplifying all the frequency components. Hence, a relevant parameter for measuring ISRS is the Raman gain efficiency, defined as [42]

$$\frac{g_R(\Delta f)}{A_{\text{eff}}} \tag{2.3.6}$$

having $g_R(\Delta f)$ as the normalized Raman gain which depends on the frequency difference between the pump and the Stokes waves (Δf). Figure 2.9 plots the Raman gain efficiency for both fiber types used in this work.

It is important to note that the SSMF profile is based on experimental measurements and the PSCF profile is obtained by scaling the experimental spectrum of the SSMF through the A_{eff} of the PSCF.

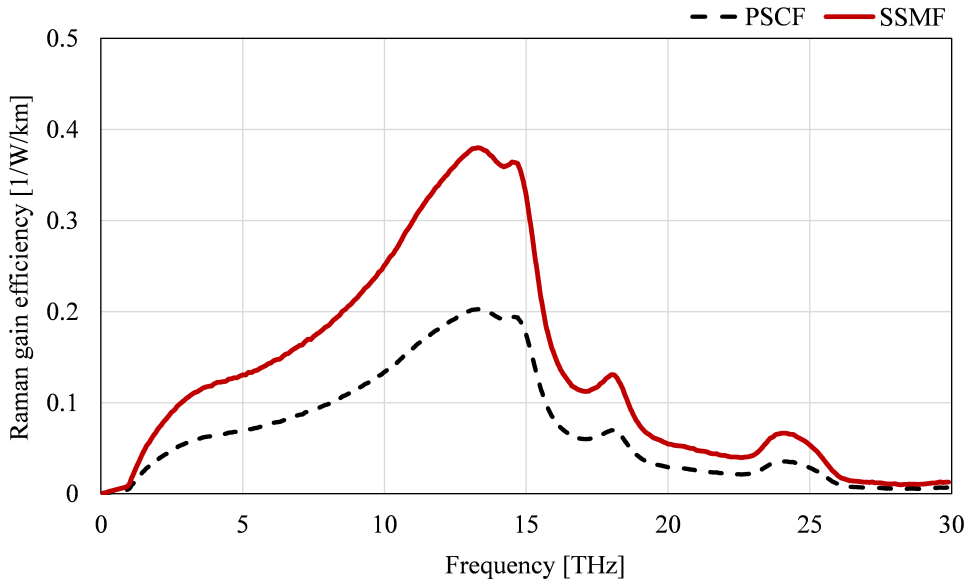

Fig. 2.9: Raman gain efficiency of SSMF and PSCF.

Moreover, Fig. 2.9 also shows the broad frequency range of the Raman gain efficiency in silica fibers, spanning up to 30 THz, with a peak around 13.2 THz. Therefore, for systems operating at bandwidths under 5 THz, the effects of ISRS are negligible, yet, this effect will have a significant impact on UWB systems.

In the context of WDM UWB systems, ISRS can be detrimental by severely limiting the performance due to the unwanted energy transfer from channels with shorter wavelengths (higher frequencies) to channels in longer wavelengths (lower frequencies), resulting in a tilted spectrum as illustrated in Fig. 2.10. Figure 2.10 a) presents the measured power profile at the entrance of the fiber of an experimental S+C+L (12 THz) fully-loaded system with uniform power spectra at a total launched power of $P_{\text{tot}} = 24.2$ dBm, and Fig. 2.10 b) shows the corresponding power profile after the transmission in 60 km of SSMF. Due to ISRS, a total tilt of 11.3 dB is observed across the entire spectrum.

The impact of stimulated Raman scattering effect has been studied since 1984 [43] and the development of models to predict the impact of ISRS in the Kerr nonlinearity has been a very active topic during the last years [44–49]. Section 3.2 will delve into this, focusing specifically on the model employed in this thesis.

Despite these detrimental effects, SRS can also transform optical fibers into broadband Raman amplifiers, turning into a valuable asset for UWB systems, a topic we will explore further in Section 2.4.3.

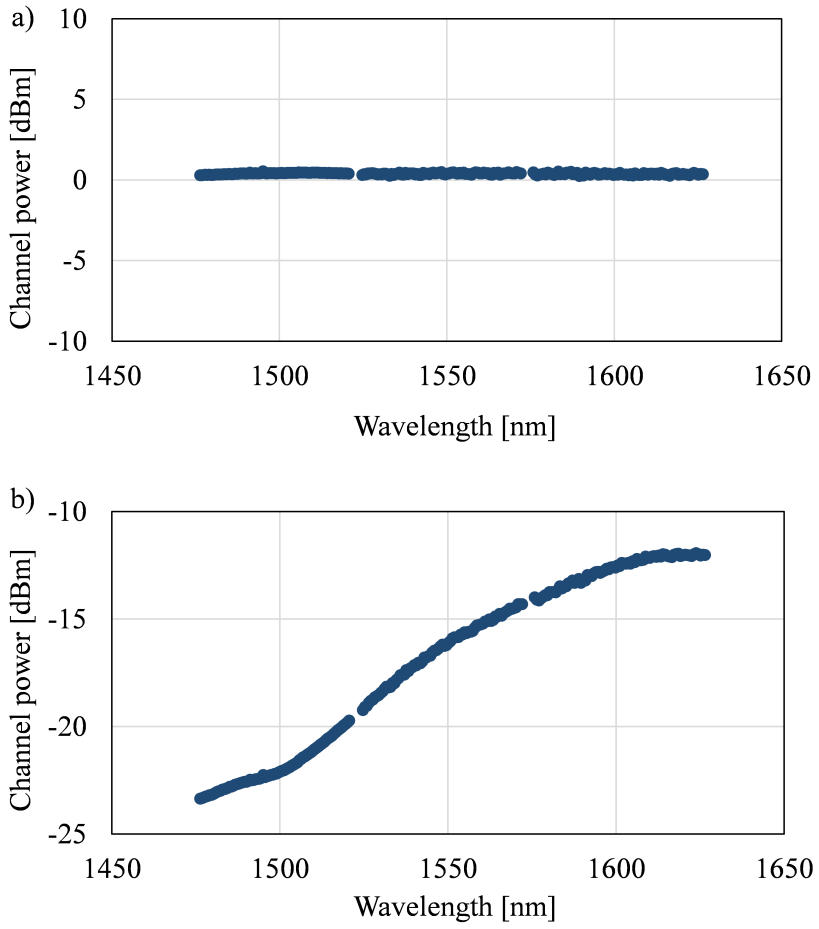

Fig. 2.10: a) Uniform power distribution at the entrance of the fiber and b) power evolution measured after 60 km SSMF for an experimental S+C+L transmission system.

2.4 Optical amplification

To counteract fiber losses and ensure successful data demodulation, optical amplifiers play a crucial role in regenerating signal power through the transmission. These elements serve various functions, including:

- Pre-amplifiers: End-of-the-link gain element, used to amplify a weak signal before it is converted from the photonic to the electronic domain. They typically offer high gain (>30 dB) and operate with small levels of input power (<-25 dBm) [42]. They can be dedicated to a single channel.
- Booster amplifiers: Designed as a multichannel WDM or single channel device. These elements are deployed at the transmitter side, to increase channel power significantly.
- Inline amplifiers: Also WDM devices, used to regenerate signal power after traversing each fiber span to compensate for span-induced and inline element losses. They typically offer gains exceeding 20 dB.

Generally, amplification in WDM systems is achieved through lumped optical gain elements (Section 2.4.1 and Section 2.4.2). Nevertheless, in

addition to these technologies, this work explores the use of distributed Raman amplification (DRA) as a complementary technique that exploits SRS effect using the fiber as a gain medium during propagation (Section 2.4.3). The DRA gain profile is determined by the Raman gain spectra of multiple pump lasers, enabling amplification at flexible wavelengths, making it particularly suited for UWB systems.

It is essential to note that all these optical amplifiers introduce amplified - spontaneous emission (ASE) noise that must be considered when modeling and estimating the performance of any WDM transmission. Additionally, some key parameters of optical amplifiers will be defined next. First, the optical gain (G) indicates the level of amplification provided to the signal and is determined by the ratio between the output and input optical signal powers

$$G = \frac{P_{\text{out}}}{P_{\text{in}}} \tag{2.4.1}$$

where P_{in} and P_{out} represent the total power at the entrance and at the output of the amplifier. The noise figure (NF) measures the amount of ASE noise introduced by the optical amplifier. This definition will be further detailed in Section 2.6. Lastly, the amplification gain bandwidth is the frequency (or wavelength) range within which the device can maintain a specified minimum level of gain, reflecting the operational bandwidth over which the amplifier is effective. Considering all these features, we will next explore the innovations in multi-band amplification that have enabled transmissions beyond the C-band.

2.4.1 Rare-earth-doped fiber amplifier

Erbium-doped fiber amplifier (EDFA) is the most common lumped amplifier used for optical communications. Introduced in 1987 [3, 4], this technology utilizes a single-mode fiber doped with erbium ions, energized by one or more pump lasers. Initially, these devices were designed to operate at the 1550 nm wavelength region, within the range of the conventional C-band having an amplification gain bandwidth of around 4 THz. Assuming a channel spacing of 50 GHz, this configuration enables the amplification of 80 WDM channels (C80). Further research has led to high gain with larger amplification bandwidths. As a result, the industry has embraced new conventional bands facilitated by these amplifiers [50], including the extended C-band (1529 nm to 1567 nm) covering up to 4.8 THz of usable spectrum [51]. Assuming again a 50 GHz channel spacing, this extended band can support 96 channels (C96), which represents a 20% increase in fiber pair capacity compared to the traditional C80. Additionally, the super C-band or C++ band (1524 nm to 1572 nm), extends up to a usable range of 6 THz [52]. For this case, a total of 120 channels can be allocated (C120), increasing the transmission capacity a 50% compared to the C80 band.

A significant milestone for EDFA-based L band amplification was achieved in 1997 with the introduction of an EDFA capable of providing a flat gain of 30 dB across 1570 nm to 1600 nm [53]. This innovation extended the amplification gain bandwidth to the L-band, enabling parallel

transmission in both bands and expanding the WDM transmission wavelength region. Nowadays, commercial EDFAs are available for L-band (1570 nm to 1603 nm) offering around 4 THz of usable spectrum and for extended L-band (1570 nm to 1617 nm) [54]. Moreover, the super L-band or L++ EDFA (1575 nm to 1627 nm) provides up to 6 THz of amplification gain bandwidth [55]. Assuming a channel spacing of 50 GHz, the L-band, extended L-band and super L-band can allocate 80 (L80), 100 (L100) and 120 (L120) WDM channels, respectively. Similar to the definition of the C band, the extended L band offers a 25% and the super L band provides a 50% increase in transmission capacity when compared to the traditional L-band. In line with industry trends and to leverage the capacity benefits of broadband amplification, this work utilizes the previously defined super C and L-band.

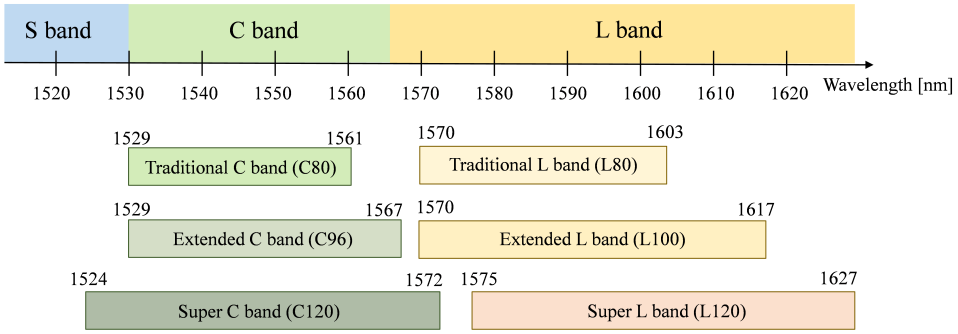

Fig. 2.11: Industry-based band definition for EDFA amplification in the range of 1524 nm to 1627 nm.

Regarding the use of EDFAs in the S-band, there have been studies involving complex cascades of multi-stage amplification. These setups use standard erbium-doped fiber sections tailored for the S-band, combined with optical filters to mitigate the ASE power from the C and L bands. Although this arrangement proves to be highly efficient, it is suitable for a relatively narrow spectral range (1502 nm to 1518 nm) and may require a gain-flattening device for gain equalization [56]. However, rare-earth ions, particularly thulium, have demonstrated significant amplification potential in the S-band. The development of thulium-doped fiber amplifiers (TDFAs) began in the early 2000s [57], and since then, these amplifiers have enabled the use of the S+C+L band for UWB transmission. Employing this amplification technology, experimental S+C+L transmissions have achieved remarkable data rates above 200 Tbit/s over approximate 54 km of SSMF [14, 15, 17].

Additionally, bismuth has emerged as a promising dopant for lumped UWB transmissions, offering an amplification window ranging from E to S-band (1370 nm to 1490 nm) [58] and from L to U-band (1600 nm to 1700 nm) [59].

The integration of the lumped amplifiers previously presented has resulted in an UWB world transmission record of 321 Tbit/s estimated generalized mutual information (GMI) throughput over a total bandwidth of 27.8 THz (212.3 nm). This remarkable transmission combined the use of EDFA for the C and L bands, TDFA for the S-band, and

BDFA for the E-band, enabling the transmission of 1097 channels transmitted at 24.5 Gbaud in 25 GHz across 150 km of SSMF [22]. More recently, the investigation of this transmission system achieved further reach, registering 264.7 Tbit/s from GMI after 200 km transmission [21].

2.4.2 Semiconductor optical amplifier

Semiconductor optical amplifier (SOA) operates on the principle of stimulated emission occurring in semiconductor materials. By inducing a population inversion through an electrical current, these devices are capable of amplifying optical signals. One of the main advantages of this technology is its integrated optics which leads to a compact solution. Given that they have a small size and are electrically pumped, this amplification technique can be power efficient.

Despite being in principle more cost-efficient, the performance of SOA still needs to be improved when compared with current commercial EDFA. Currently, a typical low-noise SOA features a NF of around 6 dB, higher than the 5 dB NF commonly associated with EDFA. This increased NF in SOAs can be partly attributed to the additional coupling losses inherent to the amplifier design. Another significant disadvantage of SOAs is the nonlinear impairment they introduce, which can distort the signals and limit their amplification applications.

Within the scope of this study, SOAs emerge as a promising technology for UWB systems, particularly due to their ability to operate across a bandwidth of approximately 80 nm, spanning from the O- to L-band, offering considerable amplification gain bandwidth flexibility. In 2017, the use of SOA enabled the first seamless transmission across a continuous 12.4 THz (100 nm) bandwidth, achieving a total data capacity of 115.9 Tbit/s over 100 km [60]. Since then, ongoing advances in SOA technology have led to the refinement of amplifier designs tailored for the denominated *super C band* (1524 nm to 1572 nm) and *super L band* (1575 nm to 1627 nm) systems, aligning with current industry standards. The experimental results included in this work rely on prototype designs that include wide-bandwidth SOA covering both the C and L bands and a high-performance SOA for the L-band, with the specifications presented in Table 2.2. Additional details on the performance of these SOA devices are available in [61], providing deeper insights into their design and development.

Working band	Amplification bandwidth [nm]	Gain [dB]	NF [dB]
C+L	100	>20	<6.5
L	50-60	>20	<6

Table 2.2: Specifications of the SOA prototypes used in this work [61].

2.4.3 Distributed Raman amplifier

As we have mentioned, optical amplification can also be achieved through the SRS effect (Section 2.3.3.1). Although SRS has been extensively studied and characterized for nearly a century [62], it was not until the mid-1990s that the development of high-power semiconductor laser pumps pushed the use of Raman amplification in optical fiber communications [63]. Particularly, distributed Raman amplification (DRA) involves injecting a high-power laser into the fiber, allocating the pump's wavelength typically with an offset of 13 THz with respect to the signal, in order to achieve the maximum Raman coupling (Raman gain peak).

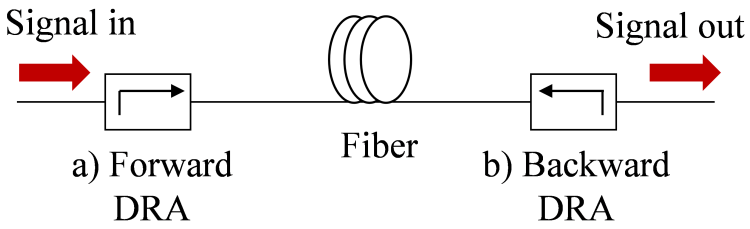

Fig. 2.12: General scheme of DRA, considering a) forward, b) backward and (both) simultaneous dual pumping.

While DRAs are less pump-efficient than lumped amplifiers, requiring higher pump powers, they offer several advantages:

- As presented in Fig. 2.12, the fiber itself acts as the gain medium, reducing the ASE noise in the system.
- Amplification at any wavelength, as long as the pump wavelength is shifted considering the Raman gain peak.
- Flat gain profiles across the amplification bandwidth can be potentially achieved by employing multiple pumps.
- Flexible system design with various pumping configurations, including forward (only Fig. 2.12 a), backward (only Fig. 2.12 b), or simultaneous dual pumping (Fig. 2.12 a and b).

Consequently, DRAs are used in both unrepeated and repeated communication systems. Recent high-capacity UWB demonstrations include DRA in combination with lumped amplification [64] and SOA [65] to improve system performance. As part of the experimental work of this thesis including SOA and DRA, an unrepeated C+L transmission was achieved through seamless amplification by using a wide-bandwidth SOA (Section 2.4.2) as a high-power booster. At the end of the fiber, a backward DRA has been applied with 6 multiplexed pumps from 1415 nm to 1515 nm spaced by 20 nm with powers of 25.7 dBm, 22.7 dBm, 22.1 dBm, 19.1 dBm, 13.2 dBm and 19.6 dBm, respectively. The resultant on-off Raman gain, defined as the increase in signal power at the amplifier output when the pumps are turned on, is plotted in Fig. 2.13.

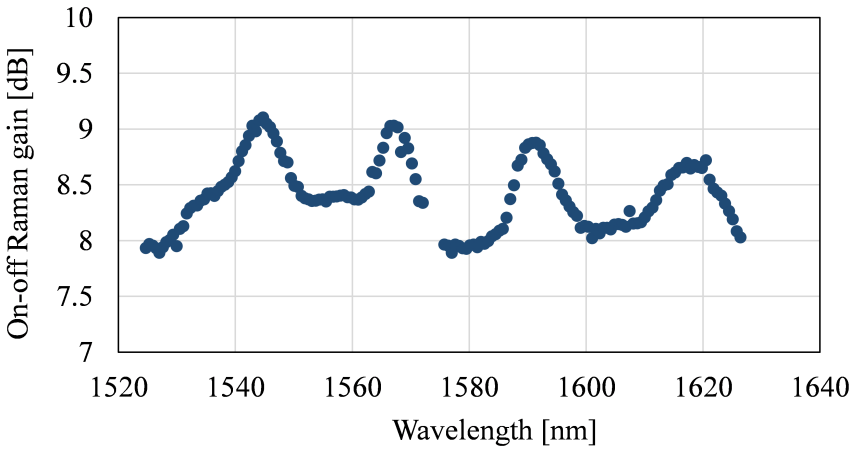

Fig. 2.13: On-off Raman gain of a backward DRA combining 6 pumps located in 1415 nm, 1435 nm, 1455 nm, 1475 nm, 1495 nm and 1515 nm.

Figure 2.13 illustrates how an effectively designed DRA system, utilizing multiple Raman pumps at varying power levels, can achieve a relatively flat on-off Raman gain across the signal bandwidth, with the most significant gain difference being less than 1.4 dB. This demonstration benefits from the combined strength of a booster SOA providing a maximum $P_{\text{tot}} = 24.4$ dBm and backward pumping DRA, with an average on-off Raman gain of about 8.4 dB (Fig. 2.13). As a result, a real-time total throughput of 59.2 Tb/s is transmitted over 201.6 km of PSCF. At the time of publication, this achievement marked one of the highest throughput rates achieved using real-time transponders with a seamless amplification in an unrepeated transmission [VIII, X].

When focusing only on the amplifier power consumption, DRA incurs at a higher cost when compared to lumped amplification. However, when evaluating the overall system power consumption, DRA can be more energy-efficient in certain scenarios. This efficiency arises from the low-noise characteristics of distributed amplification, which enable longer spans while maintaining the same optical signal-to-noise ratio (OSNR). Additionally, incorporating DRA to extend reach may prove more energy-efficient than relying on more powerful FEC techniques. In summary, power savings with DRA are achievable if the system's management power consumption and OSNR requirements are high [66].

2.5 Optical coherent receiver and digital signal processing

After the transmission through the fiber, each WDM channel arrives to their corresponding optical coherent receiver to be converted from the optical to the digital domain. The block diagram of a commonly used dual-polarization coherent receiver is depicted in Fig. 2.14. Here, the incoming optical signal is first directed through a polarization beam splitter (PBS), that separates the signal into two orthogonal polarization components. Employing intradyne coherent detection, the optical signal

is then coherently combined with the optical field of a continuous local oscillator (LO). As observed in Fig. 2.14, this occurs through two sets of independent 90° optical hybrid circuits. These devices introduce a two-by-two optical coupler with a 90°-phase delay function implemented in one arm of the coupler to recover the I and Q components.

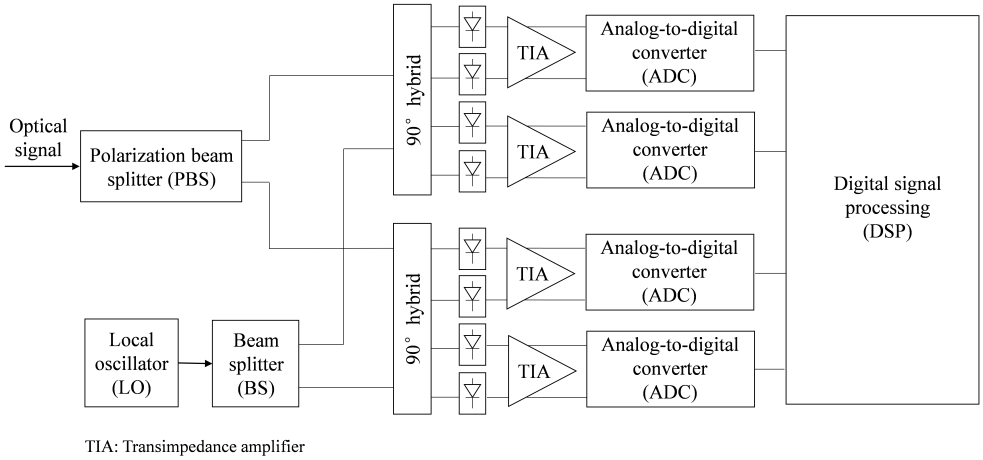

Fig. 2.14: Block diagram of a dual-polarization coherent receiver.

Subsequently, the eight resultant signals are converted from the optical to the electronic domain via balanced photodetectors [67]. The electrical signal produced by the balanced photodetector is generally weak. Hence, to raise the electrical signal, low-noise trans-impedance amplifiers (TIAs) are employed. Finally, the analog-to-digital converters (ADCs), transform the continuous-time and continuous-amplitude analog signals to discrete-time and discrete-amplitude digital samples. The DSP chain to compensate for impairments occurs in a reversed sequence than their occurrence in the transmission pathway. Initially, the DSP focuses on compensating any distortions imposed on the signal due to the bandwidth constraints of the receiver (Rx) and signal skews. Following this, the DSP tackles the compensation of fiber-related effects, where the chromatic dispersion is usually addressed first. An additional significant source of degradation corrected by the DSP includes the polarization effects such as polarization mode dispersion (PMD) and loss (PDL).

Another step of DSP is the *post equalization*, which compensates for transceiver impairments, such as IQ imbalance and skews. As the penalty of transceiver impairments increases with symbol rate [68], we should emphasize that its compensation is crucial for the new generation of transceivers operating at 100 Gbaud and beyond. Apart from the compensation of the previously mentioned linear effects, DSP can also perform compensation of fiber nonlinearities. Some nonlinear compensation technologies include Volterra equalization [69] and digital back-propagation (DBP) [70]. Conversely, the perturbation-based nonlinear pre-compensation method has demonstrated close effectiveness to DBP, yet significantly reducing the processing complexity [71]. Additionally, through adaptive digital pre-distortion (DPD) algorithm, transmitter-side DSP can compensate the nonlinear distortions present in the DAC, driver amplifier and MZM [72].

2.6 System performance estimation

Finally, after the signal has been received and the linear and nonlinear impairments have been efficiently mitigated through DSP, the performance of a coherent optical transmission system can be assessed using various metrics. These metrics are designed to estimate the quality of the transmission (QoT). In this work, we employ the signal-to-noise ratio (SNR) as one of the primary metrics to evaluate the system performance. The SNR is a well-established parameter broadly used in telecommunications to compare the signal average power (P_{ch}) in relation to the noise average power (N) for a given bandwidth (B_{ref})

$$\mathrm{SNR} = \frac{P_{\mathrm{ch}}}{N} \tag{2.6.1}$$

In the context of WDM system performance estimation, three primary sources of impairments must be taken into account: back-to-back (B2B) impairments originated from the transponder, setting most of the time a maximum achievable performance based on the transmitter and receiver; amplified spontaneous emission (ASE) noise, added by the optical amplifiers; and the nonlinear interference coefficient ($\eta_{\mathrm{N_s}}$) describing the nonlinear distortions imposed by the Kerr effect. Accounting for these three sources of noise, the total SNR at the receiver can be expressed as [35]

$$\mathrm{SNR} = \frac{P_{\mathrm{ch}}}{\underbrace{\kappa_{\mathrm{TRX}}}_{\text{B2B noise}} P_{\mathrm{ch}} + \underbrace{P_{\mathrm{ASE}}}_{\text{ASE noise}} + \underbrace{\eta_{\mathrm{N_s}}}_{\text{NL noise}} P_{\mathrm{ch}}^3} \tag{2.6.2}$$

Because these three noise sources are assumed to be uncorrelated and additive Gaussian noise sources, eq. (2.6.2) indicates that the total noise power can be obtained by simply adding the noise powers of the individual noise contributions. Section 2.6.1 and Section 2.6.2 will describe in detail the modeling of the first two noises, respectively, whereas Chapter 3 will present the nonlinear theory upon which this work was built and hence describe the modeling of the third noise.

Another valuable metric for assessing the performance of a digital communication system is the bit error rate (BER), defined as the ratio of the number of erroneous received bits to the overall number of bits transmitted. The BER can be related to the SNR, nevertheless, it is important to highlight that this relation depends on the modulation format. In the case of AWGN channels using square M-QAM modulation, BER can be approximated as follows [37]

$$\begin{aligned}\mathrm{BER} \simeq & \frac{2}{\log_2 M}\left(1-\frac{1}{\sqrt{M}}\right) \\ & \mathrm{erfc}\left(\sqrt{\frac{3}{2(M-1)}\mathrm{SNR}}\right)\end{aligned} \tag{2.6.3}$$

The Q-factor is an equivalent approach suitable for working in dB scale. Deduced from the BER, the Q-factor is estimated as

$$\text{Q-factor} = 20\log_{10}\left[\sqrt{2}\cdot \mathrm{erfc}^{-1}(2\cdot \mathrm{BER})\right] \tag{2.6.4}$$

with erfc^{-1} as the inverse of the complementary error function.

2.6.1 Transponder back-to-back penalties

In coherent optical communication systems, the maximum achievable SNR is limited by the noise from the transceiver elements. This noise reflects the system's performance in a B2B setup, without any transmission medium, gathering the noise contributions from both the transmitter and receiver. This includes quantization noise from ADC and DAC, as well as the noise from electrical amplifiers and the signal distortion due to the nonlinear behavior of electrical, and electro-optic components (modulator, photodiode). In this thesis, we model the B2B penalties through κ_{TRX}, defined by

$$\kappa_{\text{TRX}} = \frac{1}{\text{SNR}_{\text{TRX}}} \tag{2.6.5}$$

where SNR_{TRX} will impose a maximum achievable SNR independent of the signal power and obtained from experimental B2B measurements [73].

2.6.2 Amplified spontaneous emission

As the optical signal propagates along the link, it will be impaired by the ASE noise introduced by each optical amplifier. The ASE noise can be modelled as additive white Gaussian noise (AWGN) with N_{ASE} defined as the power spectral density (PSD) estimated in the form [74]

$$N_{\text{ASE}} = n_{\text{sp}} h f_0 (G - 1) \tag{2.6.6}$$

where n_{sp} is the spontaneous emission factor, h is Planck's constant, f_0 is the reference frequency and G is the gain of the amplifier. Based on this, we can estimate the ASE noise power P_{ASE} by

$$P_{\text{ASE}} = 2 N_{\text{ASE}} B_{\text{ref}} \tag{2.6.7}$$

having 2 to consider both polarizations and B_{ref} as the reference bandwidth.

A valuable metric for assessing the impact of ASE noise is the optical signal-to-noise ratio (OSNR), which estimates the power ratio between the signal and the noise. Mathematically, it is defined by

$$\text{OSNR} = \frac{P_{\text{ch}}}{P_{\text{ASE}}} \tag{2.6.8}$$

where P_{ch} is the average power per channel and P_{ASE} is the ASE noise power on both polarizations estimated as eq. (2.6.7). B_{ref} is commonly considered to be 12.5 GHz (0.1 nm).

As we presented in Section 2.4, the noise added by an amplifier is typically measured through the NF, which is estimated in linear scale as

$$\text{NF} = \frac{\text{SNR}_{\text{in}}}{\text{SNR}_{\text{out}}} = \frac{1}{G}[1 + 2 n_{\text{sp}} (G - 1)] \tag{2.6.9}$$

where SNR_{in} and SNR_{out} are the SNR at the input and output of the amplifier, respectively. This definition quantifies how much the amplifier degrades the signal's SNR after amplification, under the assumption

that the input signal is quantum limited and that the $\mathrm{SNR}_{\mathrm{out}}$ is measured with an ideal photodetector having 100% of quantum efficiency. In practice, the NF is estimated through physical parameters that can be measured through the optical spectrum analyzer (OSA), such as the OSNR. Therefore the NF in dB can be expressed in terms of the OSNR as [42]

$$\mathrm{NF}_{\mathrm{dB}} = P_{\mathrm{ch}}^{in} - \mathrm{OSNR}_{\mathrm{dB}} - 10\log(hf_0B_{\mathrm{ref}}) \tag{2.6.10}$$

Within the C-band window, having f_0 around 1550 nm, the last term in eq. (2.6.10) is commonly substituted by 58 dBm.

Special consideration is required for Raman amplifiers, as their ASE noise is produced through *spontaneous* Raman scattering. Considering a DRA along the fiber length L, that is co-pumped and counter-pumped with pump powers $P_p^{\pm}$, respectively, having a signal propagating in the $+z$-direction, the process of ASE generation and amplification in Raman amplifiers is defined by [41]

$$\begin{aligned}\pm\frac{\partial P_A^{\pm}}{\partial z} =& -\alpha_A P_A^{\pm} + \frac{g_R(\Delta f)}{A_{\mathrm{eff}}} P_p P_A^{\pm} \\ &+ \frac{g_R(\Delta f)}{A_{\mathrm{eff}}}[1+\eta(T)]hf_A B_{\mathrm{ref}} P_p\end{aligned} \tag{2.6.11}$$

having $P_A^{\pm}$ as the ASE noise power in a bandwidth B_{ref}, propagating in the $\pm z$ direction. P_p is the total pump power at position z, traveling in both directions with the Raman gain efficiency defining the strength of the coupling. Additionally, eq. (2.6.11) includes the phonon occupancy factor

$$\eta(T) = \frac{1}{\exp\left[\frac{h\Delta f}{k_B T}\right] - 1} \tag{2.6.12}$$

where k_B is Boltzmann's constant, T is the temperature of the fiber in Kelvin units, typically assumed to be 25°C (298.15 K) and Δf is the frequency separation between the pump and the signal. In addition, the boundary conditions $P_A^{+}(0) = 0$ and $P_A^{-}(L) = 0$ need to be fulfilled when solving eq. (2.6.11). Generally, DRA tends to produce less ASE noise compared to doped-fiber amplifiers and SOAs since it uses the transmission fiber as the gain medium. Commonly, the NF of a backward DRA, also referred to as *effective* NF, defines the noise of a fictitious lumped amplifier at the end of the passive span, providing the same gain and equal number of photons as the DRA and it is expressed as [42]

$$\mathrm{NF}_{\mathrm{eff}} = \frac{1 + N_{\mathrm{ASE}}}{G_R(L)} \tag{2.6.13}$$

having $N_{\mathrm{ASE}} = P_{\mathrm{ASE}}/hf_0B_{\mathrm{ref}}$ estimated by eq. (2.6.11) and $G_R(L)$ is the on-off Raman gain of the fiber span with length L.

2.6.3 Achievable information rate

The maximum information rate that can be transmitted over a specific communication channel, known as channel capacity *(C)*, was initially introduced by Shannon in 1948 [28]. Here, it was demonstrated that for

an additive white Gaussian noise (AWGN) channel, the optimal source distribution maximizing the channel capacity is Gaussian, leading to the celebrated Shannon capacity formula

$$C = \log_2(1 + \mathrm{SNR}) \tag{2.6.14}$$

This formulation was derived under the assumption that both the input and output alphabets have an infinite number of elements, leading to input and output distributions that are continuous Gaussian functions (*Gaussian-like* distributions). However, as previously mentioned (Section 2.1.1), practical optical systems employ finite alphabets that do not follow Gaussian distributions. Therefore, the channel capacity defined by Shannon is considered a fundamental limit (Shannon limit) for the mutual information (MI). The MI is a relationship between two random variables, to measure the amount of information shared between them. If X is the transmitted random variable and Y is the received random variable with probability distributions $p(x_N)$ and $p(y_N)$, respectively, and the conditional distributions $p(y_N \,|\, x_N)$, the MI estimates the information that has been successfully transferred from transmitter to the receiver in the form [37]

$$I(X_N; Y_N) = E\Big\{\log_2 \frac{p(y_N \mid x_N)}{p_N(y)}\Big\} \tag{2.6.15}$$

having N as the number of realizations of the process and $E\{\cdot\}$ as the expectation operator. Based on this, the information rate defines the maximum bit rate at which information can be reliably transmitted given by

$$I(X; Y) = \lim_{N\to\infty} \frac{1}{N} I(X_N; Y_N) \tag{2.6.16}$$

The capacity of the channel is, hence, a fundamental limit for transferring information where the information rate is maximized. The estimation of MI can be derived from eq. (2.6.15) through Monte-Carlo time averaging for long-enough N [73]. Figure 2.15 shows the MI as a function of the SNR for different modulation formats.

As we have discussed, post-FEC performance estimation is crucial to assess the different modulation formats, yet, it requires time-consuming Monte-Carlo simulations or experiments involving FEC encoding and decoding. Alternatively, optical communication systems frequently employ bit-interleaved coded modulation (BICM) due to their high flexibility in system design. This approach decouples the code from the modulation in such a way that the generated coded bits at the output of the FEC encoder are uniformly distributed among the different constellation bits. The interleaved sequence is parsed in blocks of m bits each, hence generating m parallel and independent bit streams denoted by $b^{(1)}...b^{(m)}$.

The generalized mutual information (GMI) is often referred to as the achievable rate of BICM calculated by [75]

$$\mathrm{GMI} \approx H(X) - \frac{1}{N}\sum_{k=1}^{N}\sum_{i=1}^{m} \log_2 \frac{\sum_{x\in A} q_{Y\,|\,X}(y_k \mid x_k) p_X(x)}{\sum_{x\in A_{b_{k,i}}} q_{Y\,|\,X}(y_k \,\big|\, x_k) p_X(x)} \tag{2.6.17}$$

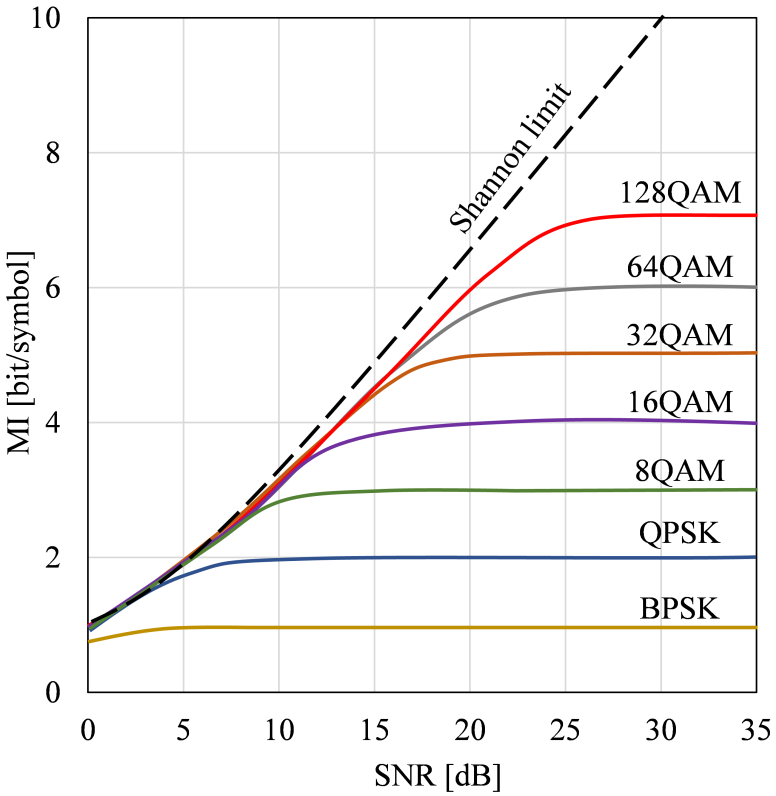

Fig. 2.15: The MI as a function of SNR for a different modulation formats.

having $q_{Y|X}$ as the auxiliary channel conditional probability, $b_{k,i}$ as the i-th bit of the k-th transmitted symbol and $A_{bk,i}$ as the set of the constellation symbols whose i-th bits is $b_{k,i}$ and $H(X)$ as the source entropy. The entropy is the average of all the possible symbols included in a constellation alphabet A that a source can transmit scaled by their probabilities [76]

$$H(X) = -\sum_{x \in A} p_X(x) \cdot \log_2 p_X(x) \tag{2.6.18}$$

The GMI stands out as a useful tool in the design of optimized modulation formats. Moreover, extensive research has demonstrated its utility as a reliable method for the accurate estimation of post-FEC BER across various M-QAM formats [75] and PCS constellations [76]. Therefore, GMI has been selected as the primary system performance metric in the experimental demonstrations presented in Chapter 4.

2.6.4 Model implementation and QoT tool

Based on the presented definition of WDM UWB optical coherent system, a Python-based quality of transmission (QoT) tool has been implemented including the models and formulas discussed in this chapter. Similar to the approach of the open source project *GNPy* [77], our platform aims to simulate physical impairments and accurately predict the performance of any WDM transmission system. Figure 2.16 presents the block diagram of the implemented Python-based solution used in this thesis.

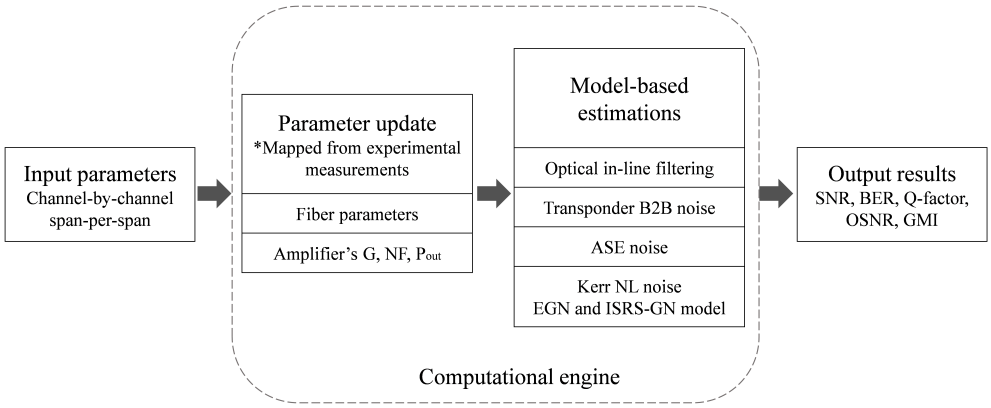

Fig. 2.16: Block diagram of the implemented Python-based QoT.

The QoT tool has been parameterized so that the input parameters can be set in a channel-by-channel fashion, accounting for different modulation formats, symbol rates and channel spacing for each WDM channel. As well as the parameter configuration span-per-span, enabling any multi-span heterogeneous transmission with diverse fiber lengths and types. These input parameters are then processed internally to define the wavelength-dependent parameters of fiber attenuation α, Raman gain efficiency, nonlinear coefficient γ and GVD β_2 and its linear slope β_3, depending on the transmission bandwidth and fiber type. For the interest of this work, the wavelength dependency of these effects has been aligned with the experimental measurements of SSMF and PSCF presented in Section 2.3.1 and Section 2.3.2. Additionally, due to the practical parametric design, amplifier values of G, NF, input and output power profile distributions can be directly mapped into the QoT from experimental laboratory measurements or monitored values from real optical networks [78].

The updated wavelength-dependent parameters are then used for the model-based performance estimation accounting for the ASE noise, transponder B2B noise, fiber Kerr nonlinear noise, ISRS effect, and optical in-line filtering. The effects of optical in-line filtering arising in the optical add-drop multiplexers (OADM) follow the model described in [79]. The definitions presented in this chapter are employed to obtain the linear ASE noise and the transponder's B2B penalties. The models for estimating the nonlinear interference power will be detailed in Chapter 3. The resultant SNR performance is estimated following eq. (2.6.2), and transformed into additional performance metrics as BER and *Q-factor* using the theoretical expressions presented in Section 2.6.

This QoT tool's development was part of my Master's internship as well as its experimental validation in a heterogeneous multi-span full-loaded WDM system operating within the C band [80]. The demonstration consisted of an 880 km fiber transmission comprising six spans of 80 km of SSMF and four 100 km spans of PSCF. Variable optical attenuators (VOAs) were used to adjust the span loss to approximately 22 dB. The study of multiple uniform power distributions was performed using C-band EDFAs working in constant gain with tilts of 2 dB fully compensating for the span loss. The markers in Fig. 2.17 show the measured

Q-factor performance for the channel centered a 1547.3 nm at different total powers, whereas the line plots the numerical estimations. Overall, a very good agreement can be observed for the predictions, having a maximum discrepancy of ~ 0.2 dB at $P_{\text{tot}} = 22$ dBm.

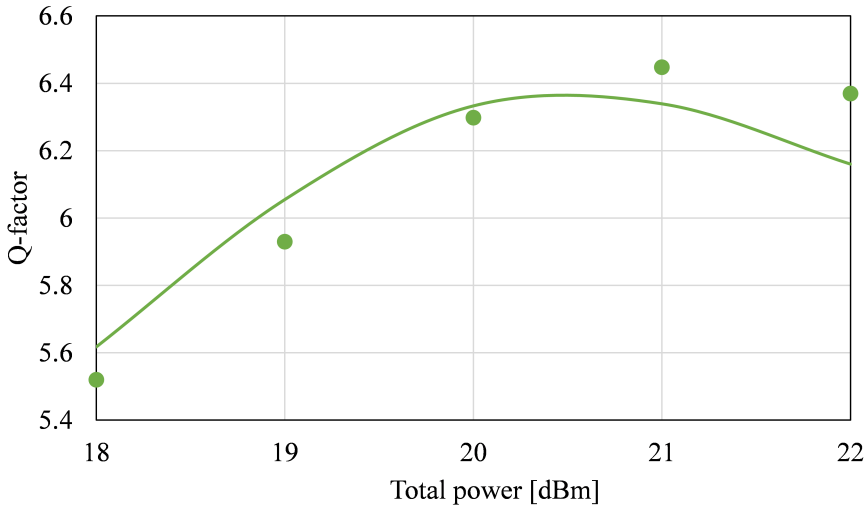

Fig. 2.17: Experimental (markers) and estimated (line) Q-factor performance as a function of the total power for a C-band transmission.

These results and additional tests included in [81] demonstrated that the implemented QoT tool is a reliable platform for estimating the performance of C-band systems. Most importantly, it can be a suitable solution for studying the potential of UWB systems. Consequently, this tool has been the basis for most of the work presented in this thesis, including the experimental validation of UWB S+C+L systems and the analysis of their results. Furthermore, based on model-based estimations obtained from it, this work presents power optimization strategies that enhance the performance of UWB transmissions.

Chapter 3

Model-based power optimization techniques for UWB systems

The presence of nonlinear interference (NLI), which arises from the nonlinear interaction between different WDM channels, represents a significant impediment to the capacity of optical transmissions [82]. Therefore, various analytical models, typically based on the Gaussian noise (GN) model [83], have been proposed during the last decade to predict the impact on performance in uncompensated coherent optical systems, each offering different levels of accuracy and complexity, applied in a wide range of transmission scenarios.

This chapter aims to provide an overview of the fundamentals of the GN model, highlighting its use in optical system optimization. Particular attention is drawn to its closed-form derivation for UWB systems, the inter-channel stimulated Raman scattering (ISRS) GN model, and its relevance in the development of fast power optimization techniques that aim to maximize the quality of transmission (QoT).

Based on these modeling tools, in Section 3.3 we present one of the main contributions of this PhD thesis, the proposed *ASE-NL heuristic*, an iterative two-step strategy employed to optimize the signal-to-noise ratio (SNR) performance. The optimization technique is validated through simulations on S+C+L transmissions showing close convergence to numerical optimizations using machine learning-based algorithms, proving to be a simpler solution with lower computational time.

Furthermore, we show the benefits of UWB systems by analyzing how capacity scales with bandwidth, highlighting the importance of power pre-emphasis to boost the throughput of UWB systems. Additionally, we propose different equalization techniques designed for practical cases without much granularity on the channel bit rate, analyzing the throughput versus distance when applying these strategies.

3.1 The Gaussian Noise model

In this section, we present one of the most widely known first-order perturbation models, able to capture the main features of nonlinear propagation in uncompensated coherent optical systems, the GN model [83]. This analytical model assumes that the transmitted signal statistically behaves as a stationary random Gaussian process, the so-called "signal-Gaussianity" assumption, valid in uncompensated long-haul coherent systems with highly dispersive channels that tend to approximate a Gaussian-like distribution. Similarly, the model assumes that the NLI manifests itself as additive Gaussian noise [83]. With these approximations, the power spectral density (PSD) of the nonlinear perturbation on frequency f can be described as [84]

$$G_{\mathrm{NLI}}(f) = \frac{16}{27}\gamma^2 L_{\mathrm{eff}}^2 \cdot \int_{-\infty}^{\infty}\int_{-\infty}^{\infty} G_{\mathrm{WDM}}(f_1)G_{\mathrm{WDM}}(f_2)G_{\mathrm{WDM}}(f_1+f_2-f) \cdot \rho(f_1,f_2,f)\cdot\chi(f_1,f_2,f)\ \ df_2 df_1 \tag{3.1.1}$$

This derivation, better known as the GN model reference formula, considers γ as the nonlinearity coefficient and L_{eff} as the effective length, defined as $[1-e^{-\alpha L_s}]/\alpha$, which depends on the span length L_s and the fiber's loss coefficient α (Section 2.3.1). In the following, we will try to provide a general view of the physical interpretation of each of the elements within it, and further explain its assumptions and limitations, focusing on the derivation of models valid in the context of UWB systems.

In the frame of the GN model, the NLI PSD is accounted as the integrated result of all the four-wave mixing (FWM) processes occurring among any three spectral components of the transmitted signal, located at f_1, f_2 and $f_3 = (f_1 + f_2 - f)$. The integrand

$$G_{\mathrm{WDM}}(f_1)G_{\mathrm{WDM}}(f_2)G_{\mathrm{WDM}}(f_1+f_2-f) \tag{3.1.2}$$

shows the FWM process as the product of the three frequency components that act as "pumps" for the FWM process itself [83]. Depending on the position of f_1, f_2 and f_3 within the WDM spectrum, Fig. 3.1 shows the different types of nonlinear interactions inside a given channel of interest (COI) centered at frequency f, classifying them into three different categories:

1. Self-channel interference (SCI) denotes the nonlinear distortions affecting a channel produced by the channel itself. Depicted in Fig. 3.1 a), where f_1, f_2 and f_3 lie within the COI.

2. Cross-channel interference (XCI) [83], denotes the distortions affecting a channel produced by the nonlinear interaction with a *single* interfering channel (INT). Illustrated in Fig. 3.1 b), where f_1 is inside the COI while f_2 and f_3 lie in only one other interference channel.

3. Multi-channel interference (MCI) [83], denotes the distortions affecting a channel produced by the nonlinear interaction with any

other two or three interfering channels. Shown in Fig. 3.1 c) and d), where f_1, f_2 and f_3 lie in two or more INT.

It has been shown that this contribution can be neglected in systems with high symbol rates and large channel spacings (>40 GHz) [85]. This approximation, known as the XPM assumption, is highly relevant and will be referred to later when defining the total nonlinear coefficient in Section 3.2.

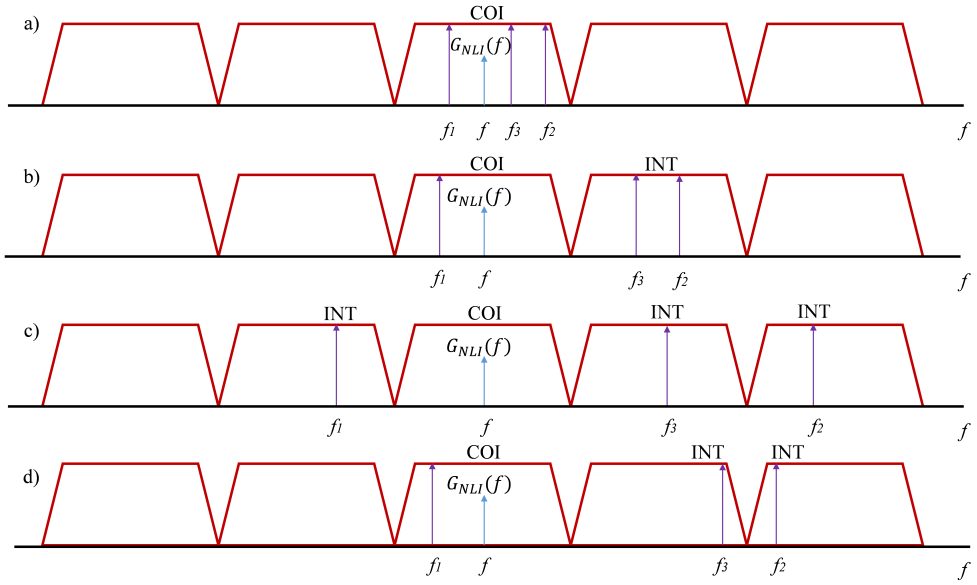

Fig. 3.1: Signal frequency components within interfering channels (INT) contributing to create NLI inside the channel of interest (COI) at frequency f. Classification of nonlinear contributions as a) self-channel interference (SCI), b) cross-channel interference (XCI), c) and d) multi-channel interference (MCI).

The factor $\rho(f_1, f_2, f)$ physically represents the FWM efficiency of the beating of the frequencies f_1, f_2 and f_3, producing a beat disturbance at frequency f. A general definition for arbitrarily distributed amplification and gain profiles was presented in [84], assuming all frequency components attenuate similarly along the fiber span [44]. However, as observed in Chapter 2, due to wavelength-dependent impairments, this assumption is no longer valid in transmission bandwidths beyond C-band, so this factor needs to be modified for UWB systems. In Section 3.2, we will review extended versions of the GN model valid for multi-band transmissions.

Finally, $\chi(f_1, f_2, f)$, sometimes called "phased-array factor", represents the nonlinear accumulation along the link. For the case of a single-span transmission, χ is assumed to be 1. Alternatively, for homogeneous and transparent multi-span scenarios with N_s number of spans in the link, β_2 as the dispersion coefficient and β_3 as dispersion slope [83]

$$\chi(f_1, f_2, f) = \frac{\sin^2(2N_s\pi^2(f_1 - f)(f_2 - f)[\beta_2 + \pi\beta_3(f_1 + f_2)]L_s)}{\sin^2(2\pi^2(f_1 - f)(f_2 - f)[\beta_2 + \pi\beta_3(f_1 + f_2)]L_s)} \quad (3.1.3)$$

This phased-array factor captures the *coherent* beating of NLI contributions produced in each span of a link occurring at the end of the

link (receiver's location) [86]. An alternative approach can be obtained by neglecting this effect, the *incoherent* GN model or IGN model, which assumes that the NLI contributions of each span can sum up in power at the receiver. In this sense, we can rewrite the NLI PSD at the end of the link as [83]

$$G_{\mathrm{NLI}}(f) = \sum_{\mathrm{n}=1}^{N_s} G_{\mathrm{NLI}}^{n}(f) \tag{3.1.4}$$

where $G_{\mathrm{NLI}}^{n}(f)$ is the NLI PSD generated in the n^{th} span. Based on this, the phased-array factor previously presented in eq. (3.1.3) can be alternatively shown as [84]

$$G_{\mathrm{NLI}}(f) = G_{\mathrm{NLI}}(f)|_{\mathrm{N_s}=1} \cdot N_s^{1+\epsilon} \tag{3.1.5}$$

having ϵ as the *coherence factor*, with values estimated between 0 and 1. When $\epsilon = 0$, the system shows *incoherent* accumulation, and similar to eq. (3.1.4), the NLI produced in one span sums up in power with the contributions of all the other spans. On the other hand, the closer ϵ is to 1, the greater the coherence among NLI from different spans, having perfect phase-matching when $\epsilon = 1$ [84].

The shape of the NLI PSD G_{NLI} is relevant when assessing system performance. Assuming that the PSD of the NLI is locally flat across the channel bandwidth B_{ch}, the nonlinear interference coefficient η can be obtained by integrating the NLI PSD over the bandwidth of interest and normalizing by the channel launch power as [35]

$$\eta_{\mathrm{Ns}}(f_i) = \frac{1}{P_{\mathrm{ch}}^3} \int_{-\frac{B_{\mathrm{ch}}}{2}}^{\frac{B_{\mathrm{ch}}}{2}} |H(f)|^2 G_{\mathrm{NLI}} \approx \frac{B_{\mathrm{ch}}}{P_{\mathrm{ch}}^3} G_{\mathrm{NLI}}(f_i) \tag{3.1.6}$$

where $\eta_{\mathrm{Ns}}(f_i)$ is the nonlinear interference coefficient of the COI, having f_i as the central frequency, estimated after N_s spans and used in the computation of SNR in eq. (2.6.2). $|H(f)|^2$ is the transfer function of the matched filter at the receiver. The approximation in eq. (3.1.6) assumes a rectangular transfer function equal to the channel bandwidth B_{ch} and that the spectral gaps between adjacent WDM channels are sufficiently small. Due to the challenging nature of analytically incorporating arbitrary matched filter shapes, this approximation proves to be highly beneficial when aiming to derive closed-form approximations of the GN model [35].

Based on the definition of the G_{NLI}, the estimation of the NLI PSD depends on the numerical integration of eq. (3.1.1), a process that can consume a significant amount of time and is unsuitable for real-time applications. In order to reduce the computational complexity, closed-form approximations of the GN model have been proposed. The following simple, closed-form expression can predict the incoherent accumulation of NLI by assuming the propagation of identical channels with approximately rectangular spectra over identical fiber spans using lumped amplification [87]

$$G_{\mathrm{NLI}}(f) = N_s \frac{16}{27} \frac{\gamma^2 L_{\mathrm{eff}}^2 P_{\mathrm{ch}}^3}{\pi |\beta_2| \alpha R_s^3} \operatorname{asinh}\left(\frac{\pi^2}{2\alpha} |\beta_2| R_s^2 \left[N_{\mathrm{ch}}^2 \right]^{\frac{R_s}{\Delta f}} \right) \tag{3.1.7}$$

where N_{ch} is the number of WDM channels, R_s is the symbol rate and Δf is the channel frequency spacing. The IGN closed-form model is notably effective for practical scenarios, proving to be sufficiently rapid and accurate for several applications, such as system analysis and optimization.

3.1.1 Link optimization based on the GN model

The relevance of estimating the nonlinear interference coefficient (η_{Ns}) in a simple and analytical form via eq. (3.1.7), relies on its use to easily predict the SNR performance through the definition introduced in eq. (2.6.2). Moreover, by setting the derivative of eq. (2.6.2) to zero, one can easily find the power per channel that maximizes the SNR, represented by

$$P_{\text{ch,opt}} = \sqrt[3]{\frac{P_{\text{ASE}}}{2\eta_{\text{N}_\text{s}}}} \tag{3.1.8}$$

This result frames a fundamental property deduced from the GN model: at the optimum transmission power, the amount of ASE noise is twice the amount of nonlinear noise, mathematically represented as $P_{\text{ASE}} = 2\eta_{\text{N}_\text{s}} P_{\text{ch,opt}}^3$. This derivation, which was initially introduced in [88], is frequently shown in various publications as the *optimum launch power* ($P_{\text{ch,opt}}$) [83, 84, 89]. However, in [35], it has been argued the *optimality* of this result because when deriving eq. (2.6.2) it is assumed that the NLI coefficient is *independent* of the launch power distribution, which is not strictly true. The nonlinear coefficient NLI itself is a function of the normalized launch power distribution.

Nevertheless, in [90] after experimentally confirming that the signal distortion due to Kerr nonlinearity can be successfully modeled as additive Gaussian noise, authors also provided experimental insights of the noise variance with respect to the launched channel power for both linear and nonlinear propagation regimes. To better understand the interactions between these two noise contributions, we can conveniently rewrite eq. (2.6.2) as

$$\frac{1}{\text{SNR}} = \frac{1}{\text{SNR}_{\text{lin}}} + \frac{1}{\text{SNR}_{\text{NL}}} \tag{3.1.9}$$

where $1/\text{SNR}_{\text{lin}} = 1/\text{SNR}_{\text{TRX}} + P_{\text{ASE}}/P_{\text{ch}}$ is the inverse of the linear part, including the transceiver noise contribution (Section 2.6.1) and the ASE noise induced by optical amplification (Section 2.6.2), and $1/\text{SNR}_{\text{NL}} = \eta_{\text{N}_\text{s}} P_{\text{ch}}^2$ represents the inverse of the nonlinear SNR, which depends on the channel power squared. As experimentally observed in [90], the linear part, represented by SNR_{lin}, increases as the signal power grows, whereas the SNR_{NL} decreases as the launch power triggers the nonlinear effects. Through the characterization of SNR_{NL} at different power levels, a slope of ~ -2 dB/dB was observed, confirming the dependence on $1/P_{\text{ch}}^2$. This behavior is shown in Fig. 3.2, where for any arbitrary WDM system, the SNR performance is plotted as a function of the channel launched power.

Figure 3.2 also introduces P_{NLT} as the optimal power per channel where the SNR has a maximum value. And it has been shown experimentally [90] that around P_{NLT}, the linear noise power doubles the nonlinear noise power, having $\sim 66\%$ of the total SNR accounted for in the

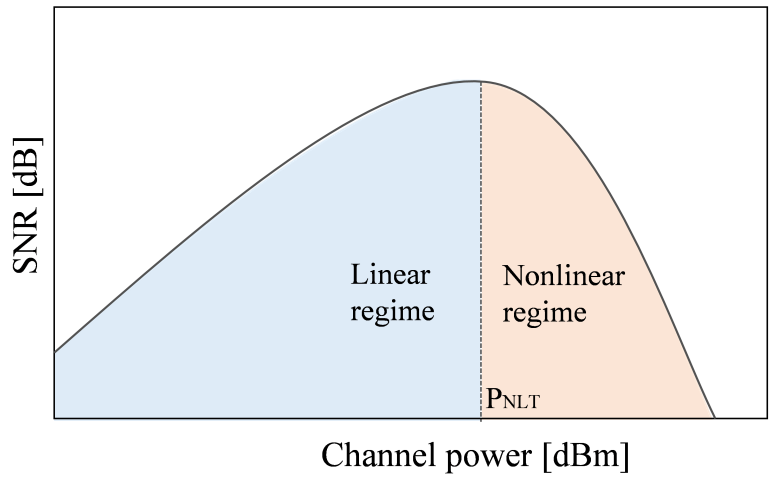

Fig. 3.2: The SNR as a function of channel power for an arbitrary transmission system.

$1/\mathrm{SNR}_{\mathrm{lin}}$ and the remaining $\sim 33\%$ in the $1/\mathrm{SNR}_{\mathrm{NL}}$. The significance of this finding holds great importance because it shows that optimal performance is achieved where the NLI noise is relatively small versus the ASE noise. As will be presented in Section 3.3, this result has inspired the development of heuristics that seek to rapidly optimize the performance of WDM transmission systems.

Thanks to its low complexity, the GN model is a valuable tool to develop simple optimization rules with great potential at the optical network level, where the inter-node links can include a variable number of channels with differing characteristics requiring a fast re-configurable routing. Therefore, the rapid optimization of the physical layer becomes a crucial task. One of the most critical challenges is optimizing power per channel within each span, considering the dynamic characteristics within the link. This problem has been simplified in [83, 91], providing a local optimization strategy that leads close to a global optimum (LOGO) at a relatively small computational effort.

Following the assumption that ASE noise and the nonlinear noise are additive Gaussian noises and assuming incoherent NLI accumulation, the SNR at the receiver can be approximated by generalizing eq. (3.1.9) as [83]

$$\frac{1}{\mathrm{SNR}} \approx \frac{1}{\mathrm{SNR}_{\mathrm{TRX}}} + \sum_{\mathrm{n}=1}^{N_s} \frac{1}{snr_n} \tag{3.1.10}$$

where

$$snr_n = \frac{P_{\mathrm{ch,n}}}{P_{\mathrm{ASE,n}} + \eta_n P_{\mathrm{ch,n}}^3} \tag{3.1.11}$$

is the SNR of any WDM channel at the output of the n^{th} lumped amplifier. These estimations are made span per span, considering only the NLI produced exclusively in the n^{th} span and the ASE noise coming from the n^{th} lumped amplifier alone, having $P_{\mathrm{ch,n}}$ as the launched power of the COI at the n^{th} span. From this derivation, we can observe that, as long as the estimation of each snr_n *are independent of one another*, the SNR at the receiver can be maximized by maximizing the SNR of

each individual span. This independence holds assuming no nonlinear coherence from span to span (incoherent GN model). Moreover, once the link has been established, we can assume that the launch powers of the WDM channels can be independently adjusted for each span, being these quantities the only values that can be set to optimize the total SNR. The relevance of this result relies on showing that by arranging the launch powers so that each snr_n is maximized, we ensure the whole link optimization. In other words, the LOGO strategy assumes that the local span optimization ensures the global link SNR optimization.

In practice, this optimization is quite challenging due to the dependence of $\eta_n P_{\mathrm{ch,n}}^3$ to the individual channel powers. A simplified strategy to overcome this complex problem has been suggested, assuming full link spectral loading. This technique, commonly known as LOGON [91], assumes that each channel spectra is rectangular with a bandwidth equal to the symbol rate R_s and that the frequency spacing is such that channel spectra touch but do not overlap, this "Nyquist limit" assumption, explains the "N" at the end of its name. In this scenario, the snr_n optimization is achieved by launching a uniform signal PSD G_{WDM} across the whole WDM system, such as the signal spectrum appears as one seamless rectangle of overall bandwidth B_{WDM} (Fig. 3.3 a). LOGON strategy proposes a set of closed-form equations that optimize the link based on the prediction of the optimum performance of each span. This is achieved by setting a launched power G_{WDM} that always fulfills the ratio described in eq. (3.1.8), static for each span and determined by the fiber and amplifier's parameters. Based on eq. (3.1.10), the optimized SNR of any lightpath in the network can be instantaneously estimated by adding up the snr_n of all the spans traversed from Tx to Rx. An important remark to consider when applying this technique is that by optimizing channels for a "limit performance", the network routing becomes quite fragile and load-dependent, so, in cases of sparsely populated links, the performance can be substantially underestimated (Fig. 3.3 b). However, it has been shown that even when the network is lightly loaded, for most cases, the performance underestimation is around 20% [91].

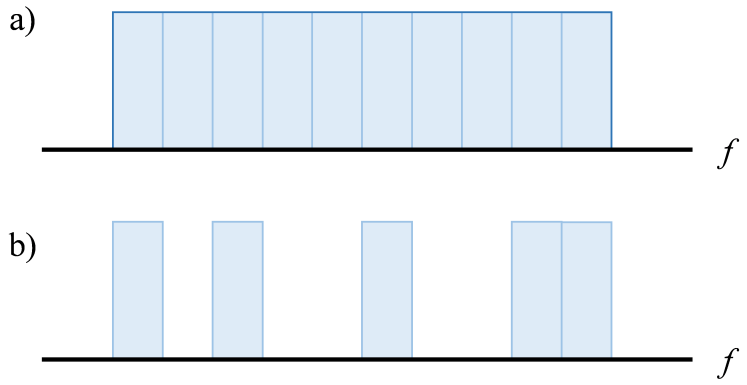

Fig. 3.3: a) WDM uniform power spectra (B_{WDM}), composed of rectangular channel spectra where $B_{\mathrm{ch}} = R_s$ and b) lightly loaded WDM potentially challenging the accuracy of the LOGON strategy.

Although the GN model enables optimization techniques that are effective for the design of point-to-point links and optical networks, it also has significant limitations. The first constraint arises from the signal definition provided by the signal Gaussianity assumption, showing that the model is modulation format agnostic, typically overestimating the NLI [35]. It has been shown that this NLI overestimation is more notable in the first spans of the link [92], especially in the case of pre-compensation at the transmitter, since the system would be close to zero dispersion. The enhanced Gaussian noise (EGN) model aims to remove the signal Gaussianity assumption, proposing a set of formulas that contain modulation correction factors to handle all formats, spacing values, and symbol rates, proving to be highly reliable [87].

The second limitation, and most relevant for this work, is that when solving the NLSE equation, the GN model only considers an instantaneous nonlinear response. This is no longer valid in transmission bandwidths beyond the C-band (5 THz), where the Raman component of the nonlinear response becomes significant and needs to be considered. Models accounting for the ISRS effect have been proposed by re-deriving the GN model in order to account for any arbitrary signal power profile [44–46].

3.2 The ISRS GN closed-form model

As we have previously discussed, numerous research groups have dedicated significant efforts to extend the accuracy of the GN model to account for the impact of the ISRS on the nonlinear interference power estimation. Moreover, multiple initiatives have been undertaken to derive closed-form versions of these ISRS GN, having advantageous computational efficiency compared to the numerical integration of the GN model, when for the case of UWB signals with more than 200 WDM channels, the computation time escalates to few hours [93]. Additionally, significant efforts have been dedicated to extending the ISRS GN closed-form model to account for arbitrary modulation formats by adding correction format contributions [94] or leveraging machine learning (ML) techniques [48].

In this section, the ISRS GN closed-form model presented in [94] is discussed, highlighting its main assumptions, formulas, and its accuracy in predicting the NLI in the presence of ISRS. For an accurate prediction of the power evolution along the fiber, we need a frequency and distance-dependent power profile, $\rho(z, f)$ that accounts for the ISRS and wavelength-dependent loss (WDL). This factor, previously presented in eq. (3.1.1) can be obtained by solving the continuous-wave Raman equations as a set of coupled ordinary differential equations (ODE) [44]

$$\frac{\partial P_i}{\partial z} = \underbrace{-\sum_{k=i+1}^{M} \frac{f_k}{f_i} g_R(\Delta f) P_k P_i}_{\text{ISRS loss}} + \underbrace{\sum_{k=1}^{i-1} g_R(\Delta f) P_k P_i}_{\text{ISRS gain}} - \underbrace{\alpha(f_i) P_i}_{\text{WDL}} \tag{3.2.1}$$

where M is the total number of WDM channels and $g_R(\Delta f)$ is the normalized (by the effective core area A_{eff}) Raman gain spectrum for a frequency

separation $\Delta f = |f_i - f_k|$. Equation (3.2.1) must be solved numerically, with the main advantage of accounting for any Raman gain profile. Obtaining a fully analytical solution to eq. (3.2.1) is feasible by assuming that the Raman gain spectrum is linear up to approximately 14 THz, as illustrated in Fig. 3.4. This assumption leads to the development of a simplified fully analytical solution, commonly called the *triangular approximation*, which only requires the slope of the normalized Raman gain spectrum C_r shown in red (Fig. 3.4).

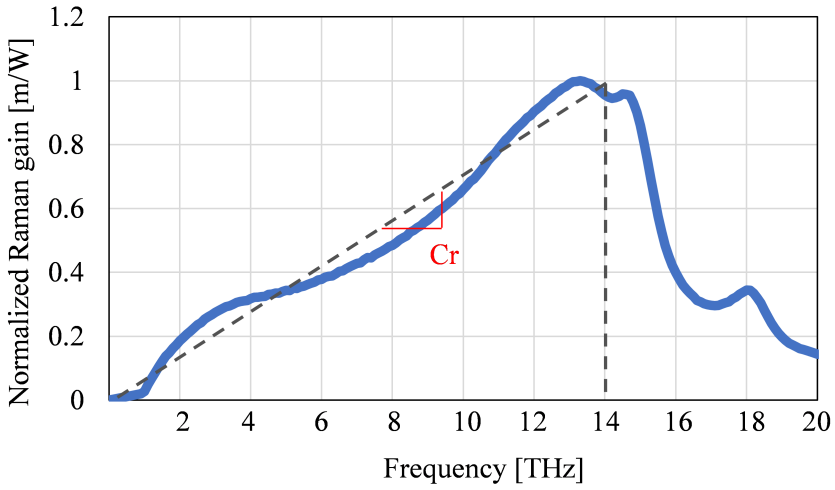

Fig. 3.4: Normalized Raman gain spectrum.

Due to its great simplicity, this approximation is preferred for fast performance estimation, resulting in a very accurate solution when working in C and C+L systems. However, this estimation fails to predict the impact of ISRS when channels are spaced more than 14 THz, limiting its use in UWB systems. Figure 3.5 shows the power profile after transmitting a fully-loaded 20 THz system through 100 km of standard single-mode fiber (SSMF), using the channel at 1550 nm as the frequency reference. The simulation accounts for an uniform power at the spectra at the entrance of the fiber with a total launched power of $P_{\text{tot}} = 26$ dBm. The numerical solution of the Raman equation (ODE in blue) shows that the power profile is no longer linear and presents a clear saturation at the optical bandwidth edges as the Raman gain drops after 14 THz, in combination with the wavelength-dependent attenuation coefficient. Moreover, a notable mismatch is observed when comparing with the triangular approximation (in green) estimations at bandwidths beyond the 14 THz threshold. The maximum observable discrepancy of 5.1 dB is located at the highest frequency.

Authors in [93] propose a parametric fitting reinterpreting the values of α and C_r, together with the additional $\bar{\alpha}$ as *channel dependent* quantities that aim to tailor the power evolution by a linear regression to the Raman ODE equations, extending it to arbitrary input power profiles and Raman gain profile at any frequency range. As presented in [80] the implementation of this strategy has been conducted and validated for fully loaded transmissions across 6 THz, 12 THz and 20 THz.

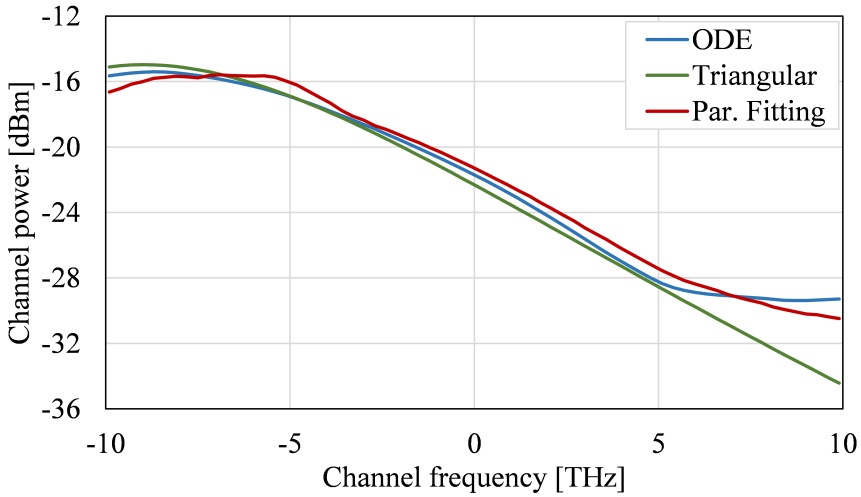

Fig. 3.5: Power evolution model comparison after 100 km SSMF transmission for a 20 THz system.

Figure 3.5 also includes the results of the parametric fitting (in red) showing a closer agreement to the numerical solution of the Raman equation (ODE in blue) with a maximum deviation of ~ 1 dB. Once the model to compute the power evolution accounting for ISRS proved to be highly accurate, especially working for C+L bands and beyond, our focus shifts to the estimation of fiber Kerr nonlinearities η by the implementation of the ISRS GN closed-form model. This work is mainly based on the models fully described in [35, 93], in which the NLI contributions in closed-form approximation can be estimated as

$$\eta_{\mathrm{Ns}}(f_i) \approx \sum_{n=1}^{N_s} \left[\frac{P_{\mathrm{i,n}}}{P_i}\right] \left[\eta_{\mathrm{SPM,n}}(f_i) N_s^{\epsilon} + \eta_{\mathrm{XPM,n}}(f_i)\right] \tag{3.2.2}$$

where, based on the XPM assumption (Section 3.1), only the $\eta_{\mathrm{SPM,n}}$ as the SPM contribution of the COI and the $\eta_{\mathrm{XPM,n}}$ as XPM contribution of all the other channels k on COI i at each n span are accounted. $P_{\mathrm{i,n}}$ is the power of channel i launched into the n^{th} span. The coherent accumulation along multiple pans is included using the coherence factor ϵ, and the SPM contribution is assumed to accumulate partially coherently, defining the coherence factor over the channel bandwidth B_i. The advantage of this approach is that the coherent accumulation is independent of the transmitted spectrum and is only a function of the channel bandwidth. Finally, the XPM contribution is assumed to accumulate incoherently to simplify the modeling.

The closed-form approximations for the SPM and XPM contributions are defined by

$$\begin{aligned} \eta_{\mathrm{SPM}}(f_i) \approx & \frac{4}{9}\frac{\gamma^2}{B_i^2}\frac{\pi}{\phi_i \bar{\alpha}(2\alpha+\bar{\alpha})} \\ & \cdot \left[\frac{T_i-\alpha^2}{\alpha}\mathrm{asinh}\left(\frac{\phi_i B_i^2}{\pi\alpha}\right) + \frac{A^2-T_i}{A}\mathrm{asinh}\left(\frac{\phi_i B_i^2}{\pi A}\right)\right] \end{aligned} \tag{3.2.3}$$

where $\phi_i = \frac{3}{2}\pi^2(\beta_2 + 2\pi\beta_3 f_i)$, $A = \alpha + \bar{\alpha}$ and $T_i = (\alpha + \bar{\alpha} - P_{\mathrm{tot}} C_r f_i)^2$

and

$$\eta_{\mathrm{XPM}}(f_i) \approx \frac{32}{27} \sum_{k=1,k\neq i}^{N_{\mathrm{ch}}} \left(\frac{P_k}{P_i}\right)^2 \frac{\gamma^2}{B_k \phi_{\mathrm{i,k}} \bar{\alpha}(2\alpha+\bar{\alpha})} \cdot \left[\frac{T_k-\alpha^2}{\alpha}\mathrm{atan}\left(\frac{\phi_{\mathrm{i,k}}B_i}{\alpha}\right) + \frac{A^2-T_k}{A}\mathrm{atan}\left(\frac{\phi_{\mathrm{i,k}}B_i}{A}\right)\right] \tag{3.2.4}$$

with $\phi_{\mathrm{i,k}} = 2\pi^2(f_k - f_i)[\beta_2 + \pi\beta_3(f_i + f_k)]$. Having f_i as the channel of interest (COI) with bandwidth B_i, and C_r as the slope of a linear regression of the normalized Raman gain spectrum, shown in Fig. 3.4. The sum in eq. (3.2.4) represents the summation over the XPM contribution of each individual interfering channel. Equations (3.2.3) and (3.2.4) can be extended to account for the real Raman gain profile and any input distribution by proper fitting of parameters α, $\bar{\alpha}$ and C_r, as previously shown in Fig. 3.5 (with parametric fitting). Under this approach, these three parameters are defined in a WDM channel basis, tailored to the real power evolution by linear regression to the Raman ODE equations, so eq. (3.2.1) approximates to

$$\rho(z,f) \approx (1+\widetilde{T_k})e^{-\alpha z} - \widetilde{T_k}e^{-Az} \tag{3.2.5}$$

having $\widetilde{T_k} = -\frac{P_{\mathrm{tot}}Cr}{\bar{\alpha}}f_k$. With this, the ISRS GN closed-form model is adapted to improve accuracy for non-uniform launch power distributions extended beyond the triangular region of the Raman gain spectrum by setting the parameters that best-fit eq. (3.2.5) with the profile estimated by eq. (3.2.1).

The implementation of the ISRS GN closed-form model, based on equations (3.2.3) and (3.2.4) is available on a public repository [95]. This tool facilitates rapid estimation of performance within an optical transmission system. Nonetheless, as being based on the GN model, it relies on the signal Gaussianity assumption, which as we have presented in Section 3.1, restricts the model for accounting for non-Gaussian modulation formats. Inspired by the EGN model, a first contribution to account for the format-dependent NLI generation was made in [94], deriving a modulation format correction formula for the ISRS GN closed-form model. It is assumed that the total NLI can be computed based on two contributions, one "GN-like" modulation format independent contribution and a correction factor that accounts for the transmitted modulation format. Therefore, the nonlinear coefficient can be written as

$$\eta_{\mathrm{Ns}}(f_i) = \eta_{\mathrm{GN,Ns}}(f_i) + \eta_{\mathrm{corr,Ns}}(f_i) \tag{3.2.6}$$

where $\eta_{\mathrm{GN,Ns}}$ is the ISRS GN model contribution per N_s span estimated through eq. (3.2.2) and $\eta_{\mathrm{corr,Ns}}$ is the modulation format correction term. In the case of Gaussian modulated signals, the correction term $\eta_{\mathrm{corr,Ns}}$ vanishes, leading to the ISRS GN closed-form model described previously. In other words, the total NLI can be written as a superposition of a Gaussian constellation and a modulation format-dependent correction term. The latter depending on $\Phi = \frac{E[|X|^4]}{E^2[|X|^2]} - 2$, being the right-hand side term the kurtosis of each modulation format [96] with values of

$\Phi_{\text{QPSK}} = -1, \Phi_{\text{16QAM}} = -0.68$, and for *Gaussian-like* modulation formats $\Phi_{\text{Gauss}} = 0$. It can be seen that Φ takes negative values in the case of common modulation formats, meaning that the NLI is *reduced* by the modulation format correction term. Overall, the modulation format correction is smaller (in absolute value) for more *Gaussian-like* modulation formats. The mathematical expression for this modulation format correction term is presented in [94], including the approximation of two main contributions: one originated in the first span, and an asymptotic contribution originated in the limit of a large span number.

Considering equations (3.2.3) and (3.2.4), the wavelength-dependent power evolution $\rho(z, f)$ accounting for the parametric fitting and the modulation format correction, the ISRS GN closed-form model that estimates the *total* NLI coefficient can be written as [35, 94]

$$\begin{aligned}
\eta_{\text{Ns}}(f_i) \approx{}& \frac{4}{9}\frac{\gamma^2\pi n^{1+\epsilon}}{B_i^2\phi_i\bar{\alpha}(2\alpha+\bar{\alpha})} \\
&\cdot\left[\frac{T_i-\alpha^2}{\alpha}\text{asinh}\left(\frac{\phi_i B_i^2}{\pi\alpha}\right)+\frac{A^2-T_i}{A}\text{asinh}\left(\frac{\phi_i B_i^2}{\pi A}\right)\right] \\
&+\frac{32}{27}\sum_{k=1,k\neq i}^{N_{\text{ch}}}\left(\frac{P_k}{P_i}\right)^2\frac{\gamma^2}{B_k}\Bigg\{\frac{n+\frac{5}{6}\Phi}{\phi_{\text{i,k}}\bar{\alpha}(2\alpha+\bar{\alpha})} \\
&\cdot\left[\frac{T_k-\alpha^2}{\alpha}\text{atan}\left(\frac{\phi_{\text{i,k}}B_i}{\alpha}\right)+\frac{A^2-T_k}{A}\text{atan}\left(\frac{\phi_{\text{i,k}}B_i}{A}\right)\right] \\
&+\frac{5}{3}\frac{\Phi\pi\tilde{n}T_k}{|\phi|B_k^2\alpha^2A^2}\left[(2|\Delta f|-B_k)\log\left(\frac{2|\Delta f|-B_k}{2|\Delta f|+B_k}\right)+2B_k\right]\Bigg\}
\end{aligned} \tag{3.2.7}$$

with $\phi_i = \frac{3}{2}\pi^2(\beta_2+2\pi\beta_3 f_i)$, $T_k = (\alpha+\bar{\alpha}-P_{\text{tot}}C_r f_k)^2$, $\Delta f = f_k - f_i$, $\phi_{\text{i,k}} = 2\pi^2(f_k-f_i)[\beta_2+\pi\beta_3(f_i+f_k)]$, $A = \alpha+\bar{\alpha}$ and

$$\tilde{n} = \begin{cases} 0, & \text{if } n = 1. \\ n, & \text{otherwise.} \end{cases} \tag{3.2.8}$$

The motivation behind the use of this analytical formula in this work relies on its simplicity and very good accuracy without involving the deployment of large data training [48]. Showing an average mismatch of ~ 0.3 dB compared to SSFM numerical simulations, for the transmission of channels modulated with Gaussian, 16QAM and 64QAM symbols over 10 THz of optical bandwidth after 100 km SSMF [94]. Moreover, the computational time in the order of milliseconds for the case of the analytical solution based on the triangular approximation or a few seconds for the semi-analytical approach based on the parameter fitting, make it a fundamental tool in the design and real-time optimization of UWB transmission systems beyond 14 THz.

3.2.1 Power optimization techniques in UWB systems

The development of accurate and fast ISRS GN closed-form models to estimate the nonlinear interference NLI generation in UWB scenarios has enabled launch power optimization techniques in order to maximize the QoT. However, it has been demonstrated in [45] that the SNR expression accounting for ISRS is incompatible with direct convex optimization, leading to multiple local solutions. Nevertheless, optimization techniques aiming to maximize the minimum channel margin were explored and to cope with the non-convex nature of the optimization problem, the authors suggested a sequence of convex optimizations able to find good locally optimal solutions with loose bounds on the sub-optimality of those solutions. In [97], to effectively reduce the search space for optimization, the SNR is maximized by considering a uniform launch power across the different transmission bands. An exhaustive search has also been addressed, simplifying the optimization problem by reducing the N_{ch} variables to $2N_{\mathrm{band}}$, in such a way that the only variables considered in the optimization were the launch power of the central channel per band and its tilt [98]. However, both approaches lead to sub-optimal solutions since the launch powers are not optimized per individual channel.

Alternatively, the use of deep neural networks [99] and *metaheuristics* such as the *particle swarm optimization* (PSO) algorithm has been investigated. In [100, 101], the launch power was optimized to achieve the highest total achievable information rate (AIR), mathematically described as

$$P_{\mathrm{ch,opt}} = \underset{\mathrm{P_{ch}}}{\operatorname{argmin}} \sum_{\forall ch} \underbrace{-\log_2\left(1+\frac{P_{\mathrm{ch}}}{P_{\mathrm{ASE}}+\eta_{\mathrm{N_s}}P_{\mathrm{ch}}^3}\right)}_{\mathrm{AIR}} \tag{3.2.9}$$

The optimization of this N_{ch}-*dimensional problem* was carried out using PSO followed by a gradient descent (GD) algorithm. The PSO method is efficient when exploring the optimization space of dimension N_{ch}. However, it does suffer from some inaccuracy in locating the exact minima. To mitigate this issue, the solution obtained from the PSO is utilized as an initial solution for the GD. It is well-known that the GD algorithm converges to a local minimum when a good initial solution is provided. Hence, the combination of these two algorithms strikes a fine balance between global and local search. This approach is suitable for non-convex optimization problems but at a very high computational cost. Computation times over 24 hours using a single-core desktop computer have been registered for the power optimization of 182 channels across the S+C+L band [102]. To reduce the complexity of the search, adjacent channels can be grouped into one *super channel*.

Finally, following the line of convex approximation and considering the launch power in log-space ($x_{\mathrm{ch}} = \log P_{\mathrm{ch}}$), an approach based on *freezing* the ISRS terms, in order to have the launch power optimization convex in x_i, is studied [102]. To freeze the ISRS terms during each iteration, a constraint limiting the total launch power during a sub-optimization step is introduced. The approach consists of iteratively increasing the

total permitted power $P_{\text{tot,m}}$ at each sub-optimization step m. In each convex sub-optimization, the initial value is the optimum launch power distribution of step m-1, the total launched power is limited to a delta increase ($\Delta_P = 0.1$ dB) from the total power from the previous iteration and all the ISRS are frozen and calculated based on $\Delta_P \cdot x_{\text{ch,opt}}$ with $x_{\text{ch,opt}}$ of step m-1. The algorithm ensures that ISRS is calculated a prior based on the total power allocated within each step, and the approximation of the approach only concerns the relative power distribution. Moreover, the power distribution does not change significantly across iteration steps when Δ_P is small. This methodology has been numerically validated, showing close results compared to the PSO algorithm but with around 15 minutes of computational time.

3.3 ASE-NL heuristic system optimization

In the previous sections, we have discussed the GN and the ISRS GN model and power strategies based on this model. For UWB, systems we have seen that by combining the efficient exploration of the search space with a second step of optimization, the PSO + GD have shown to provide sufficiently good solutions for the non-convex problem of launch power optimization in UWB transmissions. Nevertheless, its high computational cost (in the order of days depending the simulated transmission) makes it unfeasible to design UWB systems. Iterative convex approximations have shown close convergence to this technique but still with non-negligible computational times. This section details our proposed link power optimization strategy for multi-band WDM transmission systems, which relies on the simple derivations of link optimization deduced from the GN model. As will be shown, the proposed strategy performs similarly to the PSO + GD optimization at the lowest computational time.

As introduced in Section 3.1.1, it is well known from the GN noise model that in the absence of ISRS, at the optimum channel power, the ASE noise is twice the NLI noise power ($P_{\text{ASE}} = 2P_{\text{NL}}$) turning power optimization as a straightforward process. In this section, we evaluate the validity of this property in the presence of ISRS through a heuristic that aims to optimize the system performance based on the balance of linear and nonlinear noises. This solution, *ASE-NL heuristic* hereafter, is a very simple iterative power optimization approach derived analytically with the use of the ISRS GN closed-form model, implemented in our QoT tool. Next, we explain step-by-step the methodology of the solution, the system parameters, and the modeling assumptions on which it relies to later study the validity of the predicting results versus accurate but highly time-consuming machine learning (ML) techniques.

3.3.1 System definition

A system modeling accounting for all main physical effects is necessary for accurate optimization. Figure 3.6 illustrates a generic optical meshed network with different nodes. The connection between two nodes also

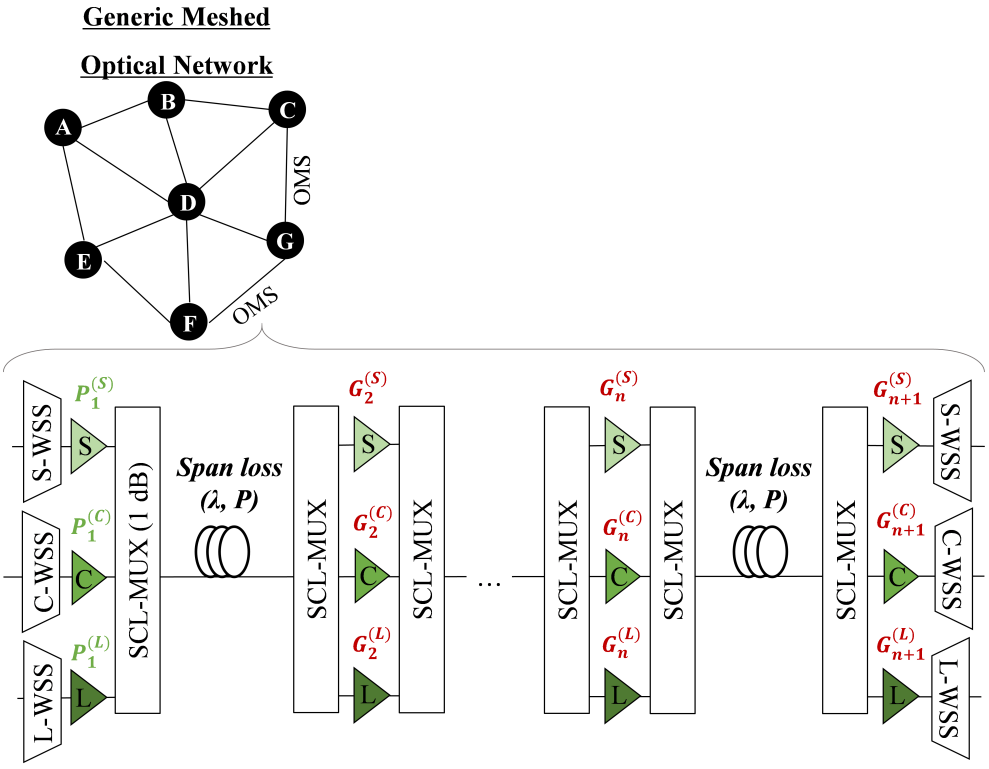

Fig. 3.6: Generic meshed optical network composed by multiple S+C+L OMS accounting for WSS, optical per-band amplifiers, SCL multiplexer/demultiplexers, and fiber spans.

called the optical multiplexing section (OMS), comprises the concatenation of fiber spans and optical amplifiers. Wavelength selective switches (WSSs) are placed at each OMS input and output for service re-routing and per-channel power equalization. Individual per-band amplifiers are employed to compensate for span loss and to adjust launched power into the fiber. SCL multiplexers/demultiplexers with arbitrary insertion loss are used at each amplification stage. The system is assumed to be fully loaded.

In this way, generalizing eq. (3.1.10) at network level, the end-to-end SNR performance of any WDM channel over a given optical link composed of K OMS can be estimated by the sum of the B2B noise imposed by the transponder and the estimated snr_{OMS} of each traversed OMS as

$$\frac{1}{\text{SNR}} \approx \frac{1}{\text{SNR}_{\text{TRX}}} + \sum_{k=1}^{K} \frac{1}{snr_{\text{OMS,k}}} \tag{3.3.1}$$

where

$$\frac{1}{snr_{\text{OMS,k}}} = \sum_{n=1}^{N_s+1} \underbrace{\frac{hf\text{NF}_n G_n R_s}{P_n}}_{\text{Amplifier's ASE noise}} + \sum_{n=1}^{N_s} \underbrace{\eta_{\text{Ns}} P_n^2 \delta_n^2}_{\text{Fiber Kerr nonlinearities}} \tag{3.3.2}$$

describes the SNR of each OMS arising from the independent contributions of ASE noise and the NLI noise at each n^{th} span inside the OMS. The ASE noise power added by each optical amplifier is based on its NF_n, G_n and output power P_n frequency profiles. h is Planck's constant

and f is the central frequency of the considered channel. Each span is distinguished by its input/output SCL multiplexer/demultiplexers with intrinsic lumped losses δ and δ', respectively. The key point of the ASE-NL heuristic to work in UWB systems relies on computing the nonlinear interference (η_{Ns}) and the power evolution (ρ) accounting for ISRS effect as presented in Section 3.2. Power evolution along the OMS is estimated as

$$P_{\mathrm{Ns+1}} = P_1 \prod_{n=1}^{N_s} \underbrace{\delta_n \rho_n \delta'_n}_{\text{Span loss}} \cdot G_{\mathrm{n+1}} \tag{3.3.3}$$

the computation of ρ relies on the solution of ODE using experimentally measured Raman gain using eq. (3.2.1). Optical in-line filtering is left out of the scope of this work as optimum power is independent of filtering [79]. This system modeling and the computation of eq. (3.3.1), eq. (3.3.2) and eq. (3.3.3) are part of the QoT tool implementation reviewed in Section 2.6.4. Therefore, the optimization method could be applied to heterogeneous systems having different span lengths and fiber types.

Dynamic per-channel equalization is assumed to be possible only thanks to the WSS at the input of the OMS, having for all the in-line amplifiers *static* gain profiles for a given load. In the interest of practical system design and without loss of generality, we consider ideal flat-tilted amplifier gain profiles defined by their nominal gains (g_μ) and tilts (g_τ). Real measured gain profiles for different g_μ, g_τ could eventually be used. The booster output power profile is also considered flat-tilted and defined by its mean power ($P_{1\mu}$) and tilt ($P_{1\tau}$) for each band.

3.3.2 Link power optimization method

The first step of the power optimization process consists of finding the optimum per-band $P_{1\mu}$ and $P_{1\tau}$ as well as the per-band inline amplifiers g_μ and g_τ that maximize capacity. For that, we perform the iterative N_s-span optimization approach depicted in Fig. 3.7, described as follows:

For the first span (n=0), each band's booster output power $P_1(f)$ is initialized using a uniform (flat) power profile. Input power to the next amplification stage ($n+1$) is computed from δ, δ' and ρ. $n+1$ amplifiers g_μ and g_τ are set to compensate for per-band span loss. The mean and tilt of the frequency-dependent $P_{\mathrm{ASE}}/P_{\mathrm{NL}}$ ratio for each band is computed, from which the power distance to optimum is derived as $\Delta P = [P_{\mathrm{ASE}}/P_{\mathrm{NL}}]_{\mathrm{dB}}/3 - 1$. Booster mean output power and tilt are updated based on a fraction (ϵ) of ΔP. The operation is repeated until ΔP is below a desired threshold. This process is repeated sequentially for all consecutive spans. However, from the second span, all in-line amplifiers' mean gains and tilts are optimized, for which the output power is computed based on eq. (3.3.3) accounting for the entire power evolution from n=1 to n. Similarly, the accumulated $P_{\mathrm{ASE}}/P_{\mathrm{NL}}$ is estimated for each new optimized span.

We consider an ideal-tilted launch power profile with no ripples for practical system design purposes. However, once the optimized parameters (P_μ, P_τ, g_μ and g_τ) are found, a second step of per-channel equaliza-

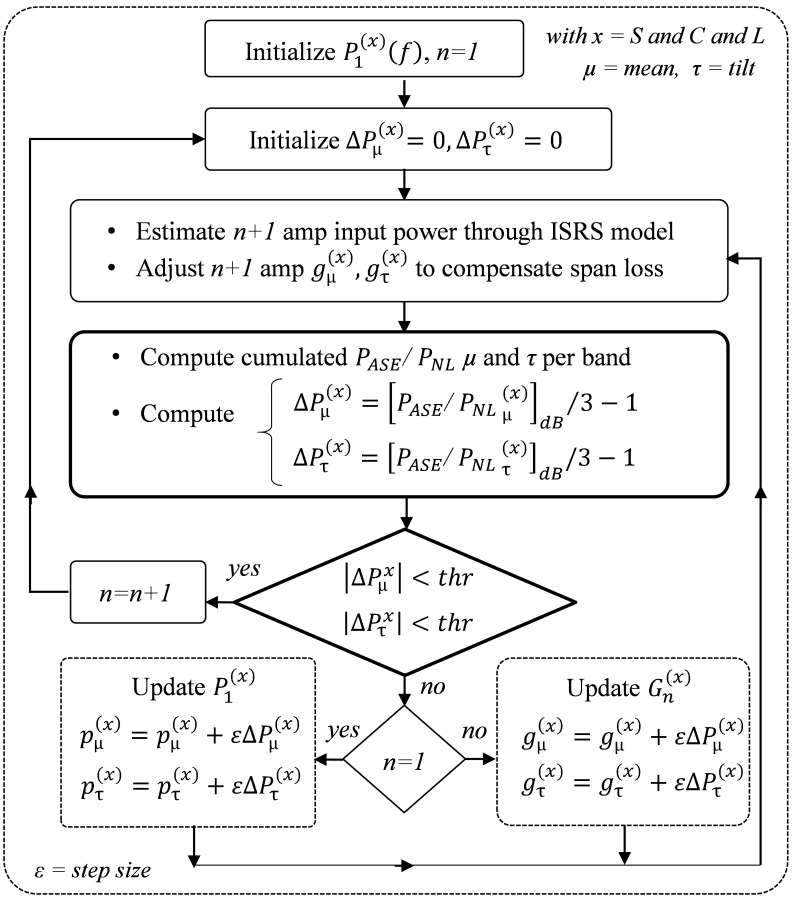

Fig. 3.7: Block diagram of OMS-based amplifier gain/power optimization based on heuristic $P_{\mathrm{ASE}}/P_{\mathrm{NL}}$ ratio.

tion can be performed at WSS level to account for power ripple accumulation. In this sense, at the booster level, granular power optimization is performed at each channel applying the ASE-NL heuristic under the constraint that total output power per band should be maintained to avoid significant changes in ISRS power transfer.

3.3.3 Numerical assessment

We compare our fast and simple heuristic versus more complex ML-based evolutionary algorithms, such as the genetic algorithm (GA) and, as presented in Section 3.2.1, the PSO followed by GD. For the GA- and PSO-based optimizations, we perform a sequential accumulated span-by-span process where $P_{1\mu}, P_{1\tau}, g_\mu$ and g_τ are updated such that the total Shannon capacity $\sum_{\forall ch} \log_2(1 + \mathrm{SNR})$ is maximized.

Considering a single OMS with 5x80 km SSMF spans, transmitting 184 PCS-64QAM channels with 100 GHz channel spacing over S, C and L bands (18.4 THz). The NF for the amplifiers in the three bands is considered to be 4.5 dB. Figure 3.8 a) shows the optimized booster output power for each studied algorithm. It can be observed that both ML-based techniques converge to very similar tilted power distributions, having a maximum of 0.2 dB difference in the L-band, as presented in the inset of Fig. 3.8 a). For the ASE-NL heuristic, the booster power tilts (P_τ) are

set to 2.2 dB and 2.6 dB for S and C-band, respectively, while the GA and PSO+GD require 3 dB of power tilt for S-band and $\sim$ 3.6 dB for C-band. Nevertheless, the three optimization techniques show a small power tilt in the L band, with $P_{1\tau}^{(L)}$<0.4 dB for all the cases. It can be observed from the power spectra, that the main difference between the ASE-NL heuristic and the other two power distributions starts at the end of the C band and continues along the entire L band.

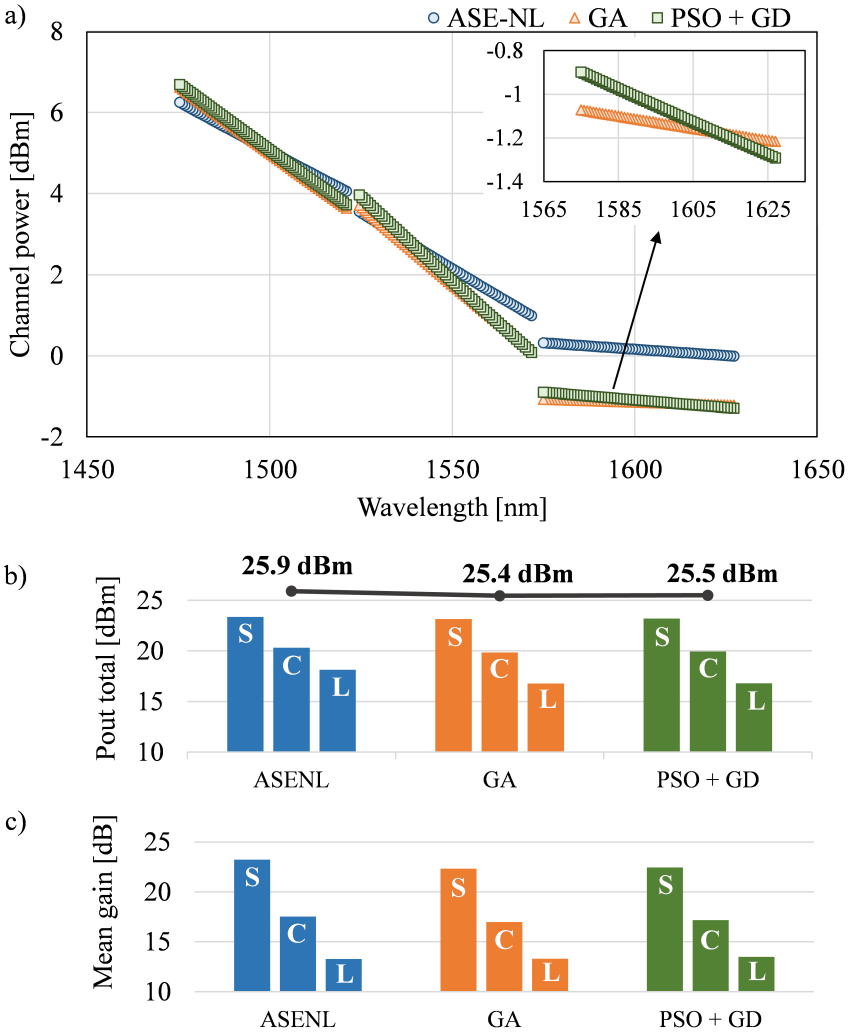

Fig. 3.8: a) Optimized booster output power, b) per-band and total booster output power (bold), and c) amplifier's mean gain per band for the ASE-NL heuristic (blue), the GA(orange) and the PSO+GD (green).

Regarding the total power distribution among bands (Fig. 3.8 b), for the three cases a large part of the power is allocated to the S band, having $\sim$ 6.5 dB more output power than the L-band for the three techniques. The GA and PSO+GD strategies show a total booster's power of $\sim$ 25.4 dBm; in comparison, the ASE-NL heuristic requires a total booster's power of 25.9 dBm, translated to $\sim$ 0.3/0.4/1.3 dB of additional launched power for S/C/L bands respectively. Figure 3.8 c) shows the mean amplifier's gain per band for the three optimization techniques. It is clear that for all the cases, there is a big imbalance in the required amplifier output powers and gains between the three bands. Notably,

the power distributions suggested by the algorithms increase the power allocated in the bands with shorter wavelengths (S-band) to cope with the higher fiber losses and the ISRS power transferred to the neighboring channels.

Figure 3.9 a) shows the $P_{\mathrm{ASE}}/P_{\mathrm{NL}}$ ratio for the three methods. As expected, the mean ratio per band closely converges to 3 dB for the ASE-NL, while for GA and PSO+GD, both C and L bands are slightly pushed to the *linear* regime. The WDL assumed for this simulation is presented in Fig. 3.9 b), along with the frequency-dependent span loss resultant after transmitting the power profiles of the three optimization techniques. Thus, the estimated span loss accounts for the WDL and the ISRS effect. Compared to the ASE-NL heuristic, the GA and PSO+GD achieve a lower span loss in both S and C bands while it is mainly unchanged for the L band as a result of allocating lower power in the L band, leading to less ISRS depletion.

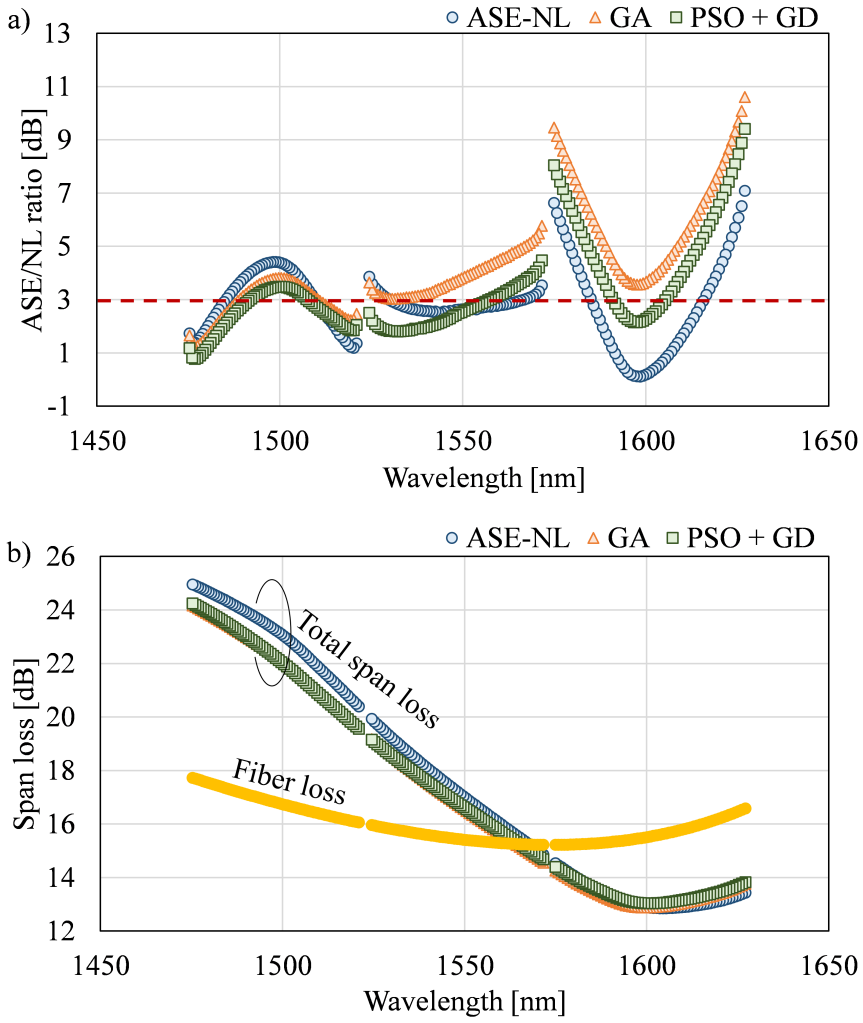

Fig. 3.9: a) $P_{\mathrm{ASE}}/P_{\mathrm{NL}}$ ratio and b) span loss for the ASE-NL heuristic (blue circles), the GA (orange triangles) and the PSO+ GD (green squares). In yellow, the WDL assumed for the S+C+L transmission.

The calculated SNR for the entire OMS is presented in Fig. 3.10, showing that the GA and PSO+GD achieve a slightly higher SNR compared to the ASE-NL heuristic for both S- and C-band with a maximum

difference of 0.4 dB for both bands. However, for these ML-based techniques, the SNR experiences a global decrease in the L-band, with a degradation of up to approximately 1 dB for higher wavelengths. The difference between the worst and the best SNR channel is $\sim$ 6 dB, evolving almost linearly in both the S and the C bands. The curved shape of the L-band is due to the curved behavior of the span loss, characterized in Fig. 3.9 b).

The total achieved OMS Shannon capacity using the ASE-NL heuristic is 225.8 Tbit/s, while 227.6 Tbit/s and 227.4 Tbit/s are registered for the GA and the PSO+GD respectively. The capacity gain provided by the ML-based methods can be explained by the enhanced SNR performance observed in the S-band and C-band. The simple and fast ASE-NL heuristic leads to a total capacity loss of 0.7% with a computation time of 3 minutes using a single-core standard desktop computer, while the computation of the GA and the PSO+GD took more than 24 hours to execute on the same machine.

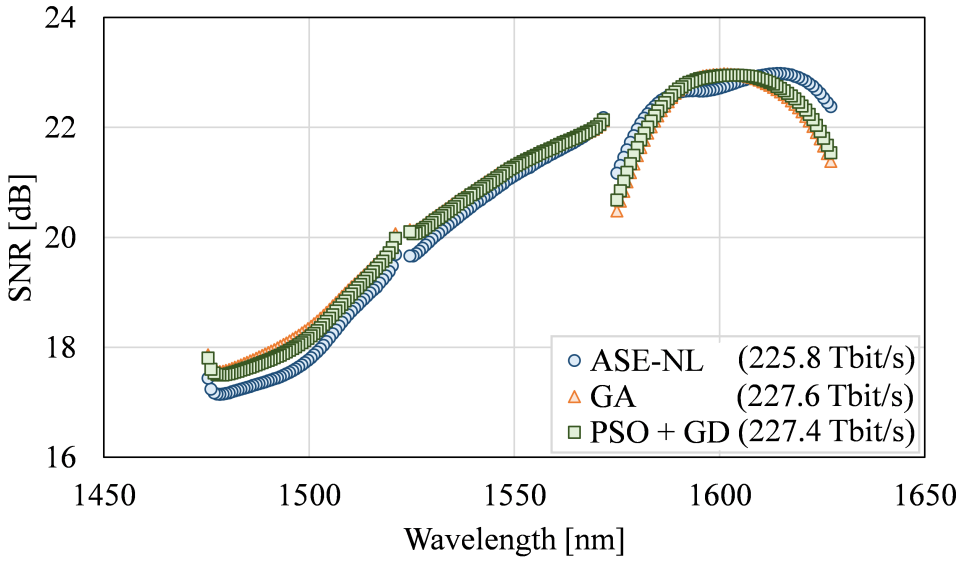

Fig. 3.10: SNR and total achieved capacity for the ASE-NL heuristic (blue circles), the GA (orange triangles) and the PSO+GD (green squares).

Figure 3.11 a) plots the power profile at the output of the booster (unfilled markers) and the last amplifier (dotted line) of the OMS when launching the optimized pre-emphasis given by the ASE-NL heuristic. It can be observed that the power evolution after each amplification stage accounts for considerable power ripple accumulation, reaching $\sim$ 6 dB in the L band. Therefore, to further enhance the throughput, a per-channel equalization process can be carried out at the WSS. This second step estimates a new booster output power distribution maintaining the optimized total power per band found by the ASE-NL heuristic.

Figure 3.11 b) shows the resultant power profile at the output of the booster (filled markers) and the last amplifier (dotted line) of the OMS after applying the per-channel equalization of the ASE-NL heuristic. The newly proposed power profile shows slight ripples in the S- and

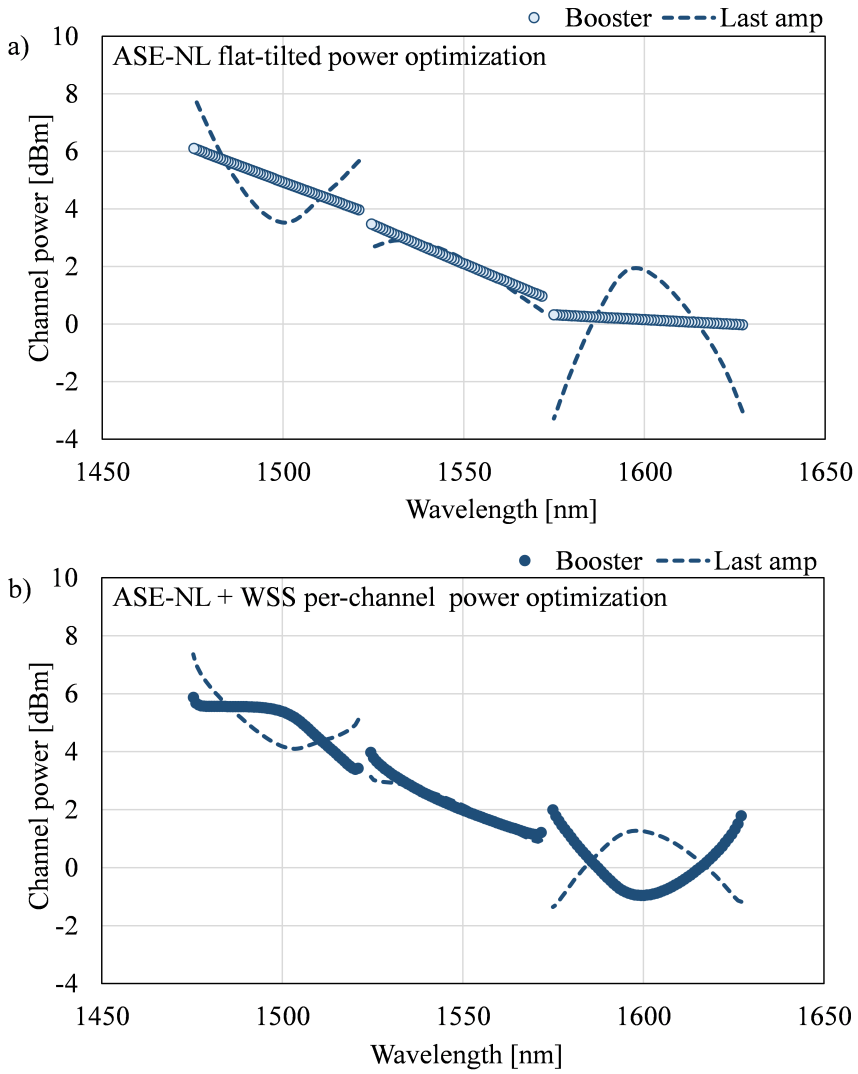

Fig. 3.11: a) Per-band tilted-linear (unfilled markers) and b) per-channel equalized (filled markers) power optimization based on the ASE-NL heuristic at the output of the booster and at the output of the last amplifier (dotted lines).

C- bands, while a curved power shape distribution is presented in the L-band. As mentioned, the power distribution per band is the same as the one proposed for the ASE-NL heuristic in Fig. 3.8 b), with a total power of 25.9 dBm. The amplifier's mean gain and tilt (g_μ and g_τ), previously obtained with the ASE-NL heuristic (Fig. 3.8 c), are maintained for the estimation of the power evolution after each amplification stage and SNR. Thanks to the new equalized pre-emphasis, a notable reduction of ripples is observed at the output of the last amplifier, with less than 4 dB in the L-band compared to the more than 6 dB observed in the first step of the ASE-NL heuristic.

The calculated SNR for the entire OMS after the per-channel equalization is presented in Fig. 3.12. The SNR is improved for all channels, with a maximum gain of 1 dB at short wavelengths of the L-band. This performance enhancement leads to a total Shannon capacity increase from 225.8 Tbit/s to 226.6 Tbit/s.

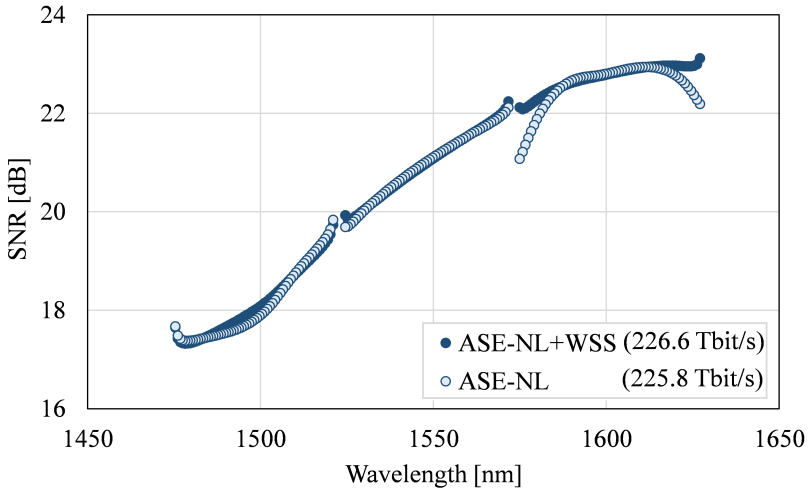

Fig. 3.12: SNR (unfilled markers) and per-channel equalized (filled markers) power distributions based on the ASE-NL heuristic.

3.4 Throughput analysis in UWB systems

The relevance of using model-based launch power optimization techniques lies in its capacity to further enhance system performance in UWB systems. Using the two-step ASE-NL heuristic previously presented (Section 3.3), this section assesses the capacity gain with respect to bandwidth when uniform and optimized power distributions are launched, emphasizing the importance of power pre-emphasis in transmissions with larger optical spectra. The simulations for this study case account for the experimental characterization of the transmission elements involved in our S+C+L demonstrations [II,III,VI,X] (Chapter 4) and aim to investigate performance in extended scenarios with more and longer spans.

The transmission link consists of an OMS with five 80 km SSMF spans, transmitting 140 Gbaud channels spaced by 150 GHz. We progressively transmit 40, 80 and 120 PCS-64QAM channels within C, C+L and S+C+L bands, assuming a total of 18 THz of bandwidth for the triple-band transmission. The link is assumed to use lumped amplifiers with no ripple, having the following NF: 5 dB for the C band and 6 dB for both the L and S-band. Multiplexers and demultiplexers with 1 dB and 2 dB insertion loss, respectively, are used at each amplification stage. The B2B penalty, mathematically represented in $\mathrm{SNR}_{\mathrm{TRX}}$ in eq. (2.6.2) is set to 22 dB for all the bands [III].

Table 3.1: Per-band output power with a) optimized pre-emphasis and b) uniform launch power profile

	a) Pre-emphasis (dBm)			b) Uniform (dBm)		
C		21.8			21.3	
C+L		22.7	19.3		20.8	20.8
S+C+L	24.5	20.9	16.3	19.8	19.8	19.8

Using the two-step ASE-NL heuristic, we perform system optimization to compare the capacity benefits of the pre-emphasis versus the equivalent optimal uniform power profile, considering the uniform case as a flat power spectra with the same power per channel (no pre-emphasis). Table 3.1 presents the per-band total output power predicted by the algorithm and the uniform power spectrum that maximizes the total Shannon capacity. The optimal uniform powers are found by sweeping the total power level while setting the same power per channel for all the cases, estimating the OMS SNR and selecting the case for which $\sum_{\forall ch} \log_2(1+\text{SNR})$ is maximized.

For the C-band transmission, the optimized pre-emphasis requires 0.5 dB more of total power than when launching uniform power spectra. A similar effect is observed in the C+L transmission, where the optimal total power for uniform distribution is 23.8 dBm and 24.3 dBm is the total power found by the ASE-NL heuristic. Nevertheless, for the S+C+L band, the total power predicted by the algorithm is 26.5 dBm, 2 dB more

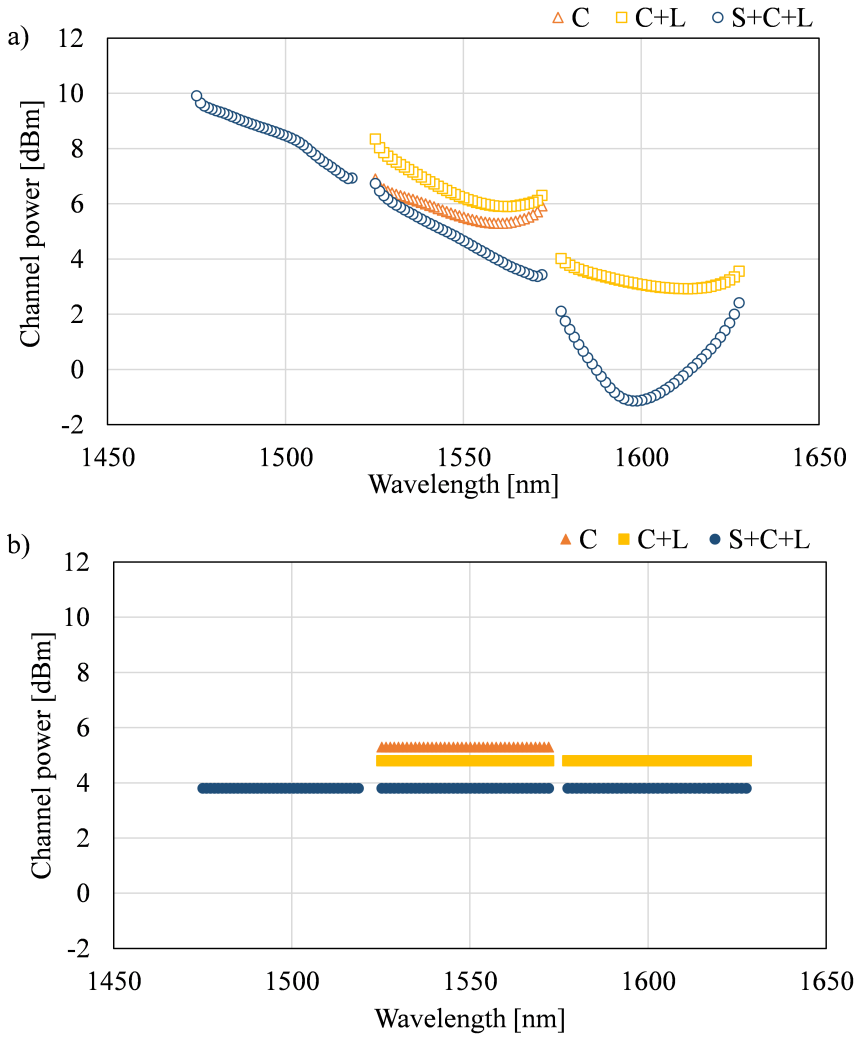

Fig. 3.13: Booster channel power for a) the ASE-NL optimized pre-emphasis (unfilled markers) and b) uniform power distribution (filled markers) when transmitting in C (triangles), C+L (squares) and S+C+L (circles).

than the optimal total power required by the uniform power distribution. Notably, the power distribution suggested in Fig. 3.13 a) increases the power allocated in the bands with shorter wavelengths to cope with the higher fiber losses and the ISRS power transferred to the neighboring channels, also explaining the larger difference in total power incurred by the model-based optimization when compared with the uniform power distribution. Consistent with the results presented in Fig. 3.11 b), the proposed pre-emphasis shows a curved-shape profile in the L-band to reduce the ripple accumulation across the multi-span transmission.

Figures 3.14 a) and b) plot the estimated SNR for C (triangles), C+L (squares) and S+C+L (circles), for the case of power pre-emphasis and uniform launch power distribution, respectively. It can be observed that with the power pre-emphasis (unfilled markers), the SNR performance of the short wavelengths in the C-band is slightly reduced when adding the L-band. This effect is more evident with the uniform power, so

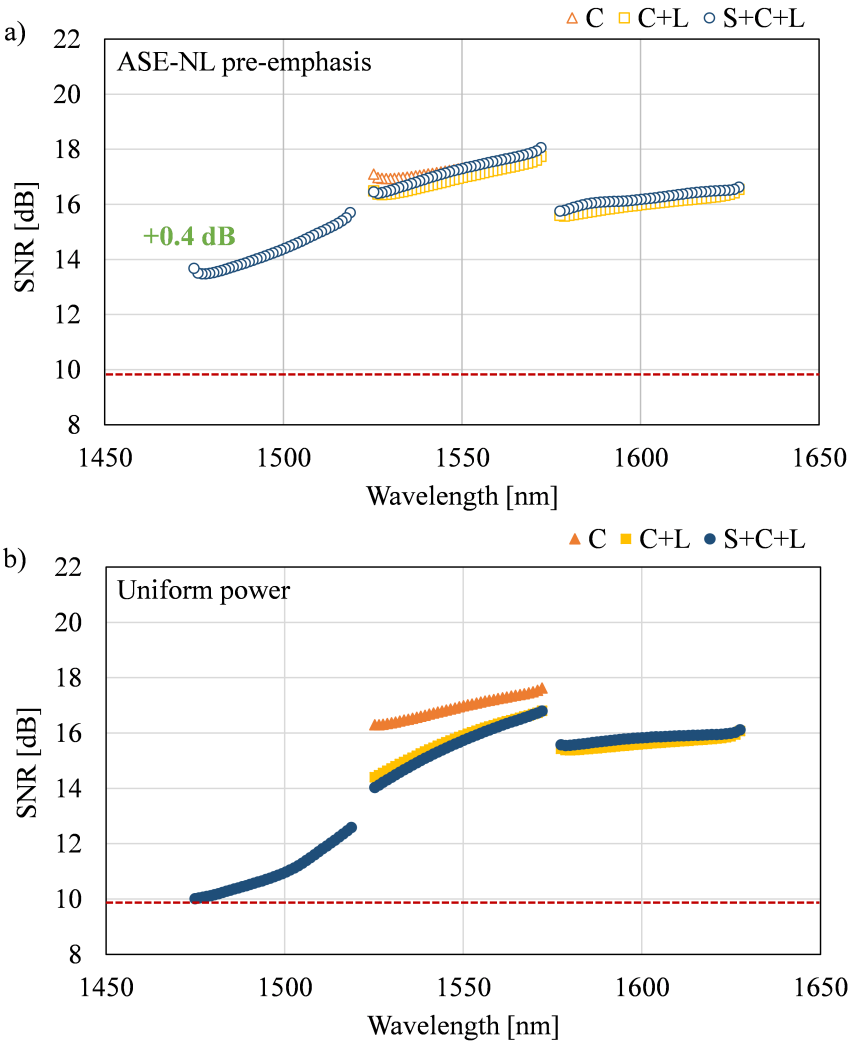

Fig. 3.14: SNR using a) the ASE-NL optimized pre-emphasis (unfilled markers) and b) uniform power distribution (filled markers) when transmitting in C (triangles), C+L (squares) and S+C+L (circles). In green, the SNR gain of the worst channel SNR with respect to uniform power distribution.

the resultant SNR for C+L transmission shows worse SNR for all the channels in the C-band with a maximum difference of $\sim$ 2 dB. When adding the S-band, thanks to the use of model-based power equalization techniques accounting for ISRS, the SNR of all the channels is higher than what is achieved with the optimal uniform power profile. This is especially observed in the S-band, where a gain of 4 dB is maintained along the entire band, illustrated in Fig. 3.14 a).

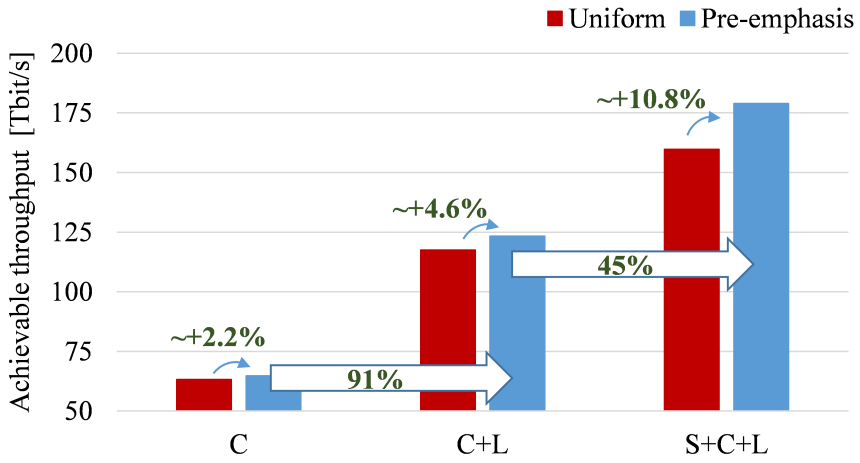

Fig. 3.15: Achievable throughput when transmitting uniform power spectrum (red) and optimized pre-emphasis (blue) in C, C+L and S+C+L systems.

Moreover, Fig. 3.15 quantifies the throughput increase with respect to bandwidth for uniform power distribution (red) and equalized pre-emphasis (blue), showing that we almost double the capacity when we move from C to C+L band. When adding the S-band, the increase is 45%, close to the 50% bandwidth increase. Additionally, for all the scenarios, capacity is higher when using power pre-emphasis, being more relevant with a larger bandwidth. With the S+C+L system, the use of power optimization provides more than 10% capacity increase, proving the importance of power pre-emphasis in ultra-wideband systems. The total capacity for the S+C+L transmission when all the channels are optimized is 178.9 Tbit/s. This high-throughput performance is achieved by targeting all the WDM channels to fulfill the ASE-NL heuristic so the system capacity is maximized.

3.5 Alternative equalization techniques

The use of the ASE-NL heuristic results in a high-throughput performance achieved by targeting all the WDM channels to fulfill a $P_{\mathrm{ASE}}/P_{\mathrm{NL}}$ ratio of 3 dB (Fig. 3.17 a). However, the observed significant variance in SNR among channels (Fig. 3.12 and Fig. 3.14 a) requires adjusting the bit rate for each channel, which could not be feasible in deployed optical networks. Consequently, various research groups have developed model-based optimization methods designed to achieve uniform SNR across all

bands in UWB systems. For instance, a brute-force optimization strategy managed a minimal discrepancy of 0.2 dB between the estimated average SNR values across the C and L bands [103]. Moreover, for extended UWB scenarios across the E+S+C+L bands, a disparity of up to 1 dB was achieved, but restricting the maximum total power to 21 dBm to limit the ISRS effect [104]. Similar to these approaches, this section examines the application of the ASE-NL heuristic to develop two novel equalization techniques tailored for different transmission scenarios:

- Intra-band equalization, which targets a flat SNR within each band.
- Inter-band equalization, which targets a flat SNR across all bands.

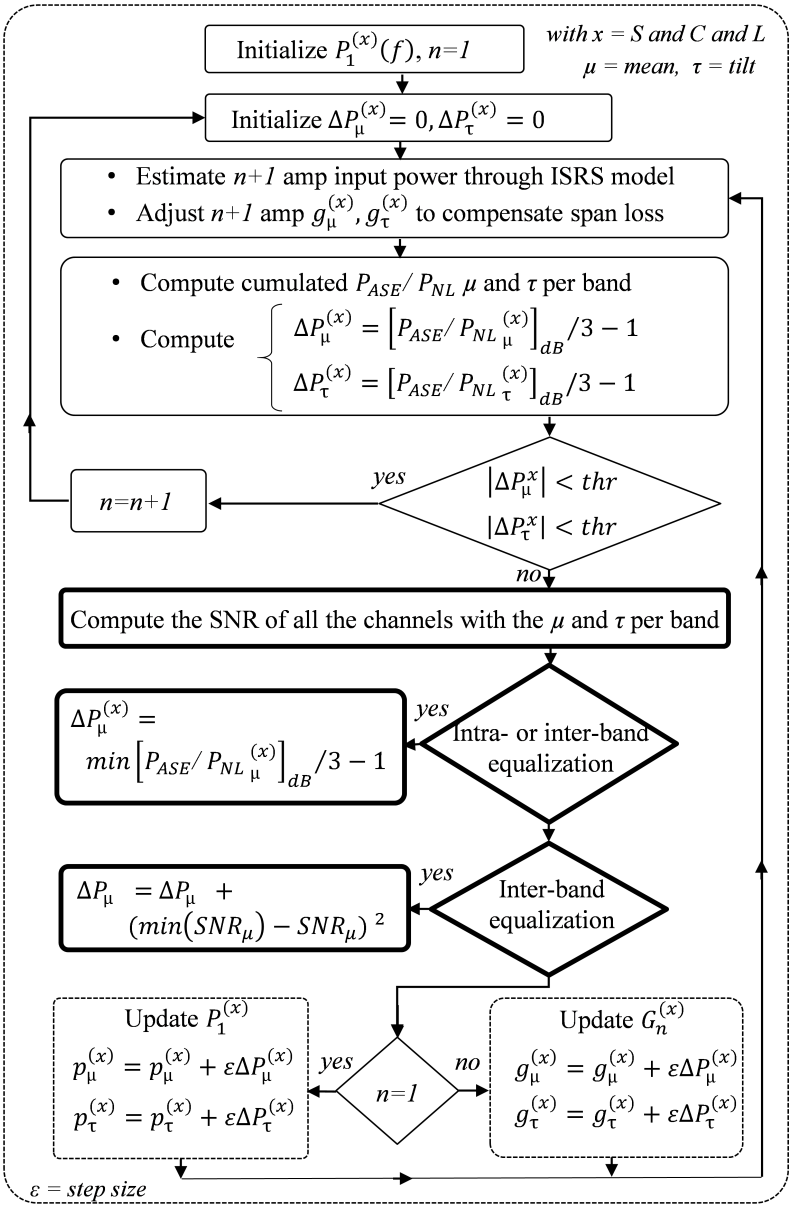

Fig. 3.16: Block diagram of the first step of the ASE-NL heuristic as presented in Section 3.3.2. The additional blocks corresponding to the new equalization methods are highlighted.

Figure 3.16 recalls the algorithm followed by the first step of the ASE-NL heuristic presented in Section 3.3.2, which aims to calculate the optimal per-band P_μ, P_τ, g_μ and g_τ that achieve a $P_{\text{ASE}}/P_{\text{NL}}$ ratio of 3 dB by adjusting the values of power and gain based on a proportional factor ΔP. Additionally, Fig. 3.16 introduces the new block components for achieving intra- or inter-band SNR equalization. Initially, the SNR for each channel is estimated, as well as their mean and tilt per band ($\text{SNR}_\mu, \text{SNR}_\tau$). These SNR estimations become crucial to consider in our cost function, guiding further adjustments in ΔP.

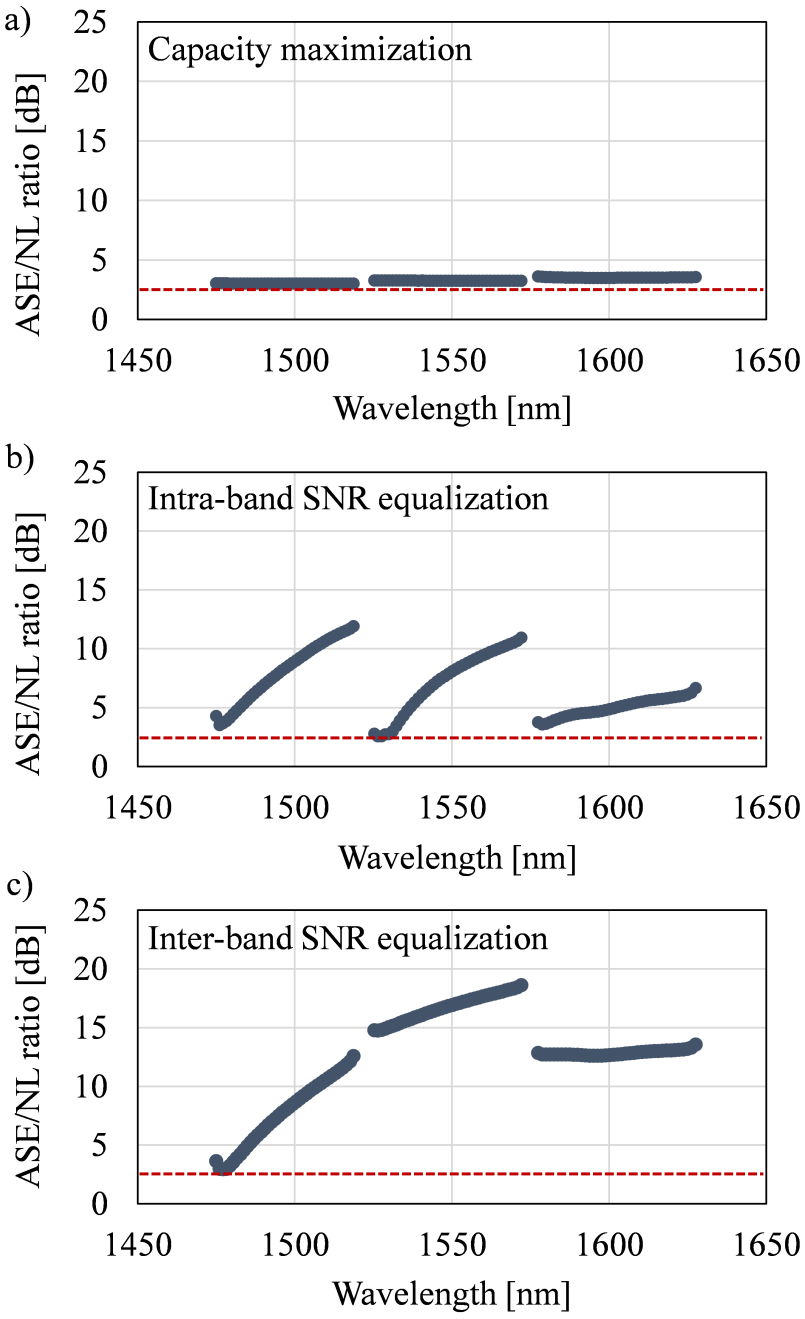

Fig. 3.17: $P_{\text{ASE}}/P_{\text{NL}}$ for different equalization techniques: a) capacity maximization, b) intra-band SNR equalization and c) inter-band SNR equalization.

For both intra- and inter-band optimization, the value of ΔP per band is changed towards the direction of the band's minimum P_{ASE}/P_{NL} ratio. This means that the channel with the lowest P_{ASE}/P_{NL} within the band is prioritized for updating the booster and output power levels. In the case of inter-band equalization, an extra step reduces the disparity between the minimum and average SNR across all the bands, to achieve a consistent uniform SNR profile throughout the entire spectrum. We show in Fig. 3.17, the resultant P_{ASE}/P_{NL} after applying all the equalization techniques to the S+C+L system discussed in Section 3.4. It is observed that the original ASE-NL heuristic (Fig. 3.17 a) aims to *maximize capacity* by applying a 3 dB rule across all WDM channels. The *intra-band equalization* (Fig. 3.17 b) applies the 3 dB ratio to the least performing channel in each band (Fig. 3.17 b), and the *inter-band equalization* (Fig. 3.17 c) applies the 3 dB ratio to the overall worst performing channel in the entire system.

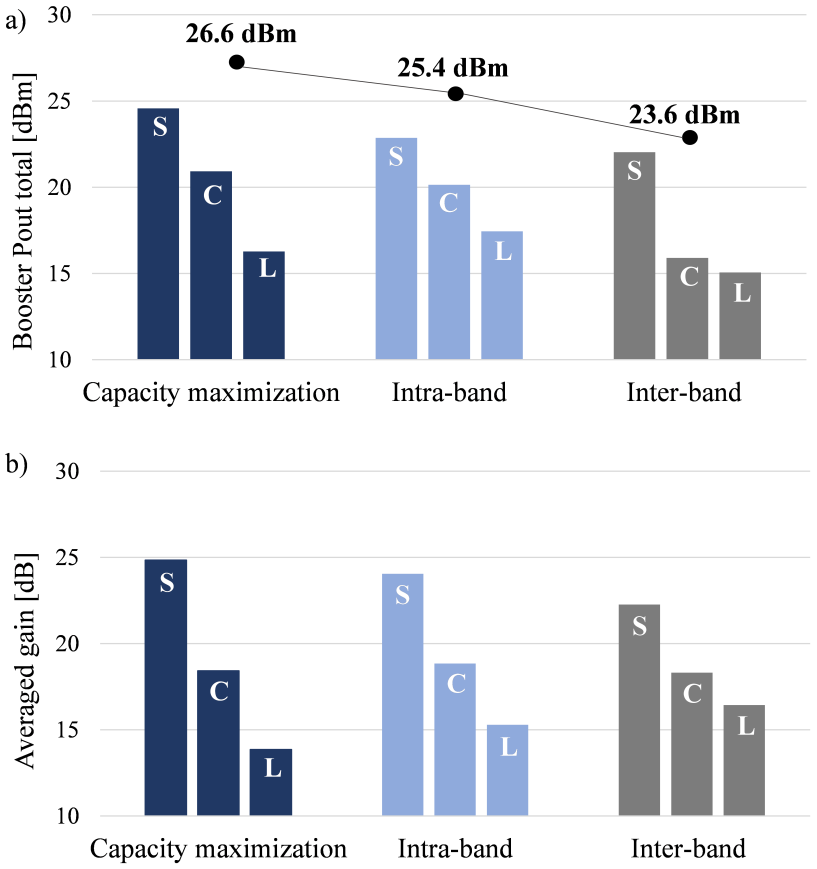

Fig. 3.18: a) Per-band and total booster output power (bold) and b) averaged gain per-band for each equalization technique.

The resultant power allocation per band for each of the equalization strategies is shown in Fig. 3.18 a), having for all the cases, a clear imbalance between the S-band and the other bands. Particularly, for the inter-band equalization, the power gap between S and C- bands is 6 dB. It can also be observed that the proposed methods are more power efficient regarding the total booster output power. Besides the optimized powers, the algorithm also provides the optimized mean gain for the inline amplifiers.

Figure 3.18 b) shows the average gain per band set by each equalization technique for the amplification stage after the first span. It is shown that for both intra-band and inter-band equalization, the L-band amplifiers require more gain due to less ISRS power transfer induced by the S-band, explained by the lower power allocated in this band when compared with the capacity maximization equalization. Similarly, we observe a lower gain in the S-band for the new equalization designs since they are less depleted by ISRS.

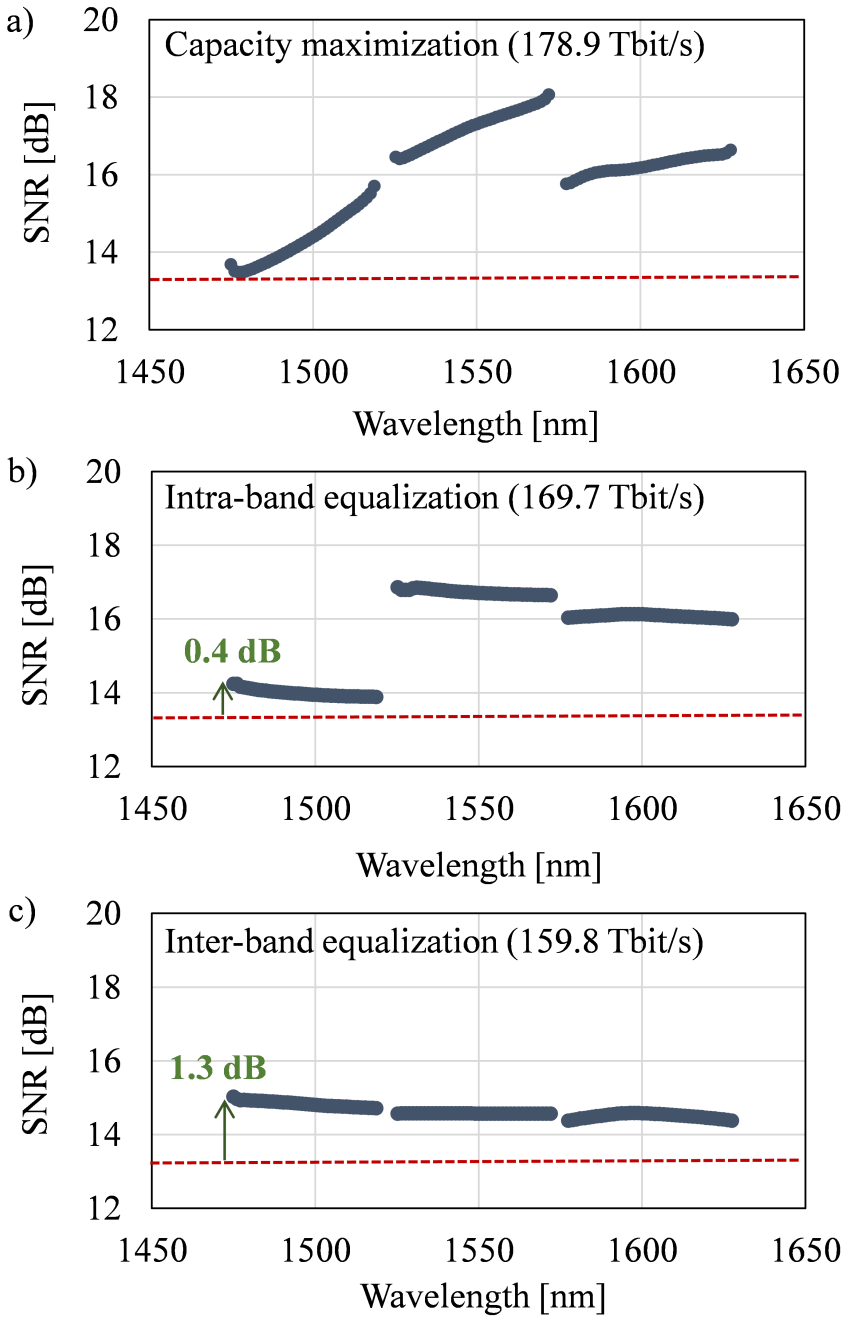

Fig. 3.19: SNR-based system performance and achievable throughput for different equalization techniques: a) capacity maximization, b) intra-band SNR equalization and c) inter-band SNR equalization. In green is the SNR gain of the worst channel SNR with respect to capacity maximization.

The resultant SNR for each strategy is presented in Fig. 3.19. Applying the ASE-NL heuristic for capacity maximization results in a total throughput of 178.9 Tbit/s. In this case, the worst channel SNR is located in the S-band with a value of 13.4 dB (Fig. 3.17 a). Compared with this, intra-band equalization provides 0.4 dB of SNR gain in the worst channel (Fig. 3.17 b), achieving flat SNR per band at the cost of 5% Shannon capacity loss (169.7 Tbit/s). Finally, the inter-band equalization improves the worst channel by 1.3 dB (Fig. 3.17 c) compared to capacity maximization, achieving flat SNR across all the bands at expenses of 11% of Shannon capacity (159.8 Tbit/s). Overall, the intra- and inter-band equalization techniques improve the channel with the worst SNR at the expense of the degradation of the rest of the channels and, therefore, reducing the total system capacity.

These alternative pre-emphasis have a lot of potential in realistic transmission scenarios, limited to fixed bit rate transponders at each band or in the entire system. Additionally, the feature of improving the channel with the worst SNR enables us to extend the transmission over greater distances while maintaining the same bit rate per channel or only a few discrete options. To study this, we now assess the same transmission along several OMS, comparing the three equalization strategies in terms of performance and reached distance. Figure 3.20, illustrates the SNR performance of the channel with the worst SNR for each equalization technique as a function of distance. Based on recent demonstrations using transceivers operating at data rates of 800 Gbit/s and 1 Tbit/s [105], in our study case we assume a required SNR (RSNR) of 9 dB and 11.3 dB, which will determine the reach of the intra- and inter-band equalization.

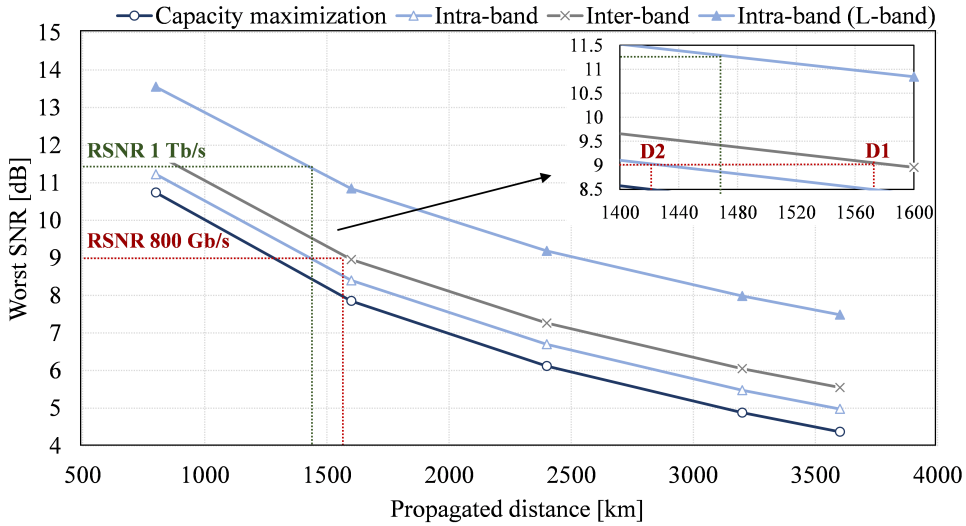

Fig. 3.20: Achievable transmission distance for the channel with worst SNR using different equalization techniques. D1 is the distance reached by 3x40 channels transmitted at 800 Gbit/s. D2 is the achievable distance of 2x40 channels with 1 Tbit/s and 40 channels at 800 Gbit/s.

To exploit the potential of the inter-band equalization, we assume a fixed bit rate of 800 Gbit/s for all bands. With this, the transmission

of 120 channels (40 at each band) is possible up to 1570 km (D1), as shown in the inset of Fig. 3.20. This is 300 km more than what could be reached by having the same fixed bit rate of 800 Gbit/s across the three bands but using the capacity maximization pre-emphasis (circle markers in Fig. 3.20).

Now, for intra-band equalization, we assume the use of both bit rates, aiming to transmit the *best-performing* bands (C and L band) at 1 Tbit/s and the *worst-performing* band (S-band) at 800 Gbit/s. Hence, Fig. 3.20 includes the worst L-band channel performance when using intra-band equalization (filled triangles). For this case, we transmit 80 channels (40 channels in the C band and 40 channels in the L band) at 1 Tbit/s plus 40 channels (S-band) with 800 Gbit/s up to 1420 km (D2), illustrated in the inset of Fig. 3.20.

These results show the relevance of optimized pre-emphasis to boost the capacity of S+C+L systems, providing a playground of equalization strategies based on the ASE-NL heuristic with potential in different transmission scenarios. Whereas the use of the ASE-NL heuristic to maximize capacity enables high-throughput transmissions, as will be demonstrated in the next chapter, intra- and inter-band SNR equalization techniques are relevant for more practical scenarios.

3.6 Discussion

The GN model serves as a fundamental framework for understanding the characteristics of nonlinear distortions in optical communication systems. This chapter has provided an overview of its general definitions, main formulas, and inherent limitations. Moreover, we have highlighted some link optimization techniques derived from this model, underscoring the relevant outcome of achieving *optimum launch power per channel* where the ASE noise is approximately twice the NLI noise power.

However, the accuracy of these models is reduced in UWB systems, where wavelength-dependent impairments such as the ISRS effect, play an important role. The ISRS GN closed-form model accounts for the impact of this effect with very good accuracy. The relevance of this analytical model relies on its use to develop launch power optimization techniques that aim to maximize the QoT. Nevertheless, in the presence of ISRS, power optimization is a non-convex problem with multiple local solutions. To overcome this problem, ML algorithms such as the PSO combined with GD have shown to be a good candidate for optimization but at a very high computational cost.

Applying the ISRS GN closed-form model and inspired by the *optimum launch power per channel* deduced from the GN model, we proposed the *ASE-NL heuristic*, which is a two-step strategy that aims to optimize the SNR performance in UWB systems. First, an iterative per-band optimization is employed to find the mean and tilt of the boosters output power and inline amplifiers gain to set the ASE noise power as twice the NLI noise power. This is followed by a per-channel equalization where the total output power per band determined in the first step is maintained

to avoid important changes in the ISRS power transfer. The results of this technique have shown close convergence to evolutionary ML-based GA and PSO algorithms, with only $\sim 0.7\%$ capacity decrease. Moreover, the main benefit of this simple heuristic relies on its advantageous computational time, estimated to be 3 minutes for 184 channels along the S+C+L band. In contrast, solving the GA and PSO with GD took more than 24 hours to compute on the same single-core desktop computer. These results significantly contribute to model-based power optimization techniques for UWB that led to the publication of [I].

We have used the *ASE-NL heuristic* to examine the throughput gain with respect to the transmission bandwidth, observing that when comparing against the optimal uniform power, the ASE-NL heuristic pre-emphasis showed gains of $\sim 2.2\%$, $\sim 4.6\%$ and $\sim 10.8\%$ in C, C+L and S+C+L transmissions, respectively. These findings highlight the importance of power pre-emphasis and the advantageous opportunities offered by model-based UWB system optimization, as presented in [IV, V].

The use of the *ASE-NL heuristic* across *all the WDM channels* resulted in transmissions with high throughput. In addition, we have proposed two alternative equalization strategies that rely on the *ASE-NL heuristic* that help to maximize the transmission distance under the more practical constraint of a fixed bit rate per channel; the intra-band equalization, which optimizes *the worst channel per band*, targeting a flat SNR for each band, and the inter-band equalization, which optimizes *the worst channel in the entire system* to obtain a flat SNR across all the bands. It has been found that these alternative equalization techniques are more power efficient, improving the worst channel SNR compared with the original two-step *ASE-NL heuristic*. Nevertheless, this was achieved at the expense of reducing the total system capacity in 5% for the intra-band and 11% for the inter-band SNR equalization. It is important to note, that all these equalization strategies are based on the simple and fast *ASE-NL heuristic*, and their application can be extended to various UWB transmission scenarios. These results led to the publication of [IV, V].

The *ASE-NL heuristic* has demonstrated effectiveness in S+C+L transmission scenarios, closely aligning with the optimized solutions provided by more complex ML-based simulations. However, there are some cases where the heuristic's effectiveness is limited, and some other scenarios that require further investigation. Some limitations are originated from the theoretical models upon which it is based. For example and similar to the GN model, very short-span transmissions with small dispersion, will challenge the heuristics accuracy.

Conversely, as described in Section 3.3, this thesis estimates the NLI coefficients through the ISRS GN model described in [35, 94], which has been demonstrated to be highly accurate for UWB systems. However, the accuracy of the estimations provided by this model decreases in systems employing DRA with high on-off Raman gain, leading to underestimated NLI values. This limitation also restricts the use of the *ASE-NL heuristic* in systems with DRA. As will be thoroughly discussed in Section 4.4 the underestimation increases with the on-off Raman gain. Nevertheless,

this challenge can be addressed by updating our model to incorporate the nonlinear impairments introduced by DRAs. Specifically, based on the theoretical framework of [35, 94], the model proposed in [106] offers a closed-form solution to estimate the NLI within UWB systems that have forward or backward distributed Raman amplification with arbitrary number of pumps. Regarding accuracy, in a simulated UWB transmission (10 THz) over 5 spans, it demonstrated an error margin of 0.5 dB for forward DRA and 0.4 dB error for backward DRA in comparison to split-step Fourier method.

Moreover, reaching the 3 dB rule imposed by the *ASE-NL heuristic* can be challenging in some heterogeneous systems, especially when the maximum power and the amplifier's gain are constrained. To exemplify, let us consider a system comprising two spans, the first having 40 km and the second 120 km of SSMF. The algorithm's iterative process will adjust the first span to fulfill the 3 dB criterion. Still, the reduced output power of the first span (optimized for 40 km but insufficient for 120 km) and the constrained amplifiers gain, may restrict the 3 dB ratio in the second span. Such cases would require that the optimization approach starts with the challenging spans rather than following a sequential order.

Alternatively, there are certain scenarios where the use of the *ASE-NL heuristic* will not be so beneficial. For instance, transmissions that are predominantly constrained by the transponder penalties. Our optimization model assumes that the optimum launch power is independent of the transceiver noise, hence these penalties are beyond the optimization scope. This is clear from eq. (2.6.2), where for cases with very large B2B noise, balancing the ASE and the NL noise yields minimal benefits. The heuristic also proves to be less advantageous in very long-span transmissions subject to constrained maximum power and the amplifier's gain, as the algorithm may default maximize the available power without necessarily achieving the desired 3 dB ratio.

Finally, there are some unexplored scenarios for the *ASE-NL heuristic*, such as its reliability in lightly loaded WDM systems. As presented in Section 3.1.1, the study of cases with various WDM loading spectra, shows some limitations of applying some optimization techniques, such as LOGON, to WDM systems lightly loaded. These insights reveal the need for further research, to validate the *ASE-NL heuristic* under various WDM loading conditions. An additional case where the *ASE-NL heuristic* needs to be explored is in extreme ISRS regimes. The simulation of these scenarios requires unbounded amplifier output power and unlimited gain parameters, which is a scientifically intriguing investigation, but a practically improbable scenario. In reality, the constraints imposed by the saturation of the optical amplifiers' output power are crucial, and thus, most of the findings in this thesis are restricted to realistic operational parameters of optical amplifiers, including their output power, gain, and tilt. Hence, restricting the analysis of the *ASE-NL heuristic* in high nonlinear regimes.

Chapter 4

Modeling and optimization of experimental S+C+L systems

This chapter is focused on the study of experimental S+C+L transmissions, introducing the concept of *digital twin* as the virtual representation of the physical elements involved in optical transmissions, that allow us to:

- Experimentally validate simulations and algorithms.
- Get valuable insights into the impairments influencing transmission.
- Analyze the impact of system failure.

Thanks to the high-fidelity mapping of the components in the physical layer, in Section 4.1 we present reliable predictions of averaged data rates for uniform input power distributions. Moreover, we use the collected data as input for our proposed ASE-NL heuristic (Section 3.3), to show the experimental benefits of using propagation models for fast and effective UWB system design.

In Section 4.2 we use the model-based predictions to analyze the main system limitations of our transmission record of 200.5 Tbit/s total throughput over two 100 km PSCF spans.

Furthermore, in Section 4.3 we explore the challenges and mitigation strategies related to amplifier failure in UWB systems. We quantify the impact of ISRS power variations on system performance supported by experimental results and simulation analysis.

4.1 ASE-NL experimental validation

To further exploit the benefits of UWB transmissions, experimental power control strategies increasing the total power in the S-band have shown to be beneficial. Nevertheless, many of the model-based launch power optimization techniques presented in Section 3.2.1 have only been validated through numerical simulations. In this section, we present one of the first experimental validations of model-based power optimization techniques in S+C+L systems using our proposed ASE-NL heuristic.

We first present relevant S+C+L system parameters collected from the experimental transmission of uniform power distributions at various power levels. These parameters serve as input information for our digital twin to get accurate estimations of the SNR performance. Moreover, we optimize the system applying the ASE-NL heuristic presented in Section 3.3, presenting the resultant power distribution and amplifier settings and how they behave when inserted in the real transmission.

Finally, we profit from the model-based predictions to have a closer view of the physical impairments affecting the transmission. Based on this, we perform the *noise contribution analysis*, which quantifies the average contributions per band of the B2B, ASE and NLI noise and how they affect the total SNR performance.

4.1.1 Experimental setup

Figure 4.1 shows the experimental setup of the S+C+L transmission system. An ASE source for each band is separately shaped by a waveshaper (WS) in the S band and commercially available WSSs for C and L bands, to emulate 80 WDM channels along 6 THz of bandwidth with a channel spacing of 75 GHz.

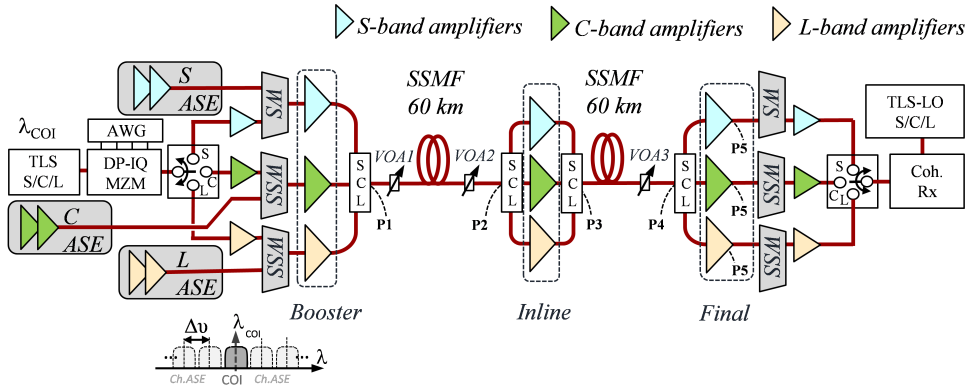

Fig. 4.1: Experimental S+C+L transmission system setup to evaluate the accuracy of the model-based performance predictions and the ASE-NL heuristic.

The COI is produced by a tunable laser source (TLS) with nominal linewidth lower than 400 kHz, modulated in a $LiNbO_3$ DP-IQ with about 35 GHz bandwidth. The modulation involves a 60 Gbaud, PCS-256QAM signal with a root-raised cosine shape and a roll-off of 0.02. This signal is created by an arbitrary waveform generator operating at 120 Gsample/s, featuring approximately 45 GHz bandwidth, and it is further enhanced by modulator drivers with a bandwidth of 55 GHz. To ensure the feasibility of employing a 256QAM scheme with probabilistic amplitude shaping (PAS) scheme, the signal's entropy is adjusted to attain a normalized generalized mutual information (nGMI) within the range of 0.8 to 0.9, given that a minimum code rate of 0.75 is required for PAS to be effective with some margin [25]. Additionally, for DSP convergence and tracking a quadrature phase shift keying (QPSK) symbol is inserted after every

63 symbols transmitted. This signal passes through a single-channel amplifier before being combined with the ASE-shaped WDM channels using the corresponding WS or WSSs. Before entering the fiber, each band undergoes separate amplification in the first stage of amplification of the link, denoted as *booster* in Fig. 4.1 and then are combined by the SCL multiplexer.

The transmission is composed of two 60 km SSMF spans. At the end of each span, a variable optical attenuator (VOA) controls the span loss (VOA2), adding extra attenuation to adjust the C band span loss to $\sim$ 16 dB. After each span, the signals are demultiplexed and amplified with the corresponding amplifiers to compensate for the losses. Prototypes of doped fiber amplifiers are employed in the S-band, while commercial EDFAs are used in the C band, and internally developed SOAs targeting C+L amplification (Section 2.4.2) are operated in the L band. To monitor the power and the OSNR at various points, marked P1 to P5 in Fig. 4.1, an optical spectrum analyzer (OSA) and a power meter are used. A final stage of amplification, referred to as *final* in Fig. 4.1, is located at the end of the line, just before the filtering of the WS or WSSs.

In the last steps, the COI is filtered and pre-amplified before being sent to the coherent receiver. There, the signal is mixed with the LO in a coherent receiver (Coh. Rx) that has a bandwidth of 70 GHz and is sampled by a real-time oscilloscope operating at 256 Gsample/s. The subsequent offline DSP includes resampling, front-end compensation, chromatic dispersion compensation, pilot-aided adaptive equalization, along with frequency and carrier phase recovery, and post equalizer (Section 2.5).

4.1.2 Digital twin and system characterization

The wavelength-dependent loss (WDL) induced by the SSMF is characterized by setting the TLS at low-power to avoid ISRS effect. The fiber attenuation profile was previously plotted in Section 2.3.1 and the coefficients for the central wavelengths of each band are shown in Table 4.1. Additionally, we present in this table the SSMF dispersion coefficients characterized for the central wavelengths of each band, with the remark that the complete spectra can be found in Section 2.3.2.

	S band	C band	L band
Bandwidth [THz]	6	6	6
λ_{central} [nm]	1498.4	1548.3	1600.3
α [dB/km]	0.21	0.19	0.20
D [ps/nm/km]	14.2	17	19.5
Average NF [dB]	5.8	4.9	5.9

Table 4.1: S+C+L system parameters per band used to evaluate the accuracy of the model-based performance predictions and the ASE-NL heuristic.

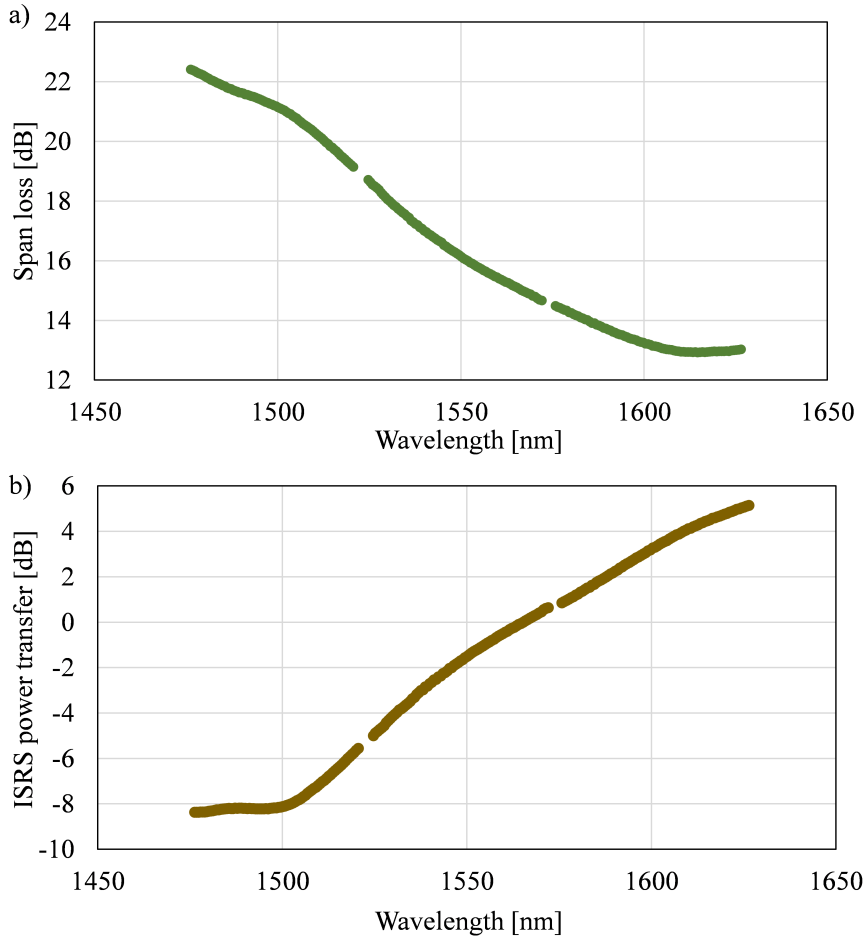

Fig. 4.2: Experimentally measured a) span loss and b) ISRS power transfer after transmitting an uniform power profile with $P_{\text{tot}} = 23.2$ dBm over 60 km of SSMF covering the S+C+L bands.

Moreover, in Fig. 4.2 a) we plot the wavelength-dependent span loss after launching a uniform power spectra of $P_{\text{tot}} = 23.2$ dBm along 60 km of SSMF. This profile accounts for the ISRS and the WDL of the fiber. The subtraction of the WDL profile from the total span loss provides the ISRS channel power transfer depicted in Fig. 4.2 b). We can observe that its shape is more complex than the typical linear-tilted profile observed for C+L experiments since we are transmitting in a total bandwidth larger than 14 THz. Based on the OSNR and power measurements, the average NF of each band amplifier is estimated and presented in Table 4.1.

The performance is evaluated in terms of the SNR and the generalized mutual information (GMI) of 15 channels in total, 5 per band. To obtain the bit rates, we multiply the GMI by 60 (symbol rate), 2 (dual polarization) and 63/64 to take into account the pilot ratio. The total achievable throughput of the system is estimated by the average measurements of each band and extrapolated for the total number of channels within it. The calculated total throughput estimations when launching uniform power spectra at different total powers (21 dBm, 22.2 dBm, 23.2 dBm, 24.4 dBm and 25.4 dBm) are plotted in Fig. 4.3, showing the system's achievable throughput at different power levels.

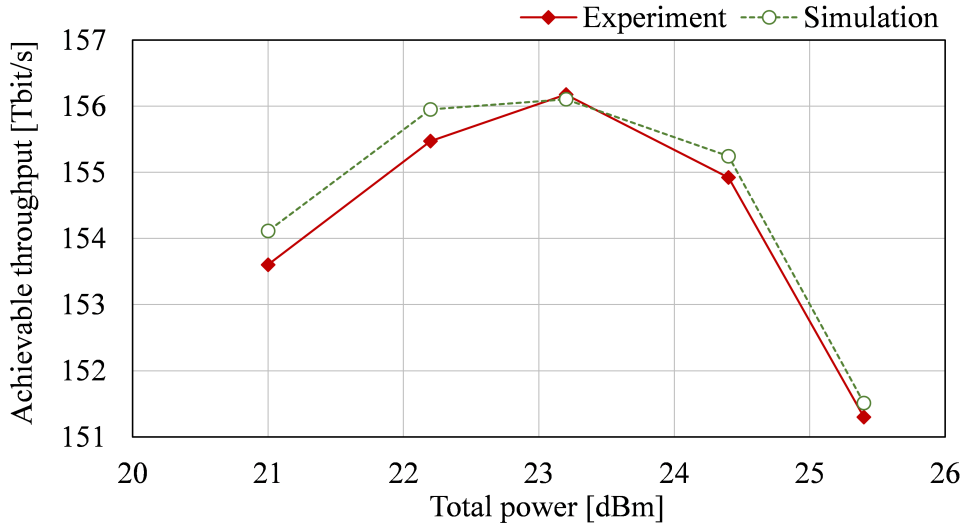

Fig. 4.3: Measured (solid) and estimated (markers) throughput at different total powers using uniform distributions.

The wavelength-dependent NF of the amplifiers and the power spectrum measurements across the two span transmission obtained at P1 and P3 (Fig. 4.1) are the inputs of our QoT to calculate the SNR and GMI-based throughput of the 240 transmitted channels at each total power level (21 dBm, 22.2 dBm, 23.2 dBm, 24.4 dBm and 25.4 dBm). Figure 4.3 also plots the accurate estimations of our modeling, with a simulation error lower than 0.4% for all the measured cases. Both simulation and experiment converge to 23.2 dBm as optimum power.

4.1.3 Power optimization and experimental results

Once the digital twin of the experiment is performed and the simulation parameters have been aligned to the physical transmission elements, we perform a per-channel power optimization based on the ASE-NL heuristic aiming to maximize system capacity. By taking around 4 minutes of computation time in a single-core standard desktop computer, close to the simulation results presented in Section 3.3.3, the ASE-NL heuristic proves once again to be a fast optimization tool.

Since it is a two-span S+C+L transmission system, the ASE-NL heuristic is used to optimize the booster launched power profile as well as the mean gains (g_μ) and tilts (g_τ) of the inline amplifiers. Figure 4.4 a) shows the optimized total output power of the booster and the gain of the inline amplifiers (g_μ) predicted by the algorithm, showing a clear imbalance among the three bands. It can be observed that the total power per band is closely maintained along the transmission line.

The booster power tilts ($P_{1\tau}$) are set to 4 dB for the S-band and 3 dB for the C-band, with an optimized total launch power of 24.5 dBm. The optimized launched power profile estimated by the ASE-NL heuristic is adjusted by the WSS at the entrance of the first span (P1) and plotted in blue in Fig. 4.4 b). As expected, higher power is allocated in the S-band to compensate for the ISRS effect and larger fiber losses, while

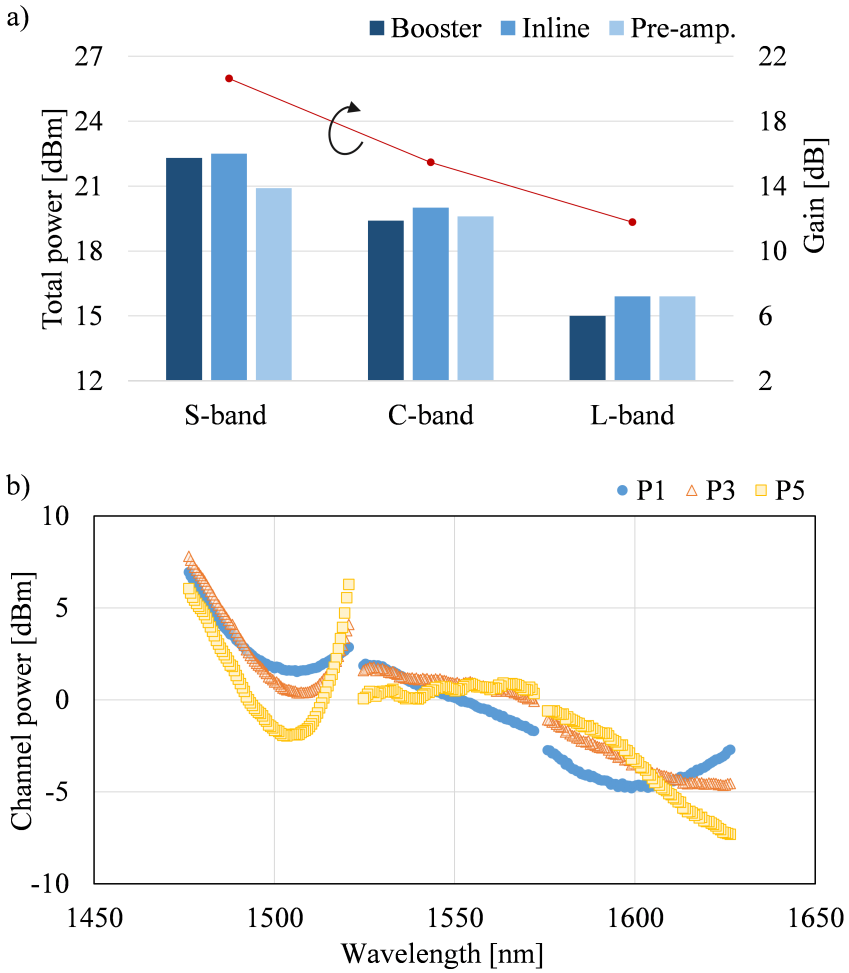

Fig. 4.4: a) Optimized amplifier total output power along the transmission system (left axis), mean gain of the inline amplifiers (right axis), and b) channel power spectra at the output of each stage of amplification P1 (circles), P3 (triangles) and P5 (squares).

both C and L-band require lower launch powers. The measured power spectrum after each amplification stage is shown in Fig. 4.4 b). One of the main design limitations is the S-band amplification without gain flattening filter (GFF), which translates to almost 8 dB ripple in the power spectrum measured at P5 (Fig. 4.4 b).

Using the optimized pre-emphasis (Fig. 4.5 a), once again, the SNR performance of 15 channels (5 per band) is measured and compared with the one predicted by our ASE-NL heuristic. Figure 4.5 b) shows in blue the SNR measured (markers) and predicted (lines) by the QoT tool. Thanks to the digital twin, we achieve a good agreement, having a maximum simulation error of 0.5 dB. To experimentally validate the benefits of power pre-emphasis in UWB systems, we compare the measured SNR performance when launching uniform spectra with the same level of total power. Figure 4.5 a) plots in blue the optimized power pre-emphasis and in red the uniform power profile, both working at $\sim$ 24.5 dBm. The same colors are used in Fig. 4.5 b) to present the SNR measured (markers) and predicted (lines) through simulations. At the same power level and thanks to the pre-emphasis, the measured SNR improves for all the

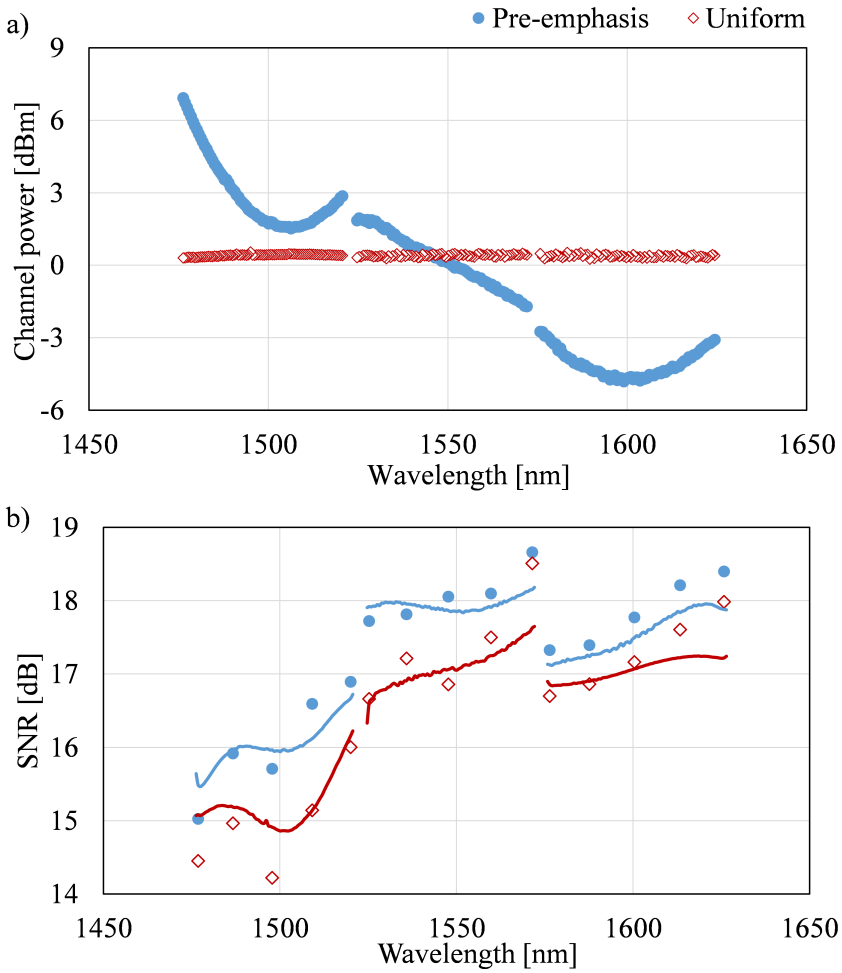

Fig. 4.5: a) Optimized power pre-emphasis using the ASE-NL heuristic (blue) and uniform launch power profile (red), b) measured (markers) and estimated (lines) SNR for the optimized pre-emphasis (blue) and the uniform power distribution (red).

channels, leading to a capacity increase from 154.9 Tbit/s to 161.1 Tbit/s.

Considering the results presented in Section 4.1.2, Fig. 4.6 compares the measured averaged data rates at different powers for uniform distribution (red) and the ASE-NL heuristic power pre-emphasis (blue). It can be observed, that the optimum power varies for both cases. Although for uniform spectra we achieve a maximum capacity of 156.1 Tbit/s at 23.2 dBm, as previously stated, the ASE-NL heuristic predicted a larger optimum launch power of 24.5 dBm. At this power and thanks to the pre-emphasis, the measured SNR improves for all the channels, leading to a capacity increase from 154.9 Tbit/s to 161.1 Tbit/s, plotted along the green dashed line of Fig. 4.6. When comparing against the maximum achievable throughput with uniform distribution, the optimized pre-emphasis offers a capacity gain of 5 Tbit/s. Therefore, the ASE-NL heuristic proves to be an accurate strategy to enhance the system performance, proposing a power pre-emphasis that experimentally shows to be beneficial.

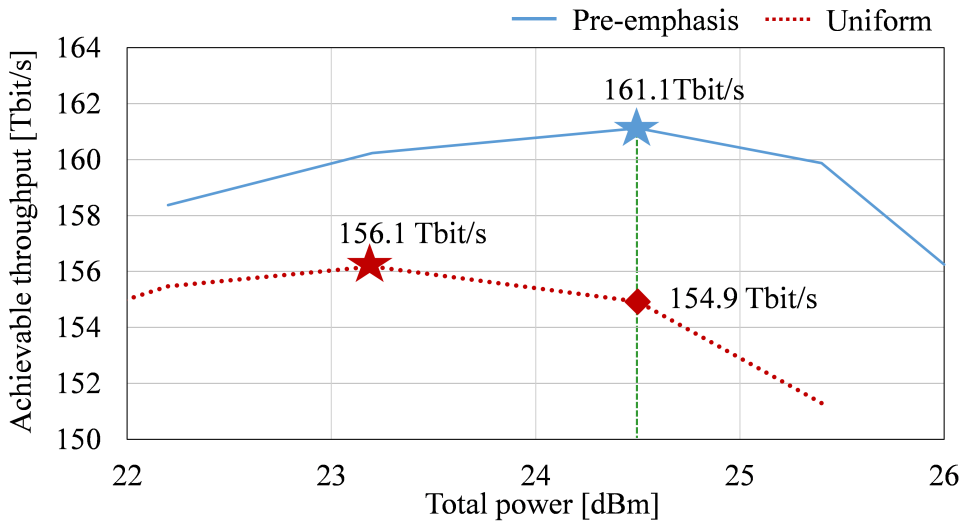

Fig. 4.6: Measured achievable throughput at different total powers using the ASE-NL heuristic power pre-emphasis (blue) and uniform distributions (red).

4.1.4 Noise contribution analysis

Besides the potential to develop power optimization schemes, estimations based on a QoT provide a clearer view to better understand the impact of the physical impairments that affect any WDM transmission system. Figure 4.7 shows the average per-band noise contributions that impact the total SNR performance expressed in the form of the noise-to-signal ratio (NSR) for simplification. Based on eq. (2.6.2), we break down the noise contributions into:

- The $\mathrm{NSR_{ASE}}$, defined as $\mathrm{NSR_{ASE}} = 1/\mathrm{SNR_{ASE}}$, where $\mathrm{SNR_{ASE}}$ includes the independent contributions of ASE noise induced by all the inline amplifiers inside the OMS. This estimation is based on the theoretical expressions presented in Section 2.6.2.
- The $\mathrm{NSR_{PRE-AMP}}$, defined as $\mathrm{NSR_{PRE-AMP}} = 1/\mathrm{SNR_{PRE-AMP}}$, where $\mathrm{SNR_{PRE-AMP}}$ contains the ASE noise contributions of the single-channel amplifiers at the transmitter and the receiver. This estimation is based on the theoretical expressions presented in Section 2.6.2.
- The $\mathrm{NSR_{NL}}$, defined as $\mathrm{NSR_{NL}} = 1/\mathrm{SNR_{NL}}$, where $\mathrm{SNR_{NL}}$ refers to the NLI noise generated along the spans within the OMS. This estimation is based on the ISRS GN closed-form model presented in Section 3.2.
- The $\mathrm{NSR_{TRX}}$, defined as $\mathrm{NSR_{TRX}} = 1/\mathrm{SNR_{TRX}}$, where $\mathrm{SNR_{TRX}}$ is the experimentally measured transponder B2B noise.

Overall, the C-band is the band having less noise, therefore and consistent with the measurements shown in Fig. 4.5, this band has the highest performance. It can be observed that the transmission is mainly limited by the transponder penalties $\mathrm{NSR_{TRX}}$ (Fig. 4.7 in green), representing around half of the noise contributions for all the bands.

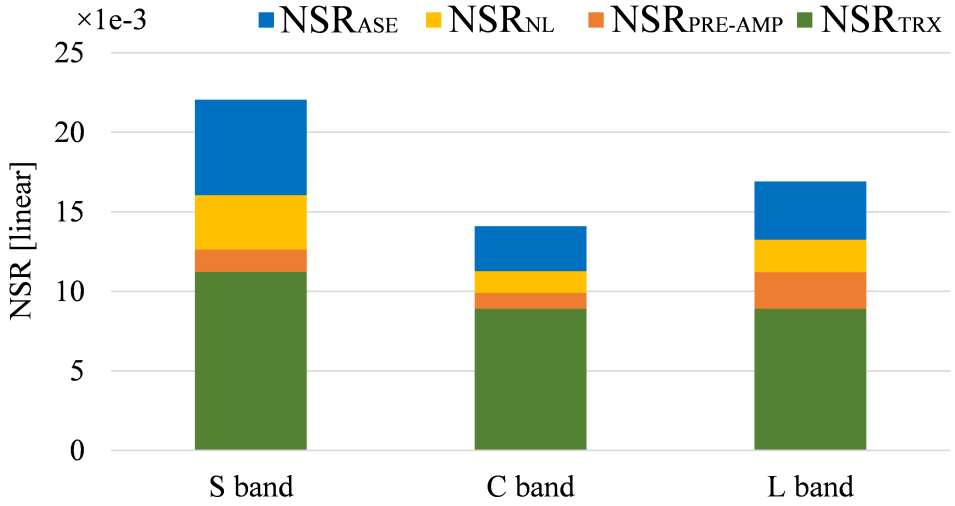

Fig. 4.7: Contributions per band, NSR_{TRX} (green), $NSR_{PRE-AMP}$ (orange), NSR_{NL} (yellow) and NSR_{ASE} (blue) from bottom to top.

We differentiate the ASE noise contributions of the single-channel amplifiers in $NSR_{PRE-AMP}$ (Fig. 4.7 in orange) because they are not included in the system definition of the ASE-NL heuristic. As presented in Section 3.3, our solution targets the balance of the noise generated inside the OMS, in other words, it accounts for all the elements within the first and last WSS, so any additional sources of noise are not included in the optimization. Nevertheless, $NSR_{PRE-AMP}$ includes the experimental measurements mapped into the modeling to improve the accuracy of the QoT estimations of SNR.

The ASE noise generated in the link is included in NSR_{ASE} (Fig. 4.7 in blue), showing that S-band is the most affected band because of the larger losses. Also, since this band has relatively higher output power, the NL contributions will be higher than other bands as presented in yellow in Fig. 4.7. Most importantly, the target of setting the ASE noise power as twice the NL noise power ($P_{ASE}/P_{NLI}= 2$) is achieved for all the bands.

4.2 Demonstration and characterization of 200.5 Tbit/s transmission

In this section, we describe our transmission record (at the time) of 200.5 Tbit/s total GMI throughput over 2x100 km PSCF employing a symbol rate of 70 Gbaud, in line with the current industry trend, to transmit 240 PCS-256QAM channels in a total bandwidth of 150 nm. Similar to the previous section, we analyze the different noise contributions to present one of the first digital twins made for a high-throughput multi-span S+C+L transmission.

4.2.1 Experimental setup

The experimental setup of the UWB transmission is shown in Fig. 4.8. The signal at the transmitter, receiver and the DSP is generated in the same manner as the one described in Section 4.1.1, except that for this case, the COI has a larger baud rate of 70 Gbaud. Moreover, the used amplification type (EDFAs, SOAs and rare doped fiber amplifiers) is consistent with our previous demonstration (Section 4.1.1). The main difference in the experimental setup is the transmission line, which now is composed of two spans of 100 km PSCF with 150 μm^2 of effective area. Additionally, at the end of each span, a distributed Raman amplifier (DRA) with four first-order backward pumps is combined with a circulator. The pump wavelengths and respective powers are 1400 nm with 28 dBm, 1415 nm with 25.2 dBm, 1435 nm with 24.2 dBm and 1455 nm with 23.9 dBm.

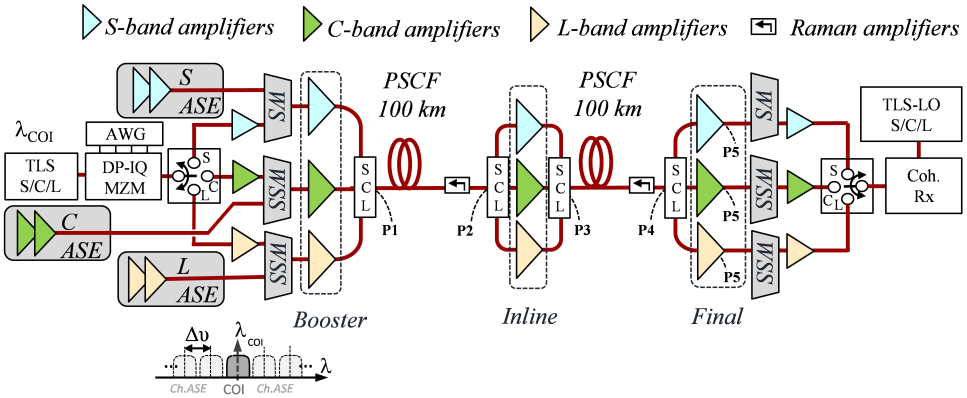

Fig. 4.8: Experimental S+C+L transmission system setup to achieve 200.5 Tbit/s over two 100 km spans of PSCF.

4.2.2 Digital twin and system characterization

The power spectra and OSNR are measured at different points along the transmission line, from P1 to P5 in Fig. 4.8. Based on the power pre-emphasis proposed by the two-step ASE-NL heuristic targeting capacity maximization, we present in Fig. 4.9 a) the power distribution set at the entrance of the first span (P1). The total power is 25.3 dBm and the total power per band is detailed in Table 4.2.

	S band	C band	L band
Bandwidth [THz]	6	6	6
λ_{central} [nm]	1498.4	1548.3	1600.3
α [dB/km]	0.17	0.16	0.16
D [ps/nm/km]	17.8	21.2	24.2
Average SNR_{TRX} [dB]	21	22	21
Total power at P1 [dBm]	22.6	20.2	17.3

Table 4.2: S+C+L system parameters used to achieve 200.5 Tbit/s over two 100 km spans of PSCF.

In Fig. 4.9 b) we plot the on-off Raman gain of our DRA, which is notably higher in the S and C-band with respect to the L-band. The entrance of the second span (P3) has a total power of 25.7 dBm distributed as 22.5 dBm, 21.2 dBm and 17.6 dBm for S, C and L bands, respectively. The amplifier output channel spectrum in the final stage of inline amplification (P5) is also shown in Fig. 4.9 a). A tilt of $\sim$ 15 dB is observed between the S and the L-band, making this significant difference a major challenge for the experiment, since the optical amplifiers do not have a GFF.

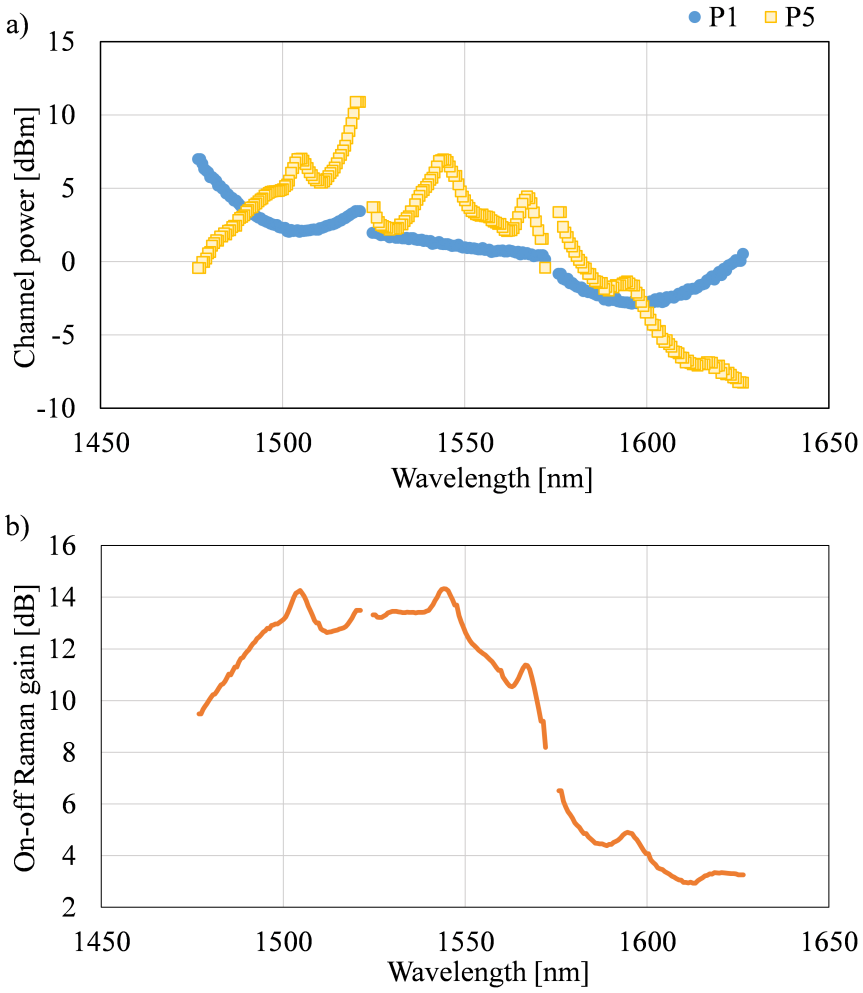

Fig. 4.9: a) Channel power spectra at P1 (circles) and P5 (squares) and b) on-off Raman gain for the backward DRA.

Similarly to the SSMF, the WDL induced by the PSCF is characterized by entering a low-power TLS to avoid ISRS effect. The PSCF fiber attenuation profile was previously plotted in Section 2.3.1 and the coefficients for the central wavelengths of each band are shown in Table 4.2. Additionally, we present in this table the PSCF dispersion coefficients characterized for the central wavelengths of each band, with the remark that the complete spectra can be found in Section 2.3.2.

Figure 4.10 a) presents the frequency-dependent span loss after launching the optimized power spectra (P1 in Fig. 4.9 a) along 100 km of PSCF without DRA. This profile accounts for the ISRS and the WDL of the

fiber. The subtraction of the WDL profile from the total span loss provides the ISRS channel power transfer depicted in Fig. 4.10 b). We can observe that the shape of the ISRS power transfer is similar to the one presented for SSMF. Nevertheless, when comparing the total slope across the S+C+L bands in both experiments, it is found that the total power transferred in PSCF ($\sim$ 8 dB) is considerably less than the one observed in SSMF ($\sim$ 13 dB). Special focus should be placed on the minimum and maximum values of the ISRS power transfer. In this experiment, the transfer profile is centered at 0 dB, with values ranging from -4 dB to 4 dB. However, in the prior demonstration (Section 4.1.2), the ISRS power transfer spanned from -8 dB to 5 dB.

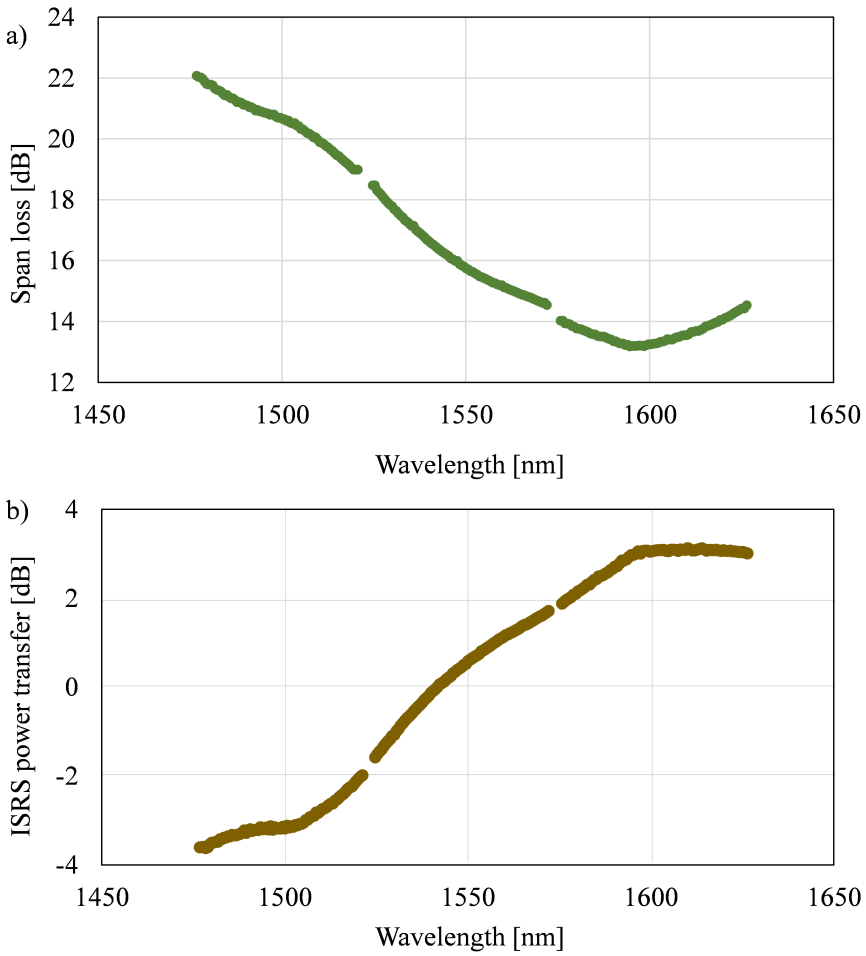

Fig. 4.10: Experimentally measured a) span loss and b) ISRS power transfer after transmitting an equalized power profile with $P_{\text{tot}} = 25.3$ dBm over 100 km of PSCF covering the S+C+L bands.

The SNR_{TRX} of five channels per band is measured and plotted with markers in Fig. 4.11. To reduce the uncertainties of the measurements, we apply a linear fitting per band, shown with dotted lines in Fig. 4.11. Table 4.2 shows the average value per band.

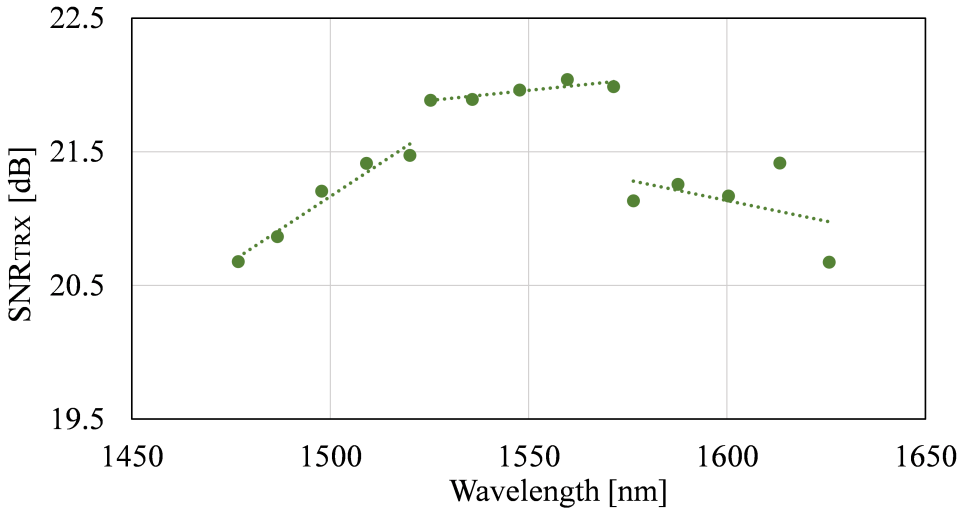

Fig. 4.11: Experimental SNR_{TRX} for S+C+L transmission system (markers). In the dotted line, we plot the linear fitting of the measurements.

4.2.3 Experimental results

The SNR of the 240 channels is measured and plotted in Fig. 4.12. It can be observed that the SNR of the S-band increases from about 16 dB in the short wavelengths to around 18 dB in the long wavelengths. The band with the best measured SNR performance is the C-band, having values between 20 dB and 21 dB. For the L-band, we observe that the SNR is around 18 dB for the short wavelength channels, dropping to about 16.5 dB for the long wavelength channels. This lower SNR registered in the longer wavelength channels can be attributed, in part, to the tilt of power shown in Fig. 4.9 a), which results in an insufficient amount of power into the oscilloscope.

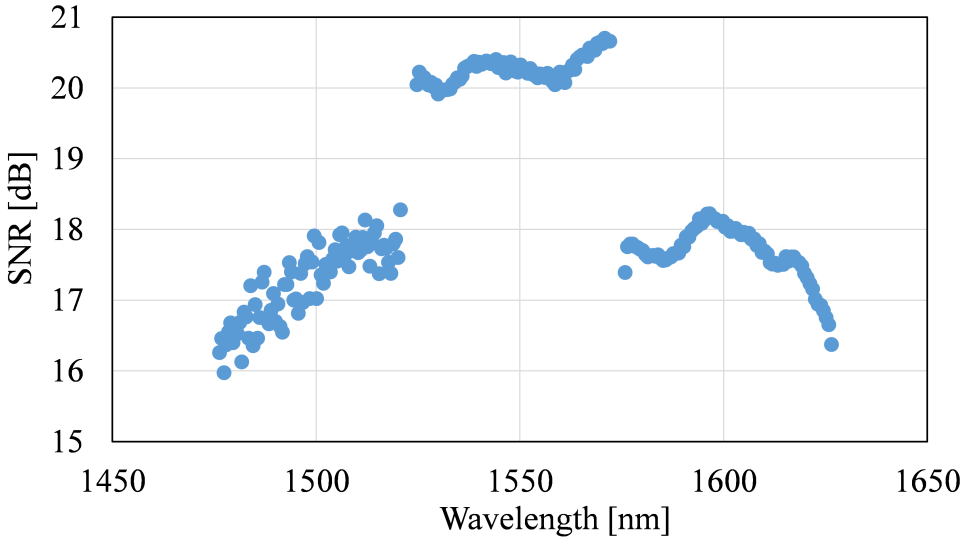

Fig. 4.12: Measured SNR for 240 channels reaching 200.5 Tbit/s.

Based on the GMI estimations per band and considering the 1.6% pilot tones overhead, data rates of 63 Tbit/s, 73 Tbit/s and 64.5 Tbit/s are obtained for S, C and L bands, respectively, and a total GMI throughput of 200.5 Tbit/s is achieved for the S+C+L band.

4.2.4 Noise contribution analysis

We perform a digital twin of the transmission, taking into account all the system parameters previously presented in Section 4.2.2 to estimate the SNR performance of the 240 channels. The predicted values are presented as *simulation* in Fig. 4.13 a) and compared with the experimental measurements (*experiment*) shown in markers. It is important to highlight that only for the S-band we have smoothed the experimental SNR curve through a second-order polynomial fit to account for the variations between channels (Fig. 4.12).

To study the reliability of the simulation, we present in Fig. 4.13 b) the absolute value of the discrepancy between the measured and the simulated SNR across all the 240 channels. To ensure precision, a threshold of

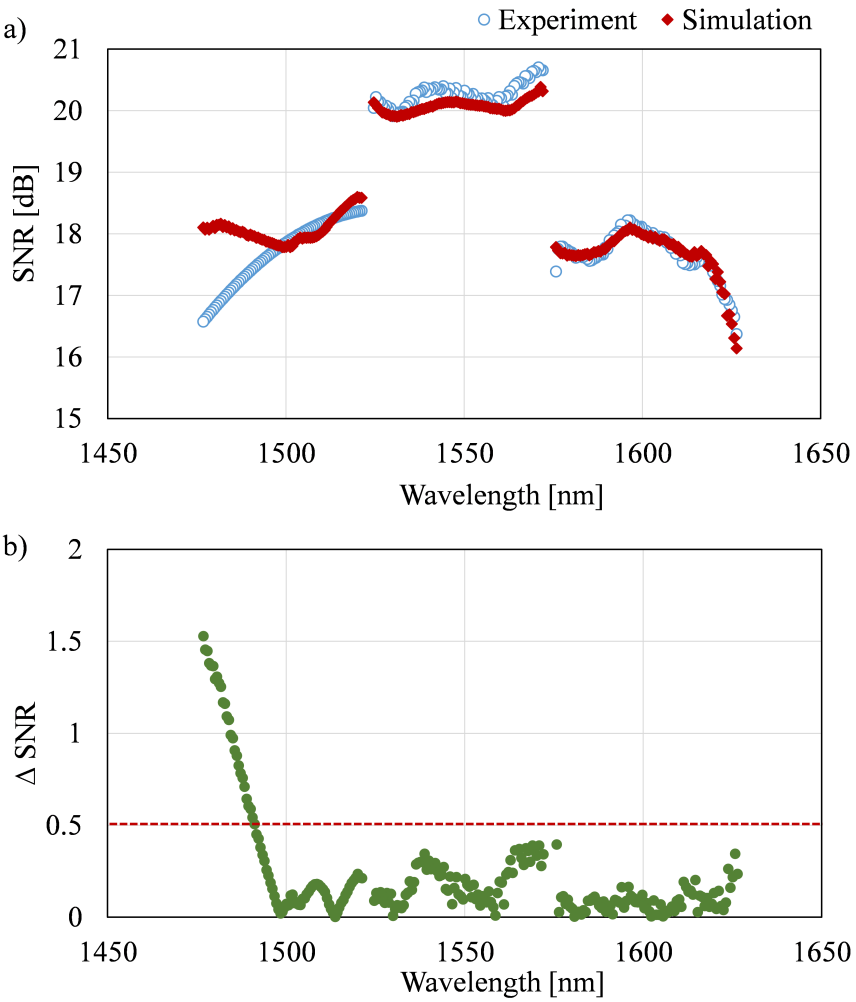

Fig. 4.13: a) Measured (markers) and simulated (solid) SNR, and b) simulation error defined by ΔSNR, computed as the absolute difference between measured and simulated SNR.

0.5 dB is established, which is met in the majority of channels, except for the shorter wavelengths in the S-band. Despite the fitting, Fig. 4.13 a) shows large differences of SNR for the channels within S and L-band, therefore we categorize the analysis of these bands into two groups: one focusing on the short wavelengths and the other on the long wavelengths. This classification allows for a more nuanced examination of the SNR.

As explained in Section 4.1.4, the total SNR is determined by the noise levels accounted in $\mathrm{NSR_{ASE}}$, $\mathrm{NSR_{PRE-AMP}}$, $\mathrm{NSR_{NL}}$ and $\mathrm{NSR_{TRX}}$. Nevertheless, for this demonstration, additional contributions accounting for the limitations of power at the receiver ($\mathrm{Rx_{POWER}}$) and unknown impairments not captured by the model (Other) are also included. Figure 4.14 illustrates the noise distribution that impacts the total SNR at different wavelength ranges.

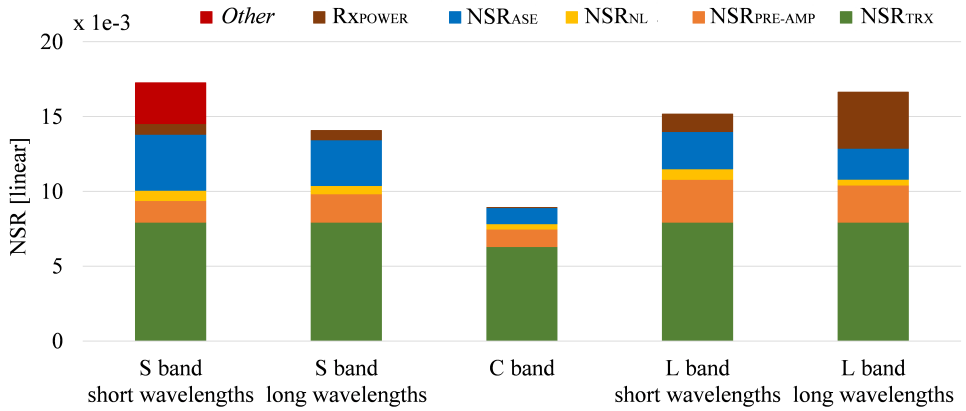

Fig. 4.14: Contributions per band, $\mathrm{NSR_{TRX}}$ (green), $\mathrm{NSR_{PRE-AMP}}$ (orange), $\mathrm{NSR_{NL}}$ (yellow), $\mathrm{NSR_{ASE}}$ (blue), $\mathrm{Rx_{POWER}}$ (brown) and Other (red) from bottom to top.

The $\mathrm{NSR_{TRX}}$ (Fig. 4.14 in green), based on $\mathrm{NSR_{TRX}} = 1/\mathrm{SNR_{TRX}}$, where $\mathrm{SNR_{TRX}}$ is the average of the experimentally measured transponder B2B SNR (Table 4.2). It can be observed that the transmission is mainly limited by this factor in all the bands. Similar to Section 4.1.4, the $\mathrm{NSR_{PRE-AMP}}$ (Fig. 4.14 in orange) includes the ASE generated by the single-channel amplifiers at the transmitter and receiver sides. The high power provided by the optical amplifiers and the large DRA gain in S-band explain that the $\mathrm{NSR_{NL}}$ (Fig. 4.14 in yellow) are higher in S-band than in the other bands. The $\mathrm{NSR_{ASE}}$ (Fig. 4.14 in blue) show that the shorter wavelengths of the S-band are more affected by ASE noise because of the higher losses induced by the large ISRS power transfer.

In this setup, the C-band was equipped with an ASE light source with higher power compared to the others. Consequently, at the transmitter, this band exhibited a better OSNR, resulting in the highest SNR performance. On the contrary, $\mathrm{Rx_{POWER}}$ (Fig. 4.14 in brown) shows that both S and L bands are degraded by the limited power into the coherent receiver. Additionally, the large power drop presented in Fig. 4.9 a) explains the drastic drop of SNR observed for the channels above 1625 nm, which is included in the contributions of the *L band long wavelengths*. Finally, we include in *Other* (Fig. 4.14 in red) the unknown impairments

that are not captured in the model. These effects are mainly affecting the performance of the short wavelengths of the S-band, potentially including crosstalk generated by the WS, and other effects that still need to be investigated and characterized.

4.3 Amplifier's failure: impact of WDM band drop

Multi-band systems face susceptibility to the system failure of the band amplifiers. These disruptions can subsequently compromise the overall performance of the unaffected bands due to power variations impacting the ISRS. Hence, the importance of investigating the repercussions of WDM band drops in UWB systems. This section presents the experimental results of an S+C+L transmission over two 60 km SSMF spans. To assess the impact of system failure and ISRS variations, we switch off either the S or the L-band and measure the SNR performance while keeping all the operational parameters the same as in the S+C+L transmission.

Additionally, we conduct a comparative analysis of the GMI throughput distribution for each case to quantitatively evaluate the effect on system capacity. Through the mapping of the system parameters, power profiles and OSNR measurements into our QoT tool, we analyze the noise contributions affecting the SNR performance. Moreover, with these accurate model-based predictions, we study in an extended multi-span S+C+L scenario the impact on throughput after losing the S-band, as well as the power variations induced after losing the L-band. Finally, in Appendix A we propose a recovery mechanism to reduce the performance impact on UWB systems in the event of the loss of a band amplifier.

4.3.1 Experimental setup

Figure 4.15 presents the experimental setup of the S+C+L transmission. The signal generation at the transmitter, receiver, and DSP follows the methodology outlined in Section 4.1.1, with the distinction that in this

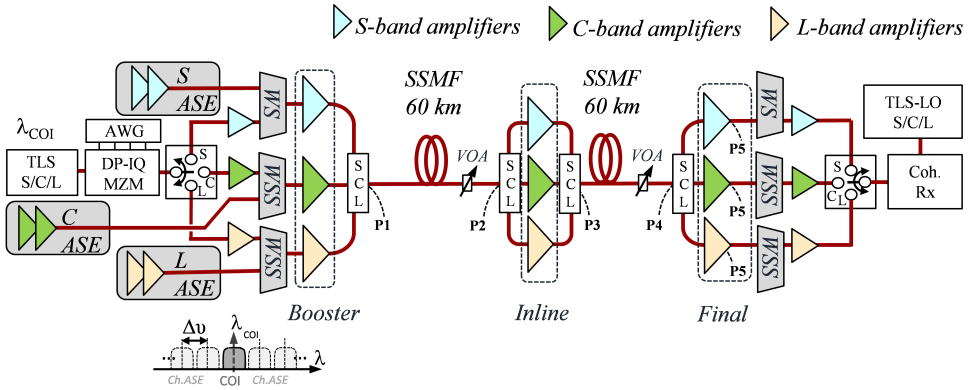

Fig. 4.15: Experimental S+C+L transmission system setup to study the impact of band drop.

scenario, the COI operates at a higher baud rate of 70 Gbaud. The amplification type (EDFAs, SOAs and rare doped fiber amplifiers) is consistent with our previous demonstrations (Section 4.1.1 and Section 4.2.1).

Similar to the experiment described in Section 4.1.1, the transmission link consists of two 60 km SSMF spans with a fiber attenuation profile and dispersion spectra previously plotted in Section 2.3.1 and Section 2.3.2, respectively. This demonstration also accounts for an additional 4 dB of attenuation provided by VOA2 to emulate conditions of field-deployed demonstrations.

We measure the power spectra and OSNR at various points along the transmission line, illustrated from P1 to P5 in Fig. 4.15. The channel power pre-emphasis at P1 is optimized by the two-step ASE-NL heuristic aiming to maximize capacity (Section 3.3). The COI is swept across all the bands using five test channels per band to get an estimation of the transmission performance. The total achievable throughput of the system is estimated by the average measurements of the five channels per band and extrapolated for the total number of channels within it. As we did in our previous experiments, the performance is estimated in terms of GMI throughput and the net bit rate is calculated by multiplying the GMI by 70 (symbol rate), by 2 (dual polarization), and by 63/64 (pilot ratio).

4.3.2 Failure of S-band amplifier

First, we analyze the impact of losing the S-band amplifier by switching off the booster's S-band amplifier and measuring the transmission performance while keeping all the operational parameters the same as in the original S+C+L transmission.

4.3.2.1 Digital twin and system characterization

Figure 4.16 a) plots the power distributions at the entrance of the first span (P1) and at the exit of the second span (P4) for the S+C+L transmission (circles) and the C+L transmission (triangles) that emulates the amplifier's failure. It can be observed that as expected, at P1 the power distribution assigned to the C+L transmission (solid triangles) is aligned with the power profile of the S+C+L transmission (solid circles).

The overall power distribution for the S+C+L configuration is divided as follows: 52.4% in the S-band, 30.9% in the C-band, and the remaining 16.7% in the L-band. Consequently, the absence of the S-band results in a power reduction of half of the total power, significantly reducing the ISRS power transfer. This effect is illustrated in Fig. 4.16 a) at the output of the second span (P4 in unfilled triangles), where the absence of the S-band leads to a noticeable decrease in the channel powers of the C and L bands, with the L-band experiencing a maximum power reduction of 7 dB. This decline is attributed to the reduction of ISRS power transfer from the S-band to the C+L bands.

Figure 4.16 b) shows that the band drop almost does not affect the performance of the C-band, having an SNR penalty of only 0.5 dB at the

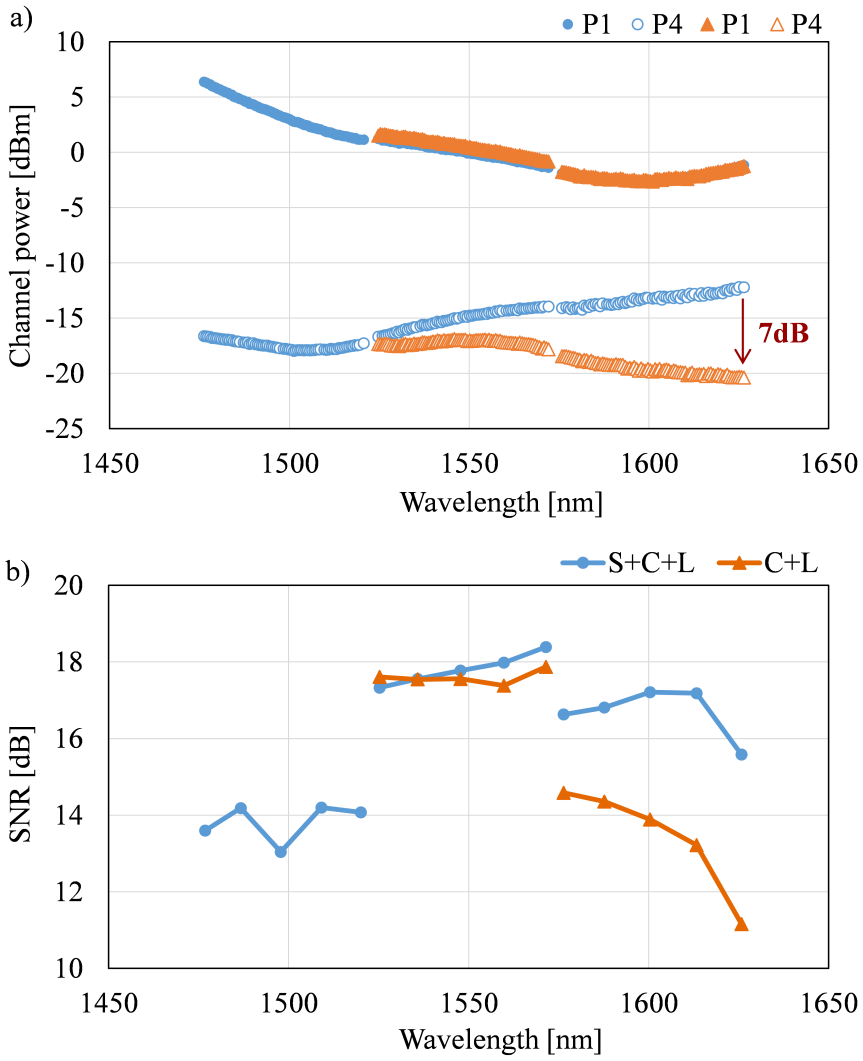

Fig. 4.16: a) Channel power spectra at P1 (filled) and P4 (unfilled) before (circles) and after (triangles) the S-band drop, and b) SNR performance for the S+C+L transmission before (circles) and after the S-band drop (triangles). In red is the maximum power drop in the case of S-band failure.

end of the band. The biggest impact is observed in the L-band, having a large drop along the band with a maximum penalty of 4 dB, mainly explained by the notable power drop experienced by the L-band when losing the power transferred from the S-band.

To quantify the capacity impact when the S-band is missing, Fig. 4.17 presents the estimated GMI-based throughput distribution of each band. Originally, with the S+C+L transmission, a total of 177 Tbit/s throughput is estimated. Following the loss of the S-band, the throughput for the C-band remains nearly unchanged from before, while the GMI throughput for the L-band decreases significantly by 11.9 Tbit/s, as highlighted in red in Fig. 4.17. The total bit rate after losing the S-band is 113.7 Tbit/s. This represents a 36% decrease in total capacity compared to the initial S+C+L transmission. The drop in the net bit rate of the L band is the result of multiple factors: first, the L-band power decreases when the

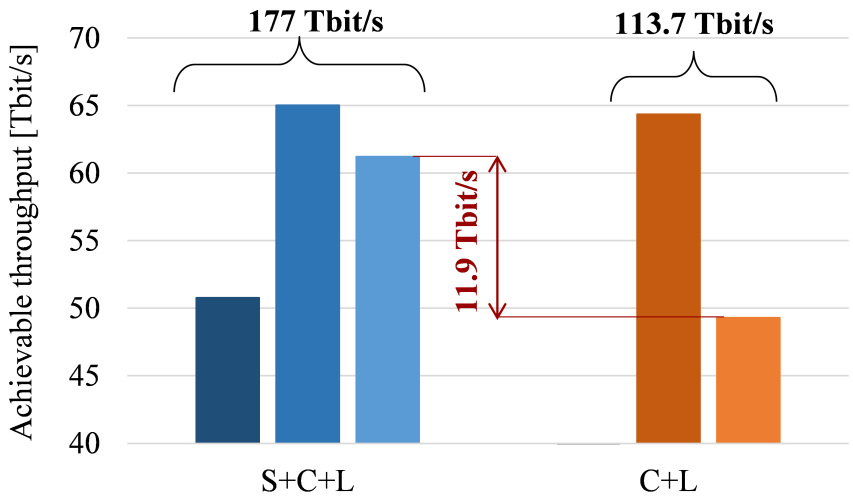

Fig. 4.17: Achievable throughput before (left) and after(right) the S-band drop. In red, the channel power and capacity penalty in the L-band after the band drop.

S-band is gone which reduces the OSNR. Furthermore, as previously discussed in Section 4.2, the limited gain of the single-channel amplifier after P5 constrains the power available to the coherent receiver ($\mathrm{Rx_{POWER}}$).

We input the experimental measurements of channel power and OSNR to our digital twin and estimate the SNR performance for the S+C+L transmission *before the failure* and the C+L transmission *after the failure* of the S-band amplifier. The accuracy of these estimations is consistent with the ones presented in previous sections (Section 4.1 and Section 4.2).

4.3.2.2 Noise contribution analysis

As we introduced earlier, the lack of ISRS power transfer and the limited power into the coherent receiver are the main reasons behind the performance degradation of the L band. In this section, we will quantify the impact of these phenomena through the noise contribution analysis resulting from our digital twin. Figure 4.18 illustrates the noise contributions that impact the SNR in two scenarios: the S+C+L transmission *before the failure* and the C+L transmission *after the failure*. We divide the analysis per band, nevertheless, due to the notable SNR decay at the end of the L-band we split this band into short and long wavelengths. Similar to the preceding noise contribution analyses (Section 4.1.4 and Section 4.2.4), the total SNR can be described through the noises introduced from $\mathrm{NSR_{ASE}}$, $\mathrm{NSR_{PRE-AMP}}$, $\mathrm{NSR_{NL}}$, $\mathrm{NSR_{TRX}}$ and $\mathrm{Rx_{POWER}}$.

As the previous demonstrations, the $\mathrm{NSR_{PRE-AMP}}$ (Fig. 4.18 in orange) includes the ASE noise of the single-channel amplifiers. For the $\mathrm{NSR_{TRX}}$ (Fig. 4.18 in green) we consider the experimentally measured $\mathrm{SNR_{TRX}}$ presented in Section 4.2.2, having $\sim$ 21 dB for all the bands. This is the main limitation in the C-band performance, representing more than half of the noise contribution *before* and *after* the failure. For the L band, the $\mathrm{NSR_{TRX}}$ is also one of the main factors limiting the performance, mainly in the S+C+L transmission *before the failure*

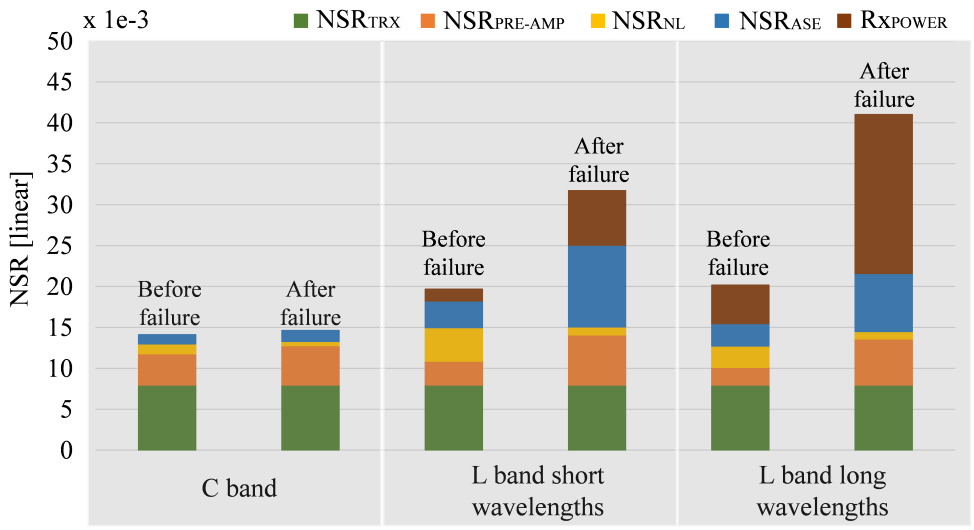

Fig. 4.18: Contributions per band, NSR_{TRX} (green), $NSR_{PRE-AMP}$ (orange), NSR_{NL} (yellow), NSR_{ASE} (blue) and Rx_{POWER} (brown) from bottom to top. On the left we present the performance estimations for the S+C+L transmission *before the failure* and on the right the C+L transmission *after the failure*.

of the S-band. On the other hand, when the S-band is missing, the NSR_{ASE} (Fig. 4.18 in blue) and the Rx_{POWER} (Fig. 4.18 in brown) are the main impairments restricting the performance of the L-band, especially in the long wavelengths.

After losing the S-band, due to lack of ISRS power transfer, the NSR_{ASE} increases and the NSR_{NL} decreases for both C and L bands. For the C-band this change does not impact the total NSR, since when operating at around the optimum launch power, small span loss variations translate into minor SNR variations since the NSR_{ASE} and the NSR_{NL} (Fig. 4.18 in yellow) will evolve in different directions. Nevertheless, for the L-band the increase of NSR_{ASE} is much larger than the reduction of NSR_{NL}, which produces an overall performance degradation. On top of that, the Rx_{POWER} greatly impacts the transmission.

Overall, the failure of the S-band amplifier, even without accounting for the Rx_{POWER}, degrades the L-band transmission performance because of the lack of power transferred from the S to the L band induced by the ISRS effect.

4.3.3 Failure of L-band amplifier

Similar to the previous section, now we analyze the impact of losing the L-band by switching off the booster's L-band amplifier and measuring the transmission performance while keeping all the operational parameters the same as in the original S+C+L transmission.

4.3.3.1 Experimental results

Figure 4.19 a) plots the power distributions at the entrance of the first span (P1) and at the exit of the second span (P4) for the S+C+L transmission (circles) and the S+C transmission (squares) that emulates the L-band amplifier's failure. It can be observed that at P1 the power distribution assigned to the C+L transmission (solid triangles) lines up with the power profile of the S+C+L transmission (solid squares).

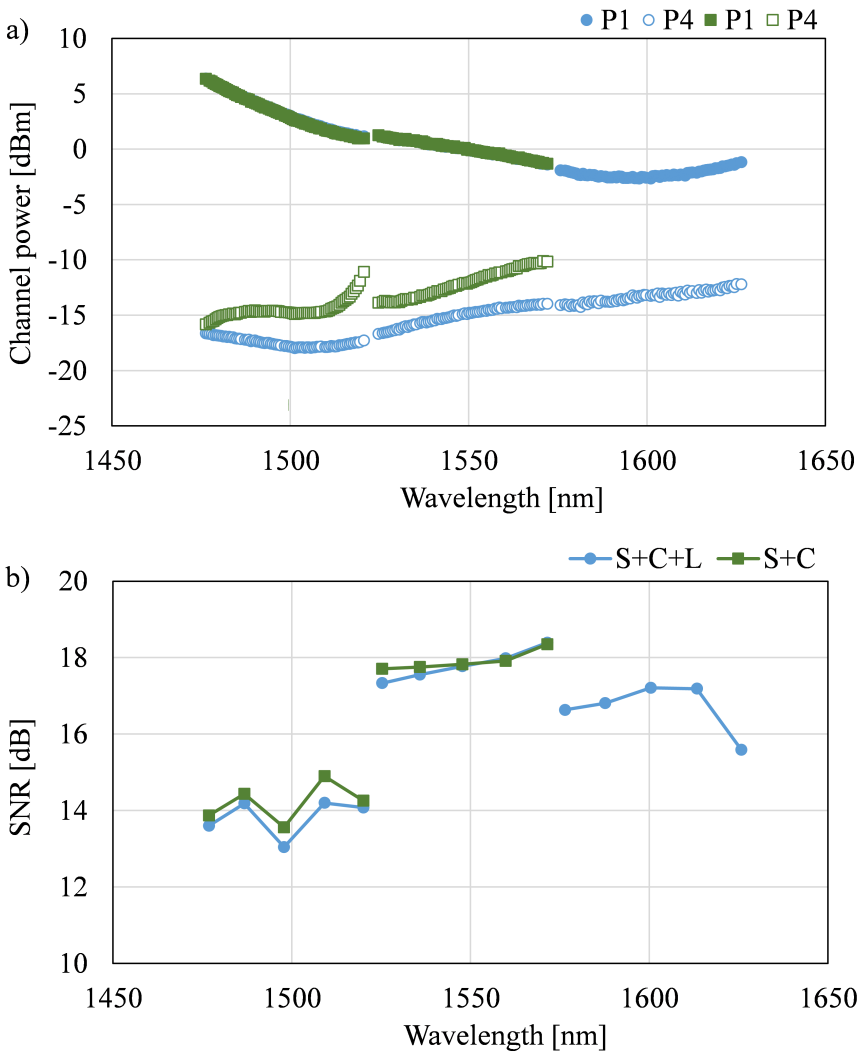

Fig. 4.19: a) Channel power spectra at P1 (filled) and P4 (unfilled) before (circles) and after (squares) the L-band drop, and b) SNR performance for the S+C+L transmission before (circles) and after the L-band drop (squares).

As mentioned, the overall power distribution for the S+C+L configuration is divided as follows: 52.4% in the S-band, 30.9% in the C-band, and the remaining 16.7% in the L-band. Therefore, when the L-band is missing, the total power decreases by only 16.7%. However, as plotted in Fig. 4.19 a), at the exit of the second span (P4) the channel powers of the S and C bands increase due to the reduction of the ISRS power transfer from the S+C bands to the L-band. With a maximum power increase of $\sim$ 6.2 dB in the S-band and $\sim$ 4 dB in the C-band. After

losing the L band, the S and C bands experience lower span loss so that the OSNR and SNR are slightly better than before. When comparing the power spectra of this section with the one of Section 4.3.2, the failure of the S-band creates larger power variations in the other bands than when the L band is missing. Therefore, we can conclude that for this case the impact of losing the S-band is larger than losing the L band.

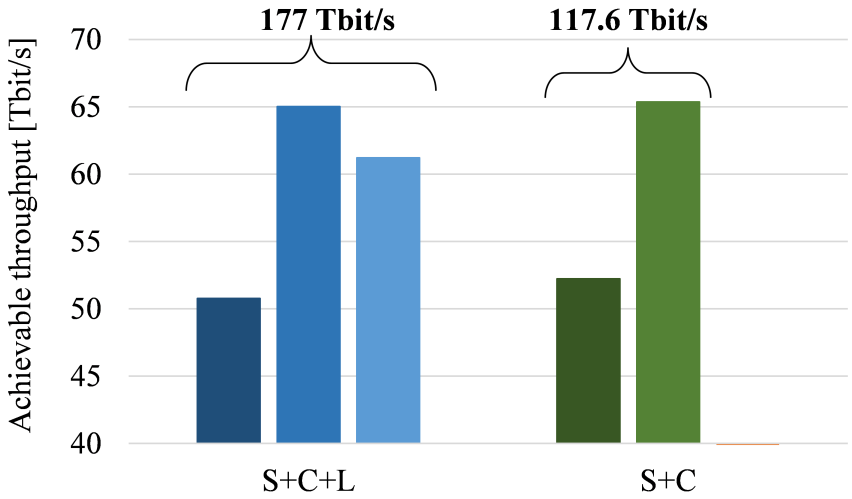

Fig. 4.20: Achievable throughput before (left) and after(right) the L-band drop.

To quantify the capacity impact when the L-band is missing, Fig. 4.20 presents the estimated GMI-based throughput distribution of each band. Originally, with the S+C+L transmission, a total throughput of 177 Tbit/s is estimated, after losing the L-band, the throughput in the S and C bands are slightly larger than before the failure, leading to a total bit rate of 117.6 Tbit/s. Although for this case the power increase produces a SNR gain; for transmissions with more spans, the power increase in addition to the gain of each amplifier could lead to very large levels of power entering the following fibers downgrading the system performance.

4.3.4 Multi-span simulation

The experimental results in Section 4.3.2 and Section 4.3.3 demonstrated that the failure of any band, specifically the S or L band, significantly impacts the performance of the remaining bands due to alterations in the ISRS effect. This phenomenon was observed in a two-span S+C+L demonstration, leading us to apply our model-based predictions to anticipate the potential consequences of amplifier system failure in transmission systems with an extended number of spans. Building on the optimized scenarios presented in Chapter 3, this section aims to investigate the repercussions of the amplifier's failure, alongside the fluctuations in ISRS, by simulating a significant reduction in the power of channels within the affected band, while retaining the original configuration in the remaining bands. Initially, we evaluate the impact of losing the S-band, comparing the SNR before and after the band drop. Additionally, we assess the changes in achievable throughput to quantify the effects on the

overall system capacity. Subsequently, we study the loss of the L-band, with a focused examination of the power fluctuations due to the ISRS effect, which includes the power increase in the remaining bands.

4.3.4.1 System description

In this section, we delve into the repercussions of the S-band amplifier's failure within the S+C+L transmission link previously discussed in Section 3.4. Figure 4.21 recalls this S+C+L configuration composed by one OMS with 5x80 km SSMF transmitting 140 Gbaud channels within 150 GHz of channel spacing across 18 THz (150 nm) of total bandwidth. We assume lumped amplifiers with no ripple, having NF of 5 dB for the C band and 6 dB for both the S and the L bands. Additionally, each amplification stage incorporates SCL multiplexers and demultiplexers, with insertion losses of 1 dB and 2 dB, respectively.

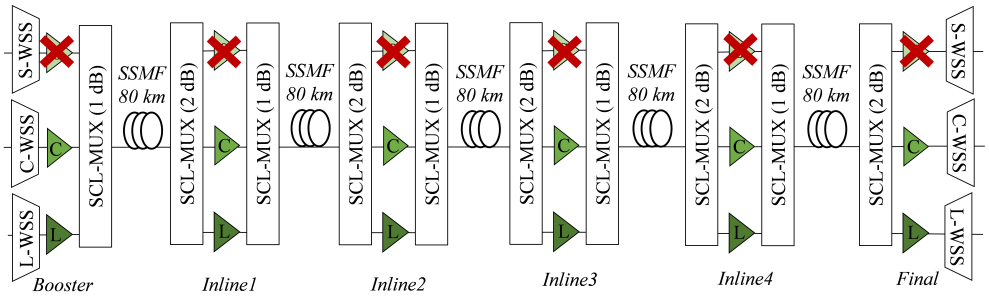

Fig. 4.21: S+C+L transmission setup used to simulate the impact of the S-band drop along 5x80 km of SSMF.

The power pre-emphasis (Section 3.4) and amplifier's gain (Section 3.5) were obtained through the two-step ASE-NL heuristic targeting to maximize capacity. These values were presented and extensively discussed in Chapter 3. Nevertheless, we summon back the power distribution across the bands: 24.5 dBm (63.3%) was allocated to the S-band, 20.9 dBm (27.3%) to the C-band, and the remaining 16.3 dBm (9.4%) to the L-band. This configuration is referred to as the S+C+L transmission *before failure*. To examine the failure's impact, we simulate the S-band amplifier's loss by drastically reducing the power in its channels, yet preserving output powers of 20.9 dBm and 16.3 dBm for the C-band and L-band booster amplifiers, respectively. This scenario, referred to as the *after failure* transmission, seeks to analyze the most severe failure case: the loss of the booster S-band amplifier, illustrated in Fig. 4.21 with red crosses.

4.3.4.2 Failure of S-band amplifier

Figure 4.22 presents the comparison of the total output power for the C and L-band amplifiers before (blue) and after (orange) the failure of the S-band, across each stage of amplification. The absence of the S-band results in a significant reduction of the system's overall power, by as much as 63.3%, which notably impacts the ISRS power transfer. Since

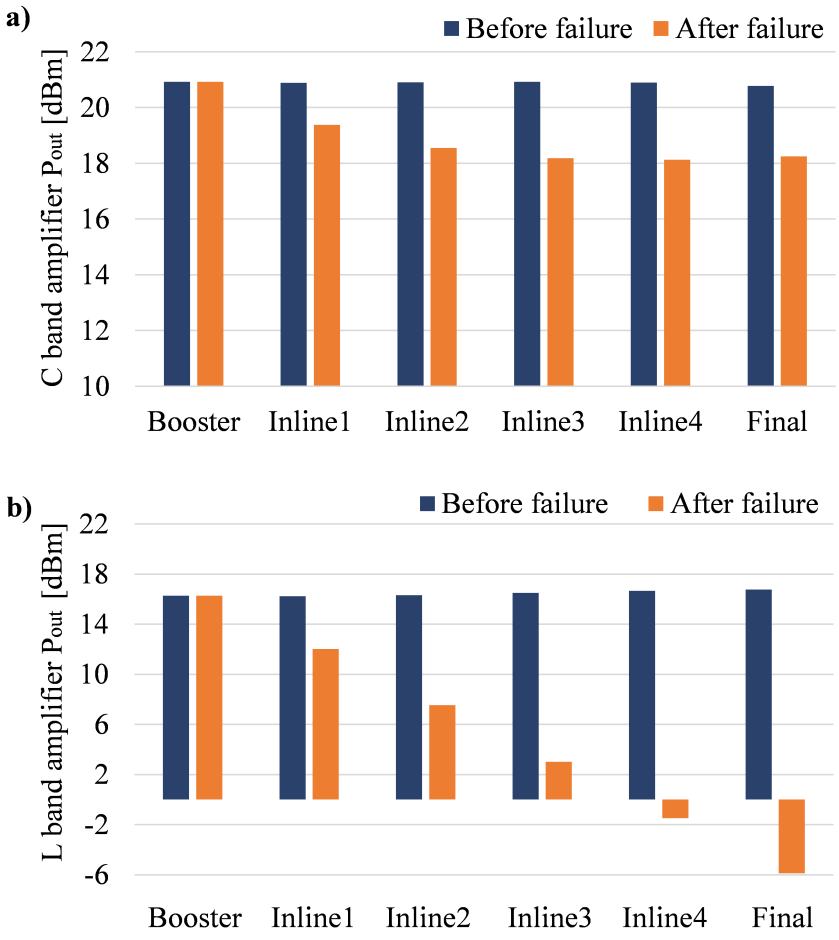

Fig. 4.22: a) C-band and b) L-band amplifier total output power at each amplification stage for the S+C+L transmission before (left) and after (right) the S-band drop.

the transmission considers homogeneous spans, the amplifier's gain by the ASE-NL heuristic remains consistent across all six amplifiers and this is observed in the total output power across all the amplification stages of Fig. 4.22 before the failure of S-band. It is assumed that the gain from the amplifiers does not increase after the S-band failure to compensate for the additional losses caused by the absence of ISRS power transfer. Therefore, as plotted in Fig. 4.22 after failure, the drop of the S-band leads to a significant decrease in the power levels of channels within both the C and L bands, especially affecting the L band. It is observed that in the case of the C-band, the total power rapidly decreases in the initial spans, but then reaches a steady state around $\sim$ 18 dBm from the third span onwards. These constant values reached by the C band could be explained by the lack of depletion due to ISRS to the L band.

The L-band, however, experiences a far more severe impact. Figure 4.22 b) demonstrates a continuous decline in power after each span, with a notable decrease of 22.6 dB at the output of the final amplifier, compared to the final output power of the S+C+L transmission before the S-band failure. These findings underscore the challenging situation in which UWB systems are exposed due to the influence of the ISRS effect.

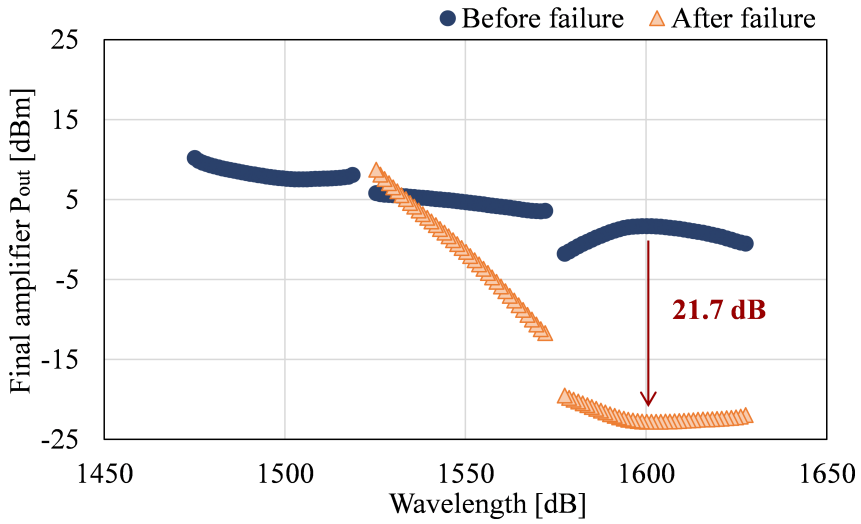

Fig. 4.23: Channel powers at the output of the final amplifier before (circles) and after (triangles) the S-band amplifiers failure. In red, the largest power loss in the L-band after the S-band drop.

While this phenomenon can provide system design benefits by enabling equalization techniques that leverage the induced power transfer, in certain cases, these approaches may prove counterproductive. This case study serves as a good example, illustrating the UWB system's particular vulnerability to S-band amplifier failures, given that less than 10% of the total power is allocated to the L-band. The comparison of channel power at the output of the final amplifier in the case of S+C+L transmission (circles) and when the S-band is missing (triangles) is plotted in Fig. 4.23. Figures 4.24 a) and b) showcase the changes in SNR and achievable bit rate, respectively, for the transmission performance before (blue) and after (orange) the failure of the S-band amplifier.

Despite the relatively small decrease in total power at the final C-band amplifier by 2.5 dB following the band loss, there is a noticeable drop in SNR across this band, as detailed in Fig. 4.24 a). Interestingly, the SNR for the first six channels of the C-band slightly improves compared to the S+C+L transmission before failure. This improvement is due to lower loss since there is lower depletion due to the L-band's low power, as shown in Fig. 4.23. Nonetheless, for the rest of the C-band channels, the output power profile of the final amplifier declines alongside their SNR performance.

The final output power (Fig. 4.23) and the SNR (Fig. 4.24 a)) profiles within the C-band exhibit a similar trend. This is explained by the gain profile of the inline amplifiers, configured with a tilted linear profile centered around 18 dB, designed to mitigate the ISRS tilt affecting the S-band's original transmission. The absence of ISRS power transfer significantly impacts the L band, leading to a notable SNR reduction, having the worst performance near 1600 nm. In this particular case, the power difference is 21.7 dB (highlighted in red in Fig. 4.23), resulting in a 14.7 dB SNR loss as indicated in Fig. 4.24 a).

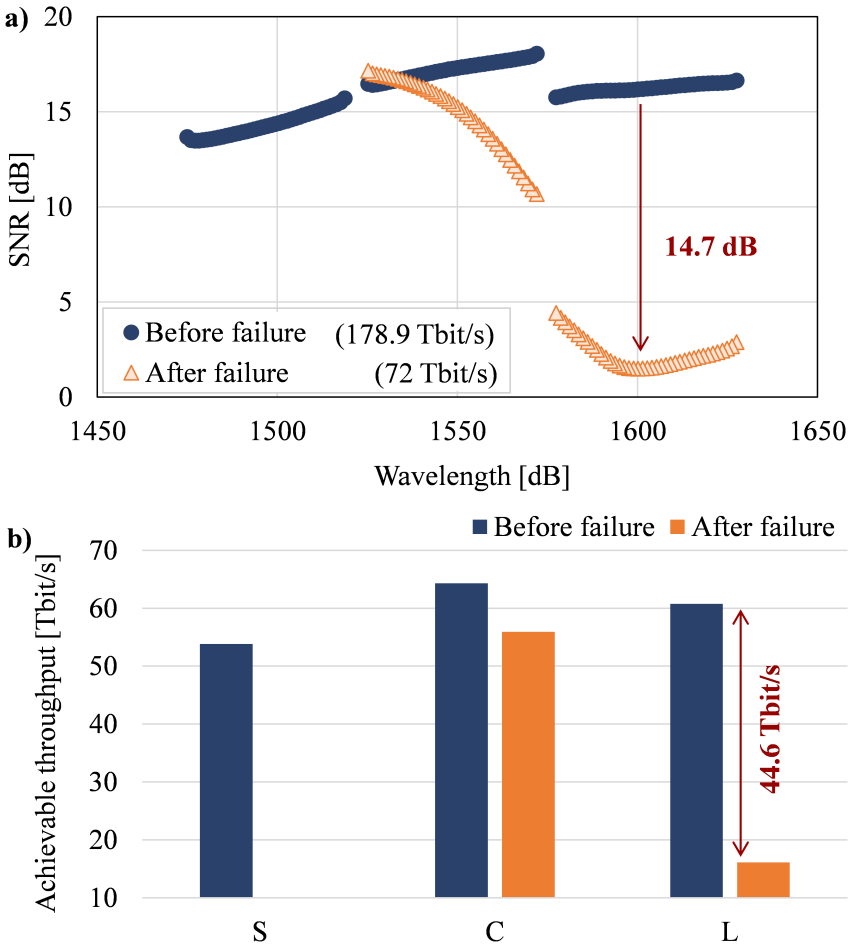

Fig. 4.24: a) SNR performance for the S+C+L transmission before (circles) and after the S-band drop (triangles). b) Achievable throughput before (left) and after (right) the band drop. In red, the worst channel SNR and capacity loss in the L-band after the band drop.

Examining the overall system throughput, the S+C+L transmission before failure reached a capacity of 178.9 Tbit/s (Fig. 4.24 a). After the S-band amplifiers failure, the total capacity decreases to 72 Tbit/s, indicating a roughly 60% decrease from the original systems capacity. The reduction in capacity after the drop can be partially explained by the missing 53.8 Tbit/s contribution from the S-band. Further analysis, as shown in Fig. 4.24 b), breaks down the capacity reduction across the C and L bands, revealing an 8.3 Tbit/s decrease for the C band and a significant 44.6 Tbit/s drop for the L band. This represents a loss of 73% of the throughput this band achieved before the S-band failure. In addition, we clarify that this capacity estimation adopts a scientific perspective, given that the low SNR levels observed in the L-band may not be practical for actual transceiver operation. These results are aligned with the experimental characterization presented in Section 4.3.2, showing a reduced total power, SNR and achievable throughput in the C and L band after the drop of the S-band. Moreover, in this section, it was observed the larger impact on system performance when the failure of the S-band amplifier affects a UWB transmission with more than two spans.

4.3.4.3 Failure of L-band amplifier

Considering the previously presented transmission setup we study the impact of losing the L band amplifier, as shown in Fig. 4.25. This is achieved by significantly reducing the power allocated to its channels while keeping the output powers of the booster amplifiers for the S-band and C-band at 24.5 dBm and 20.9 dBm, respectively. Similarly, we assume that the gain of the S and C-band amplifiers remains unchanged despite the L-band amplifier's failure.

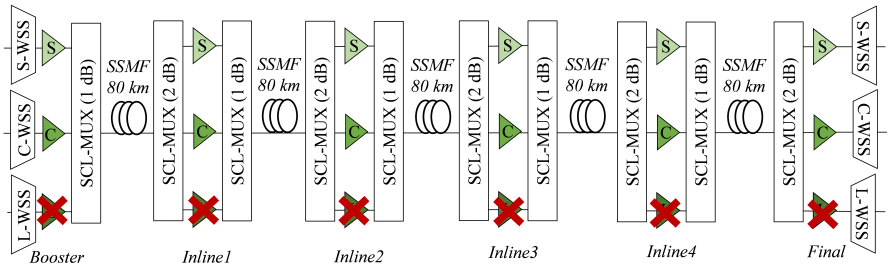

Fig. 4.25: S+C+L transmission setup used to simulate the impact of the L-band drop along five spans of 80 km of SSMF.

Figure 4.26 illustrates the total output power of the S and C-band amplifiers both before (blue) and after (orange) the failure of the L-band, at the booster stage and the first inline amplifier (Inline1). As expected, the L-band drop resulted in a slight increase in the output power for the remaining bands, having an increase of 1.6 dB in the S-band and 1.5 dB in the C-band. Although the power increase appears similar across the two bands, its implications are more critical for the S-band due to its total output power. Specifically, Fig. 4.26 b) shows that the first inline amplifier of the C-band reaches a total output power of 22.3 dBm, staying below the typical amplifiers saturation output power of 24.5 dBm as observed in our experimental measurements. However, the S-band booster is already operating at the saturation limit. Without limitations on amplifier output power, Fig. 4.26 a) shows that the S-bands first inline amplifier exhibits a total output power of 26.2 dBm, exceeding the conventional maximum output level. Consequently, the first inline S-band amplifier is likely to be saturated, functioning at power levels above its intended range, which could lead to a deviation in the amplifier's gain from its original settings.

Due to the current limitations in our model to accurately forecast the amplifier's behavior under these conditions, our simulation study is performed up to the second span, highlighting this critical limitation.

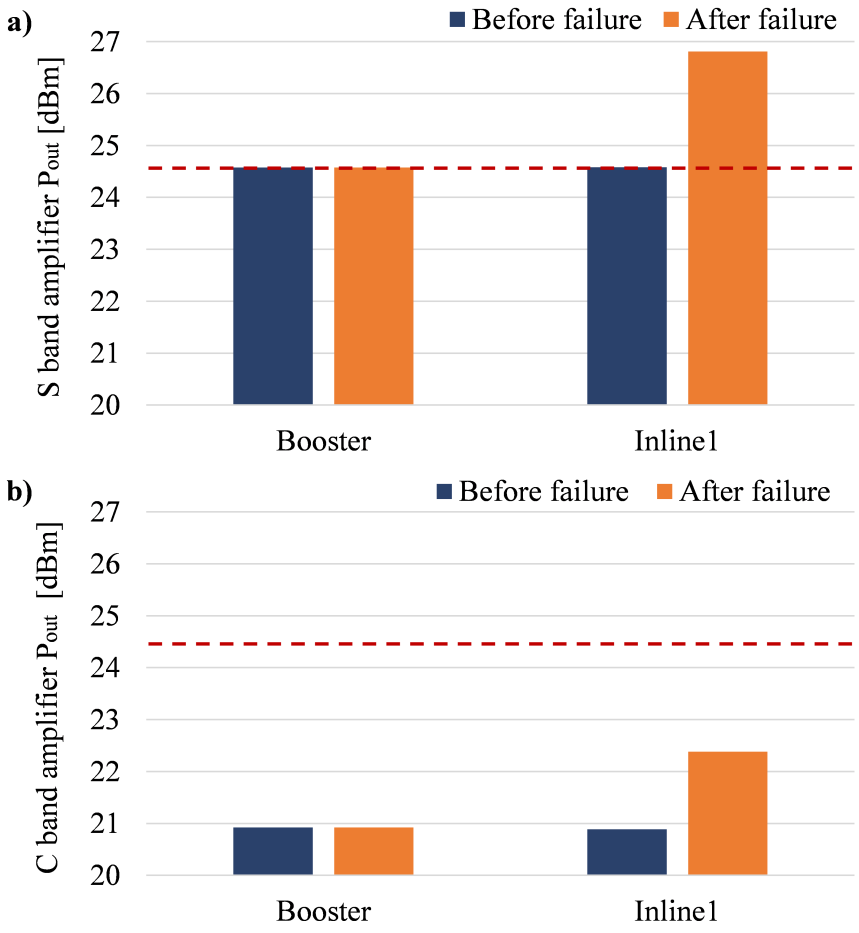

Fig. 4.26: a) S-band and b) C-band amplifier total output power at each amplification stage for the S+C+L transmission before (left) and after (right) the L-band drop.

4.4 Discussion

In this thesis, we explore the potential of S+C+L transmissions as the next frontier following the currently established and mature C+L technology. From an industry perspective, the S-band adoption presents a challenging but feasible endeavor attractive to cope with the growth of optical traffic without the need for extra cable deployment. However, given the current level of ecosystem maturity and the higher costs involved, many telecommunications operators remain skeptical about deploying these systems, especially when weighed against the long-term benefits of deploying additional parallel fibers. Whereas experimental transmissions have been demonstrated beyond S+C+L bands, the skepticism for S-band deployment also implies that no consideration is given to the deployment of extra bands in the next decade. Consequently, this chapter focused on the analysis of experimental S+C+L transmissions using the innovative concept of *digital twin*, as the virtual representation of physical elements involved in optical transmissions. Based on this, we presented model-based techniques accounting for physical impairments to improve system design, ultimately aiming to enhance transmission performance and delve deeper into the implications of triple-band transmissions.

In Section 4.1, thanks to the high-fidelity characterization of the components in the physical layer, our QoT tool has found reliable predictions of averaged data rates for various uniform power distributions having a simulation error lower than 0.4% for all the measured cases. Moreover, the collected data has been used as input for the validation of our proposed ASE-NL heuristic to optimize the power distribution of a two-span S+C+L system. We have presented the ASE-NL heuristic effectiveness in improving system performance, particularly in terms of capacity enhancement, showing 6.2 Tbit/s of gain in the measured GMI throughput when compared against uniform power distribution with the same total power, and 5 Tbit/s against the optimum capacity achieved by uniform power distributions. The experimental validation of the ASE-NL heuristic not only refers to the accuracy of the predictions when the optimized parameters are configured in the setup but also the measured capacity gain of this power pre-emphasis when compared against uniform power spectra. The results are a significant contribution to the experimental validation of model-based power optimization techniques for UWB systems, leading to the publication of [II].

In Section 4.2, we have presented the experimental of our S+C+L transmission record (at the time) of 200.5 Tbit/s total GMI throughput over two 100 km spans of PSCF. Based on the accurate predictions of SNR resultant from the *digital twin*, we have discussed relevant insights into the physical impairments affecting system performance. This examination also referred to as *noise contribution analysis*, can be performed at each band or under more granularity. This transmission had large SNR differences for the channels within the S and L bands, so we divided the analysis into short and long wavelengths for these bands. These results led to the publication of [III].

Furthermore, this experimental study has paved the way for several considerations and directions for future research. A significant point of consideration is the use of Raman amplification because, as discussed in Section 3.6, the ISRS GN closed-form model implemented in this thesis does not account for potential nonlinear interference induced by the DRAs, limiting the accuracy of the model-based performance predictions and the validity of the ASE-NL heuristic in these scenarios. Next, we will further discuss the implications of the NLI underestimation in UWB systems with distributed Raman amplification.

It is critical to note the role of the DRA's on-off Raman gain in the underestimation of NLI. Specifically, an increased Raman gain leads to reduced span loss, resulting in a higher power injection into the fiber. Consequently, the NLI underestimation will be more significant. Therefore, to assess the potential impact of the NLI underestimation in our demonstration, we plot in Fig. 4.27 the power pre-emphasis transmitted at the entrance of the span (P1) and the power profile at the output of the span after the DRA (P2). The power difference between these profiles is an alternative representation of the on-off Raman gain in terms of what we define as *effective gain gap*. Notably, for the L-band, a substantial gain gap ranging from 9 dB to 12 dB, reduces the impact of NLI underestimation in this band. A similar trend is observed in the first

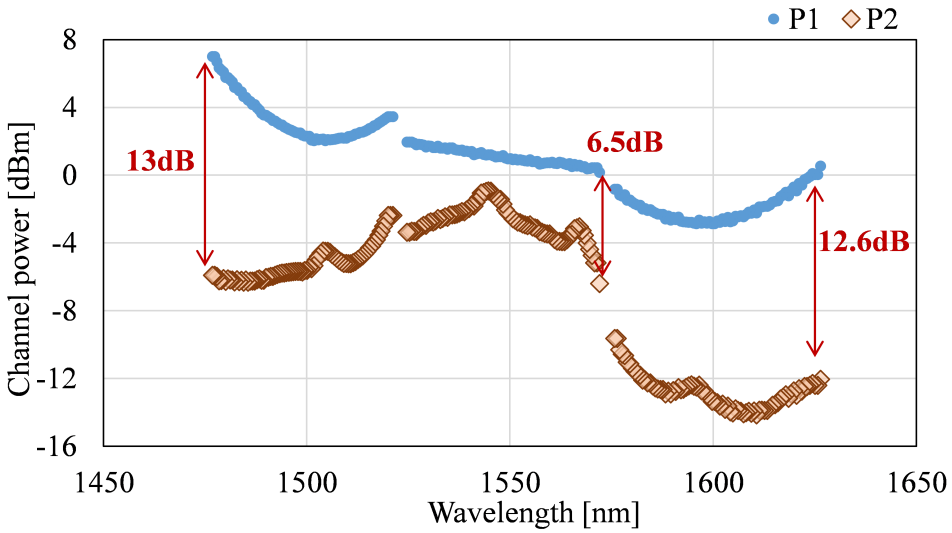

Fig. 4.27: Channel power spectra at the entrance of the fiber (P1) and the output of the fiber, after the DRA (P2) for the experiment presented in Section 4.2. In red is the maximum Raman gain gap per band estimated through the difference between both power profiles.

half of the S-band up to 1500 nm, with the gain gap varying from 12 dB to 7 dB. However, the latter half of the S-band and the entire C-band, spanning from 1500 nm to 1572 nm, exhibit the lowest gain gaps, ranging from a minimum of 2.1 dB to a maximum of 6 dB, where the NLI underestimation could be significant.

Given the DRA's importance in the development of long-haul UWB systems, new models have been proposed to overcome this challenge by presenting closed-form expressions that support DRA [106, 107]. Testing and implementing these models in UWB systems using DRA represent a promising line of inquiry. Additionally, the validity of the ASE-NL heuristic in experiments involving DRA remains to be thoroughly examined, especially after incorporating the improved NLI estimation models accounting for this type of amplification.

Nevertheless, under the context of this experimental setup, the potential benefits offered by the ASE-NL heuristic are secondary since based on the *noise contribution analysis*, the transponder penalties ($\mathrm{SNR_{TRX}}$) are the main limitation for all the bands. Additionally, the power limitations affecting the coherent receiver ($\mathrm{Rx_{POWER}}$) notably impacted the transmission of the S and the L bands. This challenge goes beyond the ASE-NL heuristic, and it could be solved in future practical implementations by using an integrated coherent receiver with trans-impedance amplifiers or larger gain amplifiers. Moreover, it was observed for this experimental demonstration the interaction of *Other* effects that have not yet been fully characterized or incorporated into our models, leading to discrepancies in our predictions, particularly affecting the S-band. To address these, further experimental research should be performed.

During the development of this thesis, numerous research groups pursued similar endeavors to experimentally assess model-based performance predictions across a variety of UWB systems. In 2023, the NLI closed-

form model proposed in [107] was experimentally validated through a C+L transmission over five spans of approximately 86 km of SSMF [108] and in an S+C+L (15.2 THz) recirculating loop of 80 km transmitted up to 400 km using G.652.D fiber [109]. In both instances, there was a remarkable agreement between the predicted performance and the measurements.

In 2024, an increasing number of publications reported significant progress in this field. A notable study on extended UWB transmissions revealed a discrepancy of 3.3 dB between model predictions and experimental measurements in a S+C+L+U system (17 THz) after traversing 80 km of SSMF [110]. Additionally, promising outcomes involving DRA have been reported [IX]. One such example included the demonstration of an average SNR estimation error of 0.22 dB in a C+L-band (10 THz) system over a 1120 km transmission amplified by a hybrid Raman-EDFA setup [111]. Furthermore, advancements in Raman amplification models were experimentally validated in the C+L band, with a maximum estimation error of approximately 2.13 dB [112]. All these findings underscore the importance of digital twins and highlight the ongoing commitment to refining accurate model-based performance predictions in diverse UWB scenarios.

In Section 4.3, we analyzed the impact of losing the S and the L bands in an S+C+L transmission over two 60 km SSMF spans. Experimentally, the S and L bands were switched off to emulate different band drops without re-optimizing the channel powers and amplifier settings. We measured the GMI-based throughput of each band observing that for this case, the impact of losing the S-band amplifier is much larger than that of losing the L-band amplifier. This is explained due to the SNR degradation caused by the limited power entering the coherent receiver ($\mathrm{Rx_{POWER}}$), but most importantly, the lack of power transferred from the S to L band induced by the ISRS effect. These results were published in [VI].

Additionally, we have analyzed the impact of the amplifiers failure, through the simulation of a five-span S+C+L transmission over 80 km of SSMF, intended to study the implications of amplifier failures in extended multi-span scenarios. In this case, a penalty of 60% in net bit rate was observed when losing the S-band and a large power accumulation in S-band was found when the L-band was lost. Overall, the findings from both simulations and experiments have demonstrated that the system failure of any band (either S or L band) significantly impacts the remaining bands due to alterations in the ISRS effect. Therefore, devising recovery mechanisms and strategies to reduce the impact on system performance becomes crucial in the design of UWB systems. These results were published in [V].

An interesting recovery strategy was introduced in [113], showcasing a fully automated system designed to manage ASE idlers as a fault recovery mechanism in UWB transmissions. This approach was analyzed within a C+L system, simulating a significant failure having the power of most channels in both the C and L bands substantially reduced. The results demonstrated that ASE idlers could be effectively utilized to

quickly substitute lost traffic by deploying protection-ASE with equivalent power and bandwidth, offering a promising direction for enhancing system resilience in the face of disruptions.

Alternatively, in Appendix A using the model-based predictions of a C+L system, we introduced a recovery strategy to mitigate the impact of L-band amplifier failure. This method involves limiting the maximum power of the C-band amplifiers, which resulted in a SNR improvement up to 5 dB when compared with the case of failure. The findings from this strategy contributed to the development of the patent [**P1**].

Chapter 5

Conclusions and perspectives

This thesis provided a detailed examination of UWB optical transmission systems, focusing on the technological advancements that have enabled their use. By incorporating experimental data with theoretical models, this work validated the model-based estimated performance of S+C+L demonstrations. Furthermore, it provided relevant insights into the impairments that affect system performance and introduced model-based power optimization techniques with promising potential in UWB transmissions.

A significant part of Chapter 2 was devoted to explaining the challenges of WDM UWB systems, including fiber attenuation, dispersion, Kerr nonlinearities and ISRS effect. Additionally, this chapter introduced the foundational methods and metrics to estimate system performance.

The first half of Chapter 3 highlighted the key role of the GN model and the ISRS GN model in deriving power optimization strategies to maximize system performance. However, it was shown that the effect of ISRS in UWB systems transforms the optimization to a non-convex problem with multiple solutions. Despite their high computational demands, ML algorithms have been investigated for their potential to tackle this issue. In addition to these complex methods, Chapter 3 reviewed alternative techniques specifically designed for optimizing launch power in UWB systems. Among these methods, the *ASE-NL heuristic* a system optimization strategy derived from the ISRS GN closed-form model was proposed. This technique was designed to enhance the SNR performance of UWB systems by equalizing the launched power and amplifiers gain so that the ASE noise power is twice the NL noise power The encouraging results presented in the second half of this chapter showed that this heuristic is a simpler and computationally efficient strategy with close convergence to more elaborated ML methods showing a capacity reduction of $\sim 0.7\%$ and a significantly reduced computational time.

Additionally, Chapter 3 emphasized the critical role of power optimization techniques in maximizing the benefits of UWB systems. Managing the ISRS effect and wavelength-dependent impairments was essential to exploit their full potential. The use of the *ASE-NL heuristic* resulted in throughput gains of 2.2%, 4.6% and 10.8% in C, C+L and S+C+L transmissions, respectively, when contrasted with the optimal uniform power spectra. Further exploration of the *ASE-NL heuristic* unveiled alternative equalization strategies that extend beyond the heuristic's original

application. These strategies are designed to optimize the performance of the worst channel within each band or across the entire system, aiming for a uniform SNR either per band or system-wide. Such additional approaches are particularly valuable as they seek to maximize transmission distance while adhering to the practical constraints of a fixed bit rate per channel. However, this advantage does come at the cost of a reduction in total system capacity compared to the initial *ASE-NL heuristic* deployment.

Despite the *ASE-NL heuristic* has demonstrated effectiveness and close convergence to optimized solutions, its application is not without limitations. Chapter 3 presented certain cases where the heuristic revealed constrained effectiveness, suggesting particular transmissions where its application may not yield the expected performance improvements. Moreover, we also underlined some transmission scenarios where the *ASE-NL heuristic* requires further exploration, these include lightly loaded WDM systems and conditions of a strong ISRS regime.

Chapter 4 delved into experimental S+C+L demonstrations through the lens of *digital twin*. Through the high-fidelity mapping of the transmission components, the model-based estimations resulted in reliable predictions of averaged data rates across various power distributions, with simulation errors below 0.4%. Additionally, this chapter extensively discussed the experimental validation of the *ASE-NL heuristic* where a gain of 6.2 Tbit/s was observed when comparing the achievable throughput using the pre-emphasis versus uniform launch power profile in an S+C+L system. These results represented a pioneer study on the experimental validation of model-based power optimization techniques in UWB systems, not only by achieving very accurate performance estimations but also by experimentally registering throughput gain reached via the heuristic's pre-emphasis.

Furthermore, the accurate model-based predictions obtained from the *digital twin*, facilitated the study of the physical impairments affecting the total system performance through the *noise contribution analysis*. Using this analysis, Chapter 4 offered valuable insights into the system performance of our record-breaking (at the time) experimental achievement of a 200.5 Tbit/s total GMI throughput over two 100 km spans of PSCF. This experimental exploration not only set a new benchmark in transmission capabilities but also laid the groundwork for various future research avenues. Among these, the integration of models that include the nonlinear interference effects introduced by Raman amplification stands out as a critical area of focus. In addition to the *Other* effects, especially affecting the predictions of the S-band. These impairments have not been fully characterized and require further experimental research.

Multi-band systems are particularly susceptible to the failure of one band, as such incidents trigger power variations that can adversely affect the ISRS effect and, by extension, the performance of the remaining bands. This vulnerability underscores the need to explore the effects of band drops on S+C+L transmission systems. Chapter 4 presented experimental and simulation approaches, to assess the impact of amplifier system failure and ISRS variations, particularly when the S or L

bands are lost, assuming no subsequent re-optimization of channel powers and amplifier settings. The experimental results were performed in an S+C+L transmission over two spans of 60 km of SSMF, indicating that the repercussions of an S-band amplifier failure were considerably more severe than those from the L-band amplifier loss. This was partially explained by some power limitations of the coherent receiver but predominantly attributed to the absence of power transfer from the S to L band. Conversely, the simulation studies were conducted over five spans of 80 km of SSMF, highlighting the implications of amplifier failures in extended multi-span scenarios. For this case, a penalty of 60% in total bit rate was observed when losing the S-band and a large power accumulation the in S-band when the L-band failed. Overall, these findings highlighted the impact that the failure of any band (either S or L) could have on the remaining bands due to ISRS-related alterations. Consequently, the development of recovery mechanisms and strategies to mitigate such impacts is critical in the design and resilience planning of UWB systems (Appendix A).

Throughout this thesis, we have discussed the substantial difficulties faced by UWB systems, as well as the strategies that enable these systems to overcome such obstacles. One of the main challenges includes wavelength-dependent impairments, which can be effectively modeled and addressed using model-based power optimization techniques. Furthermore, potential issues like system amplifier failure could be tackled through enhanced system design and robust fault recovery mechanisms. These advances position UWB systems as a promising technology for achieving high-capacity transmissions.

Looking ahead, the future of UWB technology appears bright. Notably, C+L systems have already gained traction within the industry, a trend supported by the commercialization of EDFAs working in the Super C band (C120) and the Super L band (L120). These advances indicate a strong industry forecast for the deployment of this technology in the near future. However, the lasting success of C+L systems relies on the evolution of future generations of the technology, requiring improved system architecture integration and reduction in cost.

Initial steps toward C+L integration include the development of C+L WSS and a common transponder for both C and L bands. An additional critical aspect of this system integration involves the optical amplifiers. Currently, independent modules for C and L bands are deployed, leading to additional losses due to the connection of multiple modules (such as the amplifiers for C and L bands, multiplexer, demultiplexer and patch cords). Therefore, the integration of C+L optical amplification will result in a simpler deployment and improved performance. Moreover, this system integration must result in compact and cost-effective devices that can compete against the cost of two C120 amplifiers.

The current landscape of C+L systems and the required work in system integration underscores the challenging ecosystem maturity and uncertain economic viability of UWB systems, which results even more critical in systems working in S+C+L band and beyond. The anticipated higher costs for S-band amplifiers (TDFAs) compared to current

EDFAs designed for C or L bands pose a significant challenge. Although SOAs for S-band amplification could potentially reduce this cost differential, their performance has not yet been demonstrated apart from ASE generation [114].

Adding to these challenges, we presented in this work that incorporating the additional 6 THz of the S-band yielded a capacity gain of less than 50% (Section 3.4). Achieving this gain required the use of power pre-emphasis, a technique that may not be fully practical in actual network deployments. Moreover, as we have experimentally shown in Section 4.2, UWB system performance can be improved by Raman amplification. However, it incurs additional costs due to the high-power pump lasers required. Given all these considerations, we conclude that the most challenging obstacle for S+C+L systems is its anticipated higher cost compared to simply adding parallel fibers operating in the C and/or L band.

In light of these factors, the question arises: Does this mean the adoption of UWB systems is not feasible? Analyzing the feasibility and utility of UWB systems in the face of burgeoning data traffic demands requires a nuanced assessment. Given the growth in data traffic, it is critical to project future demands accurately to assess the adequacy of UWB technology. For illustrative purposes, let us consider two hypothetical scenarios of traffic growth over the next 14 years from a base year (T0) of 2024, as depicted in Fig. 5.1.

Case 1 (squares) anticipates a robust annual growth rate of 20% per year, while case 2 (triangles) starts increasing by a rate of 10% the first year, but from the second year forward then it assumes a gradual slow-

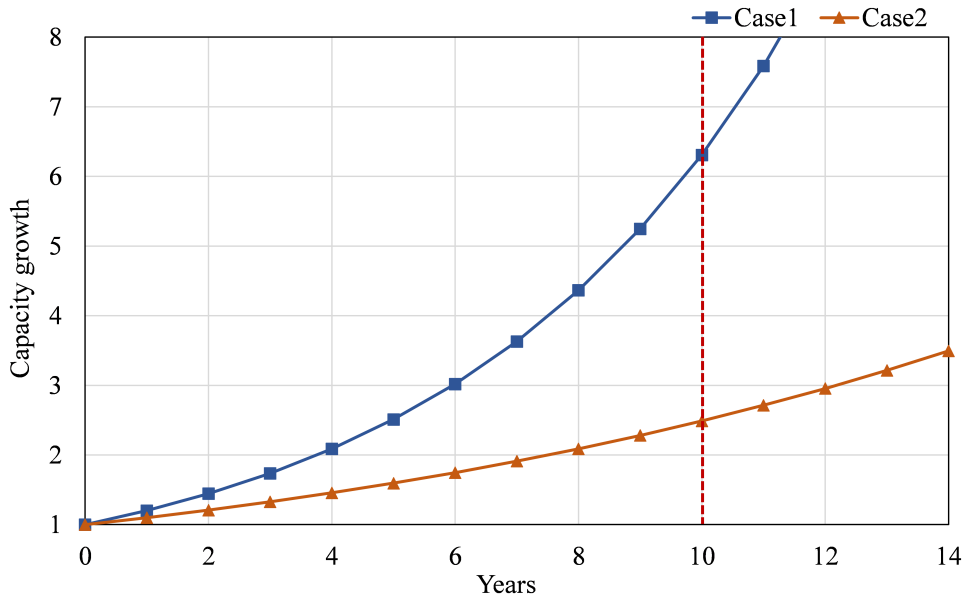

Fig. 5.1: Projected traffic growth scenarios over time from base year T0. Case 1 (squares) predicts a strong annual growth rate of 20% and case 2 (triangles) starts with a 10% increase, which decelerates to a linear rate from the second year (T2) onwards. In red we compare the two cases after 10 years (T10).

down at a rate of 1% per year. We compare these two scenarios to assess the usability of UWB systems compared to the deployment of parallel C band systems considering as a base the case of 10 years from now (T10). Moreover, based on the simulation results presented in Section 3.4, we consider that incorporating the L band would double the capacity (factor of 2) and adding the S band will increase at best half of the capacity achieved by the C+L systems (factor of 1.5). This suggests that UWB systems could adequately support the projected growth outlined in case 1 up until 2030 (T6), but would fall short by 2034 (T10), so the deployment of parallel systems will be required.

For case 2 (triangles), the rate of growth is smaller indicating that UWB systems alone could sufficiently meet the demand up to 2034 (T10). This means that the addition of the S and L bands offers sufficient capacity to cope until 2036 (T12), assuming the same rate of growth. In summary, for case 2, UWB systems alone could sufficiently meet the demand up to and beyond 2034, negating the immediate need for parallel systems under these growth patterns. Certainly, there are additional factors that interplay in this study, such as the cost and the integration challenges of UWB technology in current C-band deployed systems, as we had previously discussed.

Additionally, it is important to note that combining parallel systems with UWB technology can significantly enhance the capacity of each approach. For instance, in case 1 moving from C to C+L provides 4 years margin for the operator and from C+L to S+C+L will provide 2 additional years. In this case, parallel systems will be needed and UWB will only be deployed if they are cost-efficient. Whereas for case 2, the addition of S band could cope with the growth of many more years, so it could be worth investing in it.

This final analysis aimed to demonstrate the potential and feasibility of UWB systems in the near future, showing that for some trends of traffic growth, they represent an intermediate step towards increasing capacity before installing new fibers. Furthermore, UWB systems represent undoubtedly an attractive solution in scenarios where the deployment of parallel systems is constrained by the lack of available fibers or contractual limitations on new cable deployments.

Appendix A

Model-based amplifier recovery strategy

As discussed in Section 4.3, the system failure of any band (either S or L band) will severely affect the power and performance of the remaining bands through changes on the ISRS. Therefore, solutions to contain the impact of power variations in system performance are crucial. We can profit from the accurate modeling of our QoT to design recovery mechanisms and estimate their benefits in performance. In this appendix, we present an amplifier configuration for the protection of UWB systems, and through simulations in a C+L transmission (12 THz of bandwidth), we demonstrate its benefits when the L-band amplifier is lost.

The transmission link is presented in Fig. A.1 and consists of an OMS with 5x65 km SSMF spans, transmitting 68 Gbaud channels spaced by 75 GHz along 12 THz of C+L bands. Multiplexers and demultiplexers with 1 dB and 3 dB insertion loss, respectively, are used at each amplification stage. The fiber attenuation profile and dispersion spectra were previously plotted in Section 2.3.1 and Section 2.3.2, respectively. An additional attenuation factor of 0.05 dB/km is accounted to simulate fiber aging, to produce a total span loss of $\sim$ 21.4 dB at 1550 nm (including the multiplexer/demultiplexer loss). The link is assumed to use lumped amplifiers with no ripple, having the following NF: 5 dB for the C band and 6.5 dB for the L band.

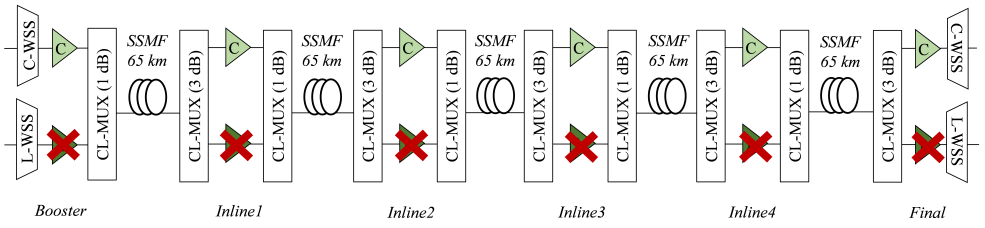

Fig. A.1: C+L transmission setup used to simulate the impact of the L-band drop along five spans of 65 km of SSMF.

We transmit uniform power spectra with 22 dBm of total power per band ($\sim$ 3 dBm per channel). Since we assume that the amplifiers have a fixed gain that compensates for the span loss of each band, Fig. A.2 shows in blue that for the C+L transmission *before failure*, the C-band amplifier

total output power is the same after each stage of amplification. Now, we simulate the loss of the L-band amplifier by setting very small values of power to the channels within this band but maintaining 22 dBm of total power for the booster amplifier in the C-band. This case is referred to as *after failure* and is presented in Fig. A.1 with red crosses, aiming to study the most extreme case of failure, which is losing the L-amplifier at the booster level.

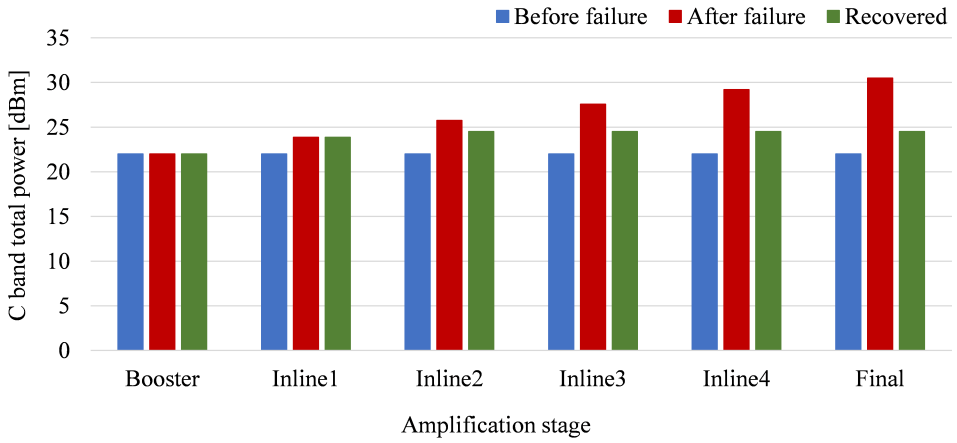

Fig. A.2: C-band amplifier total output power at each amplification stage for the C+L transmission before (blue), after (red) the L-band drop and using the recovery strategy (green), from left to right.

Moreover, Fig. A.2 shows in red the power accumulation at the output of each stage of amplification. Since we have fixed gain in the C-band amplifiers, it can be observed that around 2 dB of additional power is aggregated after each span, having up to 30.5 dBm of total output power for the final C-band amplifier. The C-band SNR performance for this case is plotted in Fig. A.3 (red squares), showing that for most of the channels, the performance is greatly reduced when comparing with the case before failure (blue circles).

Based on these results, a straightforward solution to contain the power aggregation in the C-band is to constrain its maximum amplifier output power. Hence, we propose a recovery strategy of configuring the C-band amplifiers such that the output power could not exceed a predefined power value P set before the failure detection. Applying this method to our study case, we set a maximum output power P as the typical 24.5 dBm used in C-band. Therefore, as it is observed in Fig. A.2 (green), the power of the amplifier *inline1* is still under the power threshold with a total output power of 23.8 dBm. Nevertheless, from the amplifier *inline2* until the *final* stage of amplification, the *recovered* output power for the C-band remains at 24.5 dBm.

Figure A.3 shows the resultant SNR using the proposed recovery strategy (green triangles). The performance gain is observed for all the channels, having a maximum of 5 dB when compared against the case of L-band failure (red squares). This simple recovery strategy that only involves the modification of the EDFA control software, demonstrates to

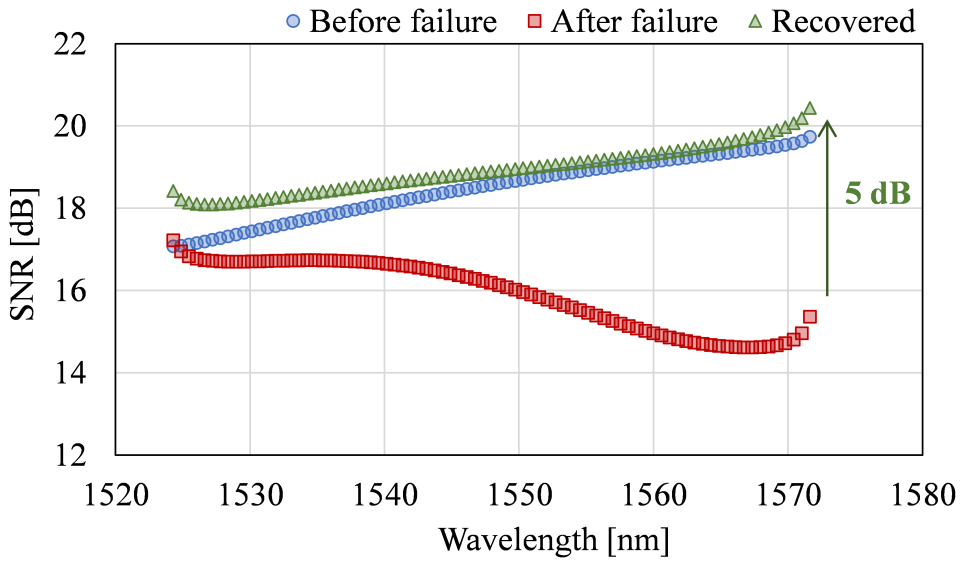

Fig. A.3: C-band SNR performance for the C+L transmission before (blue), after (red) the L-band drop and using the recovery strategy (green). In green is the maximum SNR gain of the recovery strategy concerning the L-band failure.

be greatly beneficial to reduce the power and ISRS variations, improving the system design of UWB systems.

Appendix B

Résumé de la thèse en français

B.1 Introduction

En raison de la demande mondiale toujours croissante en matière de transmission de données, alimentée par les services numériques tels que le streaming haute définition, les services cloud exhaustifs et les applications de réalité virtuelle/augmentée, des approches innovantes sont nécessaires pour augmenter la capacité des réseaux de communication optique.

Face à l'accroissement du trafic de données, les systèmes à bande ultra-large (UWB) apparaissent comme une piste prometteuse. En étendant la bande passante opérationnelle au-delà de la bande C traditionnelle, les systèmes UWB utilisent un spectre plus large au sein des infrastructures de fibre existantes, abordant efficacement les contraintes de capacité sans nécessiter la pose de nouvelles fibres.

Cette thèse de doctorat se concentre sur l'investigation des outils, défis et opportunités associés aux systèmes UWB, spécifiquement les systèmes à bandes S+C+L. Elle s'appuie sur et étend les modèles théoriques qui décrivent les dégradations dépendantes de la longueur d'onde et les distorsions non linéaires causées par l'effet de diffusion Raman stimulée (ISRS). En intégrant ces modèles avec des approches pratiques, l'un des objectifs principaux de cette thèse est de proposer une solution pour optimiser la préaccentuation de puissance et les paramètres d'amplificateur en ligne, améliorant ainsi la performance de transmission UWB. Pour évaluer la stratégie d'optimisation proposée, une validation numérique est réalisée en utilisant des algorithmes basés sur l'apprentissage automatique. Cette comparaison valide non seulement la capacité de la stratégie à offrir une solution proche de l'optimum en termes de capacité, mais met également en évidence son potentiel comme une alternative plus simple aux méthodes d'optimisation plus complexes.

La deuxième contribution majeure de cette thèse inclut la validation expérimentale de l'algorithme appliqué à un système multiplexé par division de longueur d'onde (WDM) S+C+L, confirmant l'applicabilité pratique de la stratégie proposée dans un système de transmission UWB réel. Enfin, cette thèse intègre des mesures expérimentales des transmissions UWB qui sont utilisées pour calibrer les modèles, ce qui améliore

la précision de leurs prédictions. En créant une réplique virtuelle de la couche physique, ce travail se présente comme l'une des premières études expérimentales menées pour valider la précision des estimations du rapport signal sur bruit (SNR) à travers des modèles à forme fermée, pour des transmissions au-delà de la bande C+L. De plus, en utilisant ces modèles, cette étude offre des observations précieuses sur les dégradations affectant la qualité de transmission, et examine divers scénarios de défaillance du système UWB.

Pour résumer, l'objectif de cette thèse est de combiner les mesures expérimentales et les modèles théoriques, en exploitant les prédictions basées sur les modèles et les techniques d'optimisation pour améliorer la performance du système UWB. Les sections suivantes sont organisées de la manière suivante :

- La Section B.2 décrit les avantages des systèmes UWB comme solution potentielle pour surmonter la demande croissante de capacité dans les réseaux optiques, et présente les défis techniques et limitations liés à ces systèmes. Nous introduisons ensuite les bases pour la modélisation qui sera utilisée pour prédire la performance des systèmes dans de tels scénarios.

- La Section B.3 discute de la pertinence du *ISRS GN closed-form model* dans le développement de techniques d'optimisation de puissance rapides qui visent à maximiser la qualité de transmission (QoT). Sur la base de ce modèle théorique, nous présentons l'heuristique ASE-NL, une stratégie d'optimisation simple et rapide pour les systèmes multi-bandes, et, en utilisant cette technique, nous étudions comment la capacité évolue avec la bande passante. Cette section vise à souligner l'importance des techniques d'optimisation de puissance basées sur les modèles dans la conception des systèmes UWB et développe des techniques d'égalisation concrètes. Par la suite, ces approches sont validées par simulation.

- La Section B.4 présente une analyse détaillée des transmissions expérimentales S+C+L. L'heuristique ASE-NL est validée expérimentalement comme une technique d'optimisation de puissance valable pour les systèmes S+C+L. En particulier, nous soulignons la pertinence du jumeau numérique comme nouvel outil pour fournir des prédictions précises de la performance. De plus, nous présentons un défi important dans les systèmes UWB : la défaillance du système pour une bande, causée par la perte d'amplificateurs. Nous évaluons l'impact sur la performance du système après la perte de la bande S ou de la bande L.

- La Section B.6 résume cette thèse, mettant en évidence les contributions les plus significatives de ce travail. Nous présentons également une perspective pour la recherche future, basée sur le travail établi dans cette thèse.

B.2 Systèmes au-delà de la bande C

Comme précédemment discuté, les systèmes UWB ont émergé afin d'augmenter la capacité des systèmes en exploitant la fenêtre spectrale. Suivant la définition de l'ITU-T G.sup 39, le tableau B.1 résume les bandes spectrales.

Bande	Descripteur	Longueur d'onde [nm]	Bande passante [THz]
O	Originale	1260 to 1360	17.5
E	Étendue	1360 to 1460	15.1
S	Courte	1460 to 1530	9.4
C	Conventionnelle	1530 to 1565	4.4
L	Longue	1565 to 1625	7.1
U	Ultra-longue	1625 to 1675	5.5

Table B.1: Définition de la bande spectrale selon l'ITU-T G.sup 39.

Après l'invention de l'amplificateur à fibre dopée à l'erbium (EDFA) au début des années 1990 [3, 4], les EDFAs sont apparus comme une technologie qui a ouvert la voie aux systèmes WDM dans la bande C (1530 nm à 1565 nm). La communauté s'est ensuite penchée sur le développement d'EDFA avec des bandes d'amplification aplaties et plus larges, permettant l'exploitation de nouvelles bandes. En 1998, les progrès dans l'amplification à large bande optique vers la bande L (1565 nm à 1625 nm) ont permis les premières transmissions à 1 Tbit/s dans les systèmes C+L sur plus de 400 km de fibre [6, 7]. Dans les années suivantes, le monde de la recherche s'est intéressée à la bande S voisine (1460 nm à 1530 nm) comme option pour étendre davantage la bande passante de transmission, ceci en raison de la faible perte des fibres de silice et de la disponibilité d'amplificateurs à fibre dopée au thulium à décalage de gain (TDFA). En 2001, la combinaison de TDFA et d'amplification Raman distribuée (DRA) a atteint 10,9 Tbit/s sur la bande S+C+L le long de 117 km [8].

Bien que ces efforts de recherche sur les systèmes de transmission au-delà de la bande C remontent au début des années 2000, ces technologies n'ont pas tout de suite été déployée, en raison de leur relative inefficacité à augmenter la capacité, surtout lorsqu'elle est contrastée avec les améliorations spectaculaires de l'efficacité spectrale (SE) obtenues par le biais d'émetteurs-récepteurs cohérents numériques, des systèmes WDM plus denses avec un espacement de canal plus étroit, et des formats de modulation d'ordre supérieur qui transmettent plus de bits par symbole. Cependant, après des décennies d'avancées dans la technologie des émetteurs-récepteurs cohérents numériques, il a été observé que les améliorations de SE ont commencé à ralentir à mesure qu'elles approchent de la limite de capacité de Shannon [28]. Par conséquent, l'intérêt pour l'expansion de la bande de longueur d'onde a réapparu, menant à des efforts renouvelés et des investigations dans les systèmes UWB comme approche viable pour surmonter le plateau de capacité rencontré par les technologies actuelles.

B.2.1 Défis des systèmes UWB

Nous présentons la perte de fibre comme un défi important pour les transmissions UWB. Il s'agit d'un effet dépendant de la longueur d'onde défini par le coefficient α [dB/km]. En raison de cette dépendance à la longueur d'onde, différents canaux WDM subiront des atténuations différentes lors de la propagation, conduisant à des performances variées. La Fig. B.1 montre l'atténuation mesurée pour la fibre monomode standard (SSMF) et la fibre à coeur de silice pure (PSCF), soulignant le comportement le long des différentes bandes de spectre. Ces profils caractérisent la perte dépendante de la longueur d'onde (WDL) utilisée dans les simulations de ce travail, qui s'appuient sur les mesures expérimentales effectuées dans cette thèse.

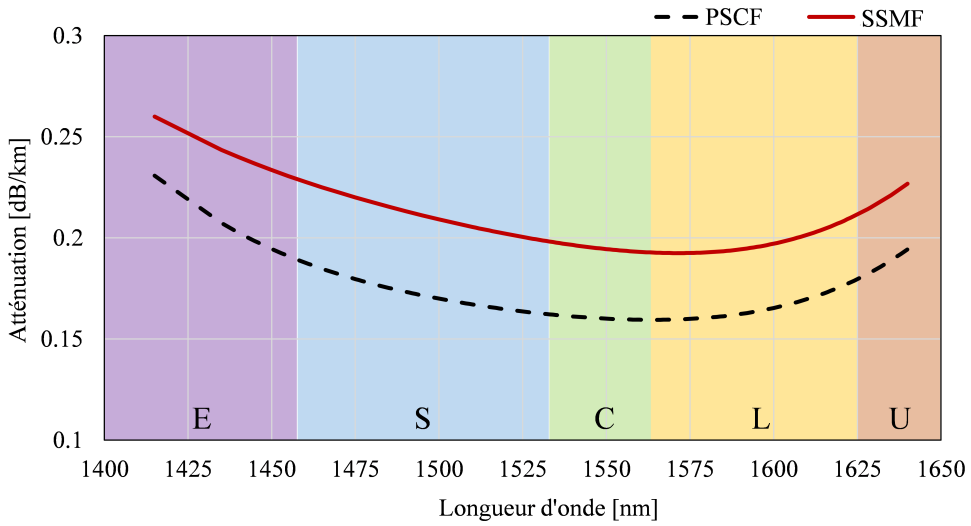

Fig. B.1: Caractérisation expérimentale du profil d'atténuation de la SSMF et de la PSCF de 1415 nm à 1640 nm

Cette thèse se concentre sur les transmissions au sein des bandes C+L et S+C+L. Cependant, il est important de reconnaître qu'une quantité significative de recherche a été consacrée à l'exploration et à l'intégration de bandes alternatives [22, 29–31].

Outre la perte dépendante de la longueur d'onde (WDL) déjà présentée, la dispersion chromatique de la fibre est un effet dépendant de la longueur d'onde qui joue également un rôle sur l'accumulation d'effets non linéaires de la fibre lors de la propagation de systèmes multi-bandes. La dépendance à la longueur d'onde est presque linéaire mais doit encore être prise en compte lors de la modélisation des transmissions WDM.

Enfin, ISRS est un effet non linéaire qui induit un transfert de puissance des fréquences plus élevées vers les fréquences plus basses. En conséquence, les fréquences plus élevées subissent une diminution de puissance qui accentue leurs pertes, tandis que les fréquences inférieures sont boostées, affectant l'évolution de la puissance des canaux WDM lors de la propagation. La caractérisation et l'étude de cet effet sont très pertinentes lors de la modélisation des systèmes UWB WDM, puisque l'efficacité maximale du transfert de puissance ISRS se trouve à 13.2 THz

($\sim$ 100 nm) de la fréquence originale. La Fig. B.2 trace la courbe de gain ISRS d'un spectre WDM.

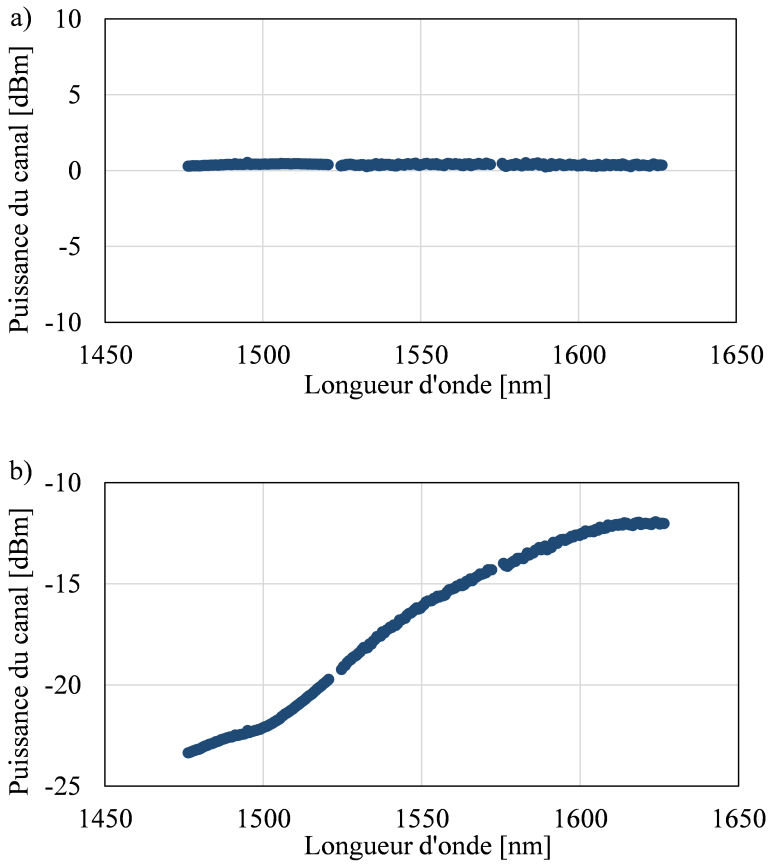

Fig. B.2: a) Distribution uniforme de la puissance à l'entrée de la fibre et b) évolution de la puissance mesurée après 60 km de SSMF pour un système de transmission expérimental S+C+L.

Les effets précédemment cités peuvent causer des variations importantes à travers les différentes bandes et doivent donc être inclus lors de l'implémentation des modèles de propagation UWB. De plus, pour étudier les avantages potentiels de capacité des systèmes UWB, les modèles de propagation tenant compte des effets linéaires et non linéaires doivent être adaptés pour fonctionner au-delà de la bande C.

B.2.2 Estimation de la performance du système

Dans le contexte de l'estimation de la performance des systèmes WDM UWB, trois sources principales de dégradation doivent être considérées : les dégradations en back-to-back (B2B) provenant du transpondeur, établissant une performance maximale atteignable basée sur l'émetteur et le récepteur ; le bruit d'émission spontanée amplifiée (ASE), ajouté par les amplificateurs optiques ; et le coefficient d'interférence non linéaire décrivant les distorsions non linéaires imposées par l'effet Kerr. En tenant compte de ces trois sources de bruit, le SNR total au récepteur peut être

exprimé comme [35]

$$\mathrm{SNR} = \frac{P_{\mathrm{ch}}}{\underbrace{\kappa_{\mathrm{TRX}}}_{\mathrm{B2B}} P_{\mathrm{ch}} + \underbrace{P_{\mathrm{ASE}}}_{\mathrm{ASE}} + \underbrace{\eta_{\mathrm{N_s}}}_{\mathrm{NL}} P_{\mathrm{ch}}^3} \tag{B.2.1}$$

Ces trois sources de bruit sont supposées être non corrélées et sont modélisées comme des sources de bruit gaussien additif, l'eq. (B.2.1) implique que la puissance de bruit totale peut être obtenue simplement en ajoutant les puissances de bruit des contributions de bruit individuelles.

Pour les pénalités du transpondeur, le κ_{TRX} impose un SNR maximal atteignable indépendant de la puissance du signal, qui est obtenu par la caractérisation expérimentale du transpondeur.

La puissance de bruit ASE inclut le bruit introduit par chaque amplificateur optique, qui dépend du gain dépendant de la longueur d'onde de l'amplificateur (G) et de la figure de bruit (NF).

Enfin, les non-linéarités Kerr de la fibre tiennent compte des distorsions non linéaires basées sur différents paramètres du système, parmi lesquels le format de modulation, le débit de symboles, le type de fibre ainsi que la distance de propagation. Dans cette thèse, puisque nous travaillons dans des scénarios au-delà de 5 THz, nous estimons ce coefficient à l'aide du *ISRS GN closed-form model* [35, 94].

En raison de la dépendance à la longueur d'onde, l'eq. (B.2.1) doit être résolue pour chaque canal WDM considéré dans la transmission. Cette équation est aussi un moyen pratique d'illustrer la performance d'un système de communication optique ; son calcul produit la courbe SNR bien connue montrée dans la Fig. B.3, où P_{NLT} est le seuil non linéaire, établissant la puissance pour le SNR optimal.

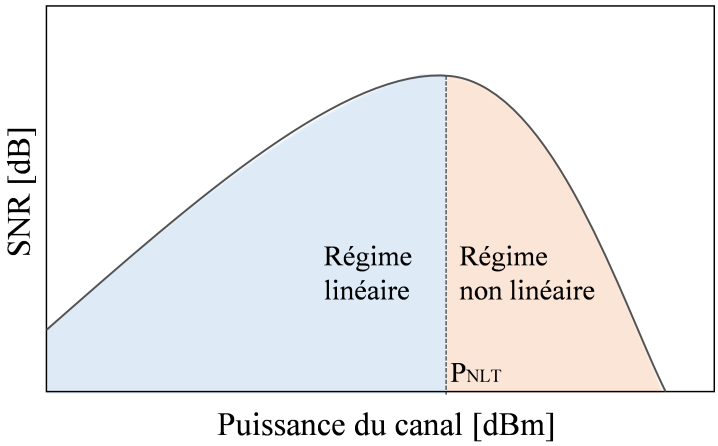

Fig. B.3: Le SNR en fonction de la puissance du canal pour un système de transmission arbitraire.

Sur la base des modèles théoriques précédemment présentés et en utilisant les formules présentées tout au long de cette section, nous avons mis en oeuvre une qualité de transmission (QoT) codée en Python avec pour objectif de prédire avec précision le comportement expérimental des systèmes UWB et de définir des stratégies d'optimisation qui améliorent leur performance.

B.3 Heuristique ASE-NL

En fixant la dérivée de l'eq. (B.2.1) à zéro, la puissance par canal maximisant le SNR peut être présentée comme suit [88] :

$$P_{\mathrm{ch,opt}} = \sqrt[3]{\frac{P_{\mathrm{ASE}}}{2\eta_{\mathrm{N_s}}}} \tag{B.3.1}$$

Ce résultat met en évidence une propriété dérivée du modèle de bruit gaussien (GN) bien connue : à la puissance de transmission optimale, la quantité de bruit ASE est le double de la quantité de bruit NL. Dans plusieurs publications, cette quantité est désignée comme la puissance de lancement optimale par canal [83, 84, 89]. Néanmoins, l'optimalité de la solution obtenue en utilisant cette propriété a été remise en question dans le cas des systèmes UWB, puisqu'il a été montré que l'expression du SNR tenant compte de l'ISRS est incompatible avec l'optimisation convexe directe, conduisant à plusieurs solutions locales [45].

Dans cette section, nous évaluons la validité de la propriété du rapport ASE et NL pour les systèmes UWB qui présentent l'effet ISRS, à travers une heuristique qui vise à optimiser la performance du système basée sur l'équilibre des bruits linéaires et non linéaires. Cette solution, mentionnée par la suite sous le nom d'*heuristique ASE-NL*, est une approche d'optimisation de puissance itérative très simple dérivée analytiquement avec l'utilisation du modèle en forme fermée ISRS GN, implémentée dans notre outil QoT. Ensuite, nous expliquons étape par étape la méthodologie de la solution, les paramètres du système et les hypothèses de modélisation sur lesquelles elle repose, pour finalement étudier la validité des résultats prédits en les comparant aux résultats obtenus via des techniques d'apprentissage automatique (ML) précises mais très chronophages.

Le processus d'optimisation de puissance consiste à trouver la puissance moyenne optimale par bande du booster ($P_{1\mu}$) et sa pente ($P_{1\tau}$) ainsi que les gains nominaux des amplificateurs en ligne par bande (g_μ) et leurs pentes (g_τ) pour maximiser la capacité. La Fig. B.4 montre la topologie généralisée S+C+L considérée pour notre optimisation. Au

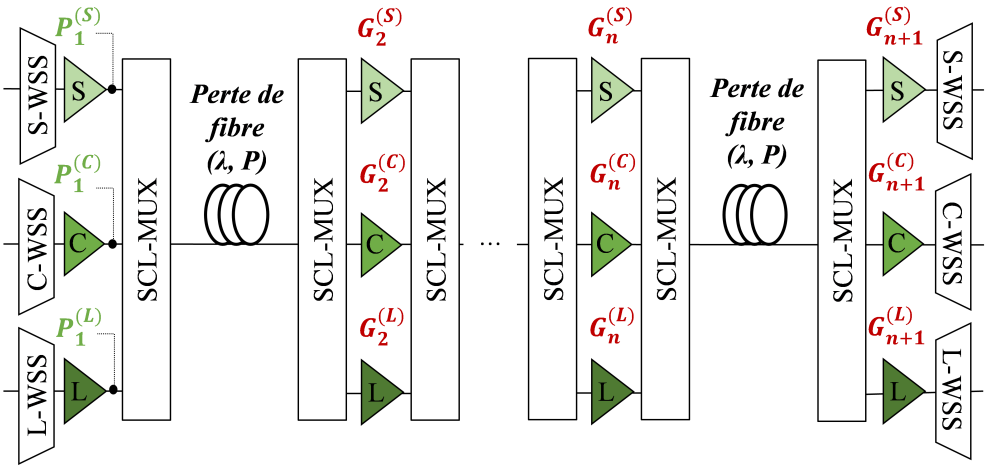

Fig. B.4: Système de transmission S+C+L

début de la ligne de transmission, des commutateurs sélectifs de longueur d'onde (WSS) sont utilisés pour les capacités d'ajout-suppression de canaux ainsi que pour l'égalisation de puissance par canal. Des amplificateurs individuels par bande sont employés pour compenser la perte de fibre et pour ajuster la puissance lancée dans la fibre. Des multiplexeurs/démultiplexeurs SCL sont utilisés à chaque étape d'amplification, ajoutant une perte d'insertion supplémentaire.

La performance SNR de bout en bout de tout canal WDM est obtenue par l'eq. (B.2.1), et correspond au SNR résultant des contributions indépendantes des bruits ASE et NL à chaque section de fibre. Chaque amplificateur est caractérisé par sa NF, son G et ses profils de puissance de sortie (P). Le point clé qui permet à l'heuristique ASE-NL de fonctionner pour les systèmes UWB repose sur le calcul du coefficient non linéaire tenant compte de l'effet ISRS.

Nous effectuons une approche d'optimisation itérative sur N sections, décrite comme suit : Pour la première section (l=0), la puissance de sortie du booster pour chaque bande est initialisée à n'importe quel profil de puissance plat. La puissance d'entrée pour l'étape d'amplification suivante (l+1) est calculée, les amplificateurs l+1 g_μ et g_τ sont réglés pour compenser la perte de fibre par bande. La moyenne et la pente du rapport fréquence dépendant $P_{\mathrm{ASE}}/P_{\mathrm{NL}}$ pour chaque bande sont calculées, à partir desquelles la distance de puissance à l'optimum est dérivée ($\Delta P = [P_{\mathrm{ASE}}/P_{\mathrm{NL}}]_{\mathrm{dB}}/3 - 1$). La puissance moyenne de sortie du booster et son inclinaison sont mises à jour sur la base d'une fraction de ΔP. L'opération est répétée jusqu'à ce que ΔP soit en dessous d'un seuil désiré.

Ce processus est répété séquentiellement pour toutes les sections consécutives. Cependant, de la deuxième sections jusqu'à la fin de la ligne de transmission, ce sont les gains moyens et les inclinaisons de tous les amplificateurs en ligne qui sont optimisés, pour lesquels la puissance de sortie est calculée sur la base de la puissance d'entrée et du gain de l'amplificateur. De même, le $P_{\mathrm{ASE}}/P_{\mathrm{NL}}$ cumulé est estimé pour chaque nouvelle section optimisée.

B.3.1 Validation numérique

Nous comparons notre heuristique rapide et simple à des algorithmes évolutionnaires ML plus complexes, tels que l'algorithme génétique (GA) et l'optimisation par essaim particulaire (PSO). Pour ces optimisations basées sur ML, nous suivons un processus séquentiel cumulé où P_μ, P_τ, g_μ and g_τ sont mis à jour de telle manière que la capacité totale de Shannon soit maximisée. Pour PSO, une descente de gradient (GD) subséquente est utilisée pour la convergence finale.

Nous considérons un système de transmission S+C+L composé de 5 sections SSMF de 80 km. 184 canaux PCS-64QAM de 600 Gbit/s sont distribués avec un espacement de 100 GHz pour une bande passante totale de 18,4 THz. Le NF de tous les amplificateurs est considéré comme étant de 4,5 dB pour simplifier la comparaison des résultats. Les approches basées sur GA et PSO convergent vers des solutions similaires,

menant à des profils de puissance inclinés avec la bande S nécessitant une puissance de sortie d'environ 6,5 dB plus élevée par rapport à la bande L. La *heuristique ASE-NL* conduit à une puissance de lancement supérieure d'environ 0,3/0,4/1,3 dB pour les bandes S/C/L comparée à GA et PSO.

Le SNR total est montré dans la Fig. B.5 indiquant que GA et PSO atteignent un SNR légèrement supérieur par rapport à ASE-NL pour les bandes S et C (environ 0,3 dB), tandis qu'il est globalement diminué pour la bande L avec jusqu'à environ 1 dB de dégradation pour les longueurs d'onde plus élevées. Comparé à l'heuristique ASE-NL, GA et PSO atteignent une perte de portée inférieure dans les bandes S et C tandis qu'elle reste essentiellement inchangée pour la bande L. Les capacités Shannon totales atteintes sont de 225,8/227,6/227,4 Tbit/s pour les approches ASE-NL/GA/PSO respectivement. L'approche heuristique ASE-NL, simple et rapide, conduit à une perte de 0,7 % en capacité totale avec un temps de calcul de 3 minutes en utilisant un ordinateur de bureau standard, tandis que GA et PSO ont chacun mis plus de 24 heures pour s'exécuter sur la même machine.

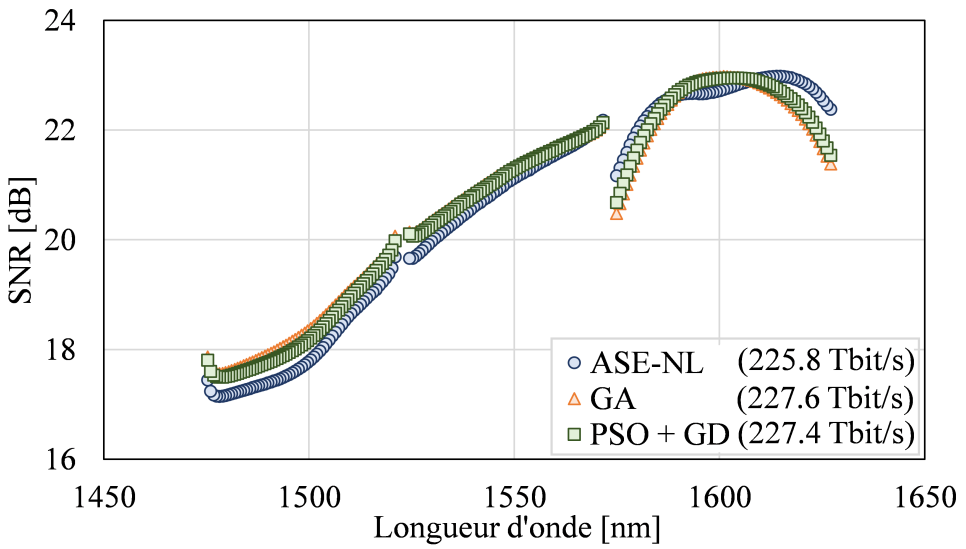

Fig. B.5: SNR et capacité totale atteinte pour l'heuristique ASE-NL (cercles bleus), GA (triangles oranges) et PSO+ GD (carrés verts)

En convergeant vers des solutions optimales basées sur ML, l'heuristique ASE-NL s'est avérée être un outil simple et rapide pour concevoir et reconfigurer des systèmes multi-bandes fortement impactés par l'effet ISRS.

B.3.2 Analyse de capacité dans les systèmes UWB

Dans cette section, nous utilisons cette stratégie d'optimisation pour évaluer, à travers des simulations, le gain de débit par rapport à la bande passante de transmission lorsque des distributions de puissance uniformes et optimisées sont lancées. La transmission consiste en une section de multiplexage optique (OMS) avec 5 *spans* SSMF de 80 km, transmettant

des canaux de 140 Gbaud espacés de 150 GHz. Nous transmettons progressivement des signaux PCS-64QAM sur les bandes C, C+L et S+C+L, en supposant un total de 18 THz de bande passante pour la transmission à triple bande, avec 6 THz par bande. Le système est supposé utiliser des amplificateurs groupés sans ondulation, ayant les NF suivants : 5 dB pour la bande C et 6 dB pour les bandes L et S. Des multiplexeurs et des démultiplexeurs avec une perte d'insertion de 1 dB et 2 dB respectivement, sont utilisés à chaque étape d'amplification.

En utilisant l'heuristique ASE-NL, nous effectuons une optimisation du système pour comparer les gains de capacité de la préaccentuation par rapport au profil de puissance uniforme optimal équivalent, considérant le cas uniforme comme un spectre de puissance plat avec la même puissance par canal (sans préaccentuation). Le tableau B.2 présente la puissance de sortie totale par bande prédite par l'algorithme et le spectre de puissance uniforme qui maximise la capacité totale de Shannon.

Table B.2: Puissance de sortie par bande en utilisant a) une préaccentuation optimisée par l'heuristique ASE-NL et b) un profil de puissance de lancement uniforme.

	a) Préaccentuation (dBm)			b) Uniforme (dBm)		
C	21.8			21.3		
C+L	22.7		19.3	20.8		20.8
S+C+L	24.5	20.9	16.3	19.8	19.8	19.8

Pour la transmission en bande C, la préaccentuation nécessite 0,5 dB de plus de puissance totale que lors du lancement de spectres de puissance uniformes. Un effet similaire est observé dans la transmission C+L, où la puissance totale optimale pour une distribution uniforme est de 23,8 dBm et 24,3 dBm est la puissance totale trouvée par l'heuristique ASE-NL. Néanmoins, pour la bande S+C+L, la puissance totale prédite par l'algorithme est de 26,5 dBm, soit 2 dB de plus que la puissance totale optimale requise par la puissance uniforme. Notamment, la distribution de puissance suggérée par l'algorithme augmente la puissance allouée dans les bandes à longueurs d'onde plus courtes pour faire face aux pertes de fibre plus élevées et à la puissance ISRS transférée aux canaux voisins. Cet effet ISRS accru induit dans la transmission à triple bande explique également la plus grande différence de puissance de lancement totale entre uniforme et préaccentuation.

De plus, la Fig. B.6 quantifie l'augmentation du débit par rapport à la bande passante pour un profil de puissance uniforme (rouge) et une préaccentuation (bleu), montrant que nous doublons presque le débit lorsque nous passons de la bande C à la bande C+L. En ajoutant la bande S, l'augmentation est de 45 %, proche de l'augmentation de 50 % de la bande passante. De plus, dans tous les scénarios, la capacité de débit est plus élevée lors de l'utilisation de la préaccentuation de puissance, étant plus pertinente avec une bande passante plus large. Avec le système S+C+L, l'utilisation de l'optimisation de puissance fournit plus de 10 % d'augmentation de capacité, soulignant l'importance de la préaccentuation de puissance dans les systèmes UWB.

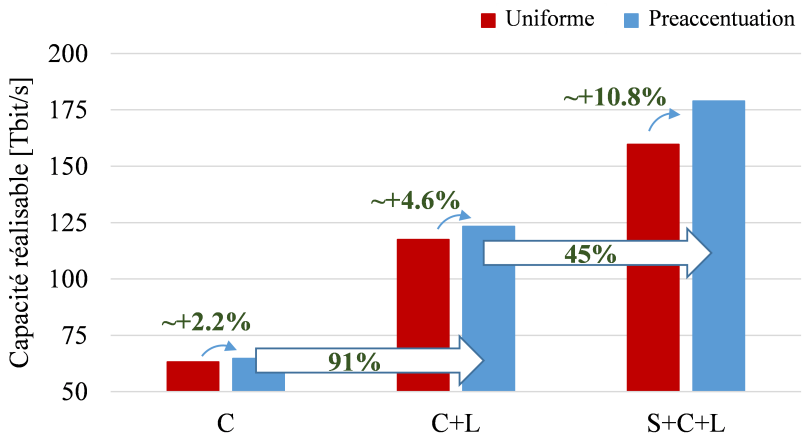

Fig. B.6: Capacité réalisable lors de la transmission d'un spectre de puissance uniforme (rouge) et d'une préaccentuation optimisée (bleu) dans les systèmes C, C+L et S+C+L.

B.3.3 Techniques d'égalisation alternatives

La capacité totale pour la transmission S+C+L lorsque tous les canaux sont optimisés est de 178,9 Tbit/s. Cette haute performance de débit est atteinte en ciblant tous les canaux WDM pour répondre à l'heuristique ASE-NL, qui tente de maximiser la capacité en ciblant un rapport $P_{\mathrm{ASE}}/P_{\mathrm{NL}}$ de 3 dB pour tous les canaux.

Cette section explore l'utilisation de l'heuristique ASE-NL pour introduire deux techniques d'égalisation supplémentaires, adaptées à différents scénarios de transmission :

- L'égalisation intra-bande, qui vise un SNR plat dans chaque bande.
- L'égalisation inter-bandes, qui vise un SNR plat sur toutes les bandes.

Nous pouvons résumer les techniques d'égalisation de la manière suivante : l'heuristique ASE-NL originale vise à maximiser la capacité en appliquant le rapport $P_{\mathrm{ASE}}/P_{\mathrm{NL}}$ de 3 dB à tous les canaux WDM, l'égalisation intra-bande cible un SNR plat dans chaque bande en appliquant le rapport $P_{\mathrm{ASE}}/P_{\mathrm{NL}}$ de 3 dB au pire canal de chaque bande et l'égalisation inter-bandes cible un SNR plat sur toutes les bandes en appliquant le rapport $P_{\mathrm{ASE}}/P_{\mathrm{NL}}$ de 3 dB au pire canal de tout le système. Ces deux préaccentuations supplémentaires ont beaucoup de potentiel dans les scénarios de transmission réalistes, limités aux transpondeurs à débit binaire fixe dans chaque bande ou dans tout le système.

La section suivante est consacrée à la validation expérimentale de notre QoT implémenté et à montrer l'amélioration de capacité obtenue en appliquant l'optimisation ASE-NL précédemment proposée dans un système de transmission S+C+L.

B.4 Modélisation et optimisation des systèmes expérimentaux S+C+L

Les avantages de l'inclusion de stratégies de contrôle de puissance basées sur le modèle ISRS GN pour améliorer les performances du système ont été abordés dans la section précédente. Dans ce chapitre, nous démontrons d'abord la précision de notre outil QoT pour prédire la performance du système UWB de bout en bout, en comparant le débit de données moyen estimé et mesuré par rapport à la puissance de lancement lorsqu'une distribution de puissance d'entrée uniforme est utilisée. Ensuite, nous utilisons notre heuristique ASE-NL pour obtenir la préaccentuation optimisée basée sur la puissance moyenne (P_μ) et la pente (P_τ) pour étudier l'amélioration du débit mesuré dans un système de transmission S+C+L réel.

B.4.1 Configuration expérimentale

La Fig. B.7 montre la configuration expérimentale du système de transmission S+C+L. Une source ASE pour chaque bande est séparément formée par le *waveshaper* de bande S correspondant, les WSS de bande C et L pour émuler respectivement 80 canaux WDM en utilisant une grille de fréquences de 75 GHz dans une bande passante de 6 THz par bande.

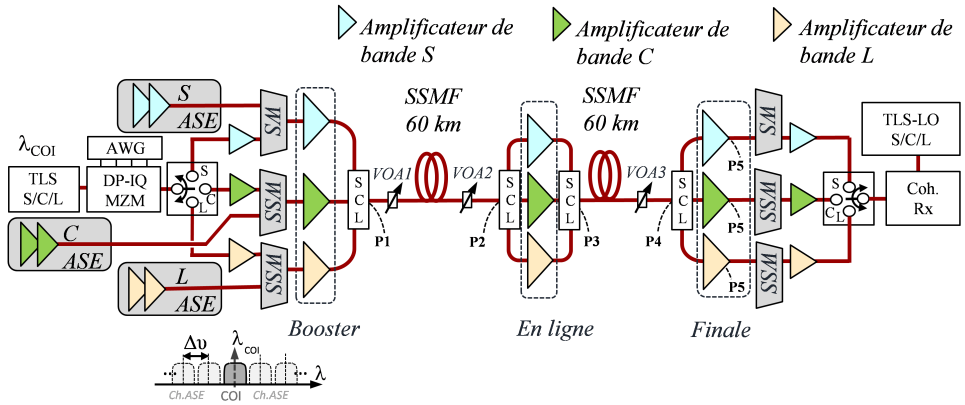

Fig. B.7: Configuration du système de transmission expérimental S+C+L pour évaluer la précision des prédictions de performance basées sur le modèle et l'heuristique ASE-NL.

Pour le COI, nous utilisons un signal PCS-256QAM de 60 Gbaud. Chaque bande est amplifiée à travers son amplificateur booster correspondant pour être ensuite multiplexée par un multiplexeur SCL. La puissance de sortie totale et le profil de puissance de sortie à l'entrée de la fibre sont ajustés par un atténuateur optique variable (VOA) et des WSS respectivement. La transmission consiste en 2 sections SSMF de 60 km. Des amplificateurs à base de fibre sont utilisés pour les bandes S et C, tandis que les SOA opèrent dans la bande L.

Le SNR de 15 canaux au total, 5 par bande, est estimé. Nous utilisons l'information mutuelle généralisée (GMI) pour estimer les débits

de données totaux. Nous multiplions le GMI de chaque canal en utilisant 60 Gbaud en considérant 2 polarisations et en tenant compte de l'overhead des pilotes de 63/64. Un jumelage numérique initial est effectué après la propagation de spectres de puissance uniformes à 25,4, 24,2, 23,2, 22,2 et 21,4 dBm, visant à caractériser les éléments du système de transmission, tels que le NF des amplificateurs, estimé à partir des mesures OSNR à P2 et P3. Ces paramètres, et les mesures de spectre de puissance obtenues avec l'analyseur de spectre optique (OSA) à P1 et P3 sont des entrées pour le modèle, pour calculer le SNR des 240 canaux transmis. Les estimations de notre modélisation sont précises, avec une erreur de simulation inférieure à 0,4 % pour les cinq puissances totales mesurées. Les simulations et les expériences convergent vers une puissance optimale de 23,2 dBm.

B.4.2 Optimisation de puissance et résultats expérimentaux

Une fois les paramètres de simulation alignés sur les éléments physiques de transmission, nous réalisons l'optimisation de la puissance par canal basée sur l'heuristique ASE-NL. Puisque l'heuristique ASE-NL repose sur une implémentation en python du modèle en forme fermée ISRS GN rapide, cela ne prend qu'environ 4 minutes pour optimiser le système étudié. Comme prévu, pour la préaccentuation optimisée une puissance plus élevée est allouée dans la bande S pour compenser l'effet ISRS et les pertes de fibre plus importantes, tandis que les bandes C et L requièrent une puissance de lancement inférieure.

Enfin, nous avons configuré le booster et les amplificateurs en ligne pour fonctionner avec les puissances et gains prédits par bande. Encore une fois, la performance de 15 canaux est mesurée et comparée avec le SNR optimisé prédit par notre heuristique ASE-NL. Grâce au jumelage numérique, nous obtenons de très bonnes prédictions, avec une erreur de

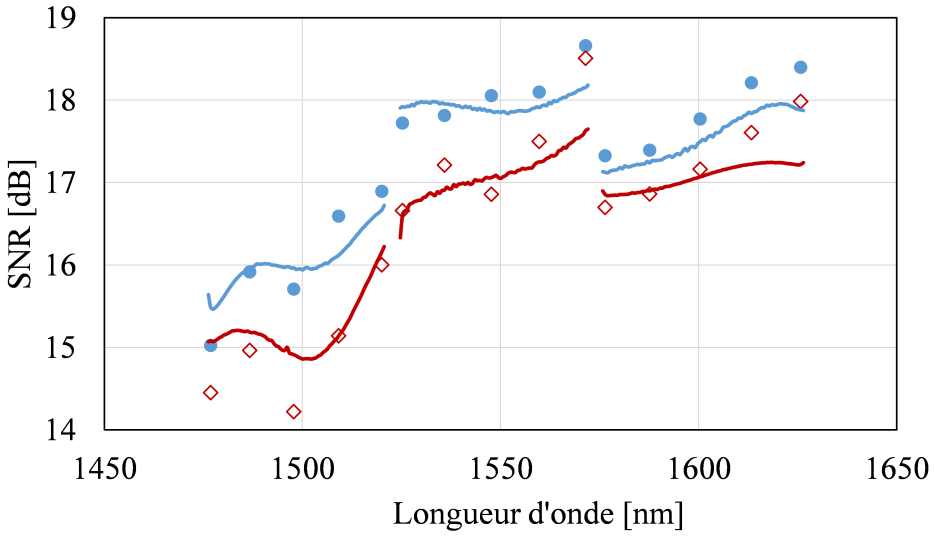

Fig. B.8: SNR mesuré (marqueurs) et estimé (lignes) pour la préaccentuation optimisée (bleu) et la distribution de puissance uniforme (rouge).

simulation maximale de 0,5 dB. Pour évaluer les avantages de la préaccentuation optimisée, nous comparons la capacité atteinte avec la puissance de lancement uniforme équivalente précédemment mesurée à 24,2 dBm, profil rouge dans la Fig. B.8.

La Figure B.8 trace le SNR mesuré (marqueurs) et prédit (lignes) pour les deux profils de puissance d'entrée. Tant les mesures que la simulation montrent une amélioration pour tous les canaux, ayant un gain maximal de 1,6 dB pour nos prédictions et 1,5 dB dans les résultats expérimentaux. La performance est améliorée pour tous les canaux, conduisant à une augmentation de capacité de 154,9 Tbit/s à 161,2 Tbit/s ; l'algorithme ASE-NL se révèle donc être une bonne stratégie pour prédire la puissance optimale totale et par canal.

B.5 Défaillance de l'amplificateur : Impact de la perte d'une bande

Les systèmes multi-bandes sont vulnérables aux défaillances des amplificateurs de bande. Ces interruptions peuvent ensuite compromettre la performance globale des bandes non affectées en raison des variations de puissance impactant l'ISRS. D'où l'importance d'explorer les répercussions des pertes de bandes WDM dans les systèmes UWB. Cette section présente les résultats expérimentaux d'une transmission S+C+L sur 2 sections de 60 km en SSMF.

Pour évaluer l'impact de la défaillance du système et des variations d'ISRS, nous désactivons soit la bande S soit la bande L et mesurons la performance SNR tout en maintenant tous les paramètres opérationnels identiques à ceux de la transmission S+C+L. De plus, nous réalisons une analyse comparative de la distribution du débit GMI pour chaque cas afin d'évaluer quantitativement l'effet sur la capacité du système.

La génération du signal au niveau de l'émetteur, du récepteur et du DSP suit la méthodologie décrite dans la section précédente, avec la distinction que dans ce scénario, le COI fonctionne à un débit en bauds plus élevé de 70 Gbaud. La configuration expérimentale est similaire à l'expérience précédente, consistant en 2 sections SSMF de 60 km. La préaccentuation de puissance du canal à P1 est optimisée par l'heuristique ASE-NL. Le COI balaie tous les bandes en utilisant cinq canaux de test par bande pour obtenir une estimation de la performance de transmission.

Pour analyser l'impact de la perte d'une bande, nous éteignons la bande S ou la bande L et mesurons la performance de transmission tout en gardant tous les paramètres opérationnels identiques à ceux du système de transmission S+C+L. La distribution de puissance totale pour le cas S+C+L est allouée comme suit : 52,4 % dans la bande S, 30,9 % dans la bande C et les 16,7 % restants dans la bande L. Cela signifie que lorsque la bande S est perdue, la puissance totale diminue jusqu'à 52,4 %, réduisant considérablement le transfert de puissance ISRS. D'autre part, après la perte de la bande L, les bandes S et C subissent une plus faible

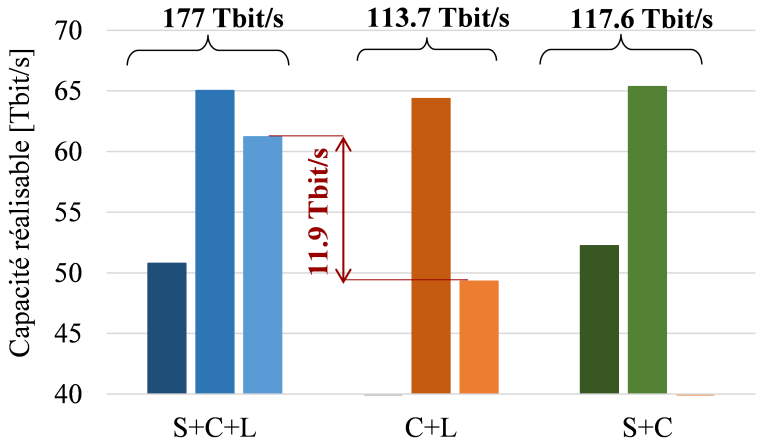

Fig. B.9: Capacité réalisable avant (gauche), après la perte de la bande S (milieu) et après la perte de la bande L (droite).

span-loss de sorte que l'OSNR et le SNR sont légèrement meilleurs qu'auparavant.

Pour quantifier l'impact sur la capacité lorsque la bande S ou la bande L manque, la Fig. B.9 présente la distribution du débit estimée basée sur le GMI de chaque bande. À l'origine, avec la transmission S+C+L, un débit total de 177 Tbit/s est estimé. Suite à la perte de la bande S, le débit pour la bande C reste presque inchangé par rapport à avant, tandis que le débit GMI pour la bande L diminue significativement de 11,9 Tbit/s, comme souligné en rouge dans la Fig. B.9. La capacité totale après la perte de la bande S est de 113,7 Tbit/s. Cela représente une diminution de 36 % de la capacité totale par rapport à la transmission S+C+L initiale.

Dans le cas de la perte de la bande L, les débits dans les bandes S et C sont légèrement supérieurs à ceux d'avant la défaillance, conduisant à un capacité totale de 117,6 Tbit/s. Bien que dans ce cas l'augmentation de puissance produise un gain de SNR pour les transmissions avec plus de sections, l'augmentation de puissance en plus du gain de chaque amplificateur pourrait conduire à des niveaux très élevés de puissance entrant dans les fibres suivantes, dégradant la performance du système.

B.6 Conclusions

Les démonstrations récentes ont montré que les systèmes UWB peuvent atteindre des transmissions de haute capacité. Comme détaillé dans la Section B.3, pour exploiter pleinement les avantages de la transmission multi-bandes, il est essentiel d'appliquer des techniques d'optimisation de puissance qui tiennent compte des effets ISRS et dépendants de la longueur d'onde. De plus, nous avons proposé deux stratégies d'égalisation alternatives qui reposent sur l'heuristique glsase-NL, l'égalisation intra-bande, qui optimise le pire canal par bande, visant un SNR plat pour chaque bande, et l'égalisation inter-bande, qui optimise le pire canal de tout le système pour obtenir un SNR plat à travers toutes les bandes.

L'heuristique ASE-NL a démontré son efficacité dans les scénarios de transmission S+C+L, s'alignant étroitement sur les solutions optimisées fournies par des simulations basées sur ML plus complexes. Cependant, il existe certains cas où l'efficacité de l'heuristique est limitée, et d'autres scénarios qui nécessitent une investigation plus poussée. Certaines limitations proviennent des modèles théoriques sur lesquels l'heuristique est basée. Par exemple, tout comme le modèle GN, les transmissions de très courtes portées avec une faible dispersion mettront au défi la précision de l'heuristique. D'autre part, il existe certains scénarios où l'utilisation de l'heuristique ASE-NL ne sera pas si bénéfique, comme dans le cas des transmissions qui sont principalement contraintes par les pénalités du transpondeur. Notre modèle d'optimisation suppose que la puissance de lancement optimale est indépendante du bruit du transceiver, ces pénalités sortent donc du cadre d'application visé.

Dans la Section B.4, grâce à la calibration du modèle avec les données expérimentales, notre outil QoT a obtenu des prédictions fiables des débits de données moyens pour diverses distributions de puissance uniformes, avec une erreur de simulation inférieure à 0,4 % pour tous les cas mesurés. De plus, les données collectées ont été utilisées comme entrée pour la validation de notre heuristique glsase-NL proposée pour optimiser la distribution de puissance d'un système S+C+L. Nous avons présenté l'efficacité de l'heuristique glsase-NL dans l'amélioration des performances du système, particulièrement en termes d'augmentation de la capacité, montrant un gain de 6,2 Tbit/s dans le débit GMI mesuré comparé à une distribution de puissance uniforme avec la même puissance totale. La validation expérimentale de l'heuristique glsase-NL ne se réfère pas seulement à la précision des prédictions lorsque les paramètres optimisés sont configurés, mais aussi au gain de capacité mesuré de cette préaccentuation de puissance comparée à des spectres de puissance uniformes.

De plus, cette section souligne l'importance de considérer la défaillance de l'amplificateur puisque son impact dépasse la bande directement affectée par la défaillance, affectant également les bandes restantes. Pour ces cas, des systèmes de récupération devraient être considérés pour atténuer les risques sur la performance du système.

En outre, la maturité actuelle de l'écosystème représente un défi clé dans le déploiement sur le terrain des systèmes S+C+L. Bien que l'adoption par l'industrie des systèmes C+L ait motivé la viabilité économique des systèmes UWB, les coûts supplémentaires nécessaires pour supporter les bandes S+C+L mettent en danger le déploiement de la technologie.

Nous croyons que le succès durable des systèmes UWB repose sur l'évolution des générations futures de la technologie, nécessitant une intégration améliorée de l'architecture système et une réduction des coûts. Néanmoins, à moyen terme, les systèmes UWB représentent une étape intermédiaire vers l'augmentation de la capacité avant l'installation de nouvelles fibres. De plus, ils continueront d'être une solution viable dans les scénarios où des transmissions parallèles ne peuvent pas être effectuées en raison de l'absence de fibres disponibles ou lorsque les opérateurs louent leurs fibres et ne peuvent pas déployer de nouveaux câbles.

Bibliography

[1] I. Hayashi, M. B. Panish, P. W. Foy, and S. Sumski. “Junction Lasers which Operate Continuously at Room Temperature”. *Applied Physics Letters* vol. 17 (1970), pp. 109–111. DOI: 10.1063/1.1653326.

[2] T. Miya, Y. Terunuma, T. Hosaka, and T. Miyashita. “Ultimate low-loss single-mode fibre at 1.55 µm”. *Electronics Letters (IET)* vol. 15 (1979), pp. 106–108.

[3] E. Desurvire, J. R. Simpson, and P. C. Becker. “High-gain erbium-doped traveling-wave fiber amplifier”. *Optics Letters* vol. 12 (1987), pp. 888–890.

[4] R.J. Mears, L. Reekie, Jauncey I.M., and D.N. Payne. “Low-Noise Erbium-Doped Fiber Amplifier Operating at 1.54 m”. *Electronics Letters* vol. 23 (1987), pp. 1026–102. DOI: 10.1049/el:19870719.

[5] H. Sun, K.T. Wu, and K. Roberts. “Real-time measurements of a 40 Gb/s coherent system”. *Optics Express* vol. 16 (2008), pp. 873–879. DOI: 10.1364/OE.16.000873.

[6] S. Aisawa, T. Sakamoto, M. Fukui, et al. “Ultra-wide band, long distance WDM transmission demonstration: 1 Tb/s (50 x 20 Gb/s), 600 km transmission using 1550 and 1580 nm wavelength bands”. *Optical Fiber Communication Conference (OFC)* (1998), paper PD11.

[7] A.K. Srivastaval, Y. Sun, et al. “1Tb/s Transmission of 100 WDM 10 Gb/s Channels Over 400 km of TrueWaveTM Fiber”. *Optical Fiber Communication Conference (OFC)* (1998), paper PD10.

[8] K. Fukuchi, T. Kasamatsu, M. Morie, et al. “10.92-Tb/s (273 x 40-Gb/s) triple-band/ultra-dense WDM optical-repeatered transmission experiment”. *Optical Fiber Communication Conference and International Conference on Quantum Information* (2001), paper PD24.

[9] A. Sano, T. Kobayashi, S. Yamanaka, et al. “102.3-Tb/s (224 x 548-Gb/s) C- and extended L-band all-Raman transmission over 240 km using PDM-64QAM single carrier FDM with digital pilot tone”. *Optical Fiber Communication Conference (OFC)* (2012), paper PDPSC.3.

[10] M. Zuo, D. Zhang, H. Zou, et al. "Field Trial of Real-time 80-λ x 400-Gb/s Single-carrier 128-GBd DP-QPSK Transmission Covering 12-THz C+L Band over 2502-km Terrestrial G.652.D Fibre". *European Conference on Optical Communication (ECOC)* (2023), paper M.A.5.3.

[11] D. Ge, M. Zuo, H. Liu, L. Gan, D. Wang, Y. Chen, D. Zhang, Q. Guo, and H. Li. "Fully-loaded 80x400Gb/s DP-QPSK Transmission with Commercial 12 THz C6T-L6T EDFAs over Record Distance of 7000km". *Asia Communications and Photonics Conference (ACP)* (2023), paper ACPPOEM-0930–2.

[12] F. Hamaoka, K. Minoguchi, et al. "150.3-Tb/s Ultra-Wideband (S, C, and L bands) Single-Mode Fibre Transmission over 40-km Using > 519 Gb/s/A PDM128QAM Signals". *European Conference on Optical Communication (ECOC)* (2018). DOI: 10.1109/ECOC.2018.853514.

[13] L. Galdino, A. Edwards, W. Yi, E. Sillekens, Y. Wakayama, T. Gerard, W. S. Pelouch, S. Barnes, T. Tsuritani, R. I. Killey, D. Lavery, and P. Bayvel. "Optical Fibre Capacity Optimisation via Continuous Bandwidth Amplification and Geometric Shaping". *IEEE Photonics Technology Letters* vol. 32.17 (2020), pp. 1021–1024. DOI: 10.1109/LPT.2020.3007591.

[14] B. J. Puttnam, R. S. Luís, G. Rademacher, et al. "S, C and Extended L-Band Transmission with Doped Fiber and Distributed Raman Amplification". *Optical Fiber Communications Conference and Exhibition (OFC)* (2021).

[15] B. J. Puttnam, R. S. Luís, G. Rademacher, M. Mendez-Astudilio, Y. Awaji, and H. Furukawa. "S-, C- and L-band transmission over a 157nm bandwidth using doped fiber and distributed Raman amplification". *Optics Express* 30.6 (2022), pp. 10011–10018. DOI: 10.1364/OE.448837.

[16] B. J. Puttnam, R. S. Luís, G. Rademacher, Y. Awaji, and H. Furukawa. "1 Pb/s Transmission in a 125μm diameter 4-core MCF". *Conference on Lasers and Electro-Optics* (2022), paper JTh6B.1.

[17] X. Zhang, M. Luo, J. Liu, D. Chen, Q. He, H. Ji, Y. Wu, P. Du, L. Mei, Y. Wang, H. Zhang, L. Wang, Z. He, X. Xiao, and S. Yu. "214.7 Tbit/s S, C, and L-band transmission over 50km SSMF based on silicon photonic integrated transceivers". *Optics Express* 31.25 (2023), pp. 41546–41555. DOI: 10.1364/OE.505912.

[18] F. Hamaoka, K. Saito, Ak. Masuda, H. Taniguchi, T. Sasai, M. Nakamura, T. Kobayashi, and Y. Kisaka. "112.8-Tb/s Real-Time Transmission over 101 km in 16.95-THz Triple-Band (S, C, and L Bands) WDM Configuration". *OptoElectronics and Communications Conference (OECC) and International Conference on Photonics in Switching and Computing (PSC)* (2022). DOI: 10.23919/OECC/PSC53152.2022.9849881.

[19] B. J. Puttnam, R. S. Luís, G. Rademacher, Y. Awaji, and H. Furukawa. "319 Tb/s Transmission over 3001 km with S, C and L band signals over >120nm bandwidth in 125 m wide 4-core fiber" (2021), paper F3B.3.

[20] B. J. Puttnam, R. S. Luís, G. Rademacher, Y. Awaji, and H. Furukawa. "Investigation of Long-Haul S-, C- + L-Band Transmission" (2022).

[21] B. Puttnam, R. Luis, Y. Huang, I. Phillips, et al. "264.7 Tb/s E, S, C + L-Band Transmission Over 200 km". *Optical Fiber Communication Conference (OFC)* (2024), paper M1F.4.

[22] B. J. Puttnam, R. S. Luís, Y. Huang, I Phillips, D. Chung, N.K. Fontaine, G. Rademacher, M. Mazur, L. Dallachiesa, H. Chen, W. Forysiak, R. Man, R. Ryf, D.T Neilson, and H. Furukawa. "301 Tb/s E, S, C+L-Band Transmission over 212 nm bandwidth with E-band Bismuth-Doped Fiber Amplifier and Gain Equalizer" (2023), paper Th.C.2.4.

[23] P. Poggiolini and M. Ranjbar-Zefreh. "Closed Form Expressions of the Nonlinear Interference for UWB Systems". *European Conference on Optical Communication (ECOC)* (2022), paper Tu1D.1.

[24] K. Roberts, Chuandong Li, L. Strawczynski, M. O'Sullivan, and I. Hardcastle. "Electronic precompensation of optical nonlinearity". *IEEE Photonics Technology Letters* vol. 18.2 (2006), pp. 403–405. DOI: 10.1109/LPT.2005.862360.

[25] G. Böcherer et al. "Bandwidth Efficient and Rate-Matched Low-Density Parity-Check Coded Modulation". *IEEE Transactions on Communications* vol. 63.12 (2015), pp. 4651–4665. DOI: 10.1109/TCOMM.2015.2494016.

[26] F. Buchali, F. Steiner, et al. "Rate Adaptation and Reach Increase by Probabilistically Shaped 64-QAM: An Experimental Demonstration". *Journal of Lightwave Technology (JLT)* vol. 34.7 (2016), pp. 1599–1609. DOI: 10.1109/JLT.2015.2510034.

[27] G. P. Agrawal. "Optical communication: its history and recent progress". *Optics in our time* (2016), pp. 177–199.

[28] C. E. Shannon. "A mathematical theory of communication". *The Bell System Technical Journal* vol. 27.3 (1948), pp. 379–423. DOI: 10.1002/j.1538-7305.1948.tb01338.x.

[29] S Shimizu, T. Kobayashi, et al. "38.4-Tbps Inline-amplified Transmission Using PPLN-based Optical Parametric Amplifier over 6 THz within L- and U-bands". *Optical Fiber Communication Conference (OFC)* (2023), paper Th3F.3. DOI: 10.1364/OFC.2023.Th3F.3.

[30] N. Taengnoi, K. Bottrill, et al. "Coherent O-band Transmission of 4×25 GBd DP-16QAM Channels Over a 50 km BDFA-Equipped Link". *Optical Fiber Communication Conference (OFC)* (2023), paper Th3F.5. DOI: 10.1364/OFC.2023.Th3F.5.

[31] D. Soma, T. Kato, S. Beppu, et al. “25-THz O+S+C+L+U-Band Digital Coherent DWDM Transmission Using a Deployed Fibre-Optic Cable”. *European Conference on Optical Communication (ECOC)* (2023), paper Th.C.2.2.

[32] Y. Yamamoto, Y. Kawaguchi, and M. Hirano. “Low-Loss and Low-Nonlinearity Pure-Silica-Core Fiber for C- and L-band Broadband Transmission”. *Journal of Lightwave Technology* vol. 34.2 (2016), pp. 321–326. DOI: 10.1109/JLT.2015.2476837.

[33] Y. Kawaguchi, Y. Tamura, T. Haruna, Y. Yamamoto, and M. Hirano. *Ultra Low-loss Pure Silica Core Fiber*. [Accessed 03 2024]. 2015. URL: https://sumitomoelectric.com/sites/default/files/2020-12/download_documents/80-11.pdf.

[34] G.P. Agrawal. “Non-Linear Fiber Optics”. *Academic Press* (2012), 5th edition.

[35] D. Semrau. “Physical Layer Modelling of Optical Fibre Communication Systems in the Nonlinear Regime”. PhD thesis. University College London (UCL), 2020.

[36] P. Geittner et al. “Dispersion-modified single-mode fibers”. *Optical Fiber Communication Conference (OFC)* (1988), paper WI1.

[37] A. Bononi, R. Dar, et al. “Fiber Nonlinearity and Optical System Performance.” *Springer Handbook of Optical Networks. Springer Handbooks.* (2020), pp. 287–351. DOI: 10.1007/978-3-030-16250-4_9.

[38] A. Carena, V. Curri, G. Bosco, P. Poggiolini, and F. Forghieri. “Modeling of the Impact of Nonlinear Propagation Effects in Uncompensated Optical Coherent Transmission Links”. *Journal of Lightwave Technology (JLT)* vol. 30.10 (2012), pp. 1524–1539. DOI: 10.1109/JLT.2012.2189198.

[39] A. Splett, C. Kurzke, and K. Petermann. “Ultimate transmission capacity of amplified optical fiber communication systems taking into account fiber nonlinearities.” *European Conference on Optical Communication (ECOC)* (1993), pp. 41–44.

[40] P. Poggiolini, A. Carena, V. Curri, G. Bosco, and F. Forghieri. “Analytical Modeling of Nonlinear Propagation in Uncompensated Optical Transmission Links”. *IEEE Photonics Technology Letters* vol. 23.11 (2011), pp. 742–744. DOI: 10.1109/LPT.2011.2131125.

[41] J. Bromage. “Raman amplification for fiber communications systems”. *Journal of Lightwave Technology* vol. 22 (2004), pp. 79–93. DOI: 10.1109/JLT.2003.822828.

[42] M. Vasilyev and S. Radic. “Optical Amplifiers.” *Springer Handbook of Optical Networks. Springer Handbooks.* (2020), pp. 51–78.

[43] A. R. Chraplyvy. “Optical power limits in multi-channel wavelength division-multiplexed systems due to stimulated Raman scattering”. *Electronics Letters* vol. 20 (1984), pp. 58–59.

[44] D. Semrau, R. I. Killey, and P. Bayvel. "The Gaussian Noise Model in the Presence of Inter-Channel Stimulated Raman Scattering". *Journal of Lightwave Technology(JLT)* vol. 36.14 (2018), pp. 3046–3055.

[45] I. Roberts, J. M. Kahn, J. Harley, and D. W. Boertjes. "Channel Power Optimization of WDM Systems Following Gaussian Noise Nonlinearity Model in Presence of Stimulated Raman Scattering". *Journal of Lightwave Technology (JLT)* vol. 35 (2017), pp. 5237–5249.

[46] M. Cantono, J. L. Auge, and V. Curri. "Modelling the Impact of SRS on NLI Generation in Commercial Equipment: An Experimental Investigation". *Optical Fiber Communications Conference and Exposition (OFC)* (2018).

[47] C. Lasagni, P. Serena, A. Bononi, and J-C. Antona. "Generalized Raman Scattering Model and Its Application to Closed-Form GN Model Expressions Beyond the C+L Band". *European Conference on Optical Communication (ECOC)* (2022).

[48] M. Ranjbar Zefreh, F. Forghieri, S. Piciaccia, and P. Poggiolini. "Accurate Closed-Form Real-Time EGN Model Formula Leveraging Machine-Learning Over 8500 Thoroughly Randomized Full C-Band Systems". *Journal of Lightwave Technology (JLT)* vol. 38 (2020), pp. 4987–4999.

[49] D. Uzunidis, K. Nikolaou, C. Matrakidis, A. Stavdas, and A. Lord. "Closed-form Expressions for the Impact of Stimulated Raman Scattering Beyond 15 THz" (2022).

[50] Huawei. *Super C+L band.* [Accessed 02 2024]. June 2023. URL: https://forum.huawei.com/enterprise/en/super-c-l-band-system/thread/670722732209356800-667213856692383744.

[51] Infinera. *Double fiber capacity with a comprehensive C+L solution.* [Accessed 02 2024]. 2023. URL: https://www.infinera.com/wp-content/uploads/Infinera-C-Plus-L-Solution-0345-AN-RevA-0623.pdf.

[52] Accelink. *Accelink press release Super C and Super L transmission device solutions at OFC.* [Accessed 02 2024]. 2021. URL: https://www.ofcconference.org/library/exhibits/OFC/2021/pdfs/913677-pr-pressRelease2.pdf.

[53] H. Ono, M. Yamada, and Y. Ohishi. "Gain-flattened Er/sup 3+/-doped fiber amplifier for a WDM signal in the 1.57-1.60-m wavelength region". *IEEE Photonics Technology Letters* vol. 9 (1997), pp. 596–598. DOI: 10.1109/68.588134.

[54] Amonics. *L Band and Extended L band DWDM EDFA.* [Accessed 02 2024]. 2023. URL: https://www.amonics.com/product/5.

[55] Accelink. *L++ EDFA.* [Accessed 02 2024]. 2022. URL: https://www.accelink.com/en/lighting_your_dreams/products_optical-amplifiers/416.html.

[56] J. B. Rosolem, A. A. Juriollo, and M. A. Romero. "S Band EDFA Using Standard Erbium Doped Fiber, 1450 nm Pumping and Single Stage ASE Filtering" (2008). DOI: 10.1109/OFC.2008.4528644.

[57] C. Brian and M. L. Dennis. "S-band amplification in a thulium doped silicate fiber". *Optical Fiber Communication Conference and International Conference on Quantum Information* (2001), paper TuQ3. DOI: 10.1364/OFC.2001.TuQ3.

[58] A. Donodin, V. Dvoyrin, E. Manuylovich, Krzczanowicz L., W. Forysiak, M. Melkumov, V. Mashinsky, and S. Turitsyn. "Bismuth doped fibre amplifier operating in E- and S- optical bands". *Optical Material Express* vol. 11.1 (2021), pp. 127–135. DOI: 10.1364/OME.411466.

[59] S. Firstov, S. Alyshev, M. Melkumov, K. Riumkin, A. Shubin, and E. Dianov. "Bismuth-doped optical fibers and fiber lasers for a spectral region of 1600-1800nm". *Optics Letters* vol. 39.24 (2014), pp. 6927–6930. DOI: 10.1364/OL.39.006927.

[60] J. Renaudier, A. Carbo Meseguer, et al. "First 100-nm Continuous-Band WDM Transmission System with 115Tb/s Transport over 100km Using Novel Ultra-Wideband Semiconductor Optical Amplifiers". *European Conference on Optical Communication (ECOC)* (2017). DOI: 10.1109/ECOC.2017.8346084.

[61] S. Yu. "Semiconductor optical amplifiers for future telecom systems". PhD thesis. Institut Polytechnique de Paris, 2024.

[62] C. V. Raman and K. S. Krishnan. "A New Type of Secondary Radiation". *Nature* vol. 121 (1928), pp. 501–502. DOI: 10.1038/121501c0.

[63] P.B Hansen and L. Eskildsen. "Remote Amplification in Repeaterless Transmission Systems". *Optical Fiber Technology* vol. 3 (1997), pp. 221–237.

[64] M. Ionescu, L. Galdino, et al. "91 nm C+L Hybrid Distributed Raman Erbium- Doped Fibre Amplifier for High Capacity Subsea Transmission" (2018). DOI: 10.1109/ECOC.2018.8535151.

[65] A. Ghazisaeidi, A. Arnould, M. Ionescu, V. Aref, H. Mardoyan, S. Etienne, M. Duval, C. Bastide, H. Bissessur, and J. Renaudier. "99.35 Tb/s Ultra-wideband Unrepeated Transmission Over 257 km Using Semiconductor Optical Amplifiers and Distributed Raman Amplification". *Journal of Lightwave Technology* vol. 40.21 (2022), pp. 7014–7019. DOI: 10.1109/JLT.2022.3198518.

[66] L. Lundberg, P. A. Andrekson, and M. Karlsson. "Power Consumption Analysis of Hybrid EDFA/Raman Amplifiers in Long-Haul Transmission Systems". *Journal of Lightwave Technology* vol. 35 (2017), pp. 2132–2142. DOI: 10.1109/JLT.2017.2668768.

[67] G. Bosco and J.P. Elbers. "Optical Transponders." *Springer Handbook of Optical Networks. Springer Handbooks.* (2020), pp. 83–136.

[68] M. S. Faruk and S. J. Savory. "Digital Signal Processing for Coherent Transceivers Employing Multilevel Formats." *Journal of Lightwave Technology* vol. 35.5 (2017), pp. 1125–1141. DOI: 10.1109/JLT.2017.2662319.

[69] J. Conçalves, F.P Guiomar, C.S Martins, T.R Cunha, J.C. Pedro, A.N. Pinto, and P.M. Lavrador. "Nonlinear compensation with DBP aided by a memory polynomial". *Optics Express* vol. 24.26 (2016), pp. 30309–30316. DOI: 10.1364/OE.24.030309.

[70] L. Galdino, D. Semrau, D. Lavery, G. Saavedra, C.B Czegledi, E. Agrell, R.I. Killey, and P. Bayvel. "On the limits of digital back-propagation in the presence of transceiver noise". *Optics Express* vol. 25.4 (2017), pp. 4564–4578. DOI: 10.1364/OE.25.004564.

[71] Z. Tao, L. Dou, W. Yan, T. Li L.and Hoshida, and J. C. Rasmussen. "Multiplier-Free Intrachannel Nonlinearity Compensating Algorithm Operating at Symbol Rate". *Journal of Lightwave Technology (JLT)* vol. 29.17 (2011), pp. 2570–2576. DOI: 10.1109/JLT.2011.2160933.

[72] G. Khanna, B. Spinnler, S. Calabrò, E. De Man, and N. Hanik. "A Robust Adaptive Pre-Distortion Method for Optical Communication Transmitters". *IEEE Photonics Technology Letters* vol. 28.7 (2016), pp. 752–755. DOI: 10.1109/LPT.2015.2509158.

[73] I. Fernandez de Jauregui Ruiz. "Advanced modulation formats and nonlinear mitigation for spectral efficient optical transmission systems." PhD thesis. Networking and Internet Architecture [cs.NI]. Institut National des Télécommunications, 2018.

[74] H. A. Haus. "The Proper Definition of Noise Figure of Optical Amplifiers". *Optical Amplifiers and Their Applications* (2000), paper OMB7. DOI: 10.1364/OAA.2000.OMB7.

[75] A. Alvarado, E. Agrell, D. Lavery, R. Maher, and P. Bayvel. "Replacing the Soft-Decision FEC Limit Paradigm in the Design of Optical Communication Systems". *Journal of Lightwave Technology (JLT)* vol. 34.2 (2016), pp. 707–721. DOI: 10.1109/JLT.2015.2482718.

[76] S. Zhang and F. Yaman. "Design and Comparison of Advanced Modulation Formats Based on Generalized Mutual Information". *Journal of Lightwave Technology (JLT)* vol. 36.2 (2018), pp. 416–423. DOI: 10.1109/JLT.2017.2779753.

[77] J. Kundrát, E. L. Rouzic, J. Mårtensson, et al. "GNPy: Lessons Learned and Future Plans [Invited]". *European Conference on Optical Communication (ECOC)* (2022), paper We3B.6.

[78] N. Morette, H. Hafermann, Y. Frignac, and Y. Pointurier. "Machine learning enhancement of a digital twin for wavelength division multiplexing network performance prediction leveraging quality of transmission parameter refinement". *Journal of Optical Communications and Networking (JCON)* vol. 15.6 (2023), pp. 333–343. DOI: 10.1364/JOCN.487870.

[79] I. Fernandez de Jauregui Ruiz, A. Ghazisaeidi, T. Zami, S. Louis, and B. Lavigne. "An accurate model for system performance analysis of optical fibre networks with in-line filtering". *European Conference on Optical Communication (ECOC)* (2019).

[80] S. Escobar-Landero. "Capacity maximization and modeling of ultra-wide band WDM Optical Systems". MA thesis. Aston University, 2020.

[81] N. Morette, I. F. Jauregui Ruiz, and Y. Pointurier. "Leveraging ML-based QoT Tool Parameter Feeding for Accurate WDM Network Performance Prediction". *Optical Fiber Communications Conference and Exhibition (OFC)* (2021), paper Th4J.4.

[82] R. J. Essiambre and R. W. Tkach. "Capacity Trends and Limits of Optical Communication Networks". *Proceedings of the IEEE* vol. 100.5 (2012), pp. 1035–1055. DOI: 10.1109/JPROC.2012.2182970.

[83] P. Poggiolini, G. Bosco, A. Carena, et al. "The GN-Model of Fiber Non-Linear Propagation and its Applications". *Journal of Lightwave Technology (JLT)* vol. 32 (2014).

[84] P. Poggiolini. "The GN Model of Non-Linear Propagation in Uncompensated Coherent Optical Systems". *Journal of Lightwave Technology (JLT)* vol. 30 (2012), pp. 3857–3879.

[85] F. Zhang, Q. Zhuge, and D. V. Plant. "Fast Analytical Evaluation of Fiber Nonlinear Noise Variance in Mesh Optical Networks". *Journal of Optical Communications and Networking (JCON)* vol. 9 (2017).

[86] P. Poggiolini. "A Closed-Form GN-Model Non-Linear Interference Coherence Term" (2020).

[87] G. Bosco. "Complexity Versus Accuracy Tradeoffs in Nonlinear Fiber Propagation Models". *Optical Fiber Communications Conference (OFC)* (2023).

[88] G. Bosco, A. Carena, R. Cigliutti, V. Curri, P. Poggiolini, and F. Forghieri. "Performance prediction for WDM PM-QPSK transmission over uncompensated links". *Optical Fiber Communications Conference (OFC)* (2011).

[89] R. Dar, M. Feder, A. Mecozzi, and M. Shtaif. "Inter-Channel Nonlinear Interference Noise in WDM Systems: Modeling and Mitigation". *Journal of Lightwave Technology (JLT)* vol. 33 (2015).

[90] F. Vacondio, O. Rival, C. Simonneau, E. Grellier, A. Bononi, L. Lorcy, J.C. Antona, and S. Bigo. "On nonlinear distortions of highly dispersive optical coherent systems". *Optics Express* vol. 20 (2012).

[91] P. Poggiolini, G. Bosco, et al. "The LOGON strategy for low-complexity control plane implementation in new-generation flexible networks". *Optical Fiber Communications Conference (OFC)* (2013).

[92] A. Carena, G. Bosco, V. Curri, Y. Jiang, P. Poggiolini, and F. Forghieri. "EGN model of non-linear fiber propagation". *Optics Express* vol. 22 (2014).

[93] D. Semrau, R. I. Killey, et al. "A Closed-Form Approximation of the Gaussian Noise Model in the Presence of Inter-Channel Stimulated Raman Scattering". *Journal of Lightwave Technology (JLT)* vol. 37 (2019), pp. 1924–1936.

[94] D. Semrau, E. Sillekens, R. I. Killey, and P. Bayvel. "A Modulation Format Correction Formula for the Gaussian Noise Model in the Presence of Inter-Channel Stimulated Raman Scattering". *Journal of Lightwave Technology (JLT)* vol. 37 (2019), pp. 5122–5131.

[95] D. Semrau, R. I. Killey, and P. Bayvel. *The ISRS GN model*. `https://https://github.com/dsemrau/ISRSGNmodel`. 2019.

[96] H. Mathis. "On the kurtosis of digitally modulated signals with timing offsets" (2001), pp. 86–89. DOI: `10.1109/SPAWC.2001.923850`.

[97] A. Ferrari, A. Napoli, J. K. Fischer, N. Costa, J. Pedro, N. Sambo, E. Pincemin, B. Sommerkohrn-Krombholz, and V. Curri. "Upgrade Capacity Scenarios Enabled by Multi-band Optical Systems". *International Conference on Transparent Optical Networks (ICTON)* (2019).

[98] A. Souza, N. Costa, J. Pedro, and J. Pires. "Optimized Deployment of S-band and Raman Amplification to Cost-Effectively Upgrade Wideband Optical Networks". *European Conference on Optical Communication (ECOC)* (2021).

[99] Z. Gan, M. Shevchenko, S.N. Herzberg, and S. Savory. "Fast and Accurate DNN-Based Approach in Maximizing Ultra-Wideband Fiber-Optic Systems Throughput." *Optical Fiber Communications Conference and Exhibition (OFC)* (2024), paper M4K.6.

[100] D. Semrau, E. Sillekens, P. Bayvel, and R. I. Killey. "Modeling and mitigation of fiber nonlinearity in wideband optical signal transmission [Invited]". *Journal of Optical Communications and Networking (JCON)* vol. 12 (2020), pp. C68–C76.

[101] H. Buglia, E. Sillekens, A. Vasylchenkova, W. Yi, R. Killey, P. Bayvel, and L. Galdino. "Challenges in Extending Optical Fibre Transmission Bandwidth Beyond C+L Band and How to Get There". *International Conference on Optical Network Design and Modeling (ONDM)* (2021).

[102] D. Semrau. "Modeling of Fiber Nonlinearity in Wideband Transmission". *Optical Fiber Communications Conference and Exhibition (OFC)* (2022).

[103] B. Correia, R. Sadeghi, E. Virgillito, et al. "Power control strategies and network performance assessment for C+L+S multiband optical transport". *Journal of Optical Communications and Networking* 13.7 (2021), pp. 147–157. DOI: `10.1364/JOCN.419293`.

[104] D. Uzunidis, C. Matrakidis, A. Stavdas, and A. Lord. "Power Optimization Strategy for Multi-Band Optical Systems" (2020). DOI: 10.1109/ECOC48923.2020.9333398.

[105] T. Richter, S. Searcy, P. Jennevé, D.s Giannakopoulos, B. Owens, M. A. Mestre, and S. Awadalla A.and Tibuleac. "1 Tb/s and 800 Gb/s real-time transmission at 138 GBd over a deployed ROADM network with live traffic". *Optical Fiber Communications Conference and Exhibition (OFC)* (2023). DOI: 10.1364/OFC.2023.Th4C.1.

[106] H. Buglia, M. Jarmoloviius, et al. "A Closed-form Expression for the ISRS GN Model Supporting Distributed Raman Amplification" (2023). DOI: 10.1364/OFC.2023.W2A.29.

[107] M. Ranjbar-Zefreh et al. "A Real-Time Closed-Form Model for Nonlinearity Modeling in Ultra-Wide-Band Optical Fiber Links Accounting for Inter-channel Stimulated Raman Scattering and Co-Propagating Raman Amplification." *ArXiv* (2020). DOI: 10.48550/arXiv.2006.03088.

[108] Y. Jiang, A. Nespola, A. Tanzi, et al. "Experimental Test of Closed-Form EGN Model over C+L Bands". *European Conference on Optical Communications (ECOC)* (2023). DOI: 10.1109/ipc57732.2023.10360723.

[109] K. Kimura, T. Kobayashi, et al. "GN-model-based SNR estimation in 15.2-THz bandwidth inline-amplified transmission with 80-km fibre spans". *European Conference on Optical Communications (ECOC)* (2023). DOI: 10.1049/icp.2023.1909.

[110] H. Muranaka, T. Kato, T. Yamauchi, H. Irie, et al. "Modeling and Experimental Verification in S+C+L+U Quadrable-Band WDM Transmission System Using C+L-Band Transceivers and Wavelength Converters." *Optical Fiber Communications Conference and Exhibition (OFC)* (2024), paper M1F.1.

[111] K. Kimura, S. Shimizu, T. Kobayashi, et al. "Accurate SNR Estimation in C+L-Band 10-THz Hybrid Raman-EDFA Amplified Transmission Using Two-Stage Power Profile Calculation Accounting for Pump Depletion." *Optical Fiber Communications Conference and Exhibition (OFC)* (2024), paper M1F.5.

[112] Y. Zhang, X. Liu, Q. Qiu, et al. "Improved Physics-Based Raman Amplifier Model in C+L Networks Through Input Parameter Refinement." *Optical Fiber Communications Conference and Exhibition (OFC)* (2024), paper M4K.4.

[113] T. Gerard, F. J. Vaquero-Caballero, et al. "ASE Idlers for Transient Suppression in Long-haul C+L Transmission Networks". *European Conference on Optical Communications (ECOC)* (2023), paper Tu.C.5.3.

[114] A. Gallet, N. E. Dahdah, S. Yu, et al. "New SOA Based ASE Source Module With High Power, Flat Output spectrum and Low PDL" (2022), paper Mo3F.1.

ECOLE DOCTORALE

Titre: Systèmes de transmission optique cohérente ultra-large bande : de la modélisation et l'optimisation aux démonstrations expérimentales au-delà de 100 Tbit/s

Mots clés: Communications optiques, systèmes ultra-large bande (UWB), diffusion Raman stimulée (ISRS), techniques d'optimisation de la puissance et égalisation.

Résumé: Les systèmes ultra-large bande (UWB) sont considérés comme une stratégie rentable pour augmenter le débit par fibre dans les communications optiques en repoussant les limites de la bande passante opérationnelle au-delà de la bande C. Des expériences récentes ont présenté des résultats prometteurs avec des transmissions à haute capacité UWB fonctionnant à travers les bandes S+C+L, et même au-delà. Ces avancées soulèvent la question de savoir si cette technologie peut être efficacement mise à l'échelle pour répondre aux demandes croissantes de trafic de données. Cette thèse fournit une étude approfondie sur les opportunités et les défis des systèmes UWB. À travers l'analyse de modèles qui tiennent compte des dégradations dépendant de la longueur d'onde, le coeur de cette thèse consiste en le développement et la validation de techniques d'optimisation de puissance basées sur ces modèles, conçues pour améliorer la performance des systèmes UWB. L'étude réalisée comprend des évaluations numériques et expérimentales des systèmes S+C+L. De plus, la précision des prédictions obtenues dans cette étude offre des aperçus précieux sur la qualité de transmission, parmi lesquels une analyse des implications associées à d'éventuelles défaillances du système UWB. Enfin, cette thèse envisage une vision pour l'avenir de cette technologie, discutant de la faisabilité de l'adoption des systèmes UWB par rapport au déploiement de systèmes parallèles en fibre.

Title: Ultra-wideband coherent optical transmission systems: from modeling and optimization to experimental demonstrations beyond 100 Tbit/s

Keywords: Optical communications, ultra-wideband (UWB) systems, inter-channel stimulated Raman scattering (ISRS), launch power optimization techniques.

Abstract: Ultra-wideband systems (UWB) are considered a cost-effective strategy to boost the per-fiber throughput in optical communications by pushing the boundaries of operational bandwidth beyond the conventional C-band. Recent experiments have showcased promising results with UWB high-capacity transmissions operating across the S+C+L bands, and even further. These advancements raise the question of whether this technology can be effectively used to meet the growing demands for data traffic. This thesis provides an extensive investigation into the opportunities and challenges of UWB systems. Through the analysis of models that address the challenging wavelength-dependent impairments, the core of this thesis consists in the development and validation of model-based power optimization techniques designed to enhance UWB system performance. The investigation is performed in numerical and experimental assessments in S+C+L systems. Moreover, the accurate model-based predictions obtained in this study offer invaluable insights into the transmission quality. These include an analysis of the implications associated with potential UWB system failures. Finally, this thesis casts a vision for the future of this technology, discussing the feasibility of adopting UWB systems over the deployment of parallel fiber systems.

Institut Polytechnique de Paris
91120 Palaiseau, France